

Selection and implementation of deterministic and probabilistic models for the prediction of stress corrosion cracking in used nuclear fuel containment material

by

Sara Elizabeth Ferry

Double B. S., Nuclear Engineering and Physics (2011)
Massachusetts Institute of Technology, Cambridge

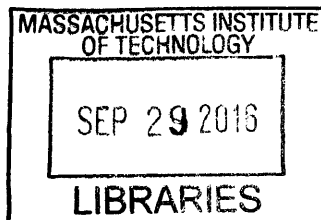
SUBMITTED TO THE DEPARTMENT OF NUCLEAR SCIENCE AND
ENGINEERING
IN PARTIAL FULFILLMENT OF THE REQUIREMENTS OF THE DEGREE OF
MASTER OF SCIENCE IN NUCLEAR SCIENCE AND ENGINEERING
AT THE
MASSACHUSETTS INSTITUTE OF TECHNOLOGY

JUNE 2016

©Massachusetts Institute of Technology
All rights reserved

Signature of author: _____ **Signature redacted** _____
Sara Elizabeth Ferry
Department of Nuclear Science and Engineering

_____ **Signature redacted** _____ April 15, 2016
Certified and accepted by: _____
Ju Li
Battelle Energy Alliance Professor of Nuclear Science and Engineering
Professor of Materials Science and Engineering
Thesis Supervisor
Chair, Department Committee on Graduate Students



ARCHIVES



77 Massachusetts Avenue
Cambridge, MA 02139
<http://libraries.mit.edu/ask>

DISCLAIMER NOTICE

Due to the condition of the original material, there are unavoidable flaws in this reproduction. We have made every effort possible to provide you with the best copy available.

Thank you.

The images contained in this document are of the best quality available.

Selection and implementation of deterministic and probabilistic models for the prediction of stress corrosion cracking in used nuclear fuel containment material

by

Sara E. Ferry

Submitted to the Department of Nuclear Science and Engineering on April 15, 2016 in Partial Fulfillment of the Requirements for the Degree of Master of Science in Nuclear Science and Engineering

ABSTRACT

Stainless steel canisters encased in vented concrete overpacks are used to store used nuclear fuel at interim spent fuel storage installations in the United States. These storage systems are exposed to the elements. There is concern that, over time, a deliquesced salt film could develop on the stainless steel canister. Such a film can create a corrosive environment in stainless steels. If a stress is present on or in then material, stress corrosion cracking (SCC) could be a possibility. Because the canister welds are not stress-relieved in order to avoid sensitization of the steel, residual stresses are expected to be present in the canisters. Thus, there is interest in determining the likelihood that (a) a sufficiently corrosive film develops on a stainless steel used fuel canister (b) there are sufficiently high stresses in the material at the location of the corrosive film (c) SCC initiates and (d) the crack propagates through the canister wall, resulting in canister failure.

This thesis begins with the assumption that a corrosive film has developed on the canister surface, and pits have begun to initiate. It investigates various methods of modeling SCC in the canister wall after the point of corrosion pit initiation.

An extensive literature review was carried out in order to understand the different SCC models that currently exist in the literature. A figure-of-merit was developed to decide which models were the most likely to be helpful to the modeling of SCC in used fuel canisters. The figure-of-merit was then used to select the most promising models. These models were then used to write MATLAB® simulations that could be used to predict time-to-failure in canisters due to SCC once corrosion pits have begun to grow. The results of these simulations are then considered and compared, and used to inform recommendations for future development of a useful predictive model of SCC in used fuel canisters.

Thesis supervisor: Ju Li

Title: Battelle Energy Alliance Professor of Nuclear Science and Engineering
Professor of Materials Science and Engineering

for Grace

Contents

| | | |
|----------|---|-----------|
| 1 | Introduction | 18 |
| 1.1 | The need for interim spent fuel storage | 18 |
| 1.2 | Stress corrosion cracking | 21 |
| 1.3 | Interim storage and stress corrosion cracking | 22 |
| 1.4 | The <i>Life Prediction of Canister Material</i> project: putting this thesis in context | 25 |
| 1.5 | An overview of this thesis | 26 |
| 2 | Selection of SCC Models | 28 |
| 2.1 | List of SCC models considered | 29 |
| 2.2 | Development of a figure-of-merit for model selection | 34 |
| 2.3 | Results of the figure-of-merit calculations | 47 |
| 2.4 | The selected SCC models | 51 |
| 3 | Implementing the selected SCC models | 54 |
| 3.1 | Model implementation strategy | 54 |
| 3.1.1 | Selection of program | 54 |
| 3.1.2 | Important assumptions | 54 |
| 3.1.3 | Modeling objectives | 56 |
| 3.1.4 | Global parameter selection | 57 |
| 3.1.4.1 | Residual stress | 57 |
| 3.1.4.2 | Threshold stress intensity | 63 |
| 3.1.4.3 | Temperature at the canister surface | 63 |
| 3.1.4.4 | Pit growth increment D | 65 |
| 3.2 | Building the models | 67 |
| 3.2.1 | Implementing the Turnbull model | 67 |
| 3.2.1.1 | Turnbull: Model structure | 67 |
| 3.2.1.2 | Turnbull: Parameter selection | 70 |
| 3.2.2 | Pitting: Henshall | 72 |
| 3.2.2.1 | Henshall: Model structure | 74 |
| 3.2.2.2 | Henshall: Parameter selection | 76 |
| 3.2.3 | Cracking: Shoji | 79 |
| 3.2.3.1 | Shoji: Model structure | 79 |
| 3.2.3.2 | Shoji: Parameter selection | 81 |
| 3.2.4 | Cracking: Wu | 89 |
| 3.2.4.1 | Wu: Model structure | 89 |
| 3.2.4.2 | Wu: Parameter selection | 90 |
| 3.2.5 | Combining the pit growth only/crack growth only models into pit-to-crack models | 95 |
| 3.3 | A note on flaw grouping and parameter variation in the models | 97 |

| | | |
|----------|--|------------|
| 3.3.1 | Henshall model | 98 |
| 3.3.2 | Shoji model | 99 |
| 3.3.3 | Wu model | 99 |
| 3.3.4 | Turnbull model | 99 |
| 4 | Results | 100 |
| 4.1 | Results: Henshall pitting model | 100 |
| 4.1.1 | Results, Henshall/Shoji pit-to-crack model | 104 |
| 4.1.2 | Results: Henshall/Wu pit-to-crack model | 107 |
| 4.1.3 | Results: Turnbull pit-to-crack model | 111 |
| 5 | Analysis of results | 114 |
| 5.1 | Implications of these results | 114 |
| 5.2 | Future work: Refining the models | 117 |
| 5.2.1 | Quantification of residual stresses | 118 |
| 5.2.2 | Experiments with weld material (general to all models) | 119 |
| 5.2.3 | Refining the Henshall pitting model | 120 |
| 5.2.4 | Refining the Henshall/Shoji model | 122 |
| 5.2.5 | Refining the Henshall/Wu model | 123 |
| 5.2.6 | Turnbull pit-to-crack model | 124 |
| 6 | Conclusions | 126 |
| 7 | Appendix A: Approaches to modeling stress corrosion cracking in stain- | |
| | less steel | 129 |
| 7.1 | Introduction | 130 |
| 7.2 | Pitting | 137 |
| 7.3 | Deterministic models of pitting, 1971-1989 | 141 |
| 7.3.1 | Sato, 1971: The electrostriction model of pitting | 141 |
| 7.3.2 | Pickering and Frankenthal, 1972: Dissolution at the pit base only | 144 |
| 7.3.3 | Galvele, 1976: Building on the work of Pickering and Frankenthal | 149 |
| 7.3.4 | Beck and Alkire, 1979: Pit growth when the pit's growth is limited by a salt film | 149 |
| 7.3.5 | Chao, Lin, and Macdonald, 1981: The point defect model of pitting | 153 |
| 7.3.6 | Okada, 1984: Halide nuclide theory and the breaching of the passive film | 159 |
| 7.3.7 | Kondo, 1989: Predicting the initiation of fatigue cracks from pits | 162 |
| 7.4 | Stochastic approaches to pitting | 166 |
| 7.4.1 | Shibata and Takeyama, 1977: A stochastic approach to modeling pitting | 166 |

| | | |
|---------|--|-----|
| 7.4.1.1 | Farmer, 1998: A model for pitting, based on the work of Shibata and Takeyama | 170 |
| 7.4.1.2 | Shibata, 1990: Later work on passivity breakdown and pitting | 172 |
| 7.4.2 | Mola, 1990: A stochastic treatment of SCC | 175 |
| 7.4.3 | Henshall, 1992: A stochastic approach to modeling pitting damage using phenomenological equations | 178 |
| 7.4.3.1 | Farmer's modifications to the Henshall model. | 186 |
| 7.5 | Crack initiation and propagation | 188 |
| 7.5.1 | Ford and Andresen, 1982-1987: A film fracture model | 188 |
| 7.5.2 | Buck and Ranjan, 1986: An expression for time to crack initiation . | 190 |
| 7.5.3 | Nakayama and Takano, 1986: A film fracture model | 193 |
| 7.5.4 | Hall, 2008: Critique of the Ford-Andresen film rupture model | 196 |
| 7.5.5 | Macdonald, 1991: Crack growth rate and current at the crack tip . . | 199 |
| 7.5.6 | Shoji, 1995: Crack tip strain and crack growth rate | 204 |
| 7.5.7 | Saito and Kuniya, 2001: Predicting SCC in Type 304 stainless steel exposed to high-temperature water | 208 |
| 7.5.8 | Ihara et al., 2013: A probabilistic approach to understanding SCC crack initiation in Type 316L Steel | 217 |
| 7.6 | Pitting to Cracking: Complete SCC Models | 221 |
| 7.6.1 | Engelhardt, 2004: A probabilistic, damage function analysis ap- proach to modeling SCC | 221 |
| 7.6.2 | Turnbull, 2006: A probabilistic model for pitting and cracking . . . | 232 |
| 7.7 | Modeling SCC in Alloy 600 exposed to primary water environments | 241 |
| 7.7.1 | Aly, 2007: SCC in Alloy 600 components used in PWRs | 241 |
| 7.7.2 | Hickling, 2002: The Materials Reliability Program (MRP) model for PWSCC in Alloy 600 | 249 |
| 7.7.3 | Wu, 2011: Combining previous models to predict SCC damage | 250 |
| 7.8 | Selected computer models for stress corrosion cracking | 258 |
| 7.9 | Wells et al., 1989: Using percolation theory to study SCC | 258 |
| 7.9.1 | Kamaya and Kitamura, 2004: A Monte Carlo study of SCC | 260 |
| 7.9.2 | Wenman, 2007: A finite element approach to studying SCC | 265 |
| 7.9.3 | Zhang et al., 2009: Simulating surface corrosion damage | 270 |
| 7.9.4 | Horner et al., 2011: Finite element analysis of corrosion pits | 272 |
| 7.10 | Modeling SCC in other systems | 277 |
| 7.10.1 | Ahn, 2013: The Sandia National Laboratory Model for SCC damage following a seismic event | 277 |
| 7.10.2 | Harlow and Wei, 1998: A probabilistic model for corrosion pits in aluminum alloys | 279 |
| 7.10.3 | Hoch et al., 1997: Mathematical models for predicting corrosion in carbon steel used fuel overpacks | 281 |
| 7.10.4 | Probabilistic approaches to predicting TGSCC in underground pipelines | 283 |

| | | |
|----------|---|------------|
| 7.10.5 | Papakonstantinou and Shinozuka, 2013: A probabilistic model for corrosion-assisted cracking in reinforced concrete structures | 288 |
| 7.11 | Other corrosion prediction techniques | 290 |
| 7.11.1 | Strutt, Nicholls, and Barbier, 1985: Predicting corrosion from corrosion profiles | 290 |
| 7.11.2 | King et al., 2012: Uncertainty in performance predictions based on experimental data | 293 |
| 7.12 | Conclusions | 296 |
| 7.13 | Future work | 298 |
| 7.14 | SCC modeling approaches summary table | 300 |
| 7.15 | Additional notes | 319 |
| 7.15.1 | SCC in the vapor-phase environment | 319 |
| 7.15.2 | Modeling species concentrations in pits and crevices | 321 |
| 7.15.2.1 | Turnbull and Thomas, 1982: Ion transport and anodic dissolution | 321 |
| 7.15.2.2 | Farmer and McCright, 1998: Modeling species concentrations during crevice corrosion | 322 |
| 8 | Appendix B | 325 |
| 8.1 | Breakdown of the $F_{\text{parameters}}$ calculation by model | 325 |
| 8.2 | Code | 330 |
| 8.2.1 | Residual stress and stress intensity functions | 330 |
| 8.2.1.1 | Implementation notes | 336 |
| 8.2.1.2 | Code for residual stress functions | 336 |
| 8.2.2 | The Turnbull model | 344 |
| 8.2.2.1 | MATLAB® code | 344 |
| 8.2.2.2 | Implementation notes | 344 |
| 8.2.2.3 | Graphs of the Gaussian distributions used to calculate constants in the Turnbull model | 348 |
| 8.2.3 | Pit growth: The Henshall model | 351 |
| 8.2.3.1 | MATLAB® code for the Henshall model | 351 |
| 8.2.3.2 | Implementation notes | 352 |
| 8.2.3.3 | Graphs of the Gaussian distributions used to calculate constants in the Henshall model | 357 |
| 8.2.4 | Pit-to-crack growth: The combined Henshall/Shoji model | 361 |
| 8.2.4.1 | MATLAB® code for the Henshall/Shoji model | 361 |
| 8.2.4.2 | Implementation notes | 361 |
| 8.2.4.3 | Graphs of the Gaussian distributions used to calculate constants in the Shoji model | 367 |
| 8.2.5 | Pit-to-crack growth: The combined Henshall/Wu model | 370 |
| 8.2.5.1 | MATLAB® code for the Wu model | 370 |

| | | |
|----------|--|------------|
| 8.2.5.2 | Implementation notes | 370 |
| 8.2.5.3 | Graphs of the Gaussian distributions used to calculate constants in the Wu model | 376 |
| 9 | Appendix C: Weld samples | 381 |
| 9.1 | Prototypical weld samples | 381 |
| 9.1.1 | Results of hardness tests | 386 |
| 9.2 | Neutron diffraction testing | 387 |

List of Figures

| | | |
|----|---|-----|
| 1 | This figure shows the size and layout of a typical dry cask storage system . . . | 19 |
| 2 | Map of locations of U.S. interim spent fuel storage installations (ISFSIs) . . . | 20 |
| 3 | Connecticut Yankee ISFSI site | 21 |
| 4 | Factors leading to stress corrosion cracking | 22 |
| 5 | Diagram of a dry storage system manufactured by Holtec | 24 |
| 6 | Graph: number of citations for each considered model | 41 |
| 7 | Numerical results of the figure-of-merit calculations, by model | 48 |
| 8 | Results of the figure-of-merit calculations, by model and category | 49 |
| 9 | Graph: estimates of residual stresses in the canister wall | 58 |
| 10 | Graph: Estimates of stress intensity K in the canister wall | 60 |
| 11 | Canister surface temperature in °C is modeled as a function of time. | 64 |
| 12 | Corrosion pit depth as a function of time for steel exposed to salt solutions | 66 |
| 13 | Turnbull model code structure flowchart | 69 |
| 14 | Henshall code structure flowchart | 75 |
| 15 | Shoji model code structure flowchart | 82 |
| 16 | Corrosion current pattern during a slip-dissolution-repassivation process | 85 |
| 17 | Corrosion current versus time for Fe-18Cr sample exposed to 1M NaCl solution | 86 |
| 18 | The schematic shows where points were collected on i_{corr} vs. time data | 88 |
| 19 | Wu model code structure flowchart | 91 |
| 20 | Flowchart of how these pitting and cracking models work | 96 |
| 21 | Henshall pitting model results: pit depth distribution | 102 |
| 22 | Henshall pitting model results: time to failure | 102 |
| 23 | Henshall pitting model results: time to failure, SD = 10% | 103 |
| 24 | Henshall pitting model results: time to failure with constant pit growth rate | 103 |
| 25 | Henshall/Shoji model results: time to failure distribution | 104 |
| 26 | Henshall/Shoji model results: time to failure distribution with 10% SD | 105 |
| 27 | Henshall/Wu model results: time to failure | 108 |
| 28 | Henshall/Wu model results: time spent in the pitting regime | 108 |
| 29 | Henshall/Wu model results: time spent in the cracking regime | 109 |
| 30 | Henshall/Wu model results: time to failure, SD = 10% | 109 |
| 31 | Turnbull model results: time to failure | 111 |
| 32 | Turnbull model results: time to failure, SD=50% | 112 |
| 33 | A crack initiated from a corrosion pit in stainless steel condenser tubes | 132 |
| 34 | Conditions leading to chloride-induced SCC in steel | 134 |
| 35 | Possible corrosion pit shapes | 138 |
| 36 | Photographs of corrosion pits with different morphologies | 139 |
| 37 | Causes of internal stress in oxide films, as identified by N. Sato. | 142 |
| 38 | Film pressure (in units of kg per cm ²) as a function of film thickness | 143 |
| 39 | Pit schematic in the Pickering and Frankenthal model | 145 |

| | | |
|----|--|-----|
| 40 | Pickering and Frankenthal: concentration profiles and corrosion current . . . | 147 |
| 41 | A schematic of a pit in the Beck and Alkire model | 150 |
| 42 | Buildup of vacancies at the metal-film interface in the point defect model . | 157 |
| 43 | Schematic of halides breaching the passive metal oxide film | 160 |
| 44 | Variation of pitting probability with pitting potential for steel samples . . . | 169 |
| 45 | Illustration of damage functions for pitting in the Henshall model | 179 |
| 46 | Henshall: Example simulation results for 10, 40, 100, and 125 timesteps . . | 180 |
| 47 | Average and maximum pit depths as a function of chloride concentration . | 185 |
| 48 | Relationship between potential, slip step formation rate, and crack propa- gation in a slip-dissolution-repassivation model | 195 |
| 49 | Slip-dissolution-repassivation in the Saito model | 209 |
| 50 | Crack growth rate as a function of stress intensity in the Saito model | 216 |
| 51 | Slow strain rate test results in the Ihara microcrack study | 219 |
| 52 | Time to SCC initiation as a function of stress in the Ihara model | 220 |
| 53 | Percentage of pits expected to initiate a crack as a function of pit depth . . | 228 |
| 54 | Turnbull model results compared with experimental results | 238 |
| 55 | Processes that affect stress corrosion cracking behavior in steel | 243 |
| 56 | Corrosion submodes for Alloy 600 | 247 |
| 57 | Crack growth rates in Alloy 600 | 251 |
| 58 | Posterior joint distribution calculations in the Wu model | 256 |
| 59 | Experimentally observed crack rates as a function of K in Alloy 600 | 257 |
| 60 | Crack progression across active grain boundaries in a percolation model . . | 259 |
| 61 | Single-crack growth rate simulation by Kamaya and Kitamura | 263 |
| 62 | A flowchart of the modeling process used by Kamaya and Kitamura | 264 |
| 63 | A finite element approach to studying SCC in steel pipes | 268 |
| 64 | A finite element approach to studying SCC in steel pipes, continued | 269 |
| 65 | Finite element analysis of strain distributions around a 100 μm pit | 273 |
| 66 | Finite element analysis of strain distributions around a 500 μm pit | 274 |
| 67 | Tomographic reconstructions of pits and cracks | 276 |
| 68 | A simplified pit as modeled in CAMLE | 283 |
| 69 | A Bayesian approach to estimating pipeline wall stress | 286 |
| 70 | Using corrosion profiles to predict future corrosion damage | 291 |
| 71 | Fitting equations to narrow data sets can lead to inaccuracies | 295 |
| 72 | Fourth-order Fourier fit for best-estimate residual stress estimate | 330 |
| 73 | Fourth-order Fourier fit for barely-above-threshold residual stress estimate . | 333 |
| 74 | Fourth-order Fourier fit for highly-tensile residual stress estimate | 333 |
| 75 | Eighth-order Fourier fit for best-estimate residual stress estimate | 334 |
| 76 | Eighth-order Fourier fit for barely-above-threshold residual stress estimate . | 335 |
| 77 | Eighth-order Fourier fit to highly-tensile residual stress estimate | 335 |
| 78 | Turnbull model: α has a mean value of 0 | 349 |
| 79 | Turnbull model: β has a mean value of 0.37 | 350 |

| | | |
|-----|--|-----|
| 80 | Turnbull model: C has a mean value of 2.6×10^{-18} | 350 |
| 81 | Turnbull: q has a mean value of 3 | 351 |
| 82 | Henshall: E_0 has an average value of 1.4 | 358 |
| 83 | Henshall: E_1 has an average value of 0.47 | 358 |
| 84 | Henshall: A_4 has an average value of 10^{-7} | 359 |
| 85 | Henshall: B_4 has an average value of 0.4 | 359 |
| 86 | Henshall: B_5 has an average value of 0.3 | 360 |
| 87 | Henshall: C_4 has an average value of 0.2 | 360 |
| 88 | Shoji: m has a mean value of 0.567 | 368 |
| 89 | Shoji: n has a mean value of 1.36 | 368 |
| 90 | Shoji: β has a mean value of 5.08 | 369 |
| 91 | Shoji: λ has a mean value of 0.11 | 369 |
| 92 | Wu: C_1 has a mean value of 9.7×10^{-12} | 377 |
| 93 | Wu: C_2 has a mean value of 2.86×10^{-12} | 377 |
| 94 | Wu: m_1 has a mean value of 0.2286 | 378 |
| 95 | Wu: m_2 has a mean value of 0.1836 | 378 |
| 96 | Wu: n_1 has a mean value of 0.8982 | 379 |
| 97 | Wu: n_2 has a mean value of 0.7360 | 379 |
| 98 | Wu: β_2 has a mean value of 0.3418 | 380 |
| 99 | A section of the weld plate used for material testing | 382 |
| 100 | A polished weld specimen showing the geometry of the weld | 383 |
| 101 | A composite micrograph of the weld showing the border of a “vee” | 384 |
| 102 | An etched and polished micrograph showing both “vees” | 385 |
| 103 | The results of a hardness test of the weld specimen. | 386 |
| 104 | Neutron diffraction testing: preliminary RS measurements, transverse | 388 |
| 105 | Neutron diffraction testing: preliminary RS measurements, normal | 389 |
| 106 | Neutron diffraction testing: preliminary RS measurements, longitudinal | 390 |

List of Tables

| | | |
|----|--|-----|
| 1 | Models considered in the figure-of-merit analysis | 35 |
| 2 | Residual stress profiles through the canister wall | 61 |
| 3 | Stress intensity through the canister wall | 62 |
| 4 | Constants used in the Turnbull SCC model | 72 |
| 5 | The average values of the constants used in the code for the Henshall model | 77 |
| 6 | Material property values for Type 304 stainless steel used in the Shoji model | 81 |
| 7 | Composition of Type 304 stainless steel weld samples by weight percent . . | 83 |
| 8 | Constant values for Equations (12) and (13) | 93 |
| 9 | Time-to-failure results of the Henshall pitting model | 101 |
| 10 | Time-to-failure results of the Henshall/Shoji pit-to-crack model | 105 |
| 11 | Time-to-failure results of the Henshall/Wu pit-to-crack model | 107 |
| 12 | Time-to-failure results of the Turnbull pit-to-crack model | 111 |
| 13 | Time-to-failure results of the Turnbull pit-to-crack model, continued | 112 |
| 14 | More information about the Henshall model | 120 |
| 15 | More information about the Shoji model | 122 |
| 16 | More information about the Wu model | 123 |
| 17 | More information about the Turnbull model | 124 |
| 18 | Composition of common stainless steels (in weight percent) | 135 |
| 19 | Boundary conditions and constraints | 146 |
| 20 | Variable definitions for Equations (21), (22), and (23) | 148 |
| 21 | Variable definitions for the Beck & Alkire Equations (Section 7.3.4) | 152 |
| 22 | Variable definitions for Section 7.3.5 | 154 |
| 23 | Passive film breakdown theories prior to 1981 | 155 |
| 24 | Variable definitions for Equations (35) - (37) | 158 |
| 25 | Variable definitions for Farmer's deterministic pitting model | 171 |
| 26 | Variable definitions for Equations (91),(92), and (93) | 189 |
| 27 | Variable definitions for Section 7.5.2 | 191 |
| 28 | Variable definitions for the Nakayama and Takano model | 194 |
| 29 | Variable definitions for the Hall model | 197 |
| 30 | Variable definitions for Equation (115) | 202 |
| 31 | Variable definitions for Equations (116) - (119) | 203 |
| 32 | Variable definitions for the Shoji model | 207 |
| 33 | Variable definitions for Equation (128) | 210 |
| 34 | Variable definitions for Equation (129) | 211 |
| 35 | Variable definitions for Equations (132) and (133) | 212 |
| 36 | Differential damage functions in the Engelhardt model | 229 |
| 37 | Variable definitions for the Engelhardt model | 229 |
| 38 | Variable definitions for Equation (167) | 244 |
| 39 | Variable definitions for the Hickling model | 249 |

| | | |
|----|--|-----|
| 40 | Variable definitions for Hickling and Wu models | 254 |
| 41 | Variable definitions for Equation (180) | 255 |
| 42 | Equations and variable definitions of the Zhang model (Section 7.9.3) . . . | 271 |
| 43 | Probability of finding a given K in canister material | 278 |
| 44 | Bayesian terms used by Jain et al. (Equation (198)) | 285 |
| 45 | Modeling approaches: a summary | 301 |
| 46 | Oxidation rates in stainless steels | 320 |
| 47 | Variable definitions for Section 7.15.2.2 | 324 |
| 48 | Calculating $F_{\text{parameters}}$ for the pit initiation models | 326 |
| 49 | Calculating $F_{\text{parameters}}$ for the pitting models | 327 |
| 50 | Calculating $F_{\text{parameters}}$ for the crack growth models | 328 |
| 51 | Calculating $F_{\text{parameters}}$ for the transition models | 329 |
| 52 | Calculating $F_{\text{parameters}}$ for the complete models | 329 |
| 53 | Data used to estimate residual stress profile through canister wall | 331 |
| 54 | Data used to estimate stress intensity profile through canister wall | 332 |

1 Introduction

1.1 The need for interim spent fuel storage

Nuclear power is an important source of electricity in the United States. As of July 2014, there are 62 operating nuclear power plants, comprising 100 individual reactors, and they supply the country with approximately 20% of its electricity [1, 2].

The United States does not reprocess commercial reactor fuel, and must therefore address the issue of used nuclear fuel disposal. Used nuclear fuel assemblies, upon being removed from the reactor core, are transferred to a storage pool, where the water acts as an efficient coolant for the decay heat and as an effective radiation shield.

However, space in these pools is limited. When a spent fuel pool's capacity is exceeded, the older fuel, which now has a lower temperature and radiation level, is transferred out of the pool and into dry storage. Assemblies are dried and placed in specially designed stainless steel canisters. These canisters are then backfilled with inert gas and bolted or welded shut. The canisters are then placed inside a secondary overpack system. In the United States, this typically takes the form of a large concrete cask with venting holes which allow for passive cooling of the steel canister surface. Figure 1 shows the typical design of a spent fuel canister inside an upright concrete overpack.

Dry cask storage was intended to be an interim storage solution, which would solve the problem of full storage pools while waiting to transfer used nuclear fuel to a completed repository. In 1987, it was determined that Yucca Mountain would become the site of this centralized nuclear waste repository, and its opening was scheduled for 1998. The cost for collection and transfer of fuel, and maintenance of the repository, was to come from the Nuclear Waste Fund. American utilities paid into this fund based on the amount of electricity generated by their nuclear plants.

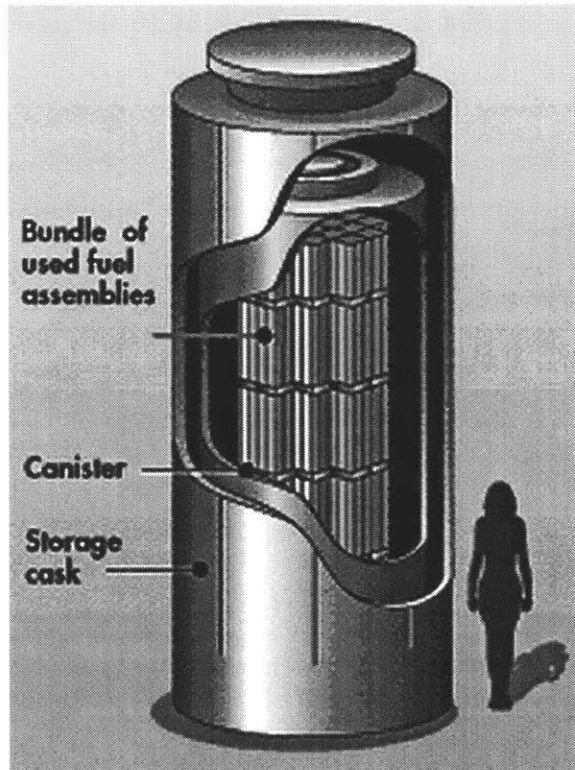


Figure 1: This figure shows the size and general layout of a typical dry cask storage system. Used fuel assemblies are sealed inside a steel canister, which is placed inside a large concrete overpack. Venting in the overpack allows for passive cooling of the canister surface. [3]

However, after years of public controversy and political opposition, the facility was never opened for use. In 2010, federal funding for Yucca Mountain ceased. Nuclear power plants continued operation as normal, but faced at-capacity storage pools and no option for fuel disposal. Interim dry cask storage effectively became *the* storage solution. There is no known timeline for the selection and completion of a used fuel repository. Cask systems that were expected to see just several years of use prior to transferral to a repository are now expected to see decades of use.

U.S. Independent Spent Fuel Storage Installations

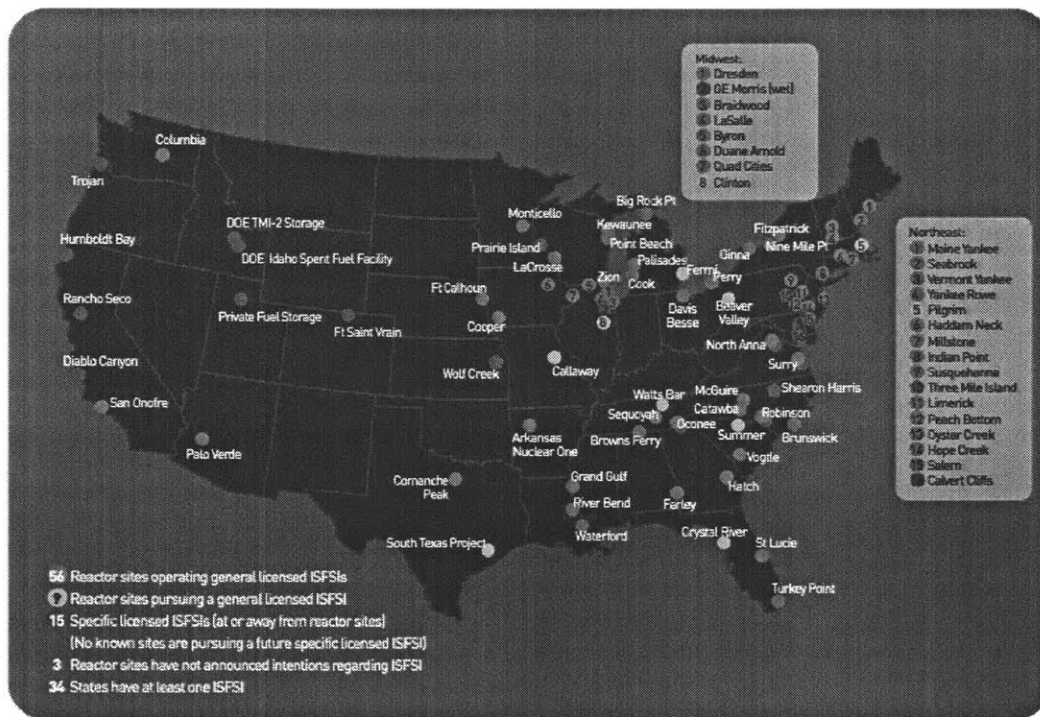


Figure 2: This map shows the locations of interim spent fuel storage installations (ISFSI) in the United States. Blue dots mark the locations of existing ISFSI sites, and red dots mark the locations of planned sites. [3]

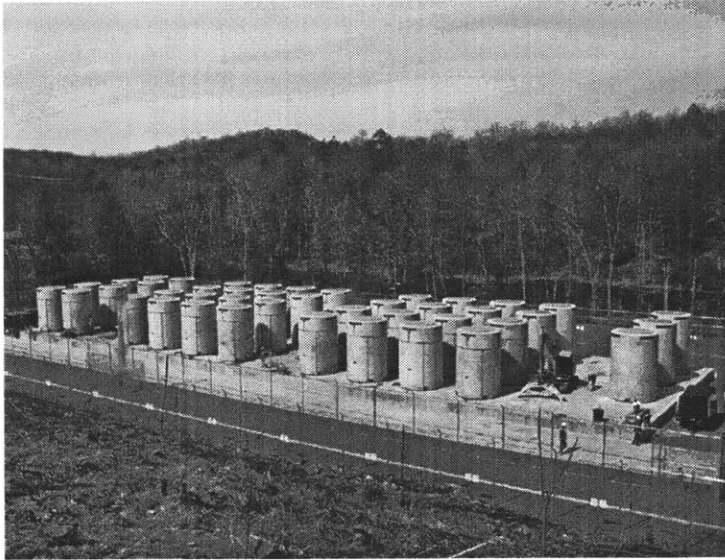


Figure 3: The ISFSI at Connecticut Yankee consists of dry cask storage systems on a secure concrete pad. [4]

Groups of casks are stored together at interim spent fuel storage installations, or ISFSIs. Figure 2 shows the locations of existing and planned ISFSI sites in the United States. As of 2012, there were approximately 1600 filled dry storage casks in the United States [5]. Figure 3 shows the ISFSI at the decommissioned Connecticut Yankee nuclear power plant. The dry casks are kept on a secure concrete pad and monitored periodically.

1.2 Stress corrosion cracking

Stress corrosion cracking (SCC) occurs when a susceptible material is exposed to a combination of an aggressive environment and stress that is sufficient to initiate a crack. SCC can lead to the rapid failure of materials that do not appear to be otherwise severely damaged by corrosive processes. Figure 4 shows the diagram that is commonly used to illustrate the situations in which SCC may occur. For a given susceptible material, SCC may only occur

under a specific subset of environments, or when a certain threshold stress is exceeded. This makes SCC particularly challenging to predict.

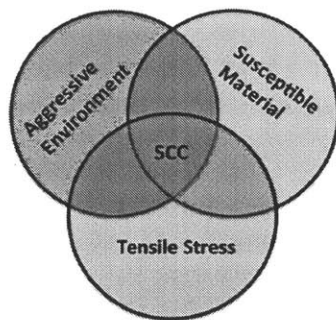


Figure 4: A combination of a susceptible material, an aggressive environment, and the presence of stress can lead to stress corrosion cracking.

Certain materials may initiate SCC directly from the material surface. Others, like stainless steels, may tend to undergo corrosion pitting prior to the initiation of a crack. The corrosion pit can act as a stress concentrator. The environment inside the pit may also be more aggressive than the bulk fluid. Section 7.2 on page 137 further explains the corrosion pitting phenomenon.

1.3 Interim storage and stress corrosion cracking

The dry cask containment systems used to store used nuclear fuel are designed to be extremely durable and resistant to the severe weather, impact forces, and general corrosion and environmental degradation that can occur when a system is exposed to the elements

for long periods of time.

However, the canisters are now expected to remain at ISFSI sites for much longer than originally anticipated, since the dry cask storage systems were only to be used until the spent fuel could be transported to Yucca Mountain. Now, the ISFSI sites will likely be used to store the used fuel until a final storage solution has been implemented.

The stainless steels used to fabricate the canisters can be susceptible to SCC when exposed to a chloride-containing solution [6]. The design of the concrete overpacks leaves the stainless steel canisters exposed to any particulates that enter through the vents. In areas with salt content in the air, such as the coastal locations where many ISFSIs are found, this could lead to the deposition of chloride particles on the canister surface.

Given sufficient chloride deposition on the canister surface, and the right combination of relative humidity in the air and temperature at the canister surface, deliquescence may occur. This occurs when the chloride deposits absorb moisture from the air, creating a highly-concentrated aqueous chloride solution. Stainless steel exposed to such a solution may experience corrosion.

This leaves one more requirement for SCC: the presence of stress. In the case of the canisters, this comes from the residual stresses created by the canister fabrication process. Typically, each half of the canister material is rolled and welded longitudinally, and then the halves are combined with a single circumferential weld. An example is shown in Figure 5.

In order to avoid sensitization and a subsequent decrease in corrosion resistance, these welds are not stress-relieved. As a result, residual stresses are present in and near the canister welds. If a chloride-containing aqueous film develops on a canister surface, it is possible that SCC could occur if the chemistry and local conditions are sufficiently aggressive and the residual stresses in the material at the location where the film develops

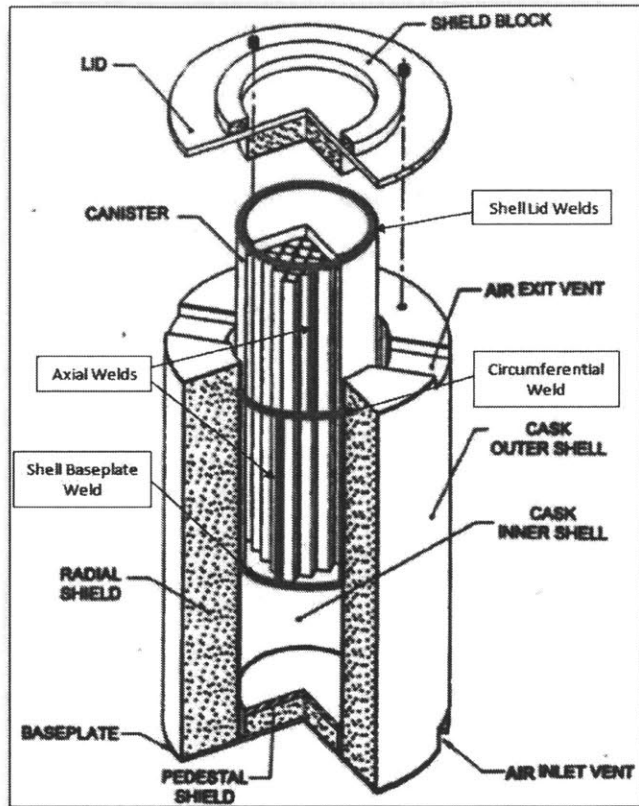


Figure 5: This diagram shows a dry storage system manufactured by Holtec. The locations of the welds used to fabricate the inner steel canister are highlighted in red. *Original diagram from Holtec; modified by B. Black.* [32]

are sufficiently high.

1.4 The *Life Prediction of Canister Material* project: putting this thesis in context

The overall goal of the *Life Prediction of Canister Material* project is to understand and predict how and when SCC can occur in the stainless steel canisters used in the dry storage cask systems at ISFSI sites. This is, in effect, a two part prediction. The first part involves modeling the evolution of the environment at the canister surface. Temperature of the canister surface, combined with the external fluctuations in temperature and humidity, salt content in the air, and the rate of chloride deposition via the overpack venting are to be modeled in order to predict the likelihood that an aggressive chloride solution could develop on the canister surface, and be sustained for long enough that corrosion or SCC could occur.

Assuming that an aggressive environment is developed and sustained on the surface, it is then necessary to predict the likelihood that SCC will occur, given the material properties and residual stresses present through the canister wall. By combining both models, it becomes possible to predict the likelihood that SCC will occur in a given canister. This thesis focuses on this aspect of the project.

In order to develop this model, it is necessary to fully understand the residual stresses present in a typical canister. To this end, prototypical weld material was obtained (see Section 9, Appendix C). The residual stresses in this material were measured experimentally.¹ It is expected that these samples will also be used for experimental testing in chloride environments.

This work contributes to the objectives of the *Life Prediction of Canister Material*

¹See Section 9.2, which includes selected preliminary results of strain measurements obtained using neutron diffraction methods.

project by focusing on the probabilistic modeling of stress corrosion cracking once flaw initiation has occurred. Multiple models of pitting, crack growth, and SCC specifically are critically considered with regard to their potential usefulness for this project. A methodology is developed for selecting the best models to implement to model SCC in canisters. In total, five pit-to-crack models are adapted for use with a typical canister, and their results are compared in order to (1) further understand the relative strengths and weaknesses of each model and (2) make an estimate as to the probability of SCC propagating through a canister wall given the evolution of an aggressive environment and the initiation of a flaw.

1.5 An overview of this thesis

This thesis begins with an overview of the expected process of stress corrosion cracking in canister material.

Next, the list of pitting, cracking, and SCC models from the literature that were considered for use in this project is given. A brief description of each model is included, along with the appendix page on which a more thorough description of the model can be found.

Next, the process used to develop a figure-of-merit to select which model(s) should be used in this project is explained. The figure-of-merit is then applied to each of the models considered from the literature, and the results are given.

For the selected models, the strategy used to implement each of them in a computer code is explained. The rationale behind the values of the various functions, parameters, and coefficients used in each model is explained: first, “global” parameter and function selection is considered. These are used in each of the selected models. Next, each model is considered individually, and the parameter selection relevant to each specific model is explained. An overview of the coding scheme for each model is provided.

Then, the results of running each model are provided. The analysis section considers

these results in the context of their implications for canister failure, and for their implications with regards to model selection and refinement. Strategies for refining each model for better predictions are included.

There are three appendices to this thesis. Appendix A is the full literature review that was carried out to survey and understand the pitting and cracking models that already exist. Appendix B contains additional information relevant to this thesis, including additional information that pertains to the calculation of the figure-of-merit and the full code used to predict failure times from each selected model. Appendix C includes research results that pertain to the study of real canister material. These results are not used in this thesis, but are relevant to the overall study of canister behavior. Appendix C includes metallography and hardness testing results for a real canister sample and the preliminary results of a neutron diffraction study carried out to measure the real residual stresses in the canister material.

2 Selection of SCC Models

Existing models for stress corrosion cracking and/or pitting, particularly those that pertain to passivating metals exposed to a chloride-containing solution, were examined in depth. A thorough review of the models considered is presented in Appendix A (see page 129) and formed the basis for the selection of SCC models to be used in this work. Stress corrosion cracking is expected to proceed in canister material as follows:

1. Pits initiate at the surface of the susceptible material when the environment is sufficiently aggressive.
2. The pit grows. Whether or not the pit continues growing, and how fast it grows, is dependent on some combination of environmental conditions, material conditions, and pit geometry.
3. When certain criteria are met, the pit transitions to a crack. Typically, these criteria include some combination of (a) a threshold material stress being exceeded at the current flaw depth (b) a threshold depth being exceeded and (c) a theoretical crack growth rate at the current depth exceeding the actual pit growth rate at that depth. Continued crack growth, and the rate of crack growth, is dependent on some combination of environmental conditions, material conditions (especially residual or applied stress), and crack geometry.
4. When the crack has propagated through the component, failure has occurred.

The models typically encompass one or several of these stages of SCC (pit initiation, pit growth, pit-to-crack transition, crack growth). The models considered in Appendix A which were deemed to have the most potential relevance to the objectives of the *Life Prediction of Canister Material* project are listed in the next section. A figure-of-merit

was developed for the purposes of identifying the models which are the most promising for use in this project. The figure-of-merit is explained in Section 2.2, and the results of the figure-of-merit calculation are given in Section 2.3.

Attention is given to models that pertain to all four SCC stages listed above. However, in this work, an initial pit distribution is assumed, and only pit growth, pit-to-crack transitions, and crack growth are modeled. Since the overall objective of this project is to develop a complete predictive model for SCC in the canisters, figure-of-merit calculations are carried out for the pit initiation models, since it is presumed that this will be useful for future efforts to develop a complete model.

2.1 List of SCC models considered

The following models were selected for further consideration. Each model is considered in greater detail in Appendix A. The page on which this information can be found is listed next to each model name. All models considered in Appendix A are also summarized in the chart in Section 7.14.

Pit initiation Models

1. **Sato, [7], page 141.** A passive film on the surface of a metal is subjected to electrostriction pressure. At a threshold level of pressure, the film ruptures, leaving the metal underneath susceptible to corrosion. The model describes the pressure in the film as a combined effect from electrostriction pressure and interfacial tension. It also provides a method of relating the ion concentrations present to the electric potential at which the electrostriction pressure becomes high enough to induce film breakdown.
2. **Chao, Lin, and Macdonald, [8, 9], page 153.** The “point defect model” describes

a scenario in which voids form at the interface between a metal surface and its passive film due to vacancy pileup. At a threshold void size, local film breakdown occurs, leaving the metal susceptible to corrosion. The model provides expressions for the grow of the passive film, the critical pitting potential, and the threshold number of vacancies required to form a breakdown-inducing void.

3. **Okada, [10], page 159.** The “halide nuclide theory” of pit initiation proposes that an aqueous halide solution forms on the film surface and eventually breaches it. The model includes expressions for the critical pitting potential as a function of halide concentration and the time to pit initiation.
4. **Shibata and Takeyama, [11, 12], page 166.** This stochastic model describes the probability that a unit area of metal surface will generate a pit in an interval of time.

Pit Growth Models

1. **Pickering and Frankenthal, [13], page 144; Galvele, page 149.** The Pickering and Frankenthal model assumes that the pit has an active base where dissolution is occurring, but inactive walls, such that pits grow deeper but not wider. The model develops expressions for the spatial flux of the relevant species (particularly the dissolved metal ions), which can then be used to understand how the pit is growing. Galvele’s modifications to the Pickering and Frankenthal model include the development of a relationship between pit potential and salt concentration.
2. **Beck and Alkire, [14], page 149.** In the Beck and Alkire model, a salt film builds up on the walls of the pit. As the film builds up, it impedes continued pit growth. The model includes expressions for the flux of salt ions from a dissolving film, for the thickness of the salt film, and for the pit radius as a function of time.

3. **Mola, [15], page 175.** Mola's stochastic model of pit growth begins by assuming that pits nucleate at inclusions in the metal, so the distribution of inclusions is the first step to determining where pits initiate. Expressions are developed for the probability that a pit will be formed at a possible site, as well as for the average time to pit nucleation. The probability, and the time-rate-of-change of that probability, that a pit will grow to an arbitrary volume is determined.
4. **Henshall, [35, 16, 17], page 178.** Henshall's stochastic model of pit growth includes expressions for the probability of pit nucleation, pit death, and pit growth. The parameters characterizing these probabilities are dependent on environmental and material conditions such as stress intensity, temperature, and chloride ion concentration. The environmental inputs used to calculate these parameters are time dependent, which allows the model to account for a changing environment.

Pit-to-crack transition models

1. **Kondo, [18], page 162.** Kondo's model estimated the pit growth rate in a low carbon steel, and predicted the point at which a pit would reach a critical size and transition to a crack. In the Kondo model, cracks initiate when the actual pit growth rate is exceeded by the theoretical crack growth rate at the current depth (crack growth rate is a depth-dependent quantity). This model provided a basis for Turnbull and other later SCC models.

Crack growth models

1. **Ford and Andresen, [19], page 188.** This crack growth model outlines the basis of the slip-dissolution-repassivation (SDR) model of SCC. In the SDR model, there is a cycling process occurring at the crack tip as the passivating metal undergoes slip,

exposing bare metal. This metal begins to dissolve, since it is in direct contact with the aggressive environment (such as a chloride-containing solution). The slip and subsequent dissolution contribute to the growth of the crack. As soon as slip occurs, the repassivation process begins, such that the observed dissolution current decays exponentially. This process repeats until the crack is arrested or the component fails.

2. **Nakayama and Takano, [20], page 193.** This is another SDR model. It provides a different version of the dissolution current density equation than the one given by Ford and Andresen. Both this model and the Ford and Andresen model provide the same general expression for crack growth rate, $\frac{da}{dt} = \frac{M\langle i \rangle}{zF\rho}$.
3. **Shoji et al., [21], page 204.** The Shoji model is an SDR model, but provides a different formulation of the crack growth rate. Here, $\frac{da}{dt}$ is a function of film strain and crack tip strain rate instead of corrosion current. An explicit expression for crack tip strain rate as a function of crack growth rate and stress intensity is provided.
4. **Hall, [22], page 196.** The M. M. Hall model is an SDR model that aims to correct alleged mathematical inconsistencies in the Ford-Andresen version of SCC crack growth.
5. **Macdonald, [23], page 199.** This is an SDR model that also provides a modified version of the crack growth rate, as it accounts for crack geometry. An expression for the average dissolution current is provided, and is dependent on various interfacial potentials.
6. **Saito, [24], page 208.** Saito's model of crack growth involves both an SDR mechanism and plastic deformation at the crack tip. This combines environmental and mechanical mechanisms of crack growth. An expression for strain rate at the crack tip (different from the one used by Shoji et al.) is provided.

7. **Aly, [25], page 241.** Aly's model for SCC in Alloy 600 components exposed to a PWR environment includes expressions for the time-to-failure (dependent on temperature, stress, and environmental constants) and crack length as a function of time.
8. **Hickling et al., [26], page 249.** This EPRI model for SCC crack growth rate in Alloy 600 components exposed to a PWR environment is dependent on stress intensity factors, temperature, and fitting parameters.
9. **Wu, [27], page 250.** This model builds on the Hickling model for crack growth rate, and adds in dependencies on yield strength, pH, and additional fitting parameters. It also models three distinct crack growth stages. The transition between these stages is determined by stress intensity.

Crack initiation models

1. **Ihara, [28], page 217.** This model relates transgranular microcracks in stainless steels exposed to a BWR environment to the onset of macroscopic cracking.
2. **Buck and Ranjan, [29], page 190.** This model developed a time to SCC onset as a function of potential and stress, and for "crack tip opening displacement." The material displacement caused by flaws affects the growth of cracks: for example, the amount of displacement caused by a pit will affect the crack propagation rate of a crack that initiates from that pit.

Complete models

1. **Engelhardt, [30], page 221.** This deterministic model develops expressions for pit growth rate, the distribution of pits propagating at a certain rate, the rate of pit repassivation, and a series of differential damage functions. These differential damage

functions pertain to active pits, passive pits (“dead” pits), and cracks. They model how the possible modes of damage proceed in a sample.

2. **Turnbull, [31], page 232.** This probabilistic model of SCC begins by using a Weibull distribution to describe the initial distribution of pits on a sample surface. All of these pits are assumed to grow, although their growth rates are distributed, and may be distributed such that some pits exhibit extremely slow growth, and can thus be modeled as “dead” pits. Expressions for pit growth and crack growth are provided. They depend on parameters that are either constants fit to data or constants selected from an appropriate distribution. Each pit has a unique pit/crack growth rate. Crack growth rate is dependent on stress. Pits transition to cracks when a flaw has both (1) propagated past a certain threshold depth, and (2) when the theoretical, depth-dependent crack growth rate for that flaw exceeds the actual pit growth rate.

Table 1 lists each model that is considered in the figure-of-merit analysis. Note that additional models not included in the figure-of-merit-analysis were considered in the SCC model review, which can be found in its entirety in the appendix section.

2.2 Development of a figure-of-merit for model selection

The objective of determining an overall figure-of-merit, F_{total} , for each considered SCC model was to determine which models would be most favorable to the initial modeling effort of the *Life Prediction of Canister Material* project. The most favorable models would be most compatible with furthering the project goals. A favorable model would:

- Be probabilistic in nature, and accurately reflect the stochastic nature of SCC.

Table 1: Models considered in the figure-of-merit analysis

| Pit initiation | Pit Growth | Crack Growth | Other |
|--|---|-----------------------------|--|
| Sato Electrostriction Model | Pickering & Frankenthal Active Pit Base | Ford & Andresen SDR | Complete |
| Chao, Lin, & Macdonald Point Defect Model | Beck & Alkire Salt film on pit walls | Nakayama & Takano SDR | Turnbull Probabilistic SCC |
| Okada Halide Nuclide Theory | Galvele Electrostriction Model | Shoji SDR | Engelhardt Deterministic SCC |
| Shibata & Takeyama Stochastic Pit Initiation | Mola Stochastic pit growth | Hall SDR | Pit-to-Crack Transition Models |
| Farmer (after Shibata & Takeyama) | Henshall Stochastic pit growth | Macdonald SDR | Kondo Fatigue CGR = PGR |
| | Henshall, with Farmer modifications | Saito SDR | Crack Initiation Models |
| | | Aly Alloy 600 | Buck & Ranjan Crack tip opening displacement Microcracking |
| | | Hickling Alloy 600 | Ihara Probabilistic crack initiation Microcracking |
| | | Wu Alloy 600 | |

- Predict how pits initiate, grow, and transition to cracks that propagate through the material. These predictions should be affected by local conditions (environment, stress).
- Be valid in the environment of interest (welded stainless steel, typically of Type 304 or Type 316, exposed to a chloride-containing aqueous film, whose formation and longevity is dependent on environmental conditions).
- Follow assumptions and conventions that are viewed as valid within the scientific community.
- Follow assumptions and conventions that are valid for the actual mode of SCC experienced in canister material (e.g. if the selected SCC model depends on a very specific theory of SCC development and propagation, it must be shown that this theory accurately describes SCC phenomena in the canisters).
- Account for the effects of residual stress in the canister material (especially in and near the weld).
- Be realistic for practical use (e.g. the model must perform well over the range of environments of interest, and not just in one specific set of environmental conditions).

Accordingly, a total figure-of-merit (F_{total}) was calculated for each model using the following equation.

$$\begin{aligned}
F_{\text{total}} = & \\
& F_{\text{stochastic}} + F_{\text{complete}} + F_{\text{envt/matl}} + F_{\text{citations}} + \\
& 2 \cdot F_{\text{stress}} + F_{\text{specificity}} + F_{\text{parameters}} + F_{\text{adapt}}
\end{aligned} \tag{1}$$

The seven terms of Equation (1) are described in more detail below.

1. $F_{\text{stochastic}} = 1$ if the model is stochastic, 0 otherwise
2. $F_{\text{complete}} = 1$ if the model is complete, 0 otherwise
3. $F_{\text{envt/matl}} = 0.5$ (if metal passivates) + 0.25 (if metal is passive and an alloy of interest) + 0.25 (if environment contains chlorides) + 0.25 (if the environment is similar to a deliquesced film), with the “metal” and “environment” here pertaining to the metal and environment considered when the model was developed
4. $F_{\text{citations}} = N_i/N_{\text{max}}$, where N is the number of citations for model i and N_{max} is the highest number of citations obtained by an individual model
5. $F_{\text{stress}} = 1$ if model has an explicit dependence on stress, 0.5 if model has a dependence on K , and 0 if model has no dependence on stress²
6. $F_{\text{specificity}} = 1$ if dependence on a specific theory is strong, 0.5 if dependence on a specific theory is weak, and 0 if there is no dependence on a specific theory

²Note that pitting models and pit initiation models are not expected to have a strong stress dependence, and should be judged relative to models in their own SCC stage subgroup. All pit initiation and pit growth models have $F_{\text{stress}} = 0$. In this thesis, crack growth is considered to be far more dependent on stress on or in the material.

7. $F_{\text{parameter}} = (0.5N_{\text{macroscopic}} + N_{\text{microscopic}} + 2N_{\text{atomic}} + 0.25N_{\text{characterizing}} + 2N_{\text{fitting}})^{-1}$,
where N_x is the number of parameters in the model that fall into category x
8. $F_{\text{adapt}} = F_{\text{temp}} + F_{\text{chem}}$, where $F_{\text{temp}} = 0.5$ if the model includes a temperature dependence, and $F_{\text{chem}} = 0.5$ if the model includes a dependence on the environment chemistry (the factor of primary interest being the chloride concentration)

Each of these seven components refer to a model criterion that was used for selection of the best models for this project. The reasons that these criteria were selected are explained below. Where relevant, additional notes regarding applications of a given criterion to a specific model are included.

Criterion 1. The Model is Stochastic in Nature

Models which were already constructed to be stochastic or probabilistic in nature were considered to be more favorable for this modeling effort, since deterministic models must be adapted to probabilistic forms if they are selected.

Defining $F_{\text{stochastic}}$: Since this is a binary criterion, $F_{\text{stochastic}}$ is equivalent to 1 if the model is stochastic, and 0 if it is not. A value of -0.5 was added to this score if the model did not include explicit expressions for the outputs of interest (e.g., an equation for dissolution current is provided, but not for the corresponding flaw growth rate).

Criterion 2. The Model is Complete

Models which are already complete, in the sense that they begin with an initial assumed distribution of pits, and proceed to model pit growth, the transition from pit to crack, and crack growth, were more favorable for the initial modeling effort. In a final modeling effort, in order to join multiple different models together (e.g. one model for pit growth,

a second for crack growth), it must be shown that the different models are compatible with each other. This presents an additional challenge because different models may have been developed under different assumptions, or may include parameters that were fit to experimental data collected under different sets of conditions.

Only the Engelhardt and Turnbull models are “complete” in this sense. Note that in the final model, pit initiation must be considered, and neither Engelhardt nor Turnbull describe pit initiation (beyond assuming an initial pit distribution). The pit initiation step will link the SCC model with the environmental evolution model in any final modeling effort.

Defining F_{complete} : Since this a binary criterion, F_{complete} is equivalent to 1 if the model is complete, and 0 if it is not.

Criterion 3. The Model was Developed for the Environment/Material Combination of Interest

In the case of the canisters, stainless steel are vulnerable to SCC if a deliquesced salt film forms on the canister surface. (Types 304, 304L, 308, 316, and 316L are the steels of the most interest.) SCC does not proceed in the same way in every material and every environment. Therefore, it is desirable to utilize a model that was developed for stainless steel that is exposed to a chloride-containing aqueous solution, since these models are more likely to accurately describe SCC in the canisters.

Some of the models that meet this criterion do so in general terms: for example, some are not developed for a specific type of steel, but for a “passivating metal.” Other models consider a passivating metal, but are concerned with the high-temperature, fast-moving environment representative of an operating light water reactor.

Calculating $F_{\text{envt/matl}}$:

Three categories are considered.

- First, if the model was developed for a passivating metal, it was assigned 0.5 points.
- Second, If the passivating metal is specifically one of the stainless steels of interest, another 0.5 points are assigned. Certain models were assigned 0.25 points for this category if they weren't developed for stainless steels, but did use SCC data from stainless steel experiments to inform their final model.
- Third, models that were developed for a metal exposed to a salt-containing solution are assigned an additional 0.5 points. If the model was developed for a solution that contained chlorides, but which was not quite representative of a deliquesced film (e.g. a boiling MgCl_2 solution), 0.25 points were assigned.

The maximum value of $F_{\text{envt/matl}}$ is 1.5.

Criterion 4. The Model is Well-Regarded by the Scientific Community.

In order to evaluate this subjective criteria, the number of citations (as recorded by Google Scholar's records of each paper) were collected. Well-established papers tend to have more citations. This criterion is obviously imperfect, since not every citation a paper receives implies agreement by the citing author; furthermore, older papers tend to have more citations simply because they have been in the scholarly databases for longer.

Figure 6 shows publication year vs. number of citations. This indicates a clear trend - older publications generally have more citations. This chart does enable useful comparisons between models that were published around the same year, however.

Calculating $F_{\text{citations}}$:

To obtain $F_{\text{citations}}$, the number of citations received by a model was divided by the highest number of citations obtained by any model (510, for Galvele). The highest possible

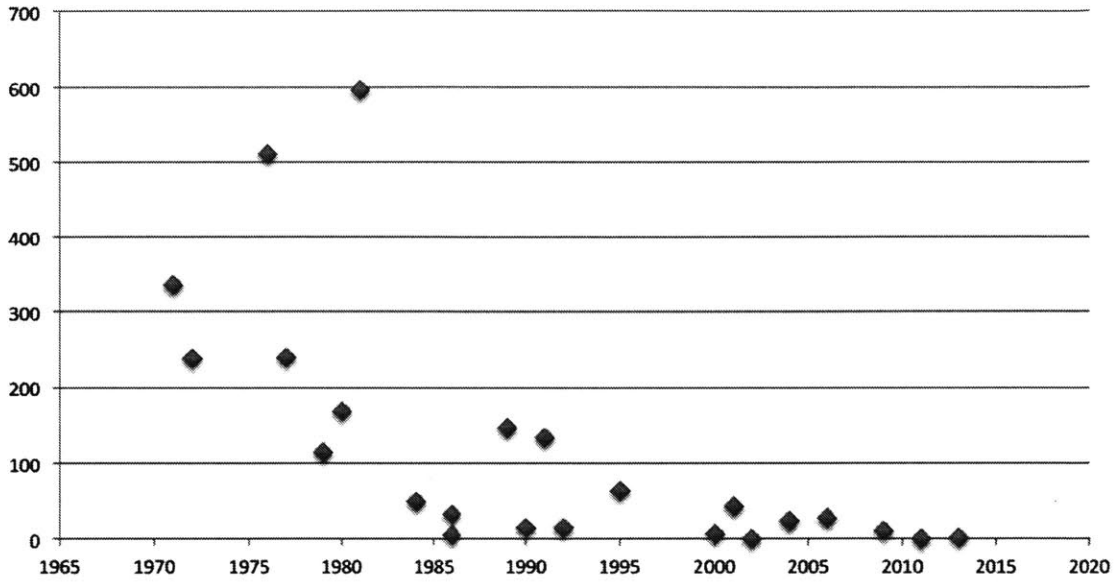


Figure 6: For each model considered, this chart shows the year a certain model was published and the number of citations it has since received as of June 2014. The general trend is obvious: the longer a model has been published, the more citations it has. Galvele (1976) and Chao, Lin, and Macdonald (1981) have the most citations - so many that they seem to be outliers.

FOM was then 1. The two Farmer models, which are modifications of the Shibata and Takeyama, and of the Henshall, models, are not counted individually. This is because they necessarily depend on the original models, and are not meaningful on their own; furthermore, they were published in a review document, and not as standalone works, and so it is difficult to accurately assign a number of citations to them. For the purposes of the $F_{\text{citations}}$, the two Farmer modifications are simply given the same $F_{\text{citations}}$ as their parent models.

Criterion 5: Stress Dependence

A key goal of this research project is understanding the role that residual stresses in the canister material (especially those near and in the canister welds) play in the development and propagation of SCC. Therefore, it is particularly desirable for a model to incorporate stress as an input. For the purposes of this preliminary modeling effort, it is assumed that “applied stress” in a model can be substituted for “residual stress,” such that a present residual stress can act as a driving stress.

Calculating F_{stress} :

If a model contains an explicit dependence on stress, $F_{\text{stress}} = 1$. If it includes a dependence not on applied or residual stress, but on K , its $F_{\text{stress}} = 0.5$. If it includes no stress dependence, $F_{\text{stress}} = 0$.

This FOM was then multiplied by two, since it was judged to be more important than certain other criteria.³ For example, a deterministic model can be adapted into a stochastic model. It was expected, however, that incorporating an explicit stress dependence into a

³This is not to say that this thesis forms a definite conclusion regarding the role of residual stress in the propagation of stress corrosion cracks in canister material. Rather, because the question of the role of residual stress was central to the project, models that included a stress dependence were particularly interesting, if only to see how they behaved when a typical residual stress profile was substituted for a constant applied stress.

model with no stress dependence would be more difficult, especially since the goal of this thesis was to use primarily existing models with limited modifications, rather than to construct an original model.

Criterion 6: Specificity Criterion

“General” models are assumed to be more favorable for the initial development of the probabilistic model. Certain SCC models are developed based on a specific underlying theory, meaning that if that theory is found to be irrelevant or inapplicable to SCC in canister material, then the model is not helpful for this project.

It should also be noted that Criterion 6 is not a “damning” criterion. Rather, models with heavier reliance on a specific theory must be considered very carefully in the context of experimental data for the relevant situation (salt solution and stainless steel) to determine their appropriateness. For the initial modeling effort, more general models, for which fitting parameters can be determined to make the model’s predictions consistent with existing experimental data, are preferable. As the research effort continues, and SCC data is obtained for the relevant material/environment combination, more “specific-theory” models can be considered, since it will be more straightforward to compare their predictions with actual data and determine whether they are consistent with observation.

Calculating $F_{\text{specificity}}$:

Models that do not depend on a specific theory - which are more general - are assigned $F_{\text{specificity}} = 1$. Models with a mild dependence on a specific theory are assigned a $F_{\text{specificity}} = 0.5$. Models with a strong dependence on a specific theory are assigned a $F_{\text{specificity}} = 0$.

All of the considered pit initiation models depend on a specific theory. In Sato’s model, electrostriction pressure builds up in the passive film until the film breaks down, making the metal surface vulnerable to pitting. In Chao, Lin, and Macdonald’s model, voids build up

at the interface between the metal and the passive film. When the void grows sufficiently large, it can cause film breakdown. In Okada's model, a halide nucleus forms on the film's surface and eventually breaches it. Each model "depends" on a specific theory: it only makes sense to use a given model if it is assumed that the model's version of film breakdown reflects reality.

Beck and Alkire's model is assigned $F_{\text{specificity}} = 0$ because it relies on the assumption that a salt film that builds up on the pit walls, affecting current and dissolution.

All slip-dissolution-repassivation models are assigned a $F_{\text{specificity}} = 0.5$. While these models are based on a specific theory, SDR is a generally accepted view of crack propagation. However, in order to use it in a certain material-and-environment combination, it must still be validated: SDR is not necessarily the mechanism of *every* crack growth situation. Kondo and Turnbull both are assigned a specificity value of 0.5 because their pit-to-crack transitions are based on the theory that pits form cracks when the actual pit growth rate equals the theoretical crack growth rate at a given depth.

Ihara's model is assigned a $F_{\text{specificity}} = 0$ because it assumes that cracks nucleate from microcracks. Buck and Ranjan's model is assigned a $F_{\text{specificity}} = 0$ for the same reasons. Further weight was then given to Ihara's specificity score, since this model assumes that microcracks initiate at the surface before coalescing into larger cracks: pitting is not a cracking precursor. At this stage of the *Life Prediction of Canister Material* project, cracks are assumed to initiate from pits. Ihara's model was assigned a final $F_{\text{specificity}} = -1$ for this reason. However, Ihara's model was still considered here and in the literature review, in case future research shows that this model of cracking is possible in the canisters. In Buck and Ranjan's model, the microcracks can initiate at the base of pits, and so it has a more favorable $F_{\text{specificity}}$ than does the Ihara model.

This thesis makes no definitive conclusion as to which SCC theory accurately describes the SCC that could occur in canisters. $F_{\text{specificity}}$ was developed as a criterion in order to give preference to models that are more likely to be useful for future research (the assumption being that a highly-theory-specific model is more likely to be disproven as relevant to SCC in the canisters, and thus less desirable for study here).

Criterion 7: Parameter Dependence is Appropriate to the Project Goals

In this project, an ideal model of SCC delivers the outputs of interest (e.g. flaw growth as a function of time) and contains dependencies on the inputs of interest (e.g. stress, chloride concentration). It does not contain so many fitting parameters or constants that the model becomes unwieldy to construct and use with accuracy. This criterion favors those models which are closest to this ideal.

To evaluate the parameter dependence FOM, the parameters in each model were separated into categories. Most of the models contain many equations; only those which pertained directly to the SCC stage of interest (e.g. pit growth, crack growth) were considered.

The first parameter category was macroscopic parameters. These are typically environmental parameters that may change in time, but which are easy to measure. Microscopic parameters are environmental or material, but are more difficult to measure.

Atomic-scale parameters or quantities (such as void flux) are even more difficult to quantify. These may be important to detailed simulations of a process, but are too detailed for the model being developed in this project.

Characterizing parameters are quantities that are constant for a given material or material/environment combination. In this study, the atomic weight (M) and density (ρ) of a metal, and its associated dissolution reaction charge transfer z , are treated as one constant, since they appear together in electrochemical reactions.

Fitting parameters may either be true fitting parameters, or characterizing parameters that are not commonly known and which require experimental data fitting.

Calculating $F_{\text{parameters}}$:

The number of parameters in each category were totaled, allowing $F_{\text{parameters}}$ to be calculated.

$$F_{\text{parameters}} = (0.5N_{\text{macroscopic}} + N_{\text{microscopic}} + 2N_{\text{atomic}} + 0.25N_{\text{characterizing}} + 2N_{\text{fitting}})^{-1} \quad (2)$$

Parameters that make the model more unwieldy, or which are difficult to determine, result in a smaller value of $F_{\text{parameters}}$. This makes $F_{\text{parameters}}$ a useful indicator of the relative difficulty of constructing and using a model. Note that it does not weight parameters individually for importance (or sensitivity of the model output). Note also that fitting functions are treated as single fitting parameters for the purpose of this estimate.

The detailed breakdown of these calculations can be found in Appendix B on page 325 in Tables 48-52. For each of the model categories, the parameters and constants relevant to each model are separated into the five parameter categories used to calculate $F_{\text{parameters}}$.

Criterion 8. The Model Adapts to a Changing Environment

It is expected that changes in the canister environment will affect the likelihood that corrosion damage will occur. Therefore, it is desirable to use a model which incorporates dependencies on the primary environmental factors that are expected to affect corrosion. In particular, this makes a model more directly applicable to a broad range of environments, and eliminates the need to calculate and use subsets of fitting parameters to generalize a

model to multiple environments of interest. Temperature and chloride concentration are the factors of interest to this project.

Calculating F_{adapt} :

F_{adapt} is the sum of F_{temp} and F_{chem} . Models that incorporate a temperature dependence have $F_{\text{temp}} = 0.5$. Models which incorporate either a direct dependence on chloride concentration or an indirect dependence on chloride concentration have $F_{\text{chem}} = 0.5$.⁴

2.3 Results of the figure-of-merit calculations

Figure 7 shows the results of the figure-of-merit calculations for each model. The environment/material figure-of-merit is broken into three categories for clarity. Figure 8 shows the result of the figure-of-merit for each model in bar graph form. Models are grouped by category: pit initiation, pit growth, pit-to-crack transition, crack growth, crack initiation, and complete models.

The pit initiation models can now be listed from highest F_{total} to lowest F_{total} :

1. Shibata and Takeyama's stochastic model
2. Chao, Lin, and Macdonald's point defect model
3. Farmer's surface partitioning model, after Shibata and Takeyama
4. Sato's electrostriction model
5. Okada's halide nuclide model

This analysis shows that the Shibata and Takeyama approach to modeling pit initiation is expected to be the most promising to future modeling efforts. Pit initiation will not be

⁴An example of indirect dependence on chloride concentration is a model which depends on pH, since pH can be linked to chloride concentration.

| Model | Stochastic | Complete | Envt/Mat: Passivating Metal | Envt/Mat: 304 or 316 | Envt/Mat: Salt Solution | Citations | Stress | Specificity | Temp | Chem | Parameters | Total | |
|---|------------|----------|-----------------------------------|-------------------------|-------------------------------|-----------|--------|-------------|------|------|------------|----------|----------|
| Sato | 0 | 0 | 0.5 | 0.5 | 0.5 | 0.564758 | 0 | 0 | 0 | 0.5 | 0.5 | 0.210526 | 3.275285 |
| Chao, Lin, & Macdonald | 0 | 0 | 0.5 | 0.5 | 0.5 | 1 | 0 | 0 | 0 | 0.5 | 0.5 | 0.117647 | 3.617647 |
| Okada | 0 | 0 | 0.5 | 0 | 0.5 | 0.083893 | 0 | 0 | 0 | 0.5 | 0.5 | 0.173913 | 2.257806 |
| Shibata & Takeyama | 1 | 0 | 0.5 | 0.5 | 0.5 | 0.402685 | 0 | 1 | 0 | 0 | 0 | 0.166667 | 4.069351 |
| Farmer (after Shibata & Takeyama) | 0 | 0 | 0.5 | 0.5 | 0.5 | 0.402685 | 0 | 1 | 0 | 0 | 0.5 | 0.129032 | 3.531717 |
| Pickering and Frankenthal | 0 | -0.5 | 0.5 | 0.5 | 0.5 | 0.401007 | 0 | 1 | 0 | 0.5 | 0.5 | 0.190476 | 3.591483 |
| Beck & Alkire | 0 | 0 | 0.5 | 0 | 0.5 | 0.191275 | 0 | 0 | 0 | 0 | 0.5 | 0.571429 | 2.262704 |
| Galvele | 0 | -0.5 | 0.5 | 0 | 0.5 | 0.855705 | 0 | 1 | 0 | 0.5 | 0.5 | 0.4 | 3.755705 |
| Mola | 1 | 0 | 0.5 | 0.5 | 0.5 | 0.025168 | 0 | 1 | 0 | 0 | 0 | 0.1 | 3.625168 |
| Henshall | 1 | 0 | 0.5 | 0 | 0.5 | 0.025168 | 0 | 1 | 0 | 0.5 | 0.5 | 0.014286 | 4.039454 |
| Henshall with Farmer Modificatio ns | 1 | 0 | 0.5 | 0 | 0.5 | 0.025168 | 0 | 1 | 0 | 0.5 | 0.5 | 0.012821 | 4.037988 |
| Kondo | 0 | 0 | 0 | 0 | 0 | 0.246644 | 2 | 0.5 | 0 | 0 | 0 | 0.111111 | 2.857755 |
| Ford & Andresen | 0 | 0 | 0.5 | 0.5 | 0 | 0.281879 | 0 | 0.5 | 0 | 0 | 0 | 0.235294 | 2.017173 |
| Nakayama & Takano | 0 | 0 | 0.5 | 0.5 | 0.25 | 0.063691 | 0 | 0.5 | 0 | 0 | 0 | 0.190476 | 2.004167 |
| Shoji | 0 | 0 | 0.5 | 0 | 0 | 0.105705 | 2 | 0.5 | 0 | 0 | 0 | 0.075472 | 3.181176 |
| Hall | 0 | 0 | 0.5 | 0 | 0.25 | 0.016779 | 0 | 0.5 | 0 | 0 | 0 | 0.137931 | 1.40471 |
| Macdonald | 0 | 0 | 0.5 | 0.5 | 0 | 0.223154 | 0 | 0.5 | 0 | 0.5 | 0 | 0.222222 | 2.445377 |
| Saito | 0 | 0 | 0.5 | 0.5 | 0 | 0.072148 | 0 | 0.5 | 0 | 0 | 0 | 0.166667 | 1.738814 |
| Aly | 0 | 0 | 0.5 | 0 | 0 | 0.010067 | 2 | 1 | 0 | 0.5 | 0 | 0.166667 | 4.176734 |
| Hickling | 0 | 0 | 0.5 | 0 | 0 | 0 | 1 | 1 | 0 | 0.5 | 0 | 0.173913 | 3.173913 |
| Wu | 0 | 0 | 0.5 | 0 | 0 | 0 | 2 | 1 | 0 | 0.5 | 0.5 | 0.059701 | 4.559701 |
| Ihara | 1 | 0 | 0.5 | 0.5 | 0 | 0.001961 | 2 | -1 | 0 | 0 | 0 | 0.173913 | 3.175874 |
| Buck & Ranjan | 0 | 0 | 0 | 0 | 0 | 0.001678 | 1 | 0 | 0 | 0 | 0 | 0.166667 | 1.168345 |
| Engelhardt | 0 | 1 | 0.5 | 0.25 | 0.5 | 0.038591 | 0 | 1 | 0 | 0 | 0 | 0.033058 | 3.321648 |
| Turnbull | 1 | 1 | 0.5 | 0 | 0.5 | 0.04698 | 2 | 0.5 | 0 | 0 | 0 | 0.052632 | 5.599611 |

Figure 7: Numerical results of the figure-of-merit calculations, by model

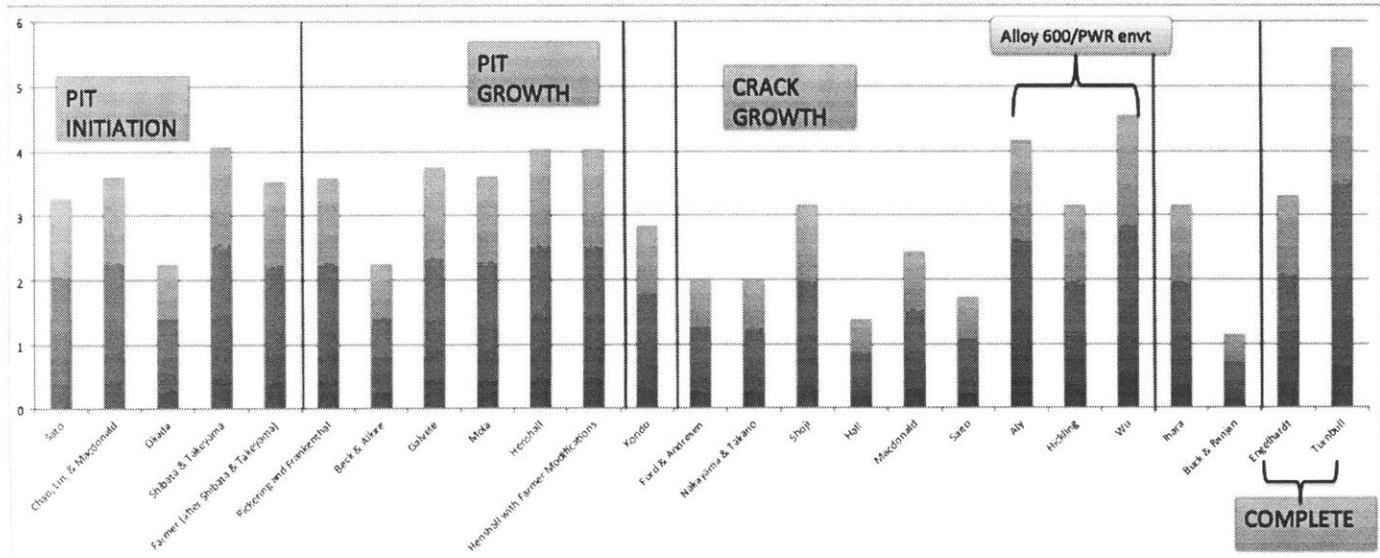


Figure 8: Results of the figure-of-merit calculations, by model and category

explicitly modeled as part of this work, but it will be modeled as part of the overall *Life Prediction of Canister Material* project.

The relative results for the pit growth models are as follows.

1. Henshall's stochastic model, Farmer's modified Henshall model
2. Galvele's model modifying the Pickering and Frankenthal model
3. Mola's stochastic model
4. Pickering and Frankenthal's dissolution-at-the-pit-base model
5. Beck and Alkire's salt-film-on-pit-walls model

F_{total} of the modified Henshall model was so close to F_{total} for the unmodified Henshall model that they are considered to be effectively tied. Note also that the Galvele model is built upon the Pickering and Frankenthal model, so if either one is utilized in future research, they should both be considered.

Kondo's pit-to-crack transition model is alone in its category, although it could be considered a pit growth model as well. In this case, Kondo's model would be ranked above the Galvele model in the list above.

The relative results for the crack growth models are as follows.

1. Wu's model for SCC in Alloy 600
2. Aly's model for SCC in Alloy 600
3. Shoji's adaptation of the SDR model of crack growth
4. Hickling and EPRI's model for SCC in Alloy 600
5. Macdonald's modified SDR model

6. Ford and Andresen's SDR model of crack growth; Nakayama and Takano's SDR model of crack growth
7. Saito's modified SDR + plastic deformation model
8. Hall's modification of the Ford and Andresen SDR model

In this case, the highest F_{total} were scored by the models developed for Alloy 600 exposed to a PWR environment. If one of these models is utilized, it will likely need to be modified in order to be usable for a stainless steel exposed to an effectively stagnant deliquesced salt film. Shoji's SDR model scored the highest for a crack growth model that was not an Alloy 600 model.

Of the crack initiation models, the Ihara model was found to be more favorable than the Buck and Ranjan model. The Ihara model depends on a theory of microcrack coalescence, so it would not be useful if microcracking was found to be irrelevant to SCC in the canister environment.

Of the complete models, the Turnbull model was found to be more favorable than the Engelhardt model. The Turnbull model had the highest F_{total} of all the models considered in this analysis.

2.4 The selected SCC models

Using the figure-of-merit analysis results presented in Section 2.3, the following models were selected for further consideration in this work.

One pit growth model and two crack growth models were selected. This yields two distinct pit-to-crack models when the pit growth model is combined with each crack growth model.

The pit growth model chosen was the Henshall model. This model had the highest F_{total}

of the pit growth models. It is probabilistic, which is in accordance with the overall goal of this project to develop a probabilistic model of SCC in used fuel canisters. The Henshall model also offers a framework for incorporating the effects of important environmental parameters, such as potential, temperature, and chloride concentration.

The crack growth models selected were the Wu model and the Shoji model. For the purposes of investigating the different genres of crack growth models, it was determined that it would be best to pick one crack growth model from the group of Alloy 600/PWR models, and one crack growth model from the group of slip-dissolution-repassivation models. If selecting the crack growth model purely on basis of highest F_{total} , then both models would be from the group of three similar Alloy 600/PWR models.

The Wu model was chosen from the Alloy 600/PWR SCC model group. Its F_{total} was only slightly higher than the F_{total} for the Aly model (the second highest-ranking crack growth model), and it is based on a master's thesis and not a published paper. However, it has a more immediately usable crack growth rate equation (the Aly model uses an integral form of crack growth that is dependent on the micro-environment of the crack tip). The Wu model was also based heavily on the Hickling model, which was developed by EPRI, and so it explicitly incorporated the findings of other research efforts and was thus more broadly representative of an Alloy 600/PWR SCC model. Finally, the Wu model's explicit dependence on temperature, stress (via stress intensity) and chemistry (as pH) made it a more natural tie-in to the goals of the *Life Prediction of Canister Material* project (which involve understanding the role that residual stress and local environment play in SCC behavior) as well as to the Henshall pit growth model (which has similar input dependencies).

The Shoji model was the highest ranking model from the slip-dissolution-repassivation group, and the third highest ranking crack growth model overall.

Finally, the Turnbull model, which had the highest F_{total} score, was also considered as a standalone model. Beginning with an initial distribution of pits, this model takes a probabilistic, experimentally-informed approach to predicting pit growth, pit-to-crack transition, and crack growth. This allows for the study of a self-contained, complete model of SCC.

3 Implementing the selected SCC models

In this section, the implementation of the models selected in Section 2 is discussed. The code structure and the methods of parameter calculation are discussed for the two pitting models (Henshall and Mola), the two cracking models (Shoji and Wu), and the complete SCC model (Turnbull). The code structure used for the two combined models (Henshall/Shoji, Henshall/Wu) is also presented.

Note that the complete code for each model can be found in Appendix B, Section 8.2.

3.1 Model implementation strategy

This section discusses the choice of coding language, the strategy used for parameter selection, and the overall objectives that drove the development of each model.

3.1.1 Selection of program

Flaw depths were to be represented as entries in a vector, with each entry representing an individual flaw. This way, each flaw could be easily be assigned either unique or identical characteristics, as required by the model in use. MATLAB® is a natural choice for the programming language since it is built to work with arrays and vectors. The plotting and probabilistic mathematics capabilities of MATLAB® were also well suited to the needs of this project.

3.1.2 Important assumptions

Note that, as a simplifying assumption for the purposes of this work, all flaws in these models grow perpendicular to the canister surface. Therefore, hoop stress, as discussed above, is the stress component that is expected to impact flaw growth the most significantly in these models. The quantification of the extent to which this simplifying assumption

accurately predicts SCC in a stainless steel canister wall, and the development of any necessary modifications, is beyond the scope of this work.

Pits are assumed to grow hemispherically. During the pitting regime, the flaw depth is then equivalent to the radius of the hemispherical pit.

Furthermore, this work does not consider the evolution of the aggressive environment, and so initial flaw depths are assigned from an appropriate distribution or assigned to have a constant value that is very close to the surface (initiating the flaws from the surface at depth 0 would lead to mathematical errors when the code is run). The modeling of the environment, and its effect on the initiation of pits, is beyond the scope of this work. Future work would combine the environment modeling, and subsequent pit development, with pitting growth/crack growth models like the ones explored here.⁵

This is especially important because each of these loops begin by deciding a number of flaws to follow, assigning them some initial depth, and then propagating them through the flaw growth loop together. In reality, pits would be expected to initiate at different times (and under different environmental conditions), and this must be taken into account when evaluating the expected time-to-failure. Since all flaws initiate at $t = 0$ in this work, time to failure (as measured from flaw initiation) is simply the shortest time in which a flaw is able to propagate through the canister material. A more refined model would account for flaws that initiate at different times. In this case, imagine that the first flaw initiates at $t = 0$. The time to failure would again be the time, counted from $t = 0$, at which a flaw (not

⁵This project does not entirely ignore time-dependent environments. For example, a reasonable expression for canister surface temperature T as a function of time t was selected for use in the coded models that have a temperature dependence. In reality, when a canister is initially filled and placed in storage at an ISFSI site, the surface temperature of the canister is probably too high to support the development of the aqueous film that is assumed to be necessary to promote corrosion phenomena. However, in these models, an environment aggressive enough to support corrosion is assumed to be present beginning at $t = 0$, even though that's not necessarily a physically realistic assumption. Future work is required to fully model the effect of the environment on the development of the chemical environment on the model surface, and to then link this changing chemical environment to corrosive effects.

necessarily the first flaw to initiate) propagates through the canister material. However, in this case, the flaw which grows the fastest is not necessarily the flaw which determines time to failure, because the fastest growing flaws may be more likely to initiate later in the canister lifetime, depending on how the environment is expected to evolve. This highlights some of the complexity and challenge associated with this modeling problem.

3.1.3 Modeling objectives

The first objective of this modeling project is to examine the common SCC models that already exist in the literature, and to identify ones which seem the most likely to be useful to the *Life Prediction of Canister Material* project. It is hoped that the literature review that accompanies this project will be a useful resource for other researchers interested in the same topic.

The second objective of this modeling effort was to further investigate a complete model (Turnbull) and to adapt stand-alone pitting and cracking models into two complete pit-to-crack models. Furthermore, all three models were to be adapted to the canister-and-salt-film situation specifically. By actually adapting and using these models, it becomes possible to clearly identify the modeling gaps and challenges that will need to be addressed in the future.

The third objective of this modeling effort was to use the four models to obtain a distribution of time-to-failure (defined as the time when the flaw first propagates all the way through the canister wall), given the caveats described above. The purpose is twofold. First, an initial estimate of time-to-failure due to SCC can be made. Second, the time-to-failure distributions from each model can be compared to obtain further insight into the strengths and weaknesses of each model, and to understand the impact of model selection on the type of results that can be expected.

3.1.4 Global parameter selection

The selected models use a variety of parameters to properly fit the equations governing pitting and cracking to the material-and-environment combination of interest. Where appropriate, the parameter values used in the original model kept. In other cases, it was necessary to refit the parameters so that the model would be more representative of the situation of interest.

The calculation process is explained for each model that required parameter value refitting. The selection of parameters that were specific to one individual model (Henshall, Shoji, Wu, or Turnbull) are explained in the individual methodology sections for those models. The selection of parameters and inputs that were used across multiple models are explained in this section.

These include residual hoop stresses the corresponding stress intensity factors through the canister wall, canister surface temperature, and pit growth rate.

3.1.4.1 Residual stress An important objective of the *Lifetime of Canister Material* project is understanding the role that residual stresses in the material play in the propagation of flaws, especially cracks. Residual stress measurements on the prototypical canister material obtained for this project had not yet been made at the time that this thesis was first written.⁶

Instead, the residual hoop stress estimates made by Black (see [32]) are used here. These estimates were made for a theoretical canister with specifications judged to be representative of the average U. S. spent nuclear fuel canister. Three estimates were made: one in which the residual stress profile was highly tensile (the worst case scenario from a cracking damage perspective), one in which the residual stress was adjusted so that it was

⁶Since then, initial measurements have been made via neutron diffraction on the prototypical flat plate welds obtained for this project.

just barely above the stress intensity threshold for cracking, and one which was judged to be the “best estimate,” and which was determined by considering the residual hoop stress profiles measured in several cylindrical geometries in the literature and estimating what the residual hoop stress in the prototypical canister geometry was expected to be in comparison. Figure 9 shows the results of these estimates. Note that in the best estimate case, stresses become compressive, a state which might lead to crack arrest.

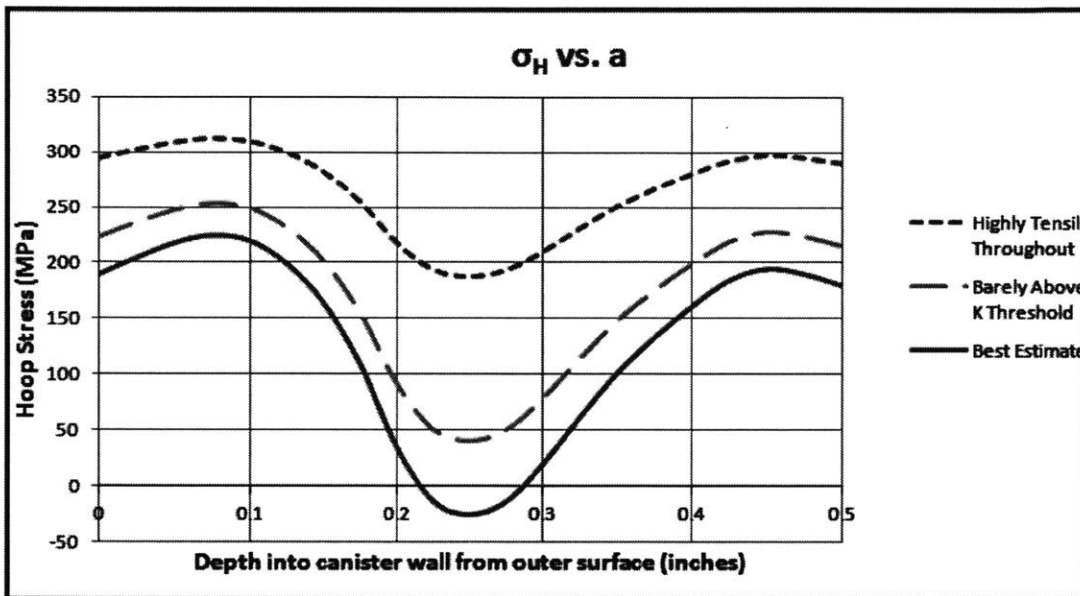


Figure 9: The top dashed line shows the estimate of residual hoop stress in a half-inch thick canister weld in the worst-case scenario (residual stresses are highly tensile throughout the canister material). The middle line shows the estimate of residual stress in the canister, if the lowest hoop stress measurement is still just barely above the stress intensity threshold for cracking. The solid line is the best-estimate case. The residual stresses in this case become compressive in a certain depth range. [32]

In order to use these stress profiles in the models, PlotDigitizer was used to obtain point coordinates for the three residual stress plots. These coordinates were imported into MATLAB®. Fourth-order Fourier fits were made in order to develop equations for residual

stress as a function of depth. These equations had an R^2 value of 0.9994. The data, plots of the data fits, and the code for these equations can be found in Appendix B.

For models that incorporated stress dependence via stress intensity factors, a similar procedure was used to obtain point coordinates for Black’s plots of stress intensity. These plots correspond to the three scenarios outlined above, and are shown in Figure 10. Eighth-order Fourier fits were used to find equations for the stress intensity as a function of depth. These equations had an R^2 value of 1. Note that the original data from [32] for the best-estimate K is used in this project: in [32], the graphs show an “effective” K value, such that $K = 0$ whenever $K < K_{\text{threshold}}$. The original data is used here in order to better accommodate possible changes to the value of $K_{\text{threshold}}$ by other users. The data, plots of the data-fit, and the code for these equations can be found in Appendix B.

Table 2 gives fourth-order Fourier fits that are used in the coded models to represent residual stress through the canister wall in the hoop direction. Units of length are in meters, and units of stress are in MPa. Table 3 gives the eighth-order Fourier fits that are used in the coded models to represent the stress intensity through the canister wall.

Figures 9 and 10 show plots of residual stress and stress intensity that were determined for a 1/2 inch (0.0127 m) thick canister wall. This is a reasonable average wall thickness to use, but in reality, the walls of different models of canisters are likely to vary. In order to accommodate this variation, the arguments of the sine and cosine functions in the Fourier fits were modified as follows:

$$\sin(C \cdot x) \rightarrow \sin\left(\frac{C \cdot 0.0127 \cdot x}{\text{thickness}}\right)$$

where C is a constant. “thickness” is an input from the main script of the model, and is the canister thickness in meters. When the canister thickness is equal to 1/2 inch (0.0127 m), terms cancel and the original form of the Fourier fit is preserved.

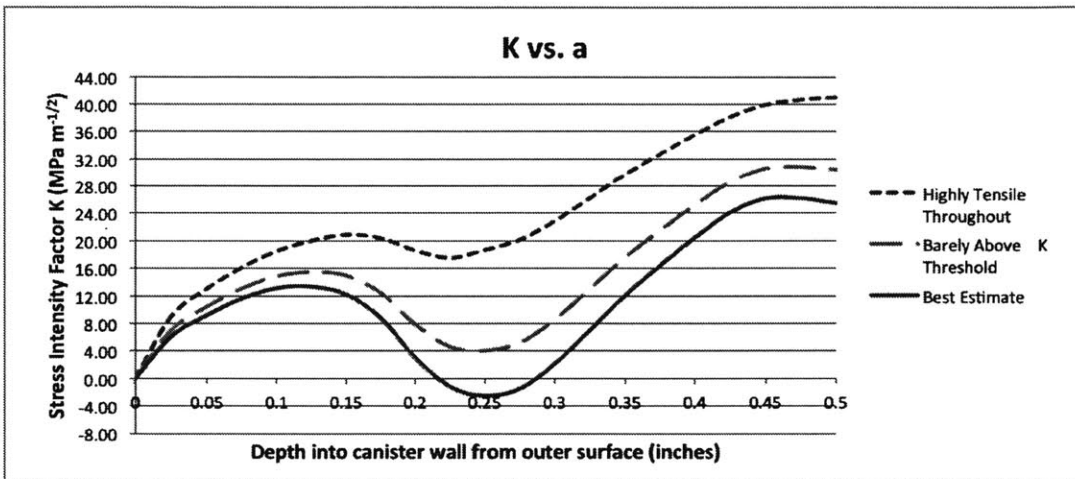


Figure 10: The top dashed line shows the estimate of stress intensity K in a half-inch thick canister weld in the worst-case scenario (residual stresses are highly tensile throughout the canister material). The middle line shows the estimate of stress intensity through the canister wall, if the lowest hoop stress measurement is still just barely above the stress intensity threshold for cracking. The solid line is the best-estimate case. [32]

Table 2: Residual stress profiles through the canister wall (based on [32]), as fit in MATLAB[®] using first and fourth-order Fourier fits. x is flaw depth, t is thickness, and $t_0 = 0.0127$, which is the width of the theoretical canister weld considered in [32]. All lengths are in meters.

| Best Estimate Case |
|---|
| $\sigma(x) = 134 + 99.7 \cos\left(\frac{438t_0x}{t}\right) - 10.01 \sin\left(\frac{438t_0x}{t}\right) - 44.87 \cos\left(\frac{2 \cdot 438t_0x}{t}\right) - 33.18 \sin\left(\frac{2 \cdot 438t_0x}{t}\right)$ $- 2.254 \cos\left(\frac{3 \cdot 438t_0x}{t}\right) - 7.955 \sin\left(\frac{3 \cdot 438t_0x}{t}\right) + 3.444 \cos\left(\frac{4 \cdot 438t_0x}{t}\right) + 5.454 \sin\left(\frac{4 \cdot 438t_0x}{t}\right)$ |
| Just above $K_{\text{threshold}}$ Case |
| $\sigma(x) = 175.9 - 84.74 \cos\left(\frac{438t_0x}{t}\right) - 8.509 \sin\left(\frac{438t_0x}{t}\right) - 38.14 \cos\left(\frac{2 \cdot 438t_0x}{t}\right) + 28.2 \sin\left(\frac{2 \cdot 438t_0x}{t}\right)$ $- 1.916 \cos\left(\frac{3 \cdot 438t_0x}{t}\right) - 6.762 \sin\left(\frac{3 \cdot 438t_0x}{t}\right) + 2.928 \cos\left(\frac{4 \cdot 438t_0x}{t}\right) + 4.636 \sin\left(\frac{4 \cdot 438t_0x}{t}\right)$ |
| Highly Tensile Case |
| $\sigma(x) = 267.7 + 49.85 \cos\left(\frac{438t_0x}{t}\right) - 5.005 \sin\left(\frac{438t_0x}{t}\right) - 22.44 \cos\left(\frac{2 \cdot 438t_0x}{t}\right) + 16.59 \sin\left(\frac{2 \cdot 438t_0x}{t}\right)$ $- 1.127 \cos\left(\frac{3 \cdot 438t_0x}{t}\right) - 3.977 \sin\left(\frac{3 \cdot 438t_0x}{t}\right) + 1.722 \cos\left(\frac{4 \cdot 438t_0x}{t}\right) + 2.727 \sin\left(\frac{4 \cdot 438t_0x}{t}\right)$ |

Table 3: Stress intensity through the canister wall, based on [32], as fit in MATLAB using fourth-order Fourier fits. x is flaw depth, t is thickness, and $t_0 = 0.0127$, which is the width of the theoretical canister weld considered in [32]. All lengths are in meters.

| Best Estimate Case |
|---|
| $K(x) = 10.52$ $- 0.7325 \cos\left(\frac{403.5t_0x}{t}\right) - 7.623 \sin\left(\frac{403.5t_0x}{t}\right) - 9.044 \cos\left(\frac{2 \cdot 403.5t_0x}{t}\right) + 4.497 \sin\left(\frac{2 \cdot 403.5t_0x}{t}\right)$ $- 2.836 \cos\left(\frac{3 \cdot 403.5t_0x}{t}\right) + 0.8395 \sin\left(\frac{3 \cdot 403.5t_0x}{t}\right) - 0.3214 \cos\left(\frac{4 \cdot 403.5t_0x}{t}\right) + 2.113 \sin\left(\frac{4 \cdot 403.5t_0x}{t}\right)$ $- 0.1261 \cos\left(\frac{5 \cdot 403.5t_0x}{t}\right) + 1.517 \sin\left(\frac{5 \cdot 403.5t_0x}{t}\right) + 0.2964 \cos\left(\frac{6 \cdot 403.5t_0x}{t}\right) + 0.7951 \sin\left(\frac{6 \cdot 403.5t_0x}{t}\right)$ $+ 0.552 \cos\left(\frac{7 \cdot 403.5t_0x}{t}\right) + 0.2279 \sin\left(\frac{7 \cdot 403.5t_0x}{t}\right) + 0.2278 \cos\left(\frac{8 \cdot 403.5t_0x}{t}\right) + 0.1059 \sin\left(\frac{8 \cdot 403.5t_0x}{t}\right)$ |
| Barely above $K_{\text{threshold}}$ Case |
| $K(x) = 13.98$ $- 3.015 \cos\left(\frac{396.5t_0x}{t}\right) - 7.957 \sin\left(\frac{396.5t_0x}{t}\right) - 9.341 \cos\left(\frac{2 \cdot 396.5t_0x}{t}\right) + 4.99 \sin\left(\frac{2 \cdot 396.5t_0x}{t}\right)$ $- 3.259 \cos\left(\frac{3 \cdot 396.5t_0x}{t}\right) + 1.922 \sin\left(\frac{3 \cdot 396.5t_0x}{t}\right) - 0.1845 \cos\left(\frac{4 \cdot 396.5t_0x}{t}\right) + 2.692 \sin\left(\frac{4 \cdot 396.5t_0x}{t}\right)$ $+ 0.2946 \cos\left(\frac{5 \cdot 396.5t_0x}{t}\right) + 1.874 \sin\left(\frac{5 \cdot 396.5t_0x}{t}\right) + 0.6274 \cos\left(\frac{6 \cdot 396.5t_0x}{t}\right) + 0.8192 \sin\left(\frac{6 \cdot 396.5t_0x}{t}\right)$ $+ 0.6546 \cos\left(\frac{7 \cdot 396.5t_0x}{t}\right) + 0.08902 \sin\left(\frac{7 \cdot 396.5t_0x}{t}\right) + 0.2489 \cos\left(\frac{8 \cdot 396.5t_0x}{t}\right) + 0.04357 \sin\left(\frac{8 \cdot 396.5t_0x}{t}\right)$ |
| Highly Tensile Case |
| $K(x) = 20.7$ $- 13.27 \cos\left(\frac{372.9t_0x}{t}\right) - 6.783 \sin\left(\frac{372.9t_0x}{t}\right) - 10.17 \cos\left(\frac{2 \cdot 372.9t_0x}{t}\right) + 7.757 \sin\left(\frac{2 \cdot 372.9t_0x}{t}\right)$ $- 3.167 \cos\left(\frac{3 \cdot 372.9t_0x}{t}\right) + 5.857 \sin\left(\frac{3 \cdot 372.9t_0x}{t}\right) + 1.325 \cos\left(\frac{4 \cdot 372.9t_0x}{t}\right) + 4.333 \sin\left(\frac{4 \cdot 372.9t_0x}{t}\right)$ $+ 2.152 \cos\left(\frac{5 \cdot 372.9t_0x}{t}\right) + 2.131 \sin\left(\frac{5 \cdot 372.9t_0x}{t}\right) + 1.518 \cos\left(\frac{6 \cdot 372.9t_0x}{t}\right) + 0.2935 \sin\left(\frac{6 \cdot 372.9t_0x}{t}\right)$ $+ 0.6665 \cos\left(\frac{7 \cdot 372.9t_0x}{t}\right) + 0.4182 \sin\left(\frac{7 \cdot 372.9t_0x}{t}\right) + 0.2448 \cos\left(\frac{8 \cdot 372.9t_0x}{t}\right) - 0.1388 \sin\left(\frac{8 \cdot 372.9t_0x}{t}\right)$ |

3.1.4.2 Threshold stress intensity The threshold stress intensity at which cracking begins - commonly referred to in the literature as K_{ISCC} and in the MATLAB code here as $K_{\text{threshold}}$ - was selected to be equivalent to $4 \text{ MPa}\sqrt{\text{m}}$ in this work. This was selected by Black [32] as the value of K_{ISCC} . Since that thesis is complementary to the present one, this value was chosen for consistency. Black notes that other studies of cracking in stainless steels identify higher values of K_{ISCC} , and that the value of $4 \text{ MPa}\sqrt{\text{m}}$ is thus a conservative approximation.⁷

3.1.4.3 Temperature at the canister surface An estimate of canister surface temperature was adapted from an NRC study of dry cask storage systems and their potential to undergo chloride-induced SCC by Ahn et al. [33]. The authors modeled canister surface temperature for a canister containing twenty-four 1 kW fuel assemblies. These results are shown in Figure 11.

For the purposes of this work, the temperature corresponding to a canister exposed to an ambient temperature of 21°C at the canister top was used. PlotDigitizer was used to obtain the coordinates of the desired line (blue with open diamond points; third line from the top) from the graph in Figure 11. These points were imported into the MATLAB® curve fitting toolbox, and a two-term exponential fit was used to estimate the form of the line.

The final form of the temperature function used in this work is given in Equation (3), with t in years.

$$T(t) = 71.75e^{-0.1126t} + 107.3e^{-0.005747t} \quad (3)$$

⁷The source for this value of K_{ISCC} , as given in [32], is B. W. Brisson, R. G. Ballinger, and A. R. McIlree. "Intergranular Stress Corrosion Cracking Initiation and Growth in Mill-Annealed Alloy 600 Tubing in High-Temperature Caustic," *Corrosion*, 54(7), 1998, 504-514, [76].

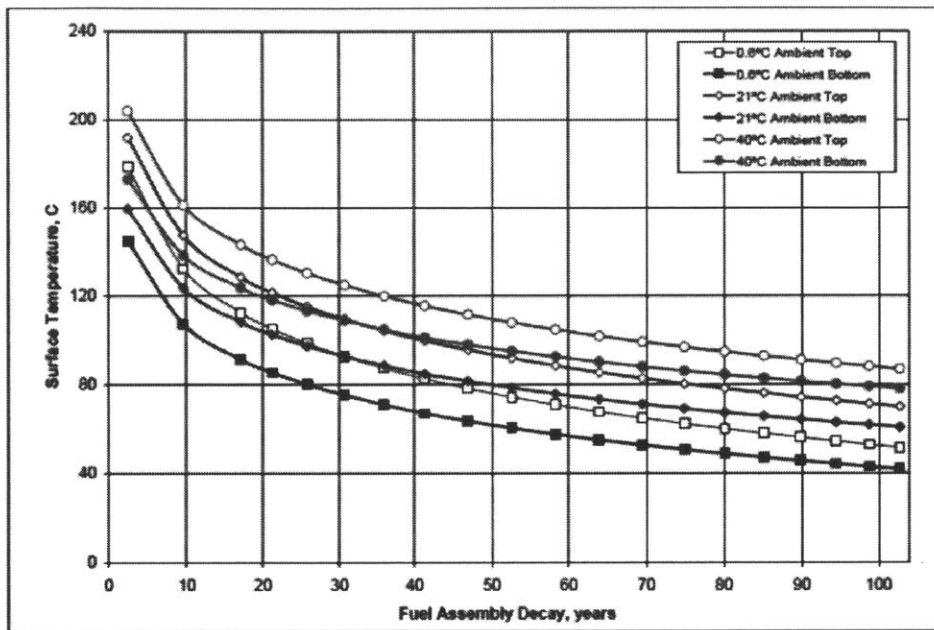


Figure 11: Canister surface temperature in °C is modeled as a function of time. The temperature is dependent on the ambient temperature. For this work, the temperature modeled for 21°C at the top of the canister was used. [33]

Note that in the model codes, when time is imported into the temperature function, it must first be converted to years because the rest of the code parameters use units of seconds.

Ahn et al. note that several factors complicate the estimation of temperature at the canister surface. First, the canister surface temperature is affected by the ambient temperatures, which vary both daily and seasonally (and which are different at each ISFSI site). The temperature also varies across the canister surface due to the geometry and burnup history of the assemblies inside. Therefore, a complete predictive model would likely evolve the canister surface temperature as a function of both time and location on the canister surface, with the geometry of the canister, the assemblies, and the burnup history of the assemblies as inputs to this function. For this model, however, the temperature profile is assumed to be the same at every point on the canister surface, and the flaws are assumed to have an equal probability of being located at any point on the canister surface.

3.1.4.4 Pit growth increment D In the Henshall pitting model, the pit grows at a given timestep if a randomly generated number exceeds the calculated growth probability at that timestep. The amount by which the pits could reasonably be expected to grow in one timestep was estimated from a joint paper by Engelhardt and Macdonald that estimated corrosion cavity growth rates in iron components exposed to a sodium chloride solution [34].

The authors' predictions of pit growth in Type 316L steel exposed to various concentrations of NaCl solutions are shown in Figure 12. For the purposes of this work, it was assumed that the behavior of Type 316L stainless steel would be reasonably similar to the behavior of Type 304 stainless steel in this regard. The second case, in which the steel is exposed to 0.5M NaCl solution, was chosen for this work.

This graph was used to estimate a pit growth rate of 1 mm/yr, or 3.169×10^{-11} m/s. Experimental tests with weld material and a characteristic environment can be carried out

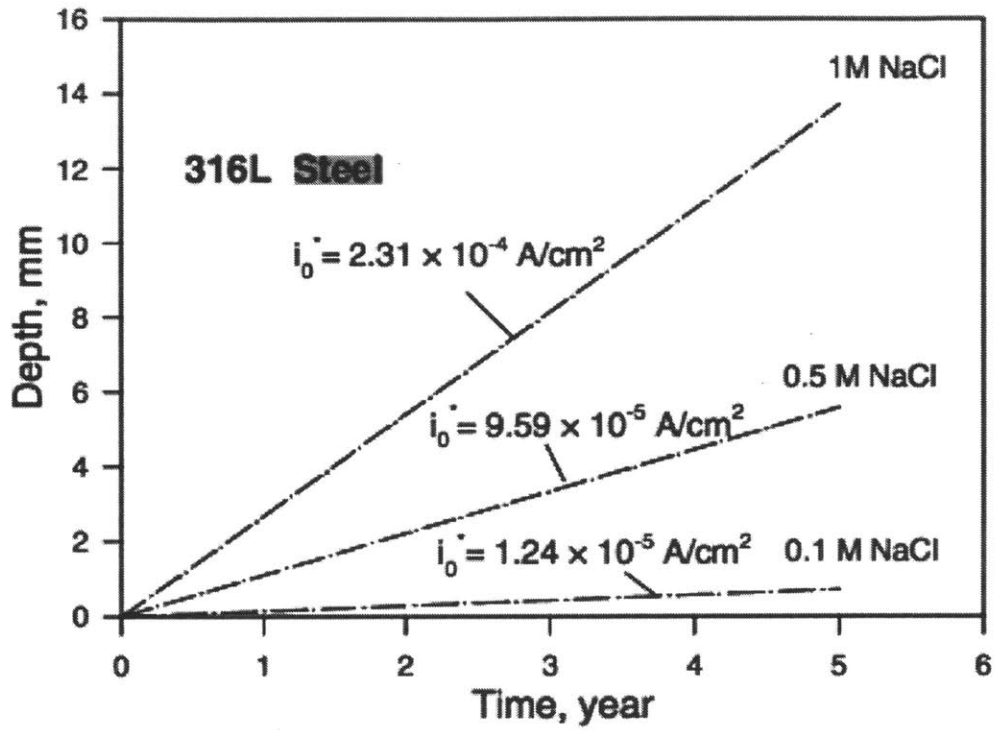


Figure 12: Corrosion pit depth as a function of time is graphed for Type 316L stainless steel exposed to various concentrations of NaCl solution. [34]

to refine this value.

Note that the observed pit growth rate in the simulations will not actually be 1 mm/yr, because the simulated pits will not grow at every timestep. Therefore, the observed pit growth rate in the models is expected to be less than the input value of D . For this reason, simulations will also be run with higher, more conservative values of D to see how this changes the distribution of times to failure.

3.2 Building the models

The methodology used to develop the code for each model is discussed in this section. References to the original code are provided. The two pitting models, the two cracking models, and the Turnbull model are discussed individually. The general strategy used to combine the pitting and the cracking models into four distinct pit-to-crack models is presented.

3.2.1 Implementing the Turnbull model

The Turnbull model (see page 232) is a complete model of SCC, and also scored the highest F_{total} during the figure-of-merit calculations.

The MATLAB code used to model the Turnbull approach to describing SCC can be found in Section 8.2.2 on page 344.

3.2.1.1 Turnbull: Model structure Figure 13 is a flowchart that shows the structure of the code used to model the SCC process described by Turnbull.

The parameters used to characterize pit and crack growth rates are calculated for each flaw using the process described in the next section. Some of these values are treated as constants, while others are selected from an appropriate distribution. Each flaw in the vector has a unique set of characteristics that govern its history.

Since this study does not incorporate environmental evolution and pit inception, the number of pits in the flaw vector is selected by the user, and the pits are assigned the same initial flaw depth. Note that in [31] the number of initial flaws is selected by the user, but a Weibull distribution is used to assign their initial sizes.

At each iteration through the loop, the stress is first calculated as a function of flaw depth. The pit growth rate is calculated using the previously assigned parameters and the current flaw depth. The crack growth rate is calculated using the previously assigned parameters, the current flaw depth, and the stress at that flaw depth.

If the pit growth rate calculated for that depth is less than the crack growth rate calculated for that depth, then the flaw is still in the pitting regime and the depth is updated by adding $(dx/dt)_{\text{pit}}$ to the current depth. If the crack growth rate has the higher value, then stress intensity K is calculated using the previously calculated stress. If it exceeds the threshold stress intensity for cracking, then it is assumed that the flaw has entered the cracking regime, and the depth is instead updated by adding $(dx/dt)_{\text{crack}}$ to the current depth. However, if the crack growth rate exceeds the pit growth rate, but $K(x)$ is still less than $K_{\text{threshold}}$, it is assumed that the flaw is still in the pit growth regime.

Two versions of this model were coded. One is for running a single group of flaws, and the second is used for simulating multiple vectors of flaws (i.e. the flaw vector becomes a two-dimensional flaw matrix). The code for these models can be found in Appendix B on page 344. (Some of the characterizing parameters apply to the entire flaw vector. This multiple-vector approach allows for the simultaneous simulation of flaw vectors with

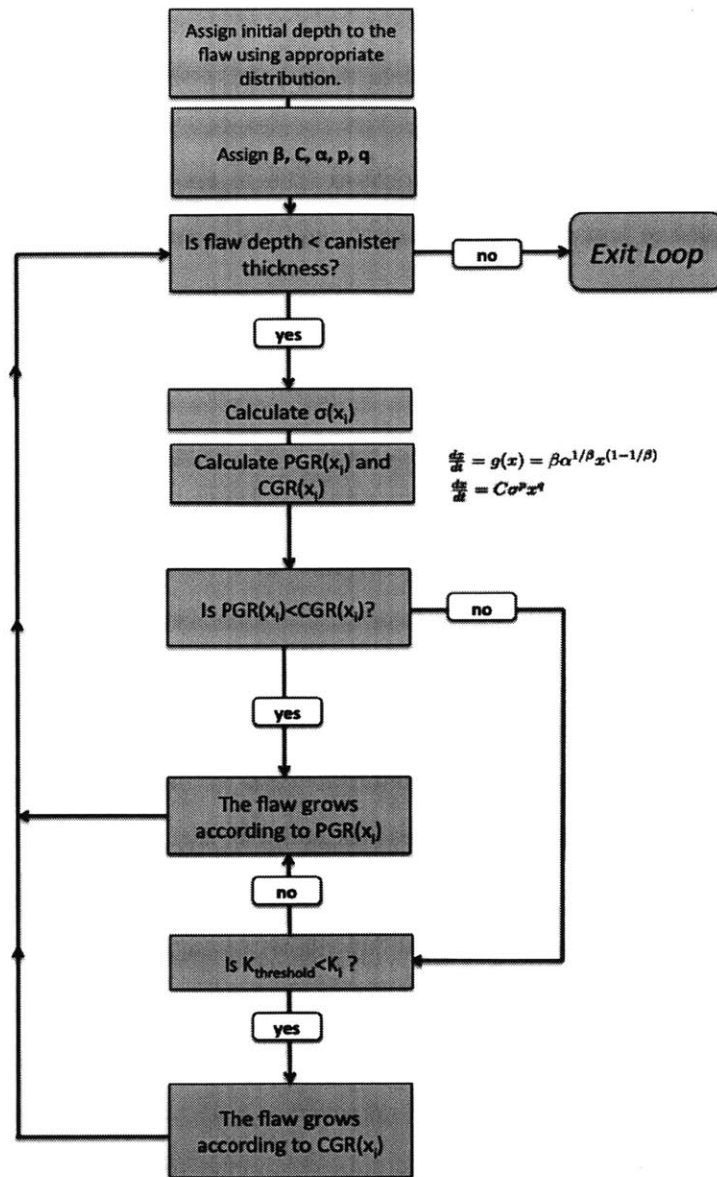


Figure 13: This flowchart illustrates the structure of the code used to model the SCC process described by Turnbull. Each flaw is assigned an initial set of characteristics. The pit and crack growth rates are calculated at each time step. When $CGR > PGR$, and $K(x) > K_{\text{threshold}}$, the flaw transitions from a pit to a crack.

different characterizing parameters.)

The distributions of flaw depth and time-to-failure are then obtained. The shortest time-to-failure is the canister time-to-failure prediction.

3.2.1.2 Turnbull: Parameter selection There are two primary equations in the Turnbull model: the first governs pit growth, and the second governs crack growth.

The pit growth rate is given as:

$$\left(\frac{dx}{dt}\right)_{\text{pit}} = \beta\alpha^{1/\beta}x^{1-1/\beta} \quad (4)$$

where x is the flaw depth, and β and α are constants selected from normally distributions. Each flaw is characterized by its own value of β and α .

The crack growth rate is given as:

$$\left(\frac{dx}{dt}\right)_{\text{crack}} = C\sigma^p x^q \quad (5)$$

where σ is the stress present in the material, C is a constant selected from a normal distribution, q is a constant whose value is the same for a given group of flaws, and $p = 2q$.

Since the models in this project do not address the evolution of the aggressive environment and the inception of pits, an initial flaw depth is assigned first. All pits in this model have been assigned an initial depth of 1 μm .

β and α are selected from normal distributions in this version of the Turnbull model. β is a constant in the Turnbull model, and several values are reported in [31] for different possible environments. The set of constants pertaining to an aerated 1.5 ppm chloride environment in [31] were used for this study, since this was the environment studied in [31] that was judged to be the most applicable to the proposed aggressive canister environment. A normal distribution was applied to β in this study, to represent the natural variability of

the corrosion process and the uncertainty in the applicability of this value of the constant to the situation at hand. The mean of the normal distribution for β is equivalent to the constant value of β selected from [31], and the standard deviation of this distribution is equivalent to a global standard deviation s selected by the user at the beginning of the simulation.

α is selected from a normal distribution centered at 0 in [31], so this feature was preserved. The standard deviation of this distribution is also prescribed in [31], and this standard deviation is used instead of s when calculating α .

A condition is placed on the selection of β and α to prevent a negative value from being assigned to either constant. This tends to skew the normal distributions to values greater than the mean, but the effect is expected to be very small. The normal distributions for all constants in Turnbull are graphed in Appendix B on page 348 for multiple values of s to show that this is true.

C is also selected from a normal distribution that is centered around a mean prescribed in [31]. It is suggested in [31] that C is normally distributed, and for an aerated chloride environment, three sets of means and standard deviations of C are provided. The set pertaining to the longest exposure time is used here.

q is a constant in the Turnbull model, and it is the same for all pits (i.e. for a single simulation that propagates N pits through the Turnbull loop, all N pits will have the same q value). The value given for q in [31] is used as the mean value of q in this model. q is selected from a normal distribution centered around this mean value with standard deviation s at the beginning of a group. As is the case with all other constants in this model, the selection of q is modified to prevent negative values from being assigned. p is then simply calculated for the group of pits as $p = 2q$.

The values of these constants are summarized in Table 4. β , α , and C are unique

to each flaw, whereas p and q are unique to a vector of flaws. Constants whose normal distributions are characterized by the global standard deviation s are constants whose normal distributions are imposed on them in this project, but which are not normally distributed in the original model.

Table 4: Constants used in the Turnbull SCC model

| Constant | Normally Distributed | Mean Value | Standard Deviation |
|----------|----------------------|-----------------------|-----------------------|
| β | yes | 0.37 | s |
| α | yes | 0 | 0.76 |
| C | yes | 2.6×10^{-18} | 3.8×10^{-18} |
| q | yes | 3 | s |
| p | no | $2q$ | N/A |
| x_0 | no | 1 μm | N/A |

The value of σ is calculated as a function of x using the distributions described in Section 3.1.4 on page 57. Note that in [31], σ is a constant applied stress, and not a spatially-dependent residual stress.

Finally, in the version of the Turnbull model which uses $K_{\text{threshold}}$ as an additional criterion on the transition from pitting to cracking, the value of $4 \text{ MPa}\sqrt{\text{m}}$ is used, as described on page 63.

3.2.2 Pitting: Henshall

Henshall (see page 178) developed a stochastic model of pit growth. The framework for this model allows for the effects of time-dependent environmental parameters on pit growth probability to be modeled.⁸

⁸The original Henshall model also treats pit initiation and pit death, but only pit growth is considered here - i.e., flaws may not grow on every timestep, but once initiated, they do not repassivate and stop growing.

The MATLAB® code used to model the Henshall approach to pit growth can be found in Section 8.2.3 on page 351.

3.2.2.1 Henshall: Model structure The flowchart in Figure 14 shows the structure of the code used to model the pit growth process described by Henshall.

First, initial depths are assigned to each flaw. These may be arbitrary or selected from an appropriate distribution.

Second, the vector of flaw depths is propagated through the pit growth loop. Each entry in the vector cycles through the loop until the flaw depth exceeds the thickness of the canister, a condition which constitutes failure. Realistically, pits are expected to nucleate cracks well before they grow to the other side of the canister wall, and stress corrosion cracking is the primary focus of the *Life Prediction of Canister Material* project. However, for the sake of completeness, the Henshall model (pitting only) is considered on its own, as well as in conjunction with cracking models.

At the beginning of each cycle through the loop, the pit growth probability λ is newly calculated. λ is a function of applied potential, chloride concentration, and temperature. To calculate each of these three quantities, a separate function is called. These functions are time-dependent, and can be modified to return the appropriate values for the canister situation (e.g. the temperature equation can be modified to represent the surface temperature of a used nuclear fuel canister whose internal fuel assemblies have a specific power history and heat profile). The “time” input to these functions is determined by the loop index i , with all parameters appropriately normalized so that $(i + 1) - i$ is equivalent to a desired unit of time.

Once λ is calculated, a random number generator (RNG) is used to determine a value between 0 and 1. If the random number is less than λ , pit growth occurs. (For example, if $\lambda = 0.75$, then there is a 75% chance of growth, and a 75% chance that a standard random number generator will return a value that is less than 0.75.) The flaw depth is updated by adding the amount that the pit grows to the existing flaw depth. In the Henshall model,

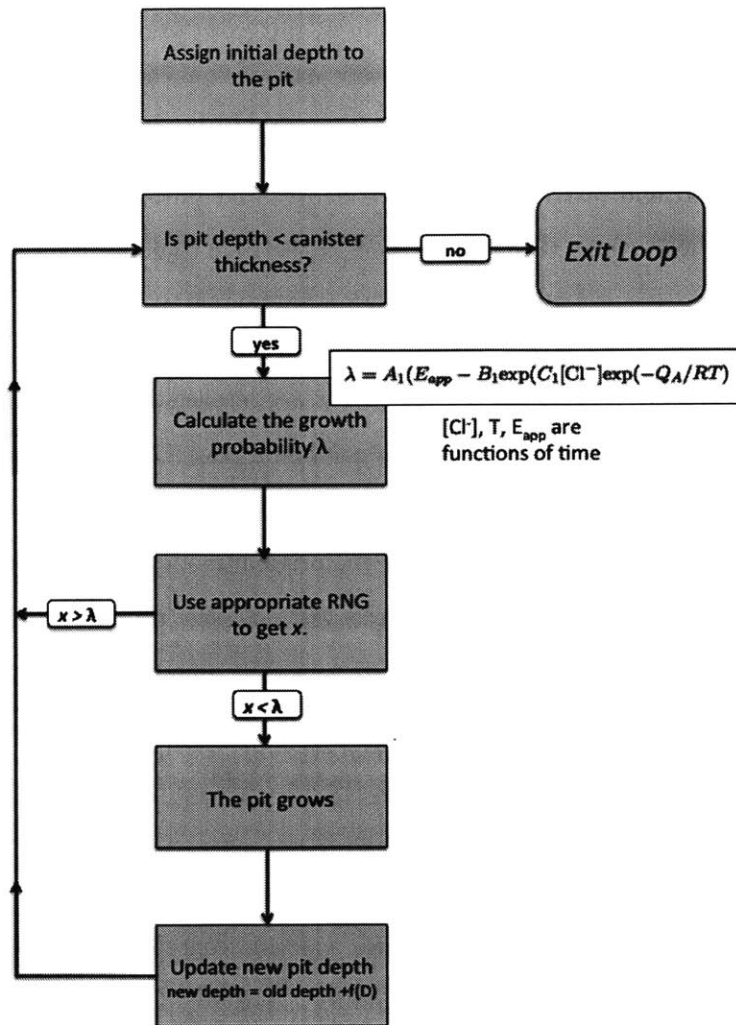


Figure 14: This flowchart illustrates the structure of the code used to model the pit growth process described by Henshall. The pit growth probability is a function of the applied potential E_{app} , chloride concentration $[Cl^-]$, and temperature T . E_{app} , $[Cl^-]$, and T are themselves separate functions of time.

the pit simply grows by an average amount D . The loop then repeats.

If the random number is greater than λ , pit growth does not occur at that timestep, and the loop simply starts over.

When all the flaws in the vector have exceeded the canister wall thickness, the simulation is over, and distributions of flaw depths and time-to-failure (here, the number of times a flaw was cycled through the loop is the time-to-failure) are shown. The shortest time-to-failure is the predicted canister time-to-failure.

3.2.2.2 Henshall: Parameter selection A detailed description of the Henshall model and its equations can be found in Section 7.4.3 on page 178. The Henshall model involves three time-dependent equations for temperature, potential, and chloride concentration.

The temperature equation given in the original model was abandoned in favor of the canister surface temperature model described on page 63. The chloride and potential equations have the form:

$$E_{\text{app}} = E_0 - e^{-E_1 t} \quad (6)$$

$$[\text{Cl}^-] = K_0 e^{K_1 t} \quad (7)$$

The calculated values of temperature, chloride concentration, and potential are then used in the growth probability expression:

$$\gamma = A_4 (E_{\text{app}} - B_4)^{B_5} ([\text{Cl}^-])^{C_4} \exp(+Q_\gamma/RT) \quad (8)$$

where t is time, R is the gas constant, Q_γ is the activation energy of the pitting process, and all other variables are constants. In [35], the author runs several distinct cases that

used different sets of values for the parameters E_0 , E_1 , K_0 , K_1 , A_4 , B_4 , B_5 , and C_4 .⁹ One set was selected for use in the model as average values for the constants. These values are given in Table 5.

Table 5: The average values of the constants used in the code for the Henshall model

| Variable | Mean value |
|----------|------------|
| E_0 | 1.4 |
| E_1 | 0.047 |
| K_0 | 0.01 |
| K_1 | 0.0465 |
| A_4 | 10^{-7} |
| B_4 | 0.4 |
| B_5 | 0.3 |
| C_4 | 0.2 |

Future iterations of this work that use the Henshall model to simulate the pit growth process in canister walls should use experimental results to determine better fits for the constants of the equations describing chloride concentration, potential, and growth probability. At present, the values reported by Henshall are used instead, and normal distributions are applied to represent uncertainty in their true value and to simulate the variable nature of corrosion processes. When the model is run, a global standard deviation parameter is first selected by the user. The standard deviation parameter is given as a decimal percentage, 0.XX, where $0.XX = XX\%$. When the constants are used in the model, the mean value (as given above) and the standard deviation are called and used to characterize the normal distribution used to select the value of the constant in each iteration of the loop. The mean of the distribution is equal to the constant's given average value μ , and its standard deviation equal to the global standard deviation parameter s multiplied by μ . The value of the constants are reselected with each iteration of the loop.

⁹The original subscripts used in the original paper are kept here for ease of comparison (see [35]).

In order to prevent unphysical results, negative values are truncated from the distributions. This is expected to have a minimal impact on the results. Graphs of these truncated distributions are provided in the appendix on page 357.

The activation energy for the pit growth process provided by Henshall was 10^{-4} kJ/mol. A new value was estimated from the results provided in [36], which considered the corrosion of four austenitic stainless steels exposed to aqueous chloride environments. The activation energy for general corrosion for Type 304L steel exposed to 2.5M NaCl solution was found to be 14 kJ/mol. General corrosion of Type 304L stainless steel exposed to 2.5M NaCl was considered to be a reasonably good approximation of pitting corrosion in Type 304 stainless steel exposed to a deliquesced chloride salt solution, and so this value was used for the activation energy in the Henshall model.

The gas constant has the value 8.3144521 J/mol·K.

3.2.3 Cracking: Shoji

The Shoji model for crack growth (see page 204) is a deterministic model that adheres to the slip-dissolution-repassivation (SDR) theory of crack growth, but incorporates the effects of strain at the crack tip into the calculation.

The MATLAB® code used to model the Shoji approach to crack growth can be found in Section 8.2.4 on page 361. The Shoji model is only used in this thesis as part of the combined Henshall/Shoji model, and not as a standalone model.

3.2.3.1 Shoji: Model structure The flowchart in Figure 15 shows the structure of the code used to model the crack growth process described by Shoji.

First, initial depths are assigned to each flaw. These may be arbitrary or selected from an appropriate distribution. When the cracking model is inserted into a pit-to-crack model, the initial cracking depth will be the depth at which that flaw transitioned from a pit to a crack.

As is the case with the pitting models, flaws cycle through the loop until they exceed the canister wall thickness. At each iteration of the loop, stress intensity K is calculated as a function of residual stress and flaw depth. At each iteration, the calculated K value is stored in a history matrix so that dK/dt can be calculated on the subsequent loop.

Once K_i and $(dK/dt)_i$ have been determined, $(dx/dt)_i$ can be calculated. This value is also stored in a history matrix, since it will be used in the calculation of $(dx/dt)_{i+1}$. (If the loop is on its first iteration, K_{i-1} and $(dx/dt)_{i-1}$ are simply assigned values of 0.)

Crack depth can then be updated by adding $(dx/dt)_i$ to x_i . The distributions of flaw depth and time-to-failure are then obtained. The shortest time-to-failure is the canister time-to-failure prediction.

Note that this is a deterministic model. Crack evolution is assumed to be determined

primarily by the material and environment conditions, whereas pit growth is modeled as a probabilistic process. However, the constants and parameters can be selected from appropriate distributions instead of assigned as constants in order to replicate the expected material/environment-independent crack growth variability.

3.2.3.2 Shoji: Parameter selection Shoji et al. use the following equation to describe crack growth [21]. A detailed explanation of the Shoji model and of this equation can be found in Section 7.5.6 on page 204.

$$\frac{da}{dt} = \frac{Mi_o}{z\rho\mathbf{F}(1-m)} \left(\frac{t_0}{e_f}\right)^m \left[\frac{\beta\sigma_y n}{E(n-1)} \cdot \left(2\frac{\dot{K}_I}{K_I} + \frac{\dot{a}}{r_0}\right) \left\{ \ln \left[\frac{\lambda}{r_0} \left(\frac{K_I}{\sigma_y}\right)^2 \right] \right\}^{1/(n-1)} \right]^m \quad (9)$$

M , z , ρ , σ_{ys} , and E are material properties, representing the steel's atomic weight, the oxidation charge exchange associated with the corrosion reaction, the steel's density, the yield stress, and the steel's Young's modulus. These values were determined for Type 304 stainless steel for use in the code, and are listed in Table 6. Values are given in their common units, but in the code, everything is converted to units of Pa, kg, and m.

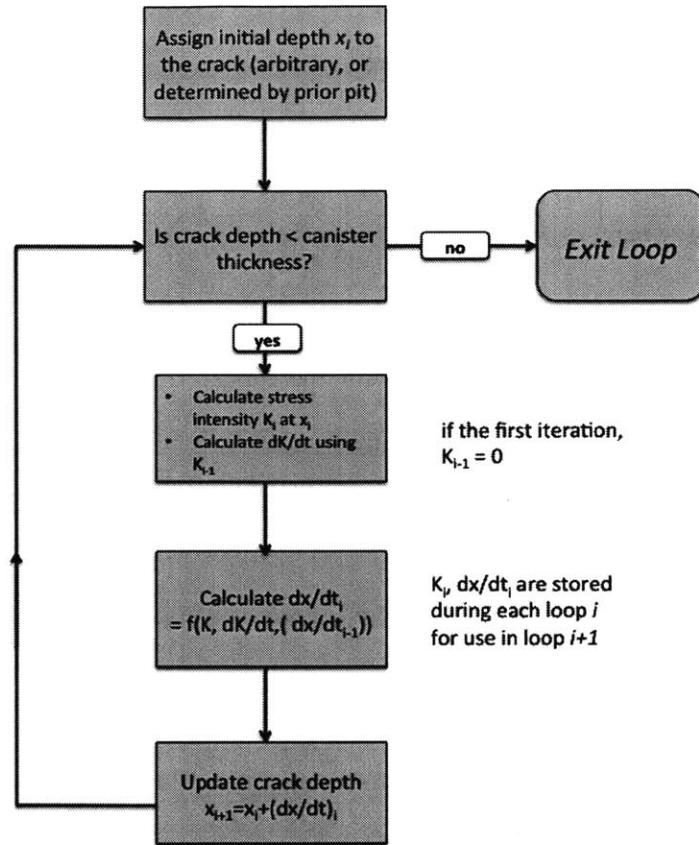
Table 6: Material property values for Type 304 stainless steel used in the Shoji model

| Parameter | Value |
|---------------|------------------------|
| M | 0.05542 kg/mol |
| z | 2 |
| ρ | 8.03 g/cm ³ |
| σ_{ys} | 205 MPa |
| E | 193 GPa |

To calculate M , the Type 304 stainless steel was assumed to have the same composition as the weld samples obtained for this project (see Appendix C). This composition is given in Table 7.

\mathbf{F} , Faraday's constant, has a value of $9.64853399 \times 10^{-4}$ C/mol.

r_0 , the characteristic distance used for formulating crack growth. This was given a value of 100 μm . Shoji et al. report using values of 85 μm to 230 μm in their calculations, and so a single value was selected from that range.



$$\frac{da}{dt} = \frac{M i_0}{z \rho F (1 - m)} \left(\frac{t_0}{e_f} \right)^m \left[\frac{\beta \sigma_y n}{E(n-1)} \cdot \left(2 \frac{\dot{K}_I}{K_I} + \frac{\dot{a}}{r_0} \right) \left\{ \ln \left[\frac{\lambda}{r_0} \left(\frac{K_I}{\sigma_y} \right)^2 \right] \right\}^{1/(n-1)} \right]^m$$

Figure 15: This flowchart illustrates the structure of the code used to model the crack growth process described by Shoji. Crack growth is affected by the stress intensity at that depth in the material, the time-rate-of-change of the stress intensity, and the immediately prior crack growth rate, as well as other parameters that are consistent with an SDR cracking model.

Table 7: Composition of Type 304 stainless steel weld samples by weight percent

| | | | | | |
|---------|--------|--------|--------|--------|---------|
| Cr | Ni | C | Co | Cu | Mn |
| 18.0215 | 8.0000 | 0.0249 | 0.1540 | 0.4845 | 1.7665 |
| Mo | N | P | S | Si | Fe |
| 0.3380 | 0.0645 | 0.0340 | 0.0025 | 0.2535 | balance |

m and n represent the slope of the oxidation rate decay curve and the strain hardening exponent, respectively. Shoji et al. report multiple values of m . A mean value of 0.567 was selected for m , since this was the value used when considering sensitized Type 304 stainless steel exposed to 288°C oxygenated water. Of the scenarios considered in [21], this one was the closest to the material and environment of interest in this project. The same reasoning was used to pick 1.36 as the mean value of n .

β and λ are fitting constants. The values reported in Shoji et al., 5.08 and 0.11 respectively, are also used here.

To represent uncertainty in the applicability of these values to this project, and to represent the expected variability in corrosion phenomena, m , n , λ , and β are selected at each iteration of the crack growth loop from a Gaussian distribution centered at their assigned mean value, and with a standard deviation equivalent to a specified percentage of that mean value. This is the same process used to select parameter values in the Henshall model, as described on page 77. Negative values are truncated from the Gaussian distributions. Plots of these Gaussian distributions are shown in Appendix B on page 367.

ε_f represents the fracture strain of the oxide film. In order to estimate this value, it is necessary to know which oxide films form in the cracks of the weld material. For the purposes of this work, it is assumed that the expected oxide films inside a stress corrosion crack are the same as those known to form on Type 304 stainless steel. Therefore, the film

fracture strains of interest are those corresponding to Cr_2O_3 and Fe_3O_4 [37].

The film fracture strain can be estimated from the following expression:

$$\varepsilon_f = K_{\text{IC}}/(fE_{\text{ox}}\sqrt{\pi c}) \quad (10)$$

where K_{IC} is a threshold stress intensity, f is a geometrical factor, E_{ox} is the Young's modulus of the oxide film, and c is the radius of the flaw precipitating the crack [38].

Since f and c would be the same for both Cr_2O_3 and Fe_3O_4 , the ratio of K_{IC} to E_{ox} was considered for both. For Fe_3O_4 , $K_{\text{IC}} = 1.4 \text{ MPa}\sqrt{\text{m}}$ and $E_{\text{ox}} = 208 \text{ GPa}$. For Cr_2O_3 , $K_{\text{IC}} = 1.8 \text{ MPa}\sqrt{\text{m}}$ and $E_{\text{ox}} = 283 \text{ GPa}$. This yields a ratio of 0.006731 for Fe_3O_4 and 0.0063604 for Cr_2O_3 . Since Fe_3O_4 has the higher value, it is assumed for the purposes of this work that this is the composition of the oxide film, since the highest fracture strain is assumed to be the threshold fracture strain.

The geometrical factor f has a value of 0.64 when the flaw that initiates the crack is a semicircular surface notch of radius c . It is assumed throughout this work that the corrosion pits are hemispherical, and so this is the value of f that is used. c is equivalent to the depth of the pit at the time that it initiated a crack, and so is unique for each crack. When the Wu model is considered apart from the pitting models, an arbitrary pit depth is chosen.

i_o and t_o describe the current associated with the SDR mechanism. Figure 16 illustrates the corrosion behavior associated with SDR. The current spikes when film rupture occurs, exposing bare metal, and decays as the film re-passivates, which inhibits corrosion. This process repeats in a cyclic manner as the crack propagates.

Experimental data from [39] was used to estimate the values of i_o and t_o to use in the Shoji model. The data considered here involved a Fe-18Cr sample exposed to 1M NaCl

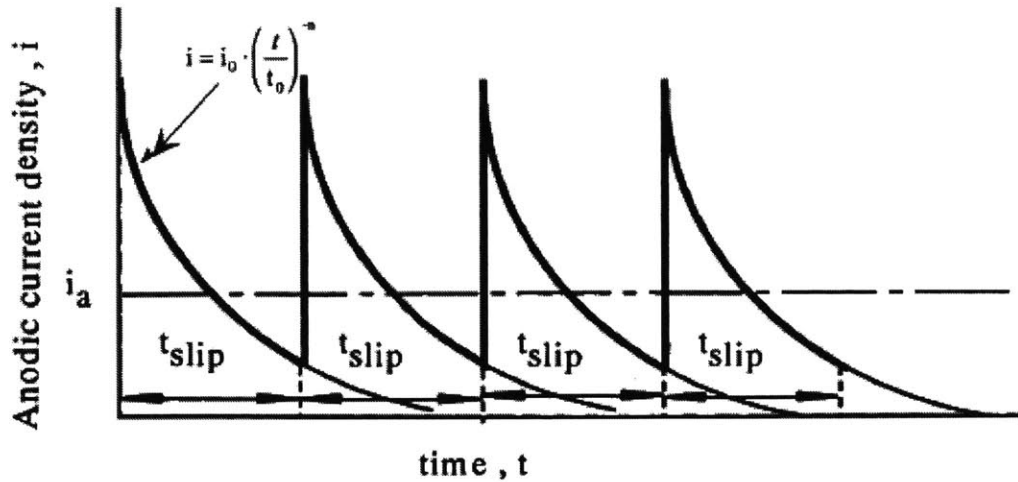


Figure 16: The current spikes when film rupture occurs, exposing bare metal, and decays as the film repassivates, which inhibits corrosion. This process repeats in a cyclic manner as the crack propagates. i_0 describes the peak current amplitude, and t_0 characterizes the period of the film rupture events. [24]

solution. This data is shown in Figure 17.^{10,11}

In order to estimate i_0 and t_0 , the graph was digitized using PlotDigitizer. Points were collected in sets of three: at the left base of a current peak (i_1, t_1), at the top of the current peak (i_2, t_2), and at the right base of the current peak (i_3, t_3). This is shown schematically in Figure 18.

To calculate t_0 , t_1 is subtracted from t_3 . After this was done for each current peak, these δ_t values were averaged to obtain a t_0 value of 54.02 seconds.

To calculate i_0 , i_1 and i_3 were averaged for each peak to obtain a lower bound for the current. This average value was then subtracted from i_2 to obtain an estimate of i_0 . The

¹⁰The study in [39] involves pitting nucleation studies, not crack propagation studies. Therefore, these values should be considered as a first estimate that should be refined by experimentation using weld material.

¹¹Experimentation may also reveal that an SDR approach to crack modeling is inappropriate for the scenario of interest.

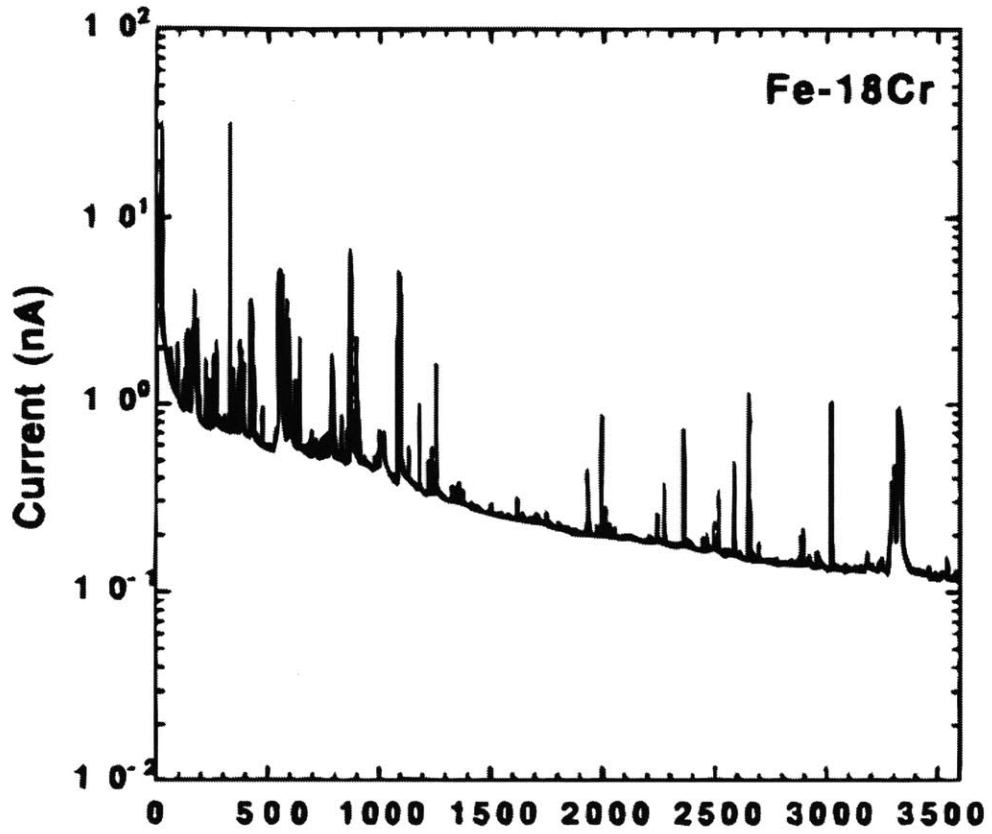


Figure 17: Potentiostatic experiments were carried out by Kobayashi et al. on an Fe-18Cr sample in a 1M NaCl solution in order to study corrosion pit nucleation. The observed current is plotted versus time. This data was used to estimate i_0 and t_0 in the Shoji model. [39]

i_0 values for each individual peak were averaged to estimate an i_0 value of 2.37 nA.

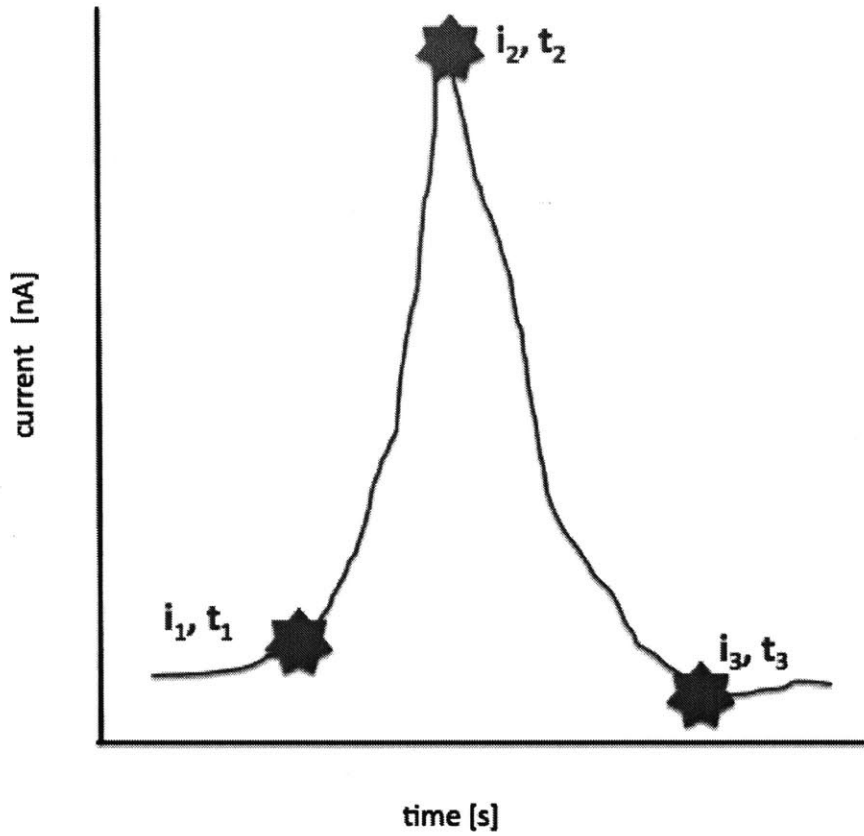


Figure 18: The schematic shows where points were collected on the data from [39]. For an individual current peak, $t_0 = t_3 - t_1$, and $i_0 = i_2 - \frac{i_1 + i_3}{2}$. t_0 and i_0 were calculated for multiple individual peaks, and averaged to estimate t_0 and i_0 values for weld material exposed to chloride solution and cracking according to the Shoji model.

3.2.4 Cracking: Wu

The Wu model of crack growth (see page 250) is adapted from the EPRI and Hickling models for crack growth in Alloy 600 exposed to a primary water environment, and accounts for three separate crack growth rate regimes [27]. The crack growth rate is influenced by temperature, stress intensity, and pH.

The MATLAB® code used to model the Wu approach to crack growth can be found in Section 8.2.5 on page 370. (It appears as part of the Henshall/Wu combined model.)

3.2.4.1 Wu: Model structure Figure 19 is a flowchart that shows the structure of the code used to model the crack growth process described by Wu.

Initial depths are assigned to each flaw in the crack vector. In a pit-to-crack model, the initial depth is simply the depth at which the flaw transitioned from a pit to crack.

The flaw is cycled through the loop until its depth exceeds the canister thickness, at which point failure is assumed to have occurred.

At each iteration of the loop, the stress intensity is calculated as a function of depth. The value of the stress intensity then determines which of the three crack growth regimes govern the flaw at that point. Note that if only one regime or two regimes are deemed necessary to describe crack growth in the stainless steel canisters, the code can easily be modified to account for this.

The appropriate expression for $(dx/dt)_i$ is then used to determine the new crack depth, by adding $(dx/dt)_i$ to the existing crack depth. The distributions of flaw depth and time-to-failure are then obtained. The shortest time-to-failure is the canister time-to-failure prediction.

Like the Shoji model, this crack growth model is also deterministic in nature.

3.2.4.2 Wu: Parameter selection The Wu model consists of three crack growth regimes, which are described by two crack growth rate expressions (the second regime is a combination of the other two). The regime is determined by the stress intensity at the present flaw depth. The crack growth rate expressions are as follows:

$$\frac{da}{dt} = \begin{cases} \left(\frac{da}{dt}\right)_I & \text{for } K < K_{\text{trs}}, \\ \left(\frac{da}{dt}\right)_I (1-x) \left(\frac{da}{dt}\right)_{II} (x) & \text{for } K < K_{\text{tre}}, \\ \left(\frac{da}{dt}\right)_{II} & \text{for } K \geq K_{\text{tre}} \end{cases} \quad (11)$$

$$\left(\frac{da}{dt}\right)_I = C_I \cdot \exp \left[\frac{Q}{R} \left(\frac{1}{T} - \frac{1}{T_{\text{ref}}} \right) \right] \cdot [\sigma_{\text{ys}}]^{m_I} \cdot [K - K_{\text{th}}]^{n_I} \quad (12)$$

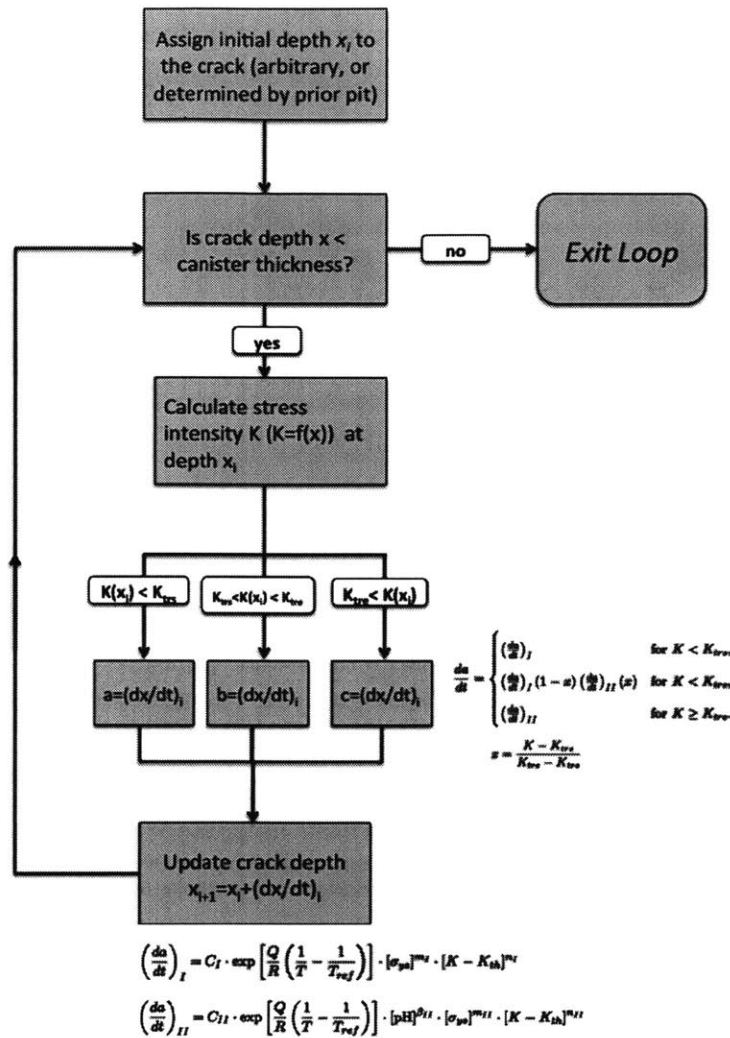


Figure 19: This flowchart illustrates the structure of the code used to model the crack growth process described by Wu. There are three possible regimes of crack growth, determined by the stress intensity in the material at the flaw depth during a given iteration. The appropriate crack growth rate is used to update the crack depth.

$$\left(\frac{da}{dt}\right)_{II} = C_{II} \cdot \exp\left[\frac{Q}{R}\left(\frac{1}{T} - \frac{1}{T_{\text{ref}}}\right)\right] \cdot [\text{pH}]^{\beta_{II}} \cdot [\sigma_{\text{ys}}]^{m_{II}} \cdot [K - K_{\text{th}}]^{n_{II}} \quad (13)$$

This model is intended to describe SCC in Alloy 600 exposed to a PWR environment. This is very different from the environment of interest in this project: Alloy 600 is a nickel-based alloy with different properties than Type 304 stainless steel, and a PWR environment involves the constant present of a bulk, high-temperature, moving fluid instead of a deliquesced salt film.

The following constants are selected from normal distributions. The means of these distributions are identical to the values Wu calculated using Bayesian regression techniques. These values are presented in Table 8. The standard deviation of these distributions is set by the user as a global parameter at the beginning of the simulation. As with the Henshall and Shoji models, these normal distributions were truncated to prevent the selection of a negative value. This truncation is not expected to have a significant impact on the results of the simulation. The distributions are plotted in Appendix B on page 376. It is recommended that any future modeling efforts using the Wu model to describe cracking in used fuel canisters use data from dedicated experiments (e.g. the measurement of cracks in weld material exposed to a chloride solution) to get a better fit for these constants.

R , the gas constant, has a value of 0.008314 kJ/mol-K. The temperature T is a time-dependent function. The equation for temperature at the canister surface described on page 63. $K_{\text{threshold}}$ is 4 MPa $\sqrt{\text{m}}$, as described on page 63. $K(x)$ is calculated based on the K distributions described in 3.1.4.

K_{trs} and K_{tre} , the K values which demarcate the bounds of each cracking regime, are given in [27] as 20 and 30 MPa $\sqrt{\text{m}}$, respectively. In order to estimate reasonable values for the weld material, $K_{\text{threshold}}$ of Alloy 600 (9 MPa $\sqrt{\text{m}}$) was compared with the $K_{\text{threshold}}$

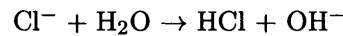
Table 8: Constant values for Equations (12) and (13)

| Constant | Value |
|----------|------------------------|
| C_1 | 9.70×10^{-12} |
| C_2 | 2.86×10^{-12} |
| m_1 | 0.2286 |
| m_2 | 0.1836 |
| n_1 | 0.8982 |
| n_2 | 0.7360 |
| b_2 | 0.3418 |

determined for Type 304 stainless steel ($4 \text{ MPa}\sqrt{\text{m}}$). As a first estimate, K_{trs} and K_{tre} were similarly shifted to lower values: K_{trs} in this model became $15 \text{ MPa}\sqrt{\text{m}}$, and K_{tre} became $25 \text{ MPa}\sqrt{\text{m}}$. Cracking studies performed on weld material should be used in conjunction with residual stress measurements in order to better refine these values (and/or determine whether a three-regime crack growth model is appropriate).

The activation energy for cracking, as given in [27], is 130 kJ/mol. In order to re-estimate this value for use with Type 304 stainless steel, a study of SCC in Type 304 stainless steel in high temperature chloride solutions was consulted [40].¹² This study found that the activation energy for cracking was 29 ± 12 kJ/mol. In the code, the activation energy is described as a Gaussian distribution with a mean of 29 kJ/mol and a standard deviation of 4 (so that 99.7% of the possible activation energies described by the distribution are within ± 12 of the average).

Finally, it was necessary to determine how to calculate the pH of the chloride solution. The following procedure was followed. First, from the reaction of NaCl with water, one obtains the following chemical reaction:



¹²Note that the stainless steel considered in [40] was sensitized, unlike the canister welds.

The base dissociation constant for this reaction is

$$K_b = [\text{HCl}][\text{OH}^-] / [\text{Cl}^-]$$

The acid dissociation constant K_a for hydrochloric acid is 1.3×10^6 . Then, we have

$$K_a \cdot K_b = 10^{-14}$$

from which one finds $K_b = 7.7 \times 10^{-21}$. Algebraic expressions for the equilibrium concentration of Cl^- , HCl , and OH^- are then assigned:

- $[\text{Cl}^-] = [\text{Cl}^-]_{\text{initial}} - x$
- $[\text{HCl}] = x$
- $[\text{OH}^-] = x$

K_b can then be expressed as

$$7.7 \times 10^{-21} = K_b = \frac{x^2}{[\text{Cl}^-]_{\text{initial}} - x}$$

and simplified to

$$7.7 \times 10^{-21} = K_b = \frac{x^2}{[\text{Cl}^-]_{\text{initial}}}$$

under the assumption that x is small. Solving for x yields $x = \sqrt{(7.7 \times 10^{-21} \cdot [\text{Cl}^-])}$. x is equivalent to the concentration of $[\text{OH}^-]$, and so $\text{pOH} = -\log(x)$. $\text{pH} = 14 - \text{pOH}$, and so we find pH as a function of chloride concentration:

$$\text{pH} = 14 + \log \left(\sqrt{7.7 \times 10^{-21} [\text{Cl}^-]} \right) \quad (14)$$

The function describing chloride concentration as a function of time is the same as the function used in the Henshall model, for the purposes of consistency across the considered models.¹³

3.2.5 Combining the pit growth only/crack growth only models into pit-to-crack models

Figure 20 is a flowchart that shows the general structure of the code used to combine the two pit growth models and the two crack growth models into four distinct pit-to-crack SCC models.

¹³This function for chloride concentration should be adapted when the canister environment is modeled more accurately in future studies.

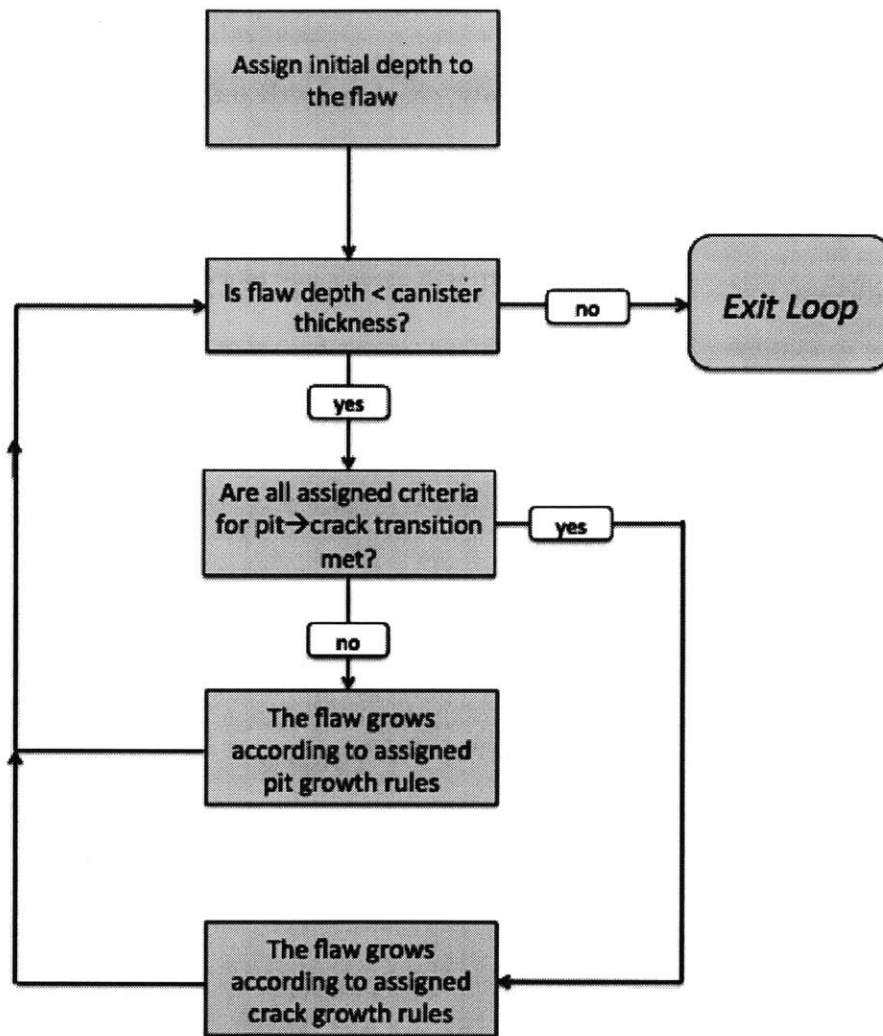


Figure 20: This flowchart illustrates the general schematic used in the combined pitting/cracking models

To begin the pit-to-crack simulation, the initial depth is assigned either arbitrarily (usually very close the surface) or from an appropriate distribution. Note that in the eventual realization of the models for the *Life Prediction of Canister Material*, the evolution of the aggressive environment will be modeled as well, and this will govern the distribution (in time and space) of the initiating pits.

Flaws remain in the loop for as long as their depth is less than the canister thickness. Their depth increases according to the selected stochastic pit growth loop until the assigned criteria for pit-to-crack transition have been met. These criteria are some combination of the following: (1) the theoretical crack growth rate at that depth exceeds the pit growth rate (2) the stress intensity factor K at that depth exceeds the threshold cracking stress intensity and (3) the flaw depth exceeds some threshold material depth for cracking. The loop can be adapted to include the appropriate criteria.

When the selected criteria have been met, the flaw continues to grow, but its growth rate is governed by the appropriate crack growth rate regime.

For more specific information on each of the four pit-to-crack models developed from the pitting model and the two cracking models selected from the figure-of-merit considerations, the full code for each is listed in Appendix B as follows:

- Henshall/Shoji: Section 8.2.4, page 361.
- Henshall/Wu: Section 8.2.5, page 370.

3.3 A note on flaw grouping and parameter variation in the models

As explained in this section, the equations that compose each model include different coefficients, exponents, and other fitting parameters. Their values are determined from the nominal values given in the original papers, or estimated based on reasonable values in the literature for other similar applications (e.g. stainless steel exposed to a chloride solution).

These are selected for each flaw (or group of flaws) from a normal distribution centered around the “official” value of the given parameter, coefficient, or exponent. These distributions are truncated at zero to prevent unphysical results (see Appendix B for graphs of all relevant distributions). These normal distributions have a standard deviation that is set at the beginning of the simulation. Multiple cases of “global” standard deviation - referred to as the standard deviation of the coefficient selection normal distributions - are considered for each model.¹⁴

Some parameters are selected for an entire group flaws. Other parameters vary between individual flaws. The “group” system allows for this type of variation. For each model, the variation classification is given here for reference.

3.3.1 Henshall model

Grouped parameters: A_4 , B_4 , B_5 , C_4 , K_0 , K_1

No variation: E_0 , E_1 , temperature coefficients

For example, the Henshall standalone pitting model was run with 5000 groups of 10,000 pits each. Within one group of 10,000 pits, all pits had the same values of A_4 , B_4 , B_5 , C_4 , K_0 , and K_1 . For a given group, these coefficients were selected from a normal distribution centered around the nominal value of each coefficient. The standard deviation of those normal distributions is set by the user at the beginning.

E_0 and E_1 are always the same, as variation led to mathematical issues in the model. The temperature function was specifically selected for modeling the canister surface (it is not the same as the original temperature function proposed by Henshall), and varying the coefficients would have altered the function.

¹⁴For some models, 0, 10, 15, 25, and 50% were considered. For others, the larger standard distributions led to very slow computation times and were not included.

3.3.2 Shoji model

Grouped parameters: m, n, β, λ

The Shoji cracking model is used in conjunction with the Henshall pitting model. The parameter variation for the Henshall model in the combined model is the same as in the standalone Henshall model.

3.3.3 Wu model

Grouped parameters: $C_1, C_2, m_1, m_2, n_1, n_2, b_2, Q$

The Wu cracking model is used in conjunction with the Henshall pitting model. The parameter variation for the Henshall model in the combined model is the same as in the standalone Henshall model.

3.3.4 Turnbull model

Grouped parameters: p, q

Parameters selected for each individual flaw: C, β, α

Note that $p = 2q$, so the selection of q for a group also determines p . C and α are selected from normal distributions whose standard deviations are prescribed in the original paper. q and β are then the only parameters selected from a normal distribution whose standard deviation is set by the user.

4 Results

4.1 Results: Henshall pitting model

In the Henshall pitting model, the probability that a pit will grow is calculated at each iteration of the code. The probability changes based on the environmental conditions at the pit. If a random number is greater than this probability, the pit grows. The rate at which the pit grows (D) is based on experimental pitting data.

Time units of years were used in these simulations. Two cases were considered when using this model. In the first, when the pit grew, it always grew by an amount equivalent to D . In the second, the pit grew by an amount equivalent to a random number between 0 and 1 multiplied by D .¹⁵ The first case is the more conservative, with the overall faster pit growth.

The coefficients associated with the Henshall model were selected from a normal distribution (with negative values truncated) with a standard deviation set at the beginning of the simulation. 5 cases of this standard deviation were tested: 0, 10%, 15%, 25%, and 50%. Coefficients were selected from normal distributions to represent the uncertainty associated with their values at this time, and to simulate the variability of corrosion phenomena.

Units of time are in years. Note that “SD” stands for “standard deviation,” and “TTF” stands for “time-to-failure.” “Breaks” refers to the number of times the flaw growth loop moved onto the next flaw when a set number of iterations was reached.

The results of these simulations are shown in Table 9. Each simulation consisted of 5000 groups of 10,000 flaws each.

Relevant distributions are shown from smaller simulations. Figures 21 and 22 show the distributions of pit depths at failure times and of pit times to failure for a simulation with

¹⁵Note that in the combined models, the second case is always used in order to further mimic the variability associated with pitting.

1000 groups of 1000 pits each, a coefficient selection standard deviation of 0, and with flaws that grow by $+(\mathbf{rand} \cdot D)$ on growth steps.

Figure 23 shows the distribution of failure times for the same simulation as the first (flaws that grow as $+\mathbf{rand} \cdot D$ but with a coefficient selection standard deviation of 10%). Figure 24 shows the distribution of failure times for the same simulation, but run for the more conservative case with flaws that grow as $+D$ on growth steps. In addition to an overall shift to shorter failure times, the shape of the distribution is more symmetric than those pictured in Figures 22 and 23.

Table 9: Time-to-failure results of the Henshall pitting model

| SD associated with simulation | Average TTF | Minimum TTF | SD of TTF | Median TTF | Breaks |
|---|--------------------|--------------------|------------------|-------------------|---------------|
| <i>Pit grows as "flaw depth + D"</i> | | | | | |
| 0 | 28.945 | 21 | 1.2688 | 29 | 0 |
| 10 | 28.006 | 21 | 1.2769 | 29.058 | 0 |
| 15 | 29.037 | 21 | 1.2779 | 29.09 | 0 |
| 25 | 29.182 | 21 | 1.2815 | 29.232 | 0 |
| 50 | 29.903 | 19 | 1.298 | 29.956 | 0 |
| <i>Pit grows as "flaw depth + rand · D"</i> | | | | | |
| 0 | 42.049 | 32 | 3.0924 | 42.05 | 0 |
| 10 | 42.064 | 27 | 3.2127 | 41.957 | 0 |
| 15 | 42.105 | 28 | 3.213 | 41.983 | 0 |
| 25 | 42.249 | 27 | 3.2143 | 42.119 | 0 |
| 50 | 42.981 | 26 | 3.2218 | 42.844 | 0 |

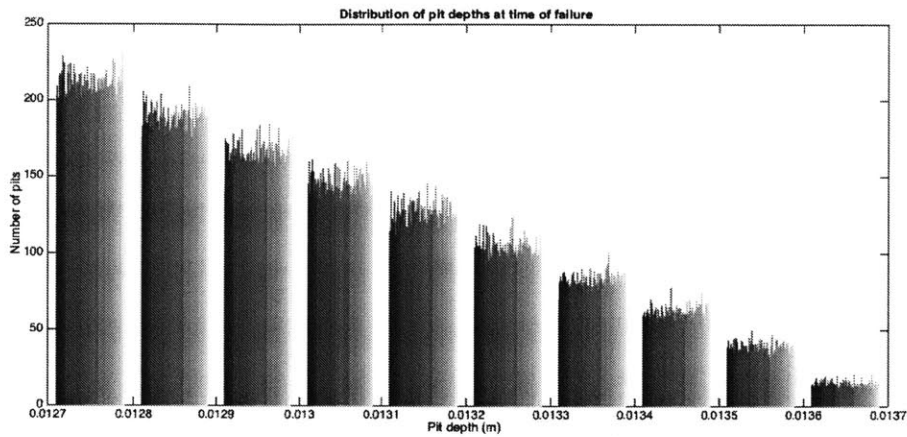


Figure 21: The Henshall pitting model was run for 1000 groups of 1000 flaws each with a SD of 0 (e.g. all coefficients had the same value) and with a randomized amount of growth. Bars of the same color correspond to the same group, showing that the groups all exhibit similar behavior. Distribution of calculated pit depths at time-to-failure is shown. Pits failed and exited the growth loop when their depth first exceeded the width of the canister wall (0.0127 m, or 1/2 inch). Depths greater than 0.0127 m are not physical. The distribution shows the expected behavior: fewer pits are growing at such a high rate that they significantly “overshoot” on the final iteration step before failure.

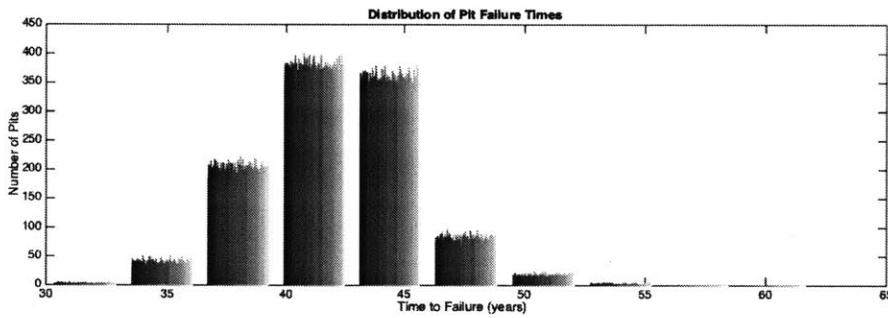


Figure 22: The Henshall pitting model was run for 1000 groups of 1000 flaws each with a SD of 0 (e.g. all coefficients had the same value) and with a randomized amount of growth. Color corresponds to group. Distribution of pit times-to-failure is shown. Pits failed and exited the growth loop when their depth first exceeded the width of the canister wall (0.0127 m, or 1/2 inch).

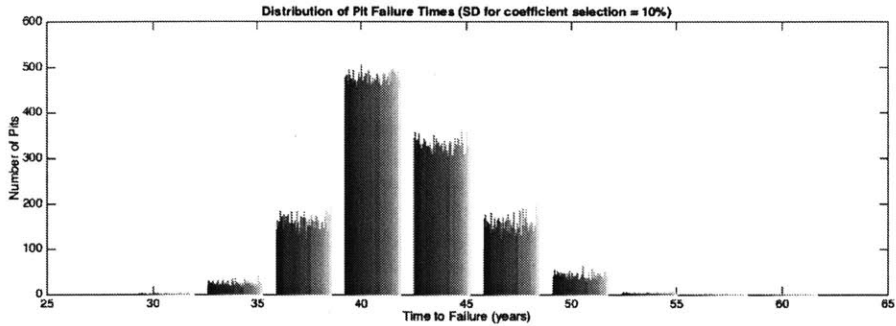


Figure 23: The Henshall pitting model was run for 1000 groups of 1000 flaws each with a SD of 10 (coefficients were selected from normal distributions characterized by a 10% SD from the nominal mean) and with a randomized amount of growth. Color corresponds to group. Distribution of pit times-to-failure is shown. Pits failed and exited the growth loop when their depth first exceeded the width of the canister wall (0.0127 m, or 1/2 inch).

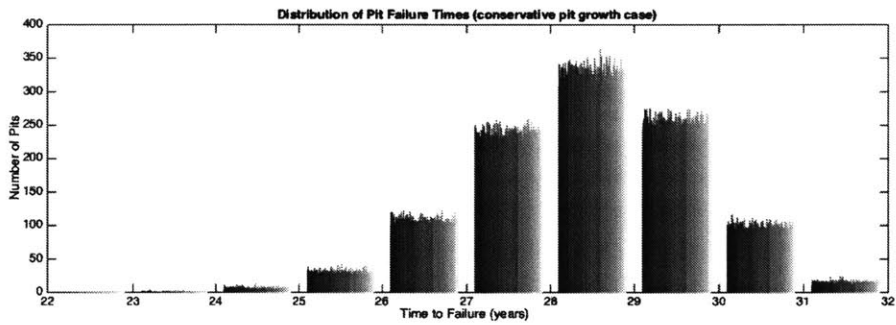


Figure 24: The Henshall pitting model was run for 1000 groups of 1000 flaws each with a SD of 0 (e.g. all coefficients had the same value) and without a randomized amount of growth (flaws grew by an amount D instead of by an amount $\text{rand} \cdot D$). Color corresponds to group. Distribution of pit times-to-failure is shown. Pits failed and exited the growth loop when their depth first exceeded the width of the canister wall (0.0127 m, or 1/2 inch). The average failure time is decreased in this more conservative case.

4.1.1 Results, Henshall/Shoji pit-to-crack model

The results from the Henshall/Shoji pit-to-crack model are presented in Table 10. Three cases were considered. In the first, all coefficients were the same ($SD = 0$). In the second case, coefficients were selected from normal distributions, each centered at the nominal mean value of the relevant coefficient and characterized by a standard deviation of 10%. In the third case, this standard deviation was equivalent to 15%. For the first two cases, 5000 groups of 10,000 flaws were simulated. In the third case, 500 groups of 10,000 flaws were simulated. Simulations took progressively longer to run as the standard deviation of the coefficient distributions was increased.

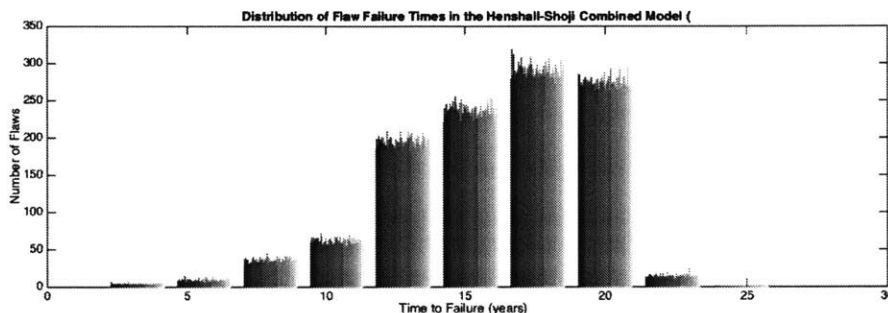


Figure 25: The Henshall/Shoji combined pit-to-crack model was run for 1000 groups of 1000 flaws each with a SD of 0 (coefficients did not vary between groups) and with a randomized amount of growth. Color corresponds to group. Distribution of flaw times-to-failure is shown. Flaws failed and exited the growth loop when their depth first exceeded the width of the canister wall (0.0127 m, or 1/2 inch).

The timestep was equivalent to one year, as shorter timesteps led to impractical calculation times. However, once the flaws in the Henshall/Shoji model transitioned to cracks, they failed in one timestep (Table 10 shows that the maximum cracking time in each step was “1 year.” However, the flaws don’t spend a full year cracking, and a consideration of the flaw depths at the time of failure showed that the final depths were significantly larger

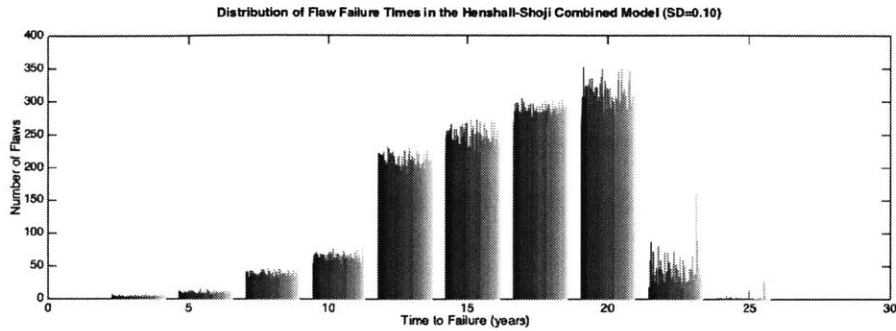


Figure 26: The Henshall/Shoji combined pit-to-crack model was run for 1000 groups of 1000 flaws each with a SD of 0.10 (coefficients for each group were selected from a normal distribution with a 10% standard deviation from the mean) and with a randomized amount of pit growth. Color corresponds to group. Distribution of flaw times-to-failure is shown. Flaws failed and exited the growth loop when their depth first exceeded the width of the canister wall (0.0127 m, or 1/2 inch).

Table 10: Time-to-failure results of the Henshall/Shoji pit-to-crack model (all results in units of years)

| SD (%) | Average Pitting Time | Average Cracking Time | Maximum Cracking Time | SD of Pit TTF | Minimum Pit TTF | Median Pit TTF |
|--------|----------------------|-----------------------|-----------------------|---------------|-----------------|----------------|
| 0 | 15.24 | 1 | 1 | 3.179 | 1 | 16 |
| 10 | 15.271 | 1 | 1 | 3.1814 | 1 | 15.768 |
| 15 | 15.24 | 1 | 1 | 3.177 | 1 | 15.734 |

than the canister. In this model, then, the time at which the pits transition to cracks is of interest (with the assumption that crack growth proceeds rapidly following the transition, thus assuring rapid failure once cracking begins). On average, it took approximately 15.24 years for this transition to occur.

The minimum observed time-to-failure (defining the pit-to-crack transition as the effective failure time) was one year. This minimum occurred for each simulation case.

Figures 25 and 26 show the distribution of times to failure for smaller simulations (1000 groups of 1000 flaws each) with 0% and 10% standard deviation of coefficient selection distributions, respectively. Increasing the standard deviation increases the number of pits that survive past 20 years, but overall, the behavior of the flaws remains largely the same.

4.1.2 Results: Henshall/Wu pit-to-crack model

Table 11: Time-to-failure results of the Henshall/Wu pit-to-crack model (all results in units of years)

| SD | Average Pitting time | Average Cracking time | Average TTF | Minimum TTF | SD of TTF | Median TTF | Breaks |
|----------------------------|----------------------|-----------------------|-------------|-------------|-----------|------------|--------|
| <i>Timesteps in years</i> | | | | | | | |
| 0 | 15.244 | 1.4623 | 16.706 | 2 | 3.224 | 17.00 | 0 |
| 10 | 15.271 | 1.4622 | 16.733 | 2 | 3.237 | 17.15 | 0 |
| 15 | 15.307 | 1.4624 | 16.769 | 2 | 3.241 | 17.22 | 0 |
| <i>Timesteps in months</i> | | | | | | | |
| 0 | 15.244 | 1.4624 | 15.365 | 1.083 | 3.172 | 16.08 | 0 |
| 10 | 15.271 | 1.4624 | 15.393 | 1.083 | 3.184 | 15.89 | 0 |
| 15 | 15.307 | 1.4624 | 15.428 | 1.083 | 3.189 | 15.89 | 0 |

The Henshall/Wu model was carried out for one set of cases with the timestep set to years, and for a second set of cases with the timestep set to months. This was done in order to investigate the effect of increased sensitivity to the environmental functions for potential, temperature, and chloride concentration that determine the growth probability in the Henshall pitting part of the model. In all cases, when pit growth occurred, flaws grew by an amount $\text{rand} \cdot D$. Results are presented in Table 11.

The average failure time for the 0% case when the timestep was in years was 16.706 years. As the standard deviation of the coefficient selection normal distributions was increased, this average grew, but did not exceed 17 years. Figure 30 shows the results of a simulation of 1000 groups of 100 flaws in which the Henshall/Wu model was set to a 10% standard deviation for the coefficient selection normal distributions. In this particular simulation, a “break” criterion was imposed when the counter for an individual flaw reached

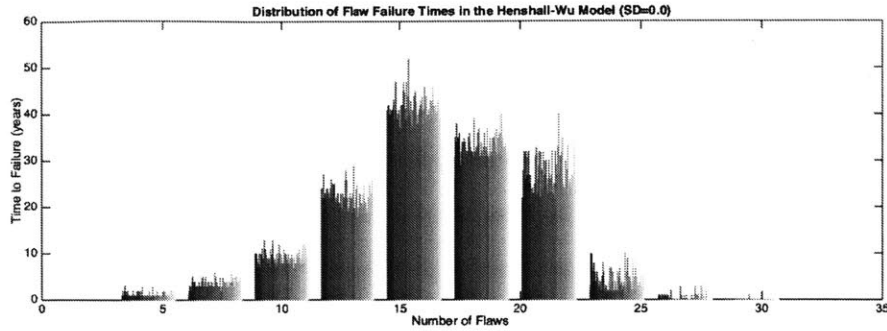


Figure 27: The Henshall/Wu combined pit-to-crack model was run for 1000 groups of 100 flaws each with a SD of 0 (coefficients did not vary between groups) and with a randomized amount of growth during the pitting regime. Color corresponds to group. Distribution of flaw times-to-failure is shown. Flaws failed and exited the growth loop when their depth first exceeded the width of the canister wall (0.0127 m, or 1/2 inch).

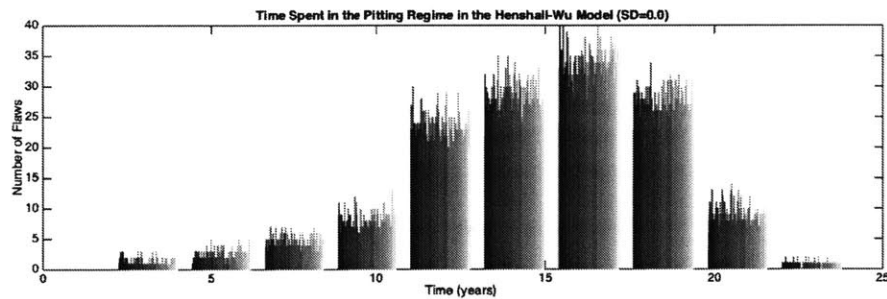


Figure 28: The Henshall/Wu combined pit-to-crack model was run for 1000 groups of 100 flaws each with a SD of 0 (coefficients did not vary between groups) and with a randomized amount of growth. Color corresponds to group. This figure shows the amount of time spent in the pitting regime.

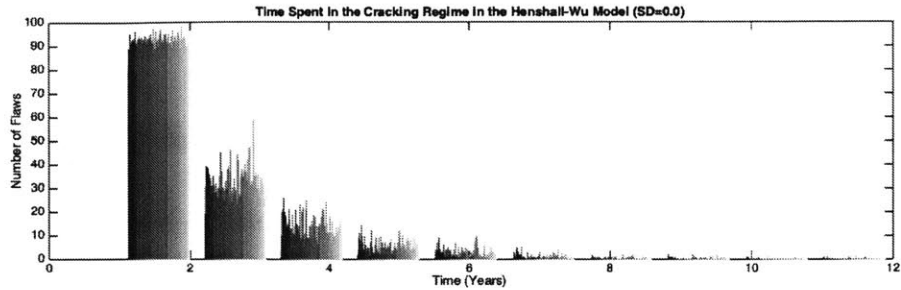


Figure 29: The Henshall/Wu combined pit-to-crack model was run for 1000 groups of 100 flaws each with a SD of 0 (coefficients did not vary between groups). Color corresponds to group. This figure shows the amount of time spent in the cracking regime. The distribution is heavily biased toward shorter times (1-2 years).

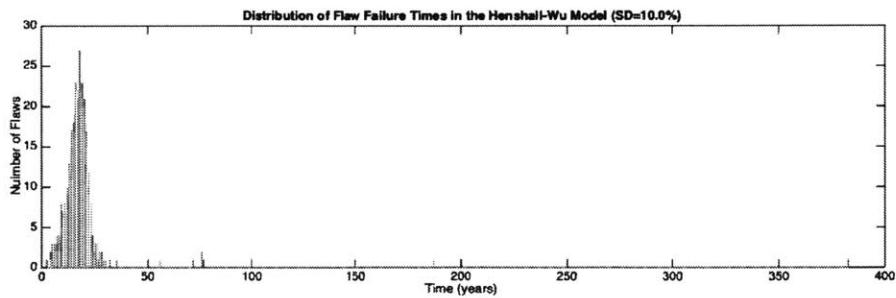


Figure 30: The Henshall/Wu combined pit-to-crack model was run for 1000 groups of 100 flaws each with a SD of 10%. Color corresponds to group. The shape of the distribution is similar to the 0% case, but there are a small number of flaws that grow very slowly.

500 years. The increased standard deviation results in a small number of very slow-growing flaws, which bring up the average failure time.

The minimum failure time was two years when the timestep was in years, but just over 1 year when the timestep was in months.

The “break criterion” in the simulations whose results are given in the table was 1000 years. No breaks occurred during these simulations.

4.1.3 Results: Turnbull pit-to-crack model

Table 12 shows the results of five Turnbull model simulations. Each simulation consisted of 100 groups of 100 flaws. Larger groups showed the same behavior represented here, and so smaller simulations were carried out in order to save time while still illustrating the model's behavior.

Table 12: Time-to-failure results of the Turnbull pit-to-crack model (all results in units of years)

| SD (%) | Average Pitting Time | Average Cracking Time | Average Failure Time | SD of TTF | Minimum TTF | Median TTF |
|--------|----------------------|-----------------------|----------------------|-----------|-------------|------------|
| 0 | 211.7081 | 0.0675 | 211.7756 | 1302.2 | 1 | 1 |
| 10 | 210.6521 | 0.0668 | 210.7189 | 1305.7 | 1 | 1 |
| 15 | 260.3089 | 0.0722 | 260.3811 | 1466.3 | 1 | 1 |
| 25 | 318.3050 | 0.0729 | 318.3779 | 1647.3 | 1 | 1 |
| 50 | 792.7782 | 0.0852 | 792.8634 | 2647.3 | 1 | 1 |

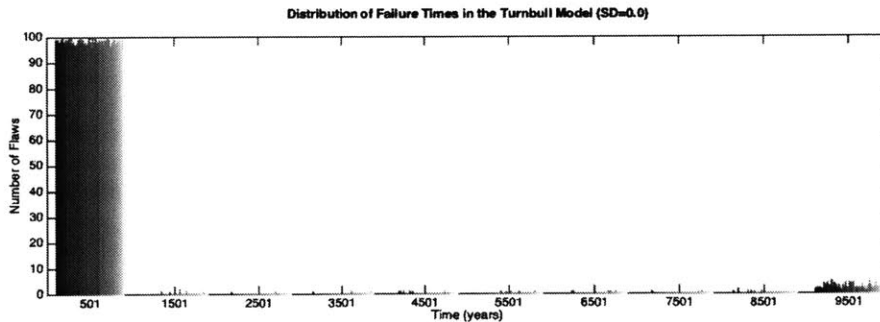


Figure 31: The Turnbull combined pit-to-crack model was run for 100 groups of 100 flaws each with a SD of 0 (no coefficient variation). Color corresponds to group. The majority of flaws fail within one year.

The average time-to-failure was in the hundreds of years for each case. As the standard deviation of the coefficient selection normal distributions was increased, this average tended

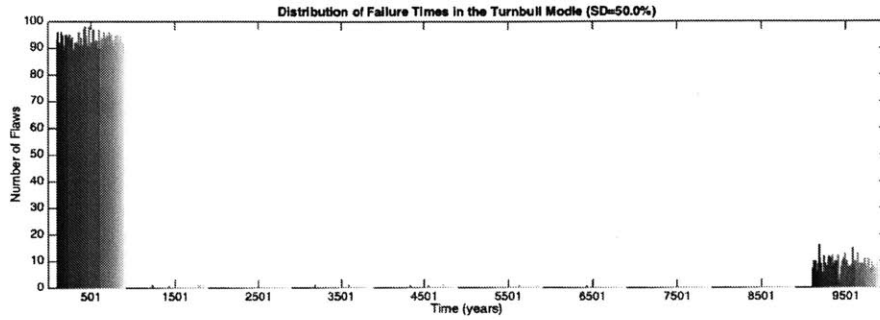


Figure 32: The Turnbull combined pit-to-crack model was run for 100 groups of 100 flaws each with a SD of 50%. Color corresponds to group. The majority of flaws fail within one year, but more flaws fail at long times.

Table 13: Time-to-failure results of the Turnbull pit-to-crack model (10 groups, 5 flaws per group, 0% case)

| Group | 1 | 2 | 3 | 4 | 5 | 6 | 7 | 8 | 9 | 10 |
|-----------------------|---|---|---|---|---|---|---|---|------|-------|
| Iterations to Failure | 1 | 1 | 1 | 1 | 1 | 1 | 2 | 1 | 1 | 10001 |
| | 1 | 1 | 1 | 1 | 1 | 2 | 1 | 1 | 1 | 1 |
| | 1 | 1 | 1 | 1 | 1 | 1 | 1 | 1 | 4056 | 1 |
| | 1 | 1 | 1 | 1 | 1 | 1 | 1 | 1 | 1 | 1 |
| | 1 | 1 | 1 | 1 | 1 | 2 | 1 | 1 | 1 | 1 |

to grow. For the 0% case, the average time-to-failure was 211.71 years. For the 50% case, the average time-to-failure was 792.8 years.

In all cases, the average time spent pitting was much larger (by four orders of magnitude) than was spent cracking. Because the timesteps were in years, the fact that many cracks spent <1 year cracking indicates that some flaws failed without ever transitioning to the cracking regime.

Despite the relatively high average failure time, the median time-to-failure of 1 year (and the standard deviation in the thousands of years for each case) indicates that most flaws experienced fast failure. Figures 31 and 32 show the distribution of failure times for the 0% and 50% cases. It is clear that most flaws fail quickly (due to the binning, it appears that the left-most cluster is centered around 500 years, but this cluster represents the flaws that failed in 1-2 years).

To further illustrate this behavior, Table 13 shows the individual flaw time-to-failures from a short simulation of 10 groups of 5 flaws each. Even in this small simulation, the behavior illustrated in Figures 31 and 32 is apparent.

5 Analysis of results

The results of running the four models are considered here. Plans for improving the utility of each model are proposed.

5.1 Implications of these results

A consideration of the Henshall-based models seems to imply that, once initiated, most flaws will propagate through the canister wall on a timescale of decades. When only pitting is considered, failure occurs in approximately 28 years (conservative case) and approximately 42 years (less conservative case). The pitting-only model is important because of the standing assumption that cracks will not propagate if the residual stress distribution becomes compressive. Because compressive stresses are expected to be present (see [32]), this means that pitting-only behavior could be a failure mode in certain canisters.

In all combined pitting and cracking models, most flaws spent much longer in the pitting regime than in the cracking regime. In the Henshall/Wu and the Henshall/Shoji models, pits transitioned to cracks in approximately 15 years (on average). Once flaws were in the cracking regime, it took, on average, less than two years for the crack to propagate through the canister. In the Henshall-based models, pits transition to cracks when a threshold stress intensity is reached. The value of $K_{\text{threshold}}$ therefore has a major impact on the predictions of the model: the further into the canister wall a pit must travel before it reaches $K_{\text{threshold}}$, the longer the average time-to-failure will be.

However, in a study such as this, the minimum time-to-failure is of the greatest interest. In the Henshall/Shoji and Henshall/Wu models, these minimums occurred between one and two years, suggesting that fairly rapid failure is possible if these models prove to be good representations of true corrosion flaw behavior in the canisters.¹⁶ The median failure

¹⁶The choice of timestep seemed to matter most with regards to the minimum failure values. For example,

time was close to the average in the Henshall-based models, which further highlights the importance of experimental tests. 1-2 year failure times have been shown to exist in simulations of 50 million flaws. These minimum failure times represented the left-most tail end of the failure time distributions. Therefore, it is important to determine how often such short failure times could occur in a real application, where perhaps only a few pits ever develop on the canister surface.

It should be noted that all of these models were run on the assumption that a sufficiently aggressive environment already existed on the canister surface. The effective time-to-failure is therefore expected to be much longer, since these results do not account for the amount of time it takes to develop an aqueous chloride environment on the canister surface, nor the probability that the aggressive environment is sustained for sufficient length of time to initiate pitting.

Another general limitation of the Henshall-based models involves the parameter D , which is the average pit growth rate. In this work, there is a “conservative” Henshall case and a less-conservative, high-variability Henshall case. In the conservative case, flaws fail faster because the pit always grows as D (1 mm/y) when they grow. In the less-conservative case, pits grow as $\text{rand} \cdot D$ when they grow. Both combined models use the less-conservative case in order to simulate the variability expected in real situations. The value of D was obtained from the literature. It should be noted that neither of these cases are as conservative as the assumption that the pit grows steadily at a rate D , because the pits only grow on timesteps for which a random number between 0 and 1 is found to be greater than the calculated growth probability. When the assumption that all cracks initiate as pits holds, the crucial step in the accurate modeling of SCC in the canisters

in the Henshall/Wu model, the minimum time-to-failure was found to be 2 years when the timestep of the simulation was set to years. However, setting the timestep to months revealed that the minimum time-to-failure was just over 1 year. It may also be found that the environmental functions for temperature, chloride concentration, and potential, once updated, require the use of a smaller timestep for improved accuracy.

is therefore ensuring that the simulated pit growth rates reflect real pitting behavior in canister material.

This study also highlights the differences between models. For example, the Henshall/Shoji and Henshall/Wu models both share the same pitting model. The cracking models, on the other hand, are quite different. The Shoji model predicts cracking at an extremely rapid rate - so rapid that predicted flaw depths at the time-of-failure were in the hundreds and thousands of meters. In order for this model to be valid as it stands, experiments would need to show that cracking was extremely rapid in the canisters, such that failure was effectively instantaneous once the pits transitioned. Otherwise, the Shoji cracking model requires extensive parameter refitting - or perhaps it simply isn't the appropriate model for the physical reality of cracking in the canisters. The Henshall/Wu model, on the other hand, indicates that flaws spend approximately 1 year in the cracking regime before the canister wall is completely breached.

As for the Turnbull model, the results show that it is not likely - at least in its current form - to be the best model for the purpose of predicting SCC. The majority of flaws fail very rapidly, in just one iteration. A small number of flaws fail only after thousands of years.¹⁷ Because this is a pit-to-crack model, this indicates that the majority of flaws are failing in the pitting regime, since they initiate as pits. However, rapid failure via pitting is not physically representative of the behavior of stainless steels. The Turnbull model therefore is likely to require significant parameter refits if it is to be used. (Note that this model was originally developed for disc steel and not stainless steel.)

To summarize, the Henshall/Shoji and Henshall/Wu models predicted average and median failure times of around fifteen years, with minimum failure times of one to two years. Importantly, these failure times are counting from the point of aggressive environment

¹⁷This is consistent with the findings of Turnbull et al., who indicate that the parameters associated with certain flaws will result in extremely slow flaw growth.

formation and flaw initiation, and not from the point at which the canister is first placed outside at the ISFSI site. The pitting-only model predicted longer failure times, as expected. The Turnbull model's predictions, using the parameter values prescribed in the original model, did not yield a time-to-failure distribution that was consistent with the expected physical behavior of real flaws.

In particular, this study showed the importance of the pitting regime in the prediction of failure times. If the Henshall model is used in the future to predict pitting behavior, the pit growth rate applied to the flaw on growth-positive steps significantly impacts the model's predictions, and will be very important to fit experimentally. Another very important value to confirm via experimentation is $K_{\text{threshold}}$, since this also has a major impact on the amount of time the flaw spends in the pitting regime.

Of the four options considered here, the Henshall/Wu model seems the most promising at this time. This model simulates pits that transition to cracks, with crack growth that is significantly faster than the pit growth, but not so rapid that failure occurs immediately following the transition to the cracking regime.

5.2 Future work: Refining the models

Recommended future work includes the further refinement of these models so that they can be used to make more definitive predictions regarding the pitting and cracking of canister material.

Updating the values of coefficients, parameters, and exponents with experimental data means that the current scheme of selecting values from a normal distribution centered around a mean and with a standard deviation set by the user can be refined. This strategy was implemented to represent both the uncertainty in the applicability of these values to the canister situation, and to mimic natural variation. However, experimental data can be

used to determine the actual distribution of values the parameters can take. It is expected that the standard deviation of these distributions would be unique to each parameter value distribution.

5.2.1 Quantification of residual stresses

The Turnbull model, the Wu cracking model, and the Shoji cracking model all depend on stress or stress intensity. In this model, functions for stress and stress intensity through the canister wall are developed using the through-wall stress and stress intensity predictions in [32]. However, it is desirable to have a more definitive understanding of the residual stresses present in the weld material.

To accomplish this, experiments are planned that will enable the researchers continuing on this project to measure residual stresses in canister weld material. One method is neutron diffraction, which requires the use of beamtime at a facility familiar with such measurements. A proposal was submitted to the Canadian Institute for Neutron Scattering to obtain beamtime at such a facility, and was successful. The measurements were carried out at Chalk River Laboratories in Canada in the fall of 2014. Select initial residual stress measurement results from this collaboration can be found in Appendix C in Section 9.2. These measurements were not in hand at the time that the research for this thesis was being carried out, which is why they were not used as the residual stress inputs for the models studied herein.

Once obtained, this data can be used to fit a new residual stress function. Note that only one type of canister weld will be measured, so if possible, future research should include residual stress measurement in welds from various vendors and of various geometries to determine if the through-wall residual stress patterns vary significantly. If it does, then predicting SCC in a given canister may require a canister-type-specific residual stress

distribution.

Note that in this study, only one of the three residual stress distributions was considered. This was the “barely-above K-threshold” distribution first described in [32]. The “best-estimate” residual stress was not used because of the starting assumptions that (1) cracks and pits grow in a straight path, normal to the canister surface and (2) cracks do not grow if residual stresses become compressive. The “best-estimate” case included compressive stresses, and so was not considered for use with the cracking models. A more thorough understanding of the three-dimensional residual stresses throughout a canister would enable understanding of where cracking is a possibility. It may also be found that cracks grow in three dimensions as well, and may be able to grow “around” compressive regions. The “highly-tensile” case resulted in very rapid failure that did not seem representative of physical reality. Therefore, for this initial study, only the “barely-above-K-threshold” case was used, as it did not result in crack arrest nor immediate failure.

5.2.2 Experiments with weld material (general to all models)

Weld material should be used for cracking and exposure experiments in order to better understand the expected pitting and cracking behavior. The initiation and growth of pits and cracks can be monitored and measured. This allows for the refinement of the models (for example, by allowing for the calculation of the coefficients on crack growth rate laws, or for improving the estimate of the pit growth rate D).

Experiments will also allow for an improved understanding of how flaws grow, and can be used to validate or update the current set of assumptions, including

- Cracks always initiate as pits first
- Pits always transition to cracks when a certain $K_{\text{threshold}}$ is reached

- $K_{\text{threshold}} = 4 \text{ MPa}\sqrt{\text{m}}$
- Cracks are always arrested in regions of compressive stress
- Cracks can be modeled as growing normal to the surface; lateral crack growth can be neglected

These experiments can also determine whether additional assumptions should be included, such as whether the crack growth rate must exceed the pit growth rate in order for the pit to transition (this is the Kondo pit-to-crack criterion, which was adopted by Turnbull [18]).

Exposure experiments can be used to understand the conditions that must develop in order for flaws to initiate in real weld material. They can also be used to update the environmental functions used in the Henshall pitting model. In particular, the functions for potential and chloride concentration are merely estimates in their current form. Ideally, a thorough model would be able to account for the specific conditions at a given ISFSI site in order to create the most accurate functions for the potential and chloride concentration.

5.2.3 Refining the Henshall pitting model

Table 14: More information about the Henshall model

| | |
|--|----------|
| Implementing the Model | Page 72 |
| Full Description of the Henshall Model | Page 178 |
| Henshall Code | Page 351 |

Data collected from pitting experiments can be used to calculate better fits for the constants that govern pit growth. The following aspects of the Henshall model are expected to require additional future work:

- Refinement of the expected pit growth rate D should be carried out using experimental data
- Refinement of the constants A_4 , B_4 , B_5 , and C_5 used in the pit growth probability γ should be carried out using experimental data
- The functions used to determine E_{app} , $[\text{Cl}^-]$, and T as a function of time should be updated to be consistent with the environment evolution model

First, the pit growth rate D - currently estimated to be 1 mm/s - should be refined by measuring the growth rates of multiple pits under representative conditions and using that data to determine an appropriate value.

Once D has been refined, the probability that a pit will grow at each second, γ can be examined. γ is expressed as:

$$\gamma = A_4(E_{\text{app}} - B_4)^{B_5}([\text{Cl}^-])^{C_4} \exp(+Q_\gamma/RT) \quad (15)$$

and has four constants A_4 , B_4 , B_5 , and C_5 that should be refined for the specific case of stainless steel canister weld material exposed to a deliquesced chloride solution. The growth of pre-initiated pits can be tracked for various constant values of E_{app} , $[\text{Cl}^-]$, and T . It is suggested that pitting experiments be carried out which vary one of the three environmental parameters E_{app} , $[\text{Cl}^-]$, and T while holding the other two constant in order to determine the impact each environmental parameter has on the pit growth probability γ . A_4 , B_4 , B_5 , and C_5 should be adjusted such that when E_{app} , $[\text{Cl}^-]$, and T are changed in the code to reflect the experimental conditions, with D also set to the updated value, the Henshall code's predictions of pit depth as a function of time are consistent with the experimental data.

Finally, the time-dependent equations for E_{app} , $[\text{Cl}^-]$, and T should be updated to

reflect the expected environmental evolution on a canister surface. This may mean that these functions are expanded to include dependencies on inputs other than time.

5.2.4 Refining the Henshall/Shoji model

Table 15: More information about the Shoji model

| | |
|-------------------------------------|----------|
| Implementing the Model | Page 79 |
| Full Description of the Shoji Model | Page 204 |
| Henshall/Shoji Code | Page 361 |

Data collected from cracking experiments can be used to calculate better fits for the constants that govern crack growth. The Shoji model predicted extremely large crack growth rates, suggesting that most parameters would need to be refit to data from cracking experiments using the actual weld material in a representative environment (such as a stagnant, highly-concentrated chloride solution).

There are parameters specific to the Shoji model that require fitting (or validation that the original values are accurate for the canister situation), including β , λ , m , and n . Other parameters are materials properties that can be directly measured. These include i_0 , t_0 , and other constants that are factors in the Shoji crack growth rate equation. These, too, should be measured and updated: for example, the crack growth rate at a given time step is directly proportional to the value of i_0 .

Finally, the Shoji cracking model is a slip-dissolution-repassivation (SDR) model. If experimentation with the canister welds reveals that the crack behavior isn't consistent with the SDR theory, then the Shoji model should be removed from consideration as the cracking model.

5.2.5 Refining the Henshall/Wu model

Table 16: More information about the Wu model

| | |
|----------------------------------|----------|
| Implementing the Model | Page 89 |
| Full Description of the Wu Model | Page 250 |
| Henshall/Wu Code | Page 370 |

The Wu model for cracking was developed for Alloy 600 in a PWR environment. As such, it seems likely that if this model format is used, most fitting parameters (in particular, the coefficients in front of the crack growth rate laws) would need to be updated to cracking data in canister material exposure experiments.

Additionally, the pH and temperature functions would likely need to be updated in the Wu model (as well as in the Henshall pitting model). If the local environment varies significantly on the timescale of hours or days, the model would likely provide better predictions if the timescale was decreased. However, this can present significant challenges with regards to computation time.

If temperature and pH do not vary much on the timescale of the cracks (e.g. the 1-2 years predicted here), it may also be possible to calculate the time it takes for a crack to propagate through a canister wall as a function of initiation depth. In that case, it would only be necessary to predict the distribution of times spent in the pitting regime by the flaws, and the time spent in the cracking regime could be calculated from this new function based on the flaw depth at the time of transition.

Another important feature of the Wu cracking model is the three cracking regimes that are present. Experiments with canister material may reveal that the cracking behavior of the flaws does not include three distinct regimes, and it may be possible to modify the model to use only one or two crack growth rate laws. If there are distinct regimes, it also

seems likely that the K values at which crack regime transitions occur would need to either be updated or validated with experimental data.

5.2.6 Turnbull pit-to-crack model

Table 17: More information about the Turnbull model

| | |
|--|----------|
| Implementing the Model | Page 67 |
| Full Description of the Turnbull Model | Page 232 |
| Turnbull Code | Page 344 |

Pitting studies and cracking studies using canister weld material and representative environments should be carried out to better understand the expected corrosion behavior. The following aspects of the Turnbull model are expected to require additional future work:

- Refinement of the pit growth/pit growth rate parameters α and β
- Refinement of the crack growth/crackgrowth rate parameters C , q , and p
- Refinement or validation of the relationship between q and p
- Updating of the residual stress distribution and stress intensity distribution as a function of depth
- Refinement or validation of the threshold stress intensity value at which cracking is possible

Pit growth should be measured in canister material for multiple well-characterized environments in order to fit α and β to the relevant material/environment combination (in [31], they are fit to data concerning disc steel exposed to aqueous environments of different chemistries). A separate pit growth loop can be written using only the Turnbull pit growth

rate in order to fit α and β such that the pit depths as a function of time are consistent with experimental data. Note that β may be best expressed as a distribution (as it is in the current version of the model) rather than as a constant (as it is in [31]). β and α will likely need to be determined independently for a set of environments. A better alternative to this would involve designing experiments to determine the effects of the environment (e.g. chloride concentration and temperature) on the pit growth rate, and developing equations that allow for β and α to be determined from environmental inputs.

A similar procedure, only using crack growth experiments, should be used to fit C , p , and q in the crack growth rate expression. Note that p is calculated as $2q$ in [31] and in this model. It may be better to fit each exponent independently, rather than only fitting q and using it to predict p . Also note that p and q are considered to be group parameters, and not individual flaw parameters; therefore, p and q should be evaluated for data from all pits in the same material and exposed to the same conditions. C , like α (and like β in this model) has a unique value for each flaw. Therefore, it is more appropriate to use experimental data to determine the expected distribution of values for these constants, rather than a single value.

Next, the stress and stress intensity functions should be updated with the results from the experiments described above. Cracking experiments should be designed for the determination of the threshold stress intensity for cracking, since this is a key criterion for the pit-to-crack transition in the model. The assumed value of $4 \text{ MPa}\sqrt{\text{m}}$ should either be explicitly validated by these experiments or updated to reflect different findings.

6 Conclusions

This project continued the work of the H. H. Uhlig Laboratory in developing a probabilistic model to predict stress corrosion cracking in the canisters used for interim storage of used nuclear fuel in the United States.

Existing models in the literature pertaining to pitting and cracking in steels were considered. A figure-of-merit was developed to judge which models would be the most useful for beginning a model to describe the pitting and cracking of canister material. It was used to select four individual models: one was a pitting model (Henshall), two were cracking models (Shoji and Wu), and one was a combined model (Turnbull). The pitting model was considered on its own, and was also combined with the Shoji and Wu models to construct two separate pit-to-crack models. The Turnbull model was also considered on its own, since it was already constructed to account for flaws that began as pits and transitioned to cracks.

It was assumed that a sufficiently aggressive environment existed already at the canister surface, and so each model traced the lifetime of flaws beginning from the time of initiation. These assumptions must be experimentally validated later, especially with regards to the probability of a pit initiating on a canister surface. The failure times estimated in this thesis are better characterized as failure times *after* pit initiation, and in particular after the pit has grown to its assigned initial depth in these models.

For the pitting-only model, the average time to failure was approximately 28 or 43 years, depending on the growth rate scheme used. The median time to failure was very close to the average in each case. The minimum times to failure were approximately 10 years lower than the average time to failure for each case measured. As the standard deviation of the coefficient distributions was increased, the minimum time to failure dropped.

The Henshall/Shoji model predicted failure times of approximately 15 years. The

failure time was considered to be the time spent in the pitting regime, as crack growth was extremely rapid.

The Henshall/Wu model predicted slightly longer failure times, as it predicted that flaws spent about a year in the cracking regime before failure occurred. The median time to failure was higher (by 0.3-0.8 years) than the average time to failure. The minimum time to failure was just over a year.

The Turnbull model predicted that most flaws failed within one to two years, with some flaws growing extremely slowly and failing after thousands of years. This resulted in a distribution in which the median time to failure was one year, but the average failure time was in the hundreds of years. In this case, the average time to failure did not represent the physical reality of the situation.

An important finding from this study is that, once modeling a flaw that has already initiated, the choice of pit growth/crack growth model has a significant impact on the prediction of failure times. The failure times predicted by the four models were very different. Therefore, it is important that the physics of the corrosion phenomenon at hand are carefully considered, and a model is developed appropriately. This study shows that failure time prediction results can vary widely across the selected models, even starting with the same inputs and assumptions: this is reminiscent of the issues discussed by King et al. in Section 7.11.2.

Based on these findings, it was determined that the Henshall/Wu model seemed to be the most promising for use in the canister modeling project. However, further experimentation with actual canister material is required to ensure that the selected model is consistent with the physical reality of flaw behavior in a general sense, and to update the parameters of the models in order to get better predictions. Importantly, it is also important to combine the findings of a pitting-and-cracking model like the ones studied here with

a model to predict the development of an aggressive environment on the canister surface, as this expected to take many years, thus adding to the effective minimum time-to-failure for a canister that develops a flaw. Additional recommendations for updating each model were provided in the analysis section.

7 Appendix A: Approaches to modeling stress corrosion cracking in stainless steel

The following material is adapted from a white paper on SCC modeling approaches undertaken for the *Life Prediction of Spent Fuel Canister Material* project at the H. H. Uhlig Corrosion Laboratory at MIT. This project was supported by the United States Department of Energy (Award Number: DE-AC07-051D14517). Douglas Jonart and Professor Ronald Ballinger both contributed edits to initial drafts of this appendix, and their efforts are gratefully acknowledged. The main draft of the white paper was completed in 2014, and so this appendix does not include any models published after that point.

The purpose of this review was to collect the potentially relevant models for pitting, cracking, crack initiation, and stress corrosion cracking in stainless steels in one place. The explanations of the models, particularly with regards to the math, typically follow the original source material closely, as the purpose of the paper is organize this information in a way that is convenient for those interested in developing SCC models for the canister and who would like to be able to access information about many literature models quickly. The paper is not intended to be an original take on the modeling of stress corrosion cracking, although commentary on the utility of specific models for the canister project is given where warranted.

In some parts of this paper, previous research papers on pitting and cracking modeling are referred to and expand upon. The work of J. C. Farmer in particular is especially acknowledged in this regard.

Tables of variables are provided for each model for the convenience of the reader. A summary table of all models is provided at the end of the white paper.

7.1 Introduction

The objective of the *Life Prediction of Spent Fuel Canister Material* project is the development of a probabilistic model to predict the likelihood that stress corrosion cracking will occur in the welds and heat affected zones (HAZ) of used nuclear fuel canisters. The model must be validated and have explicitly quantified uncertainties. However, this presents a significant challenge. Stress corrosion cracking (SCC) is a complex phenomenon, and while attempts to build predictive models based on statistical principles have been developed, they frequently: (1) make many assumptions, (2) are only applicable to a narrow range of materials and environments, (3) only roughly agree with experimental data, and (4) make no attempt to systematically quantify associated uncertainties.

In this document we consider the contributions to SCC modeling made by previous researchers in order to define the current state of the art and to provide a baseline from which to proceed forward. The work of scientists who have approached the phenomenon of SCC quantitatively and probabilistically will be considered in this paper. In recent years, multiple researchers have also utilized advanced simulation methods to study pitting and SCC behavior. When these simulation studies involve approaches that seem particularly well-adapted for use in the *Life Prediction of Canister Material*, they are presented here as well. For all considered models, the possible interpretations of SCC mechanisms, the assumptions that are made, and the limitations of different models with respect to the goals of *Life Prediction of Canister Material* are discussed.

Broadly, stress corrosion cracking occurs in the following three steps: (1) growth of crack precursors, (2) crack initiation, and (3) crack propagation. In stainless steels, this typically proceeds as the development and growth of pits on the exposed surface. As these pits grow, cracks may initiate from the pit. The crack continues to propagate as long as local conditions support its growth, or until it propagates all the way through the material

and failure results.

A key part of model development for this project will be determining the criteria for the transition from pitting to cracking. An example of a stress corrosion crack initiating from a pit is shown in Figure 33. This is a major objective of many deterministic approaches, although many of them focus on only one or two of the stages: for example, pit growth and crack transition only, or crack propagation only. Some probabilistic approaches largely neglect the specifics of SCC development and growth, and aim only to correctly predict the number of through-cracks expected to develop given an initial pit distribution at a certain material-environment interface. This may be done through fitting parameters that are determined experimentally and then applied to a mathematical expression for an appropriate distribution.

Furthermore, when it comes to modeling stress corrosion cracking in the welds and HAZs of nuclear waste containment casks, the initiation and propagation of SCC from corrosion pits is only one part of the process. The U. S. Nuclear Waste Technical Review Board defines canister lifetime as the time it takes for a stress corrosion crack to initiate at the surface and propagate through the wall [41]. Austenitic stainless steels are susceptible to SCC when exposed to an aqueous, chloride-containing environment [6]. Such an environment may develop on the canister surface given the right conditions of humidity, salt in the air, and temperature. Therefore, a predictive model must also take into account the likelihood of developing such a salt-containing film, in addition to the likelihood that the film is sustained on the surface long enough to result in pitting and that it is in contact with those parts of the canister surface corresponding to the welds and associated HAZ, where the highest residual stresses are found. The pit's growth must then be sustained to the point that initiates a crack. Once initiated the crack growth process must also be sustained by the local environment. Figure 34 shows a schematic of the SCC process in a

used nuclear fuel canister.¹⁸



Figure 33: This image shows a crack that has initiated from a corrosion pit in stainless steel condenser tubes. The component was exposed to chloride-containing water, which induced pitting and chloride-assisted stress corrosion cracking. [43]

As early as 1935 it was recognized that corrosion generally does not proceed in a purely deterministic manner, which makes predicting its onset and effects particularly difficult. U. R. Evans and R. B. Mears carried out corrosion experiments in an effort to investigate the stochastic nature of the observed damage. It was determined that knowing the quantities that govern how, and how rapidly, a given material corrodes is not enough to fully understand and predict corrosion effects:

“From the purely scientific standpoint, measurements of probability, which give information regarding the mechanism of breakdown of passivity, are as important as measurements of velocity, which indicate the mechanism maintaining the attack. From the practical standpoint ... it may, indeed, be more important

¹⁸See Figure 3-1 in [42].

to know whether... corrosion is likely to occur at all than to know how quickly it will develop.” [44]

Predicting the multiple processes involved in corrosion accurately is a challenging endeavor. It commonly involves the coupling of deterministic or probabilistic models to probability techniques and experimental data to develop a model that can accurately predict the likelihood of corrosion damage in a given situation. The complexity of corrosion phenomena generally requires significant simplifying assumptions, or a focus of efforts very specifically on one stage of the corrosion mechanism of interest. Consequently, there is no single definitive model for predicting stress corrosion cracking in stainless steels. Additionally, there is no one model that predicts stress corrosion cracking and quantifies all associated uncertainties that can be applied generally to any material-environment combination.

In this document, the literature as it pertains to the modeling of SCC in stainless steels is explored, with the goal of understanding the advantages and limitations of multiple model-building approaches. Modeling corrosive processes that could ostensibly occur in nuclear waste storage technology has been of significant interest to the nuclear engineering community for more than twenty years. Farmer of Lawrence Livermore National Laboratory was closely involved with studies to predict corrosion in the radioactive waste containment systems that were intended to be used at Yucca Mountain for indefinite sequestration of nuclear waste. He and his coauthors carried out extensive literature research in the 1990s to understand existing approaches to modeling stress corrosion cracking [45, 46, 47, 48]. They also developed unique contributions to some of these models. Their original modeling work and their insights into the models of other scientists are referenced extensively throughout this report.

In this report we focus on models that do or could pertain to SCC in stainless steels

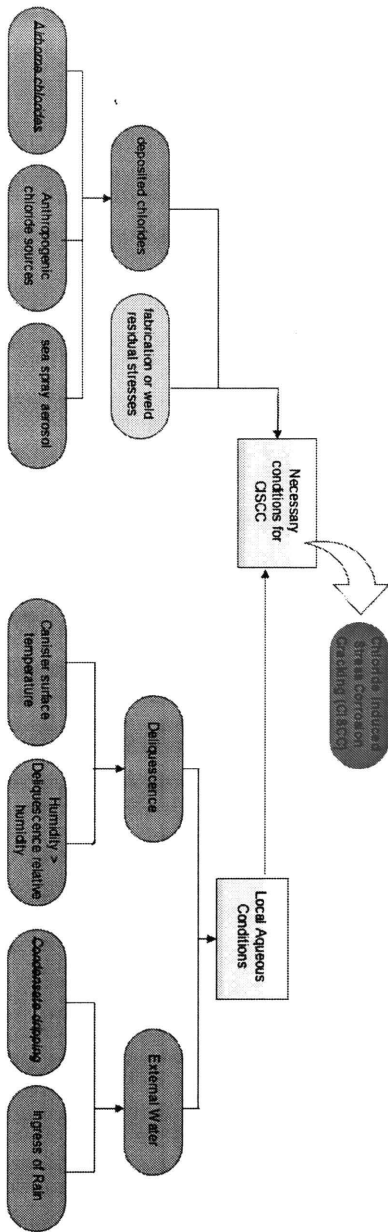


Figure 34: The conditions that lead to chloride-induced SCC in steel canisters, adapted from the FMEA flow chart for material degradation of stainless steel canisters in [42]. Conditions with strike-through text have been classified as having negligible probability of occurrence. The light blue color indicates an environmental condition, while the yellow color indicates a stress and loading condition.

exposed to atmospheric or aqueous conditions. Models will be summarized and then considered for their advantages, limitations, and potential usefulness to the ultimate goal of this project, which is to develop a probabilistic and predictive model for SCC in the welds and HAZ of the stainless steel canisters used to store used nuclear fuel. In this paper, the evolution of the aggressive environment on the canister is not considered. However, it should be noted that modeling the environment as a function of time on a canister surface is a necessary part of a final, predictive model.

Table 18: Composition of common stainless steels (in weight percent)

| Type | C | Cr | Ni | Mn | Si | P | S | Mo | N |
|------|--------|-------------|-------------|--------|--------|---------|--------|-----------|------|
| 304 | < 0.08 | 17.50-20.00 | 8.00-11.00 | < 2.00 | < 1.00 | < 0.045 | < 0.03 | | |
| 304L | 0.030 | 18.00-20.00 | 8.00-12.00 | 2.00 | 0.75 | 0.045 | 0.030 | | 0.10 |
| 316 | < 0.08 | 16.00-18.50 | 10.00-14.00 | <2.00 | < 1.00 | <0.045 | <0.03 | 2.00-3.00 | |
| 316L | < 0.03 | 16.00-18.50 | 10.00-14.00 | < 2.00 | <1.00 | <0.045 | <0.03 | 2.00-3.00 | |

All approaches are then summarized at the end of this report in chart form.

Overly simplifying stress corrosion cracking - especially when associated uncertainties are not clarified - is problematic because it is such a complex phenomenon. For example, Aly (Section 7.7.1), who worked on modeling SCC in a pressurized water reactor (PWR) nozzle, notes that the process depends on environmental chemistry and pH, the solution present on the surface of the material, partial pressures of gases, temperature, applied and residual stresses in the material, strain, carbide distribution, grain size, and history of plastic deformation - and that is an incomplete list [25]. Staehle, who also studied the prediction of SCC in Fe-Cr-Ni base alloys, notes that accurate models must account for these bulk environment and material properties, but also for local material characteristics at microscopic scales. Examples of these include: a tendency to eject passivating species at the surface (or attract depassivating species), precipitates near flaws or surfaces that affect

local electrochemistry, hydrogen embrittlement, corrosion products that exert a “wedging” force on the matrix, bubbles along the grain boundary, and the presence of anions near grain boundaries due to dissolution [49]. A totally generalized, predictive model of SCC whose uncertainties are explicitly quantified may always prove to be an elusive goal. However, with a combination of probabilistic methods, sufficient knowledge of the corrosion mechanism at hand, and experimental data, useful mathematical models for specific metal-environment combinations are within reach.

7.2 Pitting

Pitting occurs in stainless steels when local passivation breaks down. The bare metal becomes anodic, and galvanic corrosion takes place, leading to the formation of a “pit” at the site of depassivation. Depending on the environment and chemistry, the pit may later repassivate, or it may continue to grow. The pit also acts as a stress concentrator. Stress corrosion cracking in stainless steels initiates from these corrosion pits. For this reason, modeling the development and growth of pits will be a necessary aspect of the *Life Prediction of Canister Material*. Some possible corrosion pit shapes are shown in Figure 35. Examples of actual pits in steel samples are shown in Figure 36. The shape of corrosion pits that form on a steel surface depend on the composition and microstructure of the steel and the environment, and a range of pit shapes are seen in practice. In models of pitting in steels, the pits are most commonly assumed to maintain a hemispherical shape throughout their lifetime.

When an aqueous phase is present, localized corrosion can be highly problematic, particularly if the aqueous phase contains dissolved ions and oxygen from the surrounding environment. Chloride-containing solutions are known to be especially aggressive to austenitic stainless steels, and their presence can result in pits that propagate through canister walls on timescales of years or decades, and not the centuries required of sequestration structures [6]. The presence of ions like chloride that result in passive film breakdown dramatically impact the likelihood of pit formation [6].

Pits, once formed, can also be aggravated by the presence of depolarizing elements which may be reduced on the pit’s external surface. This creates a galvanic couple between the pit interior and the surrounding metal surface. Other ions (nitrate, iodine, acetate) can inhibit pitting. The SCC model must include parameters that describe solution chemistry, since it will play a significant role in the pitting behavior of the steel. In the case of interim

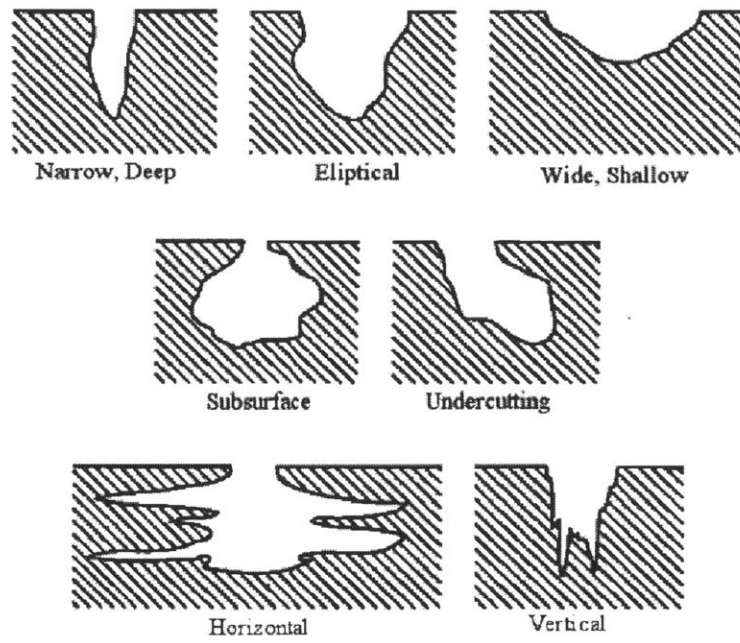


Figure 35: Some possible pit shapes, as described by ASTM-G46. Many models assume that pits are perfectly hemispherical for simplification purposes. [50]

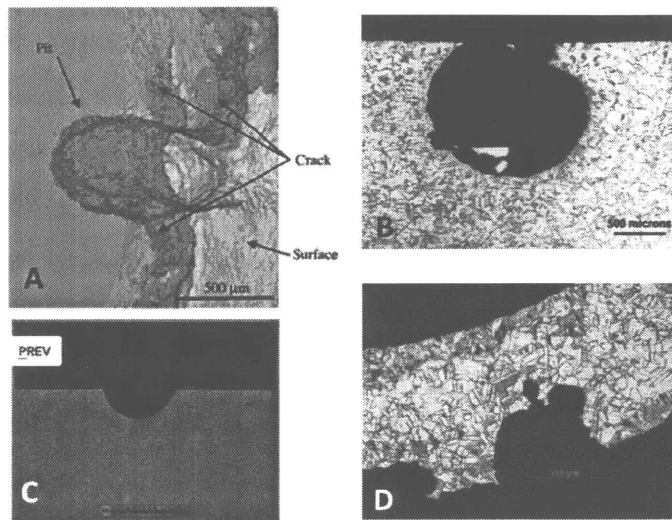


Figure 36: (A) shows a tomographic reconstruction of a corrosion pit in 3NiCrMoV disc steel exposed to aerated, chloride-containing water [51]. (B) A microbiologically-induced corrosion pit in Type 316L steel [52]. (C) Chloride-induced pitting in a Type 304L condenser tube [53]. (D) Chloride-induced pitting in a Type 316 steel tube [54].

used nuclear fuel canisters, a predictive SCC model must also describe the development of the environment at the canister surface over time: pitting is not possible if the environment is not sufficiently aggressive.¹⁹

Farmer et al. performed a comprehensive survey of published stress corrosion cracking models in the 1990s when the national laboratories were carrying out extensive studies to ensure the safety and integrity of the materials that were to be used for used nuclear fuel storage at Yucca Mountain [45], [48].

Residual stress, and any applied external stresses, must also be considered in the model. The stresses associated with SCC phenomena are typically much lower than the yield stress of the material. Pits act as stress concentrators that promote crack initiation, as K_{pit} may exceed $K_{\text{threshold}}$ even when K_{bulk} does not.

Farmer also makes the point that many pitting models assume a uniform surface and a uniform film, but it is the imperfections in a metal component that are frequently preferred sites for pit nucleation and crack growth. Therefore, the assumption of uniformity can obscure one of the driving causes of pitting. These imperfections include grain boundaries and dislocations, and so in any model it is important to:

- establish whether heterogeneities in the metal of interest are known to be preferred pit nucleation sites
- which heterogeneities are relevant
- understand the distribution of these heterogeneities on a representative surface

The key parameters that Farmer identifies as being crucial to a model that can quantitatively predict SCC are potential, ion concentration, temperature and pH.

¹⁹While modeling the environment is a key aspect of the *Life Prediction of Canister Material* project, it is beyond the scope of this paper, which will focus on corrosion models, and not environmental evolution models.

This section will consider prominent models for pitting in steels.²⁰ First, deterministic models are considered. The deterministic models, which are covered chronologically, each depend on a different set of assumptions regarding the causes of pitting in steels. Second, stochastic models are considered. These models treat pitting as a stochastic process that can be modeled using a probabilistic approach.

7.3 Deterministic models of pitting, 1971-1989

This section examines non-stochastic models of pitting in steels. These models represent multiple approaches to understanding the phenomena of pit initiation and pit growth.

7.3.1 Sato, 1971: The electrostriction model of pitting

In this model, electrostriction pressure exerts stress on the film until it ruptures. The electrostriction pressure is dependent on pressure, material properties of the film, and the electric field that is present. It was developed by N. Sato as a possible explanation for film breakdown, and as an alternative to previous models that identified electrochemical reactions as the primary cause for passive film breakdown, and which neglected the possible effects of stress [7]. The author lists the various causes of internal stress in the passive film, and identifies interfacial tension and electrostriction pressure as the two that are common to most situations, as shown in Figure 37. This is due to the fact that the electric field in a typical oxide film is typically high enough to cause electrostriction pressure. (Sato cites the range of typical electric field values as 10^6 to 10^7 V/cm) and because the typical film is thin enough that interfacial tension's effects are not negligible.²¹

²⁰The models reviewed in Section 7.2 were all cross-referenced with the modeling review work of Farmer, with the exception of the Mola model described in Section 7.4.2. Most pitting models were cross-referenced against [48], with the exception of the Henshall model (Section 7.4.3), which was cross-referenced against [45] and [46].

²¹Electrostriction pressure arises in dielectric materials like the opposite film when an electric field is present, causing the opposite sides of the electrical domains within the material to become differently

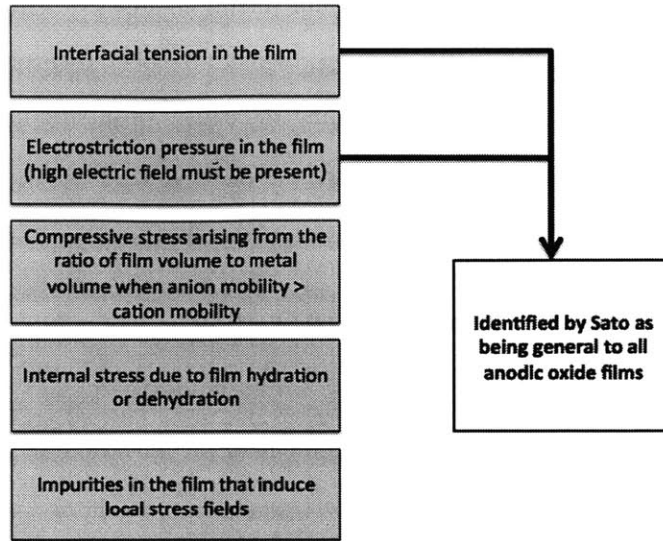


Figure 37: Causes of internal stress in oxide films, as identified by N. Sato. Internal stress can be a driver of passive film breakdown.

Film pressure is found to be:

$$P - P_0 = \underbrace{\frac{\epsilon(\epsilon - 1)e^2}{8\pi}}_{\text{Electrostriction effect}} - \underbrace{\frac{\gamma}{L}}_{\text{Interfacial tension effect}} \quad (16)$$

where P_0 is atmospheric pressure, ϵ the film's dielectric constant, E the electric field, γ the surface tension, and L the film thickness.

The breakdown potential is the lowest potential that can induce a film pressure that is sufficient to cause film breakdown. The threshold compressive stress σ_c is given by setting $P - P_0$ to σ_c in Equation (16). Figure 38 plots film pressure as a function of film thickness for four surface tension values (γ). It is shown that the critical film thickness, at which σ_c charged. The sides of the electrical domains attract each other, causing a constriction of the material in the direction parallel to the electric field.

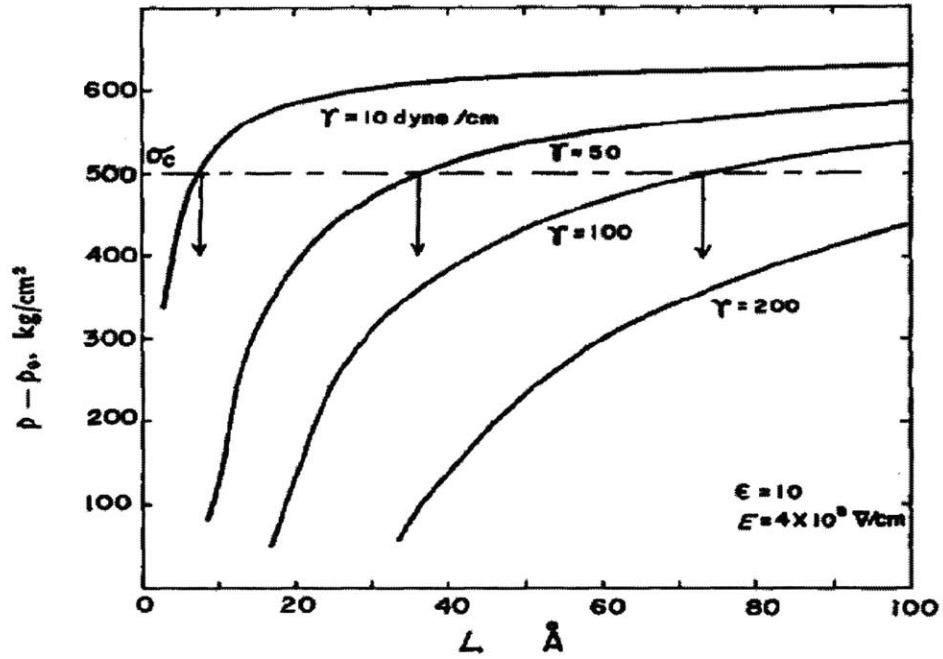


Figure 38: The pressure (in units of kg per cm^2) is calculated as a function of film thickness L (in units of angstroms). The dielectric constant ϵ is set to 10, the electric field D is set to 4×10^6 V/cm. Pressure is graphed for four values of surface tension γ : 10, 50, 100, and 200 dynes/cm. The critical pressure at which breakdown occurs is marked with a dashed horizontal line. [7]

is achieved, decreases with γ .²²

Sato then derives an expression that relates the breakdown potential, φ^* , to the concentration of the aggressive ion in solution:

$$\frac{d\varphi^*}{d(\ln(a_{KA}))} = -\frac{8\pi k T \Gamma_{A^-}^*}{\epsilon(\epsilon + 1)E} \quad (17)$$

where a_{KA} is the activity of the salt (composed of a cation K^+ and an anion A^-), T is temperature, $\Gamma_{A^-}^*$ is the adsorption density of the anion when the potential = φ^* , and k the Boltzmann constant. Consideration is also given to solutions containing multiple anion species.²³ Breakdown of the film occurs mechanically as brittle cracking, plastic slip, or plastic flow: the film's specific properties determine the mechanism. When breakdown occurs, the metal surface is vulnerable to dissolution or pitting.

In order for this model to be useful for *Life Prediction of Canister Material*, it is necessary to assume that film breakdown occurs due to the electrostriction theory proposed by Sato. It is also only an initiating theory that could be used to predict when pit initiation is possible, but it does not model pit initiation or pit growth, and so would need to be combined with an additional model.

7.3.2 Pickering and Frankenthal, 1972: Dissolution at the pit base only

In this model, the pit walls are insulated, and the base is an active metal surface. Figure 39 shows a schematic of the Pickering-Frankenthal model. The potential and concentration profiles are determined by using the Nernst-Einstein equation to approximate a solution to the transport equation for dilute solutions.

It is necessary to account for the chemistry of the pit, as its potential and species

²²Sato also suggests that the adsorption of anions in solution by the film could hasten film breakdown, since the presence of adsorbed ions decreases γ , which corresponds to an increase in film pressure [7].

²³This is omitted here, but it can be found on p.1690 of Reference [7].

At steady state, the fluxes associated with H^+ and Y^- are zero. The net change is occurring in the metal as the pit base dissolves into the electrolyte solution.

The concentration of each species is then determined according to the boundary conditions given in Table 19, and the final results are given in Equations (21), (22), and (23).²⁴ Definitions for all variables are listed in Table 20.

$$c_{Y^-} = c^\circ + \frac{i_M x}{2D_{M^+} F} \quad (21)$$

$$c_{H^+} = \frac{2D_{M^+} F c^{\circ 2}}{2D_{M^+} F c^\circ + i_M x} \quad (22)$$

$$c_{M^+} = \frac{4D_{M^+} F c^\circ i_M x + (i_M x)^2}{2D_{M^+} F (2D_{M^+} F c^\circ + i_M x)} \quad (23)$$

Graphical solutions of these three equations are shown in Figure 40 on page 147.²⁵

Table 19: Boundary conditions and constraints

| Conditions | Reasoning |
|---|--|
| $c_{H^+}, c_{Y^-} = c^\circ$ at $x = 0$ | c° is the concentration of the salt, HY, in the bulk solution |
| $c_M = 0$ at $x = 0$ | There are no metal ions at the pit opening |
| ϕ_0 at $x = 0$ | Electric potential is 0 at the pit opening |
| $c_{H^+} + c_{M^+} = c_{Y^-}$ | Electrical neutrality applies |

Qualitatively, M^+ has highest concentrations near the pit base. Inside the pit, the concentrations of Y^- and H^+ are greater than c° . Y^- has highest concentrations closer to the bottom of the pit, while H^+ has the opposite concentration gradient.²⁶

This model provides a way to describe pit growth behavior by characterizing the flux

²⁴The original paper, [13], also contains the mathematical derivation of Equations (21), (22), and (23). This is omitted here, but it can be found on page 1298 of the cited paper.

²⁵Pickering and Frankenthal also focus extensively on the resistive effects of hydrogen bubbles inside the pit. This treatment is being omitted here, but can be found in Reference [13] beginning on page 1301.

²⁶Precipitation may result in slight deviations from the calculated concentrations.

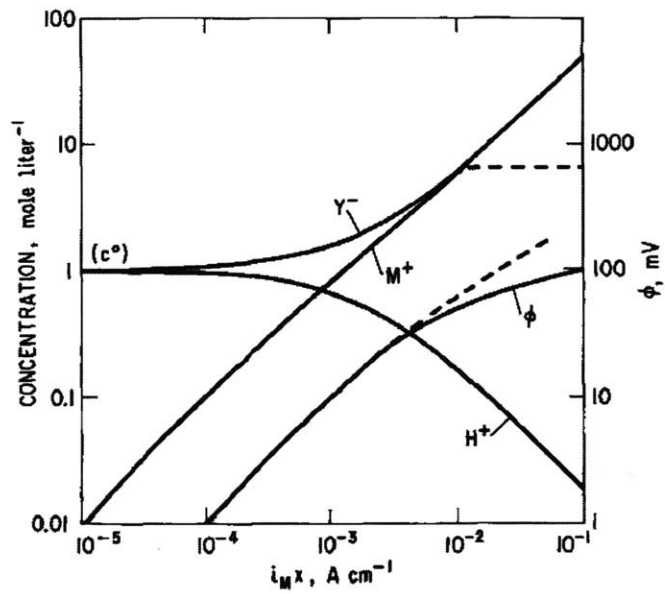


Figure 40: The concentration profiles, as solved by Pickering and Frankenthal using the relationships between pit depth x , current i_M , and the concentrations of ions from the dissolved salt and the corroding metal surface. [13]

Table 20: Variable definitions for Equations (21), (22), and (23)

| Variable | Definition |
|-----------|---|
| j_X | Flux of species X |
| D_X | Diffusion constant of species X |
| c_X | Concentration of X |
| x | Pit depth |
| F | Faraday constant |
| R | Gas constant |
| T | Absolute temperature |
| ϕ | Potential |
| i_M | Steady state current density |
| c° | Bulk concentration of the salt HX in solution |

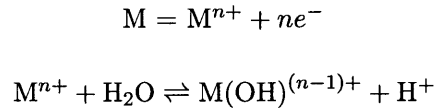
of metal dissolution at the base. It provides a direct relationship between the extent of dissolution (since this is proportional to the concentration of dissolved metal ion in solution) and local chemistry. However, it assumes that corrosion pits grow only in the direction normal to the surface, and not horizontally. While it is a useful model for understanding the solution chemistry of a single pit, it is quantitative model. In this form, it is not well-suited to probabilistic prediction of pitting behavior. It does not address the effects of other parameters, such as stress and temperature, that are known to play a role in SCC.

Pickering and Frankenthal provide a potentially useful model for pit growth, although it is perhaps too simplistic to assume that corrosion pits can be accurately modeled as only growing in the normal direction. Furthermore, for the purposes of a probabilistic model, it may be desirable to avoid dependencies on modeling the fluxes of the salt, metal, and hydrogen ions. These types of models may be better suited to small-scale simulations of the growth of a single pit.

7.3.3 Galvele, 1976: Building on the work of Pickering and Frankenthal

Galvele began with the dissolution model described in Section 7.3.2. Galvele also assumes a salt-containing electrolyte, and that no dissolution occurs at the walls of the pit.

Rather than just considering the metal dissolution reaction, Galvele assumes that dissolution is followed by hydrolysis:



This means that the pH is controlled by the solubility of the hydroxides, which in turn has an effect on passivation and thus on pitting behavior. Under certain conditions, passivation may become impossible, and the metal is more susceptible to pitting [55].

In a review of pitting models, Farmer et al. considered the Galvele modification of the Pickering and Frankenthal model, and derived an expression for the potential change inside the pit [46]:

$$[\Phi - \Phi'] = A - \frac{RT}{F} \ln(C) \quad (24)$$

with A a constant and C the salt concentration. Φ is the electrical potential, and Φ' is a reference potential.

Neither Galvele nor Pickering and Frankenthal modeled the growth of pits as a function of time. However, their work presents one way to understand the chemistry inside a pit that develops on a metal surface as a result of exposure to a salt solution.

7.3.4 Beck and Alkire, 1979: Pit growth when the pit's growth is limited by a salt film

Beck and Alkire begin with the following set of assumptions:

- There is a poreless, uniform salt film that lines the pit walls and base
- This salt film is the cause of electrical resistance within the pit
- The behavior of the salt film in time (e.g. dissolution or growth) controls pit growth
- Pits are hemispherical

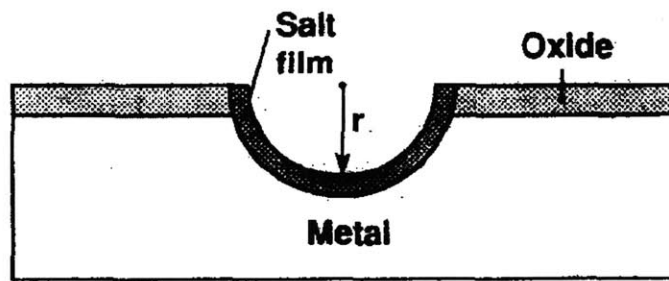


Figure 41: A schematic of a pit in the Beck and Alkire model. [48]

Pits nucleate at flaws in the passive film, such as voids at the metal/film interface. These flaws are dimensionally very small (it is suggested they are about as large as the film is thick). This small area results in a very high current density when the pit begins to grow [14]. This promotes the formation of a salt film on the interior surface of the pit. The dissolution of the metal-salt film governs the corrosion current and growth of the pit. The flux associated with the dissolution of the metal-salt film (and continued corrosion of the pit) is:

$$J = D(C_s - C_b) \left[\frac{1}{r} + \frac{1}{\sqrt{\pi D t}} \right] \quad (25)$$

Definitions of all variables are listed in Table 21. The second term is only important at short times t .

If it is assumed that there is no metal salt in the bulk electrolyte, then:

$$i_L = \frac{z\mathbf{F}DC_s}{r} \quad (26)$$

and the pit radius as a function of time in this case is given as:

$$r = \sqrt{r_1^2 + \frac{2DC_sMt}{\rho}} \quad (27)$$

The current density exhibits Tafel behavior as the salt film thickness increases:

$$i_f = i_0 \exp\left(\frac{\beta\eta_f}{t_f}\right) \quad (28)$$

Salt film thickness can then be found from Equation (28):

$$t_f = \beta\eta_f / \ln\left(\frac{z\mathbf{F}}{DC_s}i_0r\right) \quad (29)$$

Beck and Alkire heavily cite Vetter and Strehblow, who developed a pitting model based on the same pit initiation mechanism.²⁷ However, Galvele (Section 7.3.3) criticized the Vetter and Strehblow pitting model, stating that it predicted a pH increase inside the pit, while data from the literature indicated the opposite trend. Galvele leveled the same criticism at the pitting model developed by Pickering and Frankenthal [55]. If this model is to be used, it must be established that, for the situation of a deliquesced salt film on a canister surface, it is valid to assume that a salt film does in fact form on the pit surface and limit pit growth. If pitting experiments using deliquesced salt solutions and weld material

²⁷See: K. J. Vetter and H.-H Strehblow, in "Localized Corrosion," December 1971, R. W. Staehle et al., eds., NACE, Houston, 1974, 240. [75]

Table 21: Variable definitions for the Beck & Alkire Equations (Section 7.3.4)

| Variable | Definition |
|-----------------|---|
| J | Flux of the metal salt, from dissolution of the salt film in the pit |
| D | Salt diffusivity in the relevant electrolyte |
| C_s | Saturation concentration of the metal salt in the relevant electrolyte |
| C_b | Concentration of the metal salt in the bulk electrolyte outside the pit |
| r | Pit radius |
| t | Time |
| i_L | Limiting current density in the pit |
| z | Associated number of electrons for the dissolution reaction |
| F | Faraday's constant |
| r_1 | Pit nucleus radius |
| M | Metal atomic weight |
| ρ | Metal density |
| i_f | Current density from salt film growth |
| i_0 | Exchange current density |
| β | Tafel constant |
| η_f | Film overvoltage |
| t_f | Film thickness |

reveal otherwise, this model will not be helpful for *Life Prediction of Used Fuel Canister Material*.

7.3.5 Chao, Lin, and Macdonald, 1981: The point defect model of pitting

Chao, Lin, and Macdonald aimed to develop a quantitative model for the process of the passive film breakdown that precedes corrosion in stainless steels [8]. They approached the problem of corrosion in passive materials by first asserting that the film is crystalline and contains point defects. The film can be assumed to grow according to the following equation [9]:

$$\exp(2KL) - 2KL - 1 = 2KA(B - 1)t \quad (30)$$

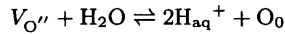
$$A = 2KD_{V_{O''}}^* \exp \left[-\frac{2F}{RT} \left(\alpha V_{\text{ext}} + \beta \text{pH} + \phi_{(f/s)}^{\circ} \right) + \frac{\Delta G_{31}^{\circ}}{RT} - 4.606 \text{pH} \right] \quad (31)$$

$$B = \exp \left[\frac{2F}{RT} (V_{\text{ext}} + \phi_R) = \frac{2 \Delta G_{21}^{\circ}}{\chi RT} - \frac{\Delta G_{31}^{\circ}}{RT} + 4.606 \text{pH} \right] \quad (32)$$

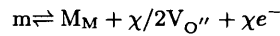
with all variables defined in Table 22.²⁸ The full derivation for Equations (31) and (32) can be found in Reference [9].

²⁸The Gibbs free energies in the equations for A and B are given here using the same notation as in the original paper for ease of cross-reference (see [9]). In the original paper, the subscripts refer to the equation number assigned to the relevant chemical reaction.

For G_{31}° , this reaction is



For G_{21}° , this reaction is



with $V_{O''}$ a vacancy point defect that occupies an oxygen site in the film, m a metal atom, and M_M a metal cation.

Table 22: Variable definitions for Section 7.3.5

| Variable | Definition |
|-----------------------|---|
| K | F_ε/RT |
| F | Faraday's constant |
| R | Gas constant |
| T | Temperature |
| L | Film thickness |
| t | Time |
| $D_{V''_O}$ | Diffusion constant for vacancies occupying oxide sites |
| " | Indicates two positive charges associated with the site |
| α | Parameter that governs potential dependence of $\phi_{(f/s)}$ |
| V_{ext} | External potential |
| β | Parameter that governs the pH dependence of $\phi_{(f/s)}$ |
| $\phi_{(f/s)}^\circ$ | Potential drop across film/solution interface |
| ΔG_{xy}° | Gibb's free energy of reaction |
| ϕ_R | Reference potential |
| χ | Associated number of negative charges |

A particular threshold potential V_c is required for the breakdown of the passive film. It is assumed that V_c depends on the activity of a halide ion, which is usually assumed to be chlorine in most studies involving passivity breakdown due to environmental exposure. V_c is expressed as:

$$V_c = A - B \log a_{[\text{Cl}^-]} \quad (33)$$

It is important to model the so-called incubation time for pitting. For the purposes of SCC in a canister, this is the time interval between the introduction of chloride ions to the surface and the initiation of pits. These assumptions are broadly true across the passivity breakdown models that were recognized at the time of the point defect model's publication. These models were briefly summarized by the authors, and are summarized

for reference here in Table 23.²⁹

Table 23: Passive film breakdown theories prior to 1981
(Based on the summaries in Chao, Lin, and Macdonald [8])

| Model | Authors | Summary |
|--|--------------------------------|---|
| Competitive ion adsorption theory | Uhlig, Kolotyркиn (1961, 1966) | Metal passivates when O^{2-} is adsorbed. Cl^{-} does not enhance passivation. At a certain potential, Cl^{-} becomes more likely to be adsorbed, and passivity breakdown can be observed. |
| Complex ion formation theory | Hoar and Jacob (1967) | The film is thinned and weakened at highly localized sites where chloride ions adsorb at a cation in the film, and the resulting complex dissolves into the solution. The site becomes more anodic, which attracts another cation, repeating the process. |
| Ion penetration theory | Kruger et al (1976) | Chloride ions migrate through the passive film. Film breakdown occurs when chloride ions travel through the film and reach the interface between the film and the metal surface. In real situations, this process takes longer than is measured experimentally. |
| Continued on next page | | |

²⁹The references for Table 23 are as follows.

- Competitive ion adsorption theory:** H. Bohni and H. H. Uhlig, *Journal of the Electrochemical Society*, **116**, 1969, [68], and J. M. Kolotyркиn, *Journal of the Electrochemical Society*, **108**, 1961, [74].
Complex ion formation theory: T. P. Hoar, *Corrosion Science*, **7**, 1967, [73].
Ion penetration theory: C. L. McBee and J. Kruger, "Localized Corrosion," R. W. Staehle et al., Eds., NACE, Houston, 1974, [71], and H. H. Strehblow, *Werkst. Korros.*, **27**, 1976, [70].
Chemico-mechanical theory: T. P. Hoar, *Corrosion Science*, **7**, 1967, [72].
Film pressure theory: N. Sato, *Electrochimica Acta*, **19**, 1971, [7].

Table 23 – continued from previous page

| Model | Authors | Summary |
|----------------------------------|-------------------------------------|--|
| Chemico-mechanical theory | Hoar (1967) | Chloride ions that adsorb into the film repel each other, and this results in film cracking. |
| Film Pressure Theory | Sato (1971) <i>Section 7.3.1</i> | Thin films have a pressure which increases when chloride ions are adsorbed. At a certain threshold pressure, film breakdown can occur. |

As the film grows, oxygen anions are transported toward the metal/film interface from the film/solution interface, promoting film growth, and metal cation transport results in the dissolution of the film into the solution. It is also necessary to consider the movement of vacancies. The vacancies form at the metal/film interface, and while most interface vacancies migrate into the metal bulk and cease to contribute to film breakdown, others may begin to build up at the interface and form larger voids. This happens when the metal cations are being transported through the film faster than the vacancies are migrating to the metal bulk: the vacancies are piling up at voids faster than they are being subsumed into the metal bulk. If this condition holds, the void will grow bigger, until it eventually collapses, resulting in local film breakdown. Pit formation becomes heavily favored at this site. This process is illustrated in Figure 42.

If J_{ca} is the steady-state rate of cation diffusion, J_m is the rate at which vacancies at the metal-film interface enter the metal bulk, and τ is the time over which transient diffusion processes are non-negligible, then

$$(J_{ca} - J_m) \times (t - \tau) \geq \zeta \quad (34)$$

where ζ is the threshold number of vacancies that must accumulate to form a void that

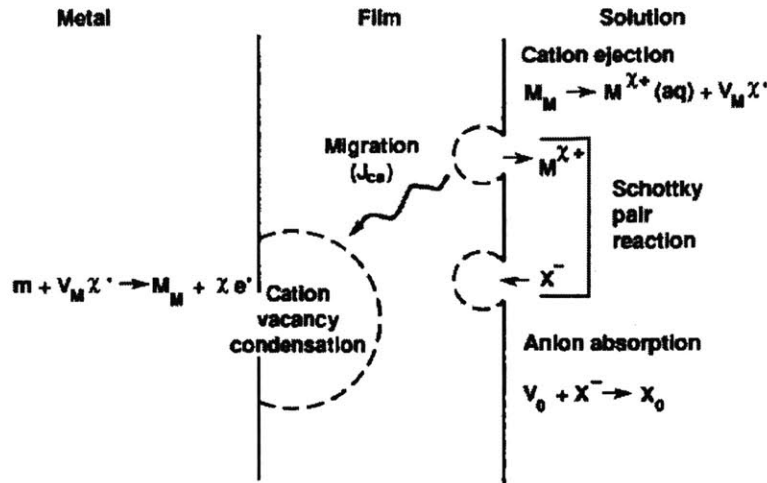


Figure 42: This schematic of the point defect model proposed by Chao et al. shows the buildup of vacancies at the metal-film interface. This can lead to film breakdown, and the exposure of the metal to the solution, resulting in localized corrosion. [48]

leads to film breakdown, and t is the amount of time it takes for that process to occur. The authors use Equation 34 to demonstrate the effect of halide (here, chloride) ions that are present in the passivating metal's environment: halide ions increase J_{ca} . From inspection of Equation (34), it is easy to see that increasing J_{ca} will decrease the required incubation time.

Expressions for J_{ca} are derived in the original paper, with a final expression of

$$J_{ca} = J^o [C_{V_{O''}^{(f/s)}}]^{-x/2} \quad (35)$$

Variables are defined in Table 24. There is assumed to be a relationship between J_{ca} and $C_{V_{O''}^{(f/s)}}$: when the number of oxygen vacancies at the film/solution interface is decreased, J_{ca} is increased as chloride ions from the solution are incorporated into oxygen vacancy sites in the film lattice.

Next, the authors derive conditions for pit initiation, and find that:

$$J^{\circ} u^{-\chi/2} \exp\left(\frac{x\mathbf{F}\alpha V_{\text{app}}}{2RT}\right) a_{[\text{Cl}^{-}]}^{-\chi/2} < J_{\text{m}} \quad (36)$$

By setting the left-hand side of Equation (36) equal to J_{m} , V_{app} becomes the critical potential for pitting to occur. This critical potential V_{c} is found to be:

$$V_{\text{c}} = \frac{4.606RT}{\chi\mathbf{F}\alpha} \log\left(\frac{J_{\text{m}}}{J^{\circ} u^{-\chi/2}}\right) - \frac{2.303RT}{\alpha\mathbf{F}} \log a_{[\text{Cl}^{-}]} \quad (37)$$

Table 24: Variable definitions for Equations (35) - (37)

| Variable | Definition |
|---------------------------------|---|
| J_{ca} | Cation diffusion rate |
| $C_{\text{vO}'}^{(\text{f/s})}$ | Concentration of oxygen vacancies at the film (f) / surface (s) interface |
| χ | Metal cation charge |
| J° | $\chi KD_{\text{VM}\chi'}^* [N_{\text{v}}/\Omega]^{1+\chi/2} \exp(-\Delta G_{\text{s}}^{\circ}/RT)$ |
| K | \mathbf{F}/RT |
| ϵ | Film electric field strength |
| R | Gas constant |
| T | Temperature |
| $D_{\text{VM}\chi'}^*$ | Metal cation vacancy diffusion rate |
| N_{V} | Avogadro's number |
| Ω | Molecular volume per cation |
| $\Delta G_{\text{s}}^{\circ}$ | Gibbs energy for the Schottky-pair reaction |
| \mathbf{F} | Faraday's constant |
| α | Constant related to film growth rate; has a specific value for a given metal |
| u | $\frac{N_{\text{v}}}{\Omega} \exp\left(\frac{\Delta G_{\text{A}-1}^{\circ} - \mathbf{F}\beta \text{pH} - \mathbf{F}\phi_{(\text{f/s})}^{\circ}}{RT}\right)$ |
| β | Constant related to the change in the film thickness with changing pH. |
| $\phi_{(\text{f/s})}^{\circ}$ | Potential difference between the solution and film flatband potentials |
| V_{app} | Applied voltage |
| $a_{[\text{Cl}^{-}]}$ | Chloride ion activity |
| J_{m} | Submergence rate of metal vacancies into the bulk |

The authors found that predictions based on the equations above were in good agreement with experimental data for iron and nickel samples that were exposed to halide-containing solutions.

In order to utilize this model, it would first need to be established that the point defect model was an accurate description of the pit initiation process for a steel canister exposed to a deliquesced salt film. This model may also be too detailed for the purposes of developing an effective probabilistic model for SCC in the canisters. The dependence of the model - in particular, the dependence of its condition for pit initiation - on the fluxes of vacancies and ions makes it adaptable to a computationally intensive, highly specific molecular kinetics simulations of a single passive film breakdown situation. It is unlikely to be as well-suited for the macro-scale prediction of pit initiation on a canister surface.

7.3.6 Okada, 1984: Halide nuclide theory and the breaching of the passive film

Okada modeled the breach of a protective oxide film by an aqueous halide solution [10]. Metal cations in the oxide combine with the halide anions to form ionic compounds, while oxygen anions combine with hydrogen to form water molecules. Okada bases his model on the premise that “pitting occurs through formation of metal halides on the passive film, thereby taking into account the microscopic stability of the halides” [10]. This process is illustrated in Figure 43. The halide nucleus forms on the surface of the oxide film that forms on the passivating metal. If the nucleus reaches the critical size for stability, it may continue growing and eventually penetrate the thickness of the oxide film. This leaves the metal surface vulnerable to pitting, because it is now exposed to the halide-containing solution.

The halide nucleus forms when halide ions in the aqueous solution adsorb onto the

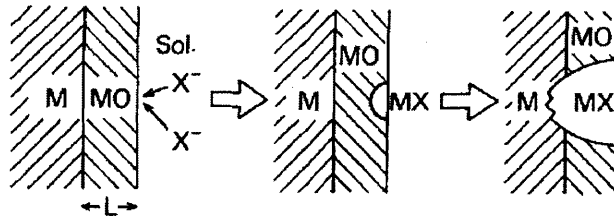
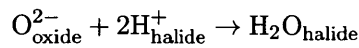
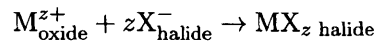


Figure 43: Halides (X^-) in the solution form a nucleus that penetrates the passive metal oxide film (MO). If the halide nucleus is stable, it will fully penetrate the film, exposing the metal surface to the halide solution. This leaves the metal vulnerable to pitting. If the halide nucleus does not reach the critical size required for stability, it will eventually dissolve back into solution, and the metal remains protected. [10]

oxide film, where they form a “transitional complex with a lattice cation at the passive film-solution interface.” The reactions assumed to take place during this process are [48]:



If the halide nucleus does not reach a critical size, described by the critical pit radius r^* , the film will repassivate and pitting will not occur.³⁰ Anodic conditions promote halide stability, because the stability of the halide nucleus exceeds that of the oxide film [48].

Expressions for the critical pitting potential and for time to pit initiation were determined using two independent methodologies, which are discussed below.

Critical pitting potential is described as:

$$E_c = C - \frac{RT}{\xi F} \ln[X^-] \quad (38)$$

³⁰A derivation of r^* is given in Reference [10]. r^* increases with film thickness, and decreases with current density.

with R the gas constant, T temperature, ξ and C constants, and F Faraday's constant. $[X^-]$ corresponds to the concentration of the halide (such as Cl^-). Constants can be determined experimentally.³¹ It is necessary to compare Equation (38) with experimental results, as certain related experiments show that the dependence on temperature and concentrations does not go exactly as described in Equation (38) in all situations.³²

Time to pit initiation is described as:

$$\ln(\tau) = C - 2n \ln[X^-] - \frac{2\xi FE}{RT} \quad (39)$$

with n the valence number for the metal cations, and τ the time required for pit initiation once a halide solution has formed on top of an oxide film. Here, pitting is assumed to occur when the halide "nucleus" grows larger than a determined critical radius.

Equations (38) and (39) were derived by Okada twice. First, Okada utilized the theories of Glansdorff and Prigogine, who described the evolution of an irreversible thermodynamic system.³³ In the second derivation, it was assumed that local electrochemical perturbations allow the nucleation of halides on the film when the potential becomes anodic.³⁴

In Farmer's survey of pitting models, he notes that dependence of pitting potential on

³¹Farmer notes that the relationship expressed in Equation (38) is consistent with experimental results in the literature. These include:

- H. J. Engell and N. D. Stolica, "Die Kinetic der Entstehung und des Wachstums von Lochfrass-stellen auf passiven Eisenelektroden," *Z. Phys. Chem.*, 20, 1959, [110].
- M. Janik-Czachor, "An assessment of the processes leading to pit nucleation on iron, Reviews and News," *Journal of the Electrochemical Society*, 128(12), 1981, [111].
- Matamala, R. G., "Correlation model of the AISI 316 stainless steel pitting potential with cellulose bleach process variables, *Corrosion*, 43(2), 1987, [112].

³²One equation for pitting potential of Type 316 stainless steel was found to go as $E_c = a - bT + cT[\text{pH}] - dT \log[X^-]$, rather than as $E_c = a - bT \ln[X^-]$ [111].

³³See: P. Glansdorff and I. Prigogine, "Thermodynamics Theory of Structure, Stability, and Fluctuations," Ch. 9, Wiley-Interscience, New York, 1974, [113].

³⁴See: T. Okada, "A Theory of Perturbation-Initiated Pitting," *Journal of the Electrochemical Society*, 132(3), 1985, [114]. This reference contains a derivation for the fluctuation of the anodic current at the passive-film/solution interface.

pH, $[\text{Cl}^-]$, and T varies for different alloys. The correct dependence must be experimentally determined and validated for the different stainless steels. Farmer suggests a more general form for the critical pitting potential than that given in Equation (38).³⁵ This potential is given as:

$$E_c = a_0 + a_1 \ln[\text{Cl}^-] + a_2 [\text{pH}] + a_3 T + a_{12} \ln[\text{Cl}^-][\text{pH}] \\ + a_{13} \ln[\text{Cl}^-]T + a_{23} [\text{pH}]T + a_{123} \ln[\text{Cl}^-][\text{pH}]T \quad (40)$$

where the coefficients a_n are established via experimentation.

The Okada model is a more manageable approach to establishing pitting criteria: it depends on chloride concentration, pH, and temperature, but it doesn't require detailed knowledge of ion fluxes in the solution or vacancy fluxes in the metal/passive film. It suggests straightforward frameworks for both critical pitting potential and the time to pit initiation, both of which could be useful for *Life Prediction of Used Fuel Canister Material* if experimental data shows good agreement with Equations (38) and (39).

7.3.7 Kondo, 1989: Predicting the initiation of fatigue cracks from pits

Kondo focused on low-alloy steel in deionized water, with the objective of gaining insight into how steel components fail due to corrosion fatigue. His 1989 paper, "Prediction of Fatigue Crack Initiation Life Based on Pit Growth," is often referenced as a starting point for certain non-fatigue-related SCC models; notably, Turnbull's modeling work built off the initial pit-to-crack model proposed by Kondo (see Section 7.6.2, or Reference [31]).

The model assumes that SCC occurs in stainless steels via the following three stages: pit

³⁵"The measured responses in such a design are the corrosion, pitting, and repassivation potentials. This experimental strategy enables experimenters to easily calculate the confidence intervals of parameters." [48], 64.

initiation and growth, crack initiation at the pit, and crack propagation [18]. In Kondo's view of SCC, there is a critical point at which a crack will initiate from a pit, and predicting this occurrence is the key goal of his model.

To construct the model, experiments were first carried out on low-alloy steel samples using a fatigue testing machine in conjunction with an environmental cell that could accurately mimic the relevant aqueous environment. Pit diameter over time was measured. Kondo then found that pit radius could be related to time (number of cycles) as:

$$r \propto t^{1/3} \quad (41)$$

Assuming a hemispherical shape for the pit, pit volume grows as:

$$\frac{2}{3}\pi r^3 = Bt \quad (42)$$

where B is the bulk dissolution rate. Kondo proposes that different environments result in different growth rates, and that these differences can be accounted for with a multiplicative coefficient in the relationship between r and t .

Kondo also found that there was a pit at each fracture surface (in agreement with the three-phase model of stress corrosion cracking). He asserted that this initial pit did not grow following crack initiation. This final pit size is taken to be the critical size for that particular crack. It was observed that higher-stress conditions lead to a smaller critical pit size. This behavior is expected because stresses in the material increase the likelihood of SCC, and a smaller critical pit size indicates that SCC has occurred more rapidly.

Kondo assumed that the critical pit size occurs when the fatigue crack growth rate (calculated based on the existing material and mechanical conditions) and the pit growth rate (calculated or observed) are equal. Once critical pit size has been reached, the pit

ceases to grow and the crack continues to propagate through the material. Kondo gives the corrosion pit growth law as:

$$c = C_p t^{1/3} = C_p (N/f)^{1/3} \quad (43)$$

where C_p is a coefficient fitted from experimental data, c is the pit radius, N is the number of stress cycles, and f is frequency. Pit growth rate can then be expressed as dc/dN , which can be formulated in terms of the stress intensity factor and the above parameters. Critical pit diameter, at which a crack is initiated, is calculated in Equation 44. In this equation, $(\Delta K)_p$ is the stress intensity factor range for a critically sized pit, σ_a is stress amplitude, $\alpha = a/c$ (aspect ratio), and Q is a shaping factor that Kondo has determined to be $1.464\alpha^{1.65}$.

$$2c_{cr} = \frac{2Q}{\pi\alpha} \left[\frac{(\Delta K)_p}{2.24\sigma_a} \right]^2 r^2 \quad (44)$$

Kondo suggests a procedure for using this model of pit and crack growth to make failure predictions over the lifetime of a component made of this particular steel. For a given material sample and stress condition, one can determine the maximum expected pit size, calculate the associated critical pit size, and from that size calculate the time (in cycles) it will take for the pit to grow to the critical size. At this point, it is assumed that a crack has initiated [18].

The Kondo model assumes the following:

- Pits are hemispherical.
- Any changes to pit size following crack initiation are insignificant and do not affect crack growth.
- Cracks initiate because the pit has reached its critical size, which occurs when the crack growth rate is first greater than the pit growth rate.

- The pit can be considered a “sharp crack” for the purposes of applying fracture mechanics.

Pitting and cracking behavior is idealized in this model: a definitive critical pit radius can be calculated for each pit, which are all of uniform hemispherical geometry. When the pit grows to reach this critical size, a crack is observed 100% of the time. These assumptions - particularly that of hemispherical pit geometry - are common in the SCC modeling literature.

These assumptions can be problematic when it comes to using the model to accurately predict SCC behavior. Every observed crack may have been found to have initiated at a pit, but is it certain that every one of these pits was at its true “critical radius” (as predicted by Equation 44) when this transition occurred? Were there pits that reached a critical radius but which did not nucleate a crack? These questions are not addressed by Kondo. SCC models like this one aim to predict general degradation trends, and so while they can give insight into the way that SCC generally proceeds in a given situation, they are not always helpful for making definitive, high-accuracy predictions.

Kondo’s model depends on a fracture mechanics view of the situation: pits and cracks grow according to rates governed by the stresses in the steel, and SCC occurs when calculated crack growth overtakes calculated pit growth. This model has no way of accounting for environmental conditions (all tests were performed at the same temperature) or microstructural variations. It allows a rough estimation of the number of cycles that will pass before SCC is observed given a known distribution of pit sizes, but it is not capable of predicting SCC for a different material, different temperature, or different solution. It assumes that the only parameter that must be accounted for is applied stress.

However, Kondo’s work is important to the study of SCC prediction. In the stainless steels that are of interest to the used fuel canister project, and to many other industrial

applications, the ability to model pit growth and the subsequent pit-to-crack transition are the key steps in predicting the onset of stress corrosion cracking. The scope of this paper is limited, but it is an informative starting-point for the statistical treatment of the occurrence of SCC in stainless steels, and Kondo's work is a key reference common to many of the modeling projects outlined in this paper.

7.4 Stochastic approaches to pitting

The following three models treat pitting corrosion as a stochastic process. The number of pits on a surface, the growth rates of these pits, and their likelihood of "dying" can all be modeled probabilistically. These models predict the expected extent of corrosion damage as a function of time.

Kondo's model may not be directly applicable for the purposes of *Life Prediction of Used Fuel Canister Material*, as it assumes a cyclic loading situation, and the canister material is subjected to a constant load defined by residual stresses incurred during canister welding. Kondo's assumption that the pit-to-crack transition occurs when the pit growth rate equals the theoretical crack growth rate may be useful for the final model, and is utilized by other authors studying SCC.³⁶

7.4.1 Shibata and Takeyama, 1977: A stochastic approach to modeling pitting

Shibata and Takeyama used stochastic methods to describe pitting, and their early, significant contributions to the field of probabilistic SCC modeling merit discussion here.³⁷

³⁶Chen et al. identify two possible assumptions for developing pit-to-crack transition criteria [56]. The first type of assumption follows Kondo's logic of cracks initiating from pits when the pit's growth rate equals the theoretical crack growth rate. The second type of assumption assumes that there is a threshold K_{ISCC} beyond which cracking always occurs. Pits act as stress concentrators, and K_{ISCC} of the material around the pit changes as the pit grows. Both assumptions are mechanical in nature (unlike the assumptions that govern the criteria for pit initiation, which are often governed by electrochemical factors).

³⁷This paper was preceded by a brief letter in *Nature* that discussed the stochastic nature of pitting in steels [11], but [12] was the primary reference for this section.

Shibata and Takeyama's interest in the probabilistic nature of pitting arose when it was found that experimental measurements of pitting potential led to consistently different results, even when experimental conditions were carefully controlled in attempts to reproduce previously obtained data [12]. When the protective film of an alloy is unbreached, the observed current corrosion is quite low. "Potential drops" occur when a protective film fails, allowing dissolution of the bulk metal (and thus pit growth). This results in a significant increase in current. The associated voltage change, current change, and time-to-potential-drop can all be measured experimentally.

Two corrosion stages are considered: pit generation and pit growth. Pitting initiation occurs when the film fails: this is considered as a two-dimensional problem, and it is assumed that the film thickness can be neglected.

The authors carried out experiments to determine the potential at which pitting occurred in Types 316 and 304 steel exposed to a 3.5% NaCl solution, using both etched and polished surface preparations. The measured potentials occurred over a range of values, and were not closely centered around a single pitting potential. The authors suggest this may be due to stochastic variations in the passivating film.

To develop the equations that describe pitting, the Markov property is assumed, meaning that if the present state of the pit is determined, the past states leading up to that point have no effect on pit's future behavior. It is a "memoryless" process. The probability that a non-pitted specimen will become pitted in dt is given as:

$$\lambda(t)dt = -dP(t)/P(t) \quad (45)$$

with $\lambda(t)dt$ the "transition probability," and $P(t)$ the "survival probability" (survival = no pitting). $\lambda(t)$ is therefore the pit generation rate. It can also be determined for a time t by graphing the logarithm of $P(t)$ versus t , and taking the negative tangent at the time

of interest. $P(t = 0) = 1$, and the proportion of unpitted specimens at time t can be calculated using the following equation:

$$P(t) = \exp\left(-\int_0^t \lambda(t) dt\right) \quad (46)$$

An estimate of $P(t)$ is given as:

$$P(t) = 1 - \frac{n}{1 + N} \quad (47)$$

with N the total number of specimens considered, and n the number of samples known to have pitted at time t . Figure 44 shows a plot of pitting probability vs. pitting potential for Type 304 and 316 samples prepared using emery polishing and chemical etching. The possible potentials at which pitting occurs was found to have a normal distribution. The authors did not find that there was a threshold potential below which pitting was impossible.

The relationship between survival (no pitting) probability $P(t)$, induction time, and potential was also investigated. When the experiment was conducted at a constant potential, it was found that $P(t)$'s behavior over time was linear, but the data showed three different regions of different behavior. Therefore, for a given $P(t)$ at constant potential, three pitting potentials (resulting in three pit generation rates, λ_1 , λ_2 , and λ_3) were governing the process. This general behavior was observed at all tested potentials. The dependence of λ on E , the experimental potential, was found to be:

$$\lambda_1 = \alpha_1(E - E_{\text{crit}}) = 8.20(E - 0.346) \quad (48)$$

$$\lambda_2 = \lambda_{20} \exp(\alpha_2 E) = 5.01 \times 10^{-19} \exp(113E) \quad (49)$$

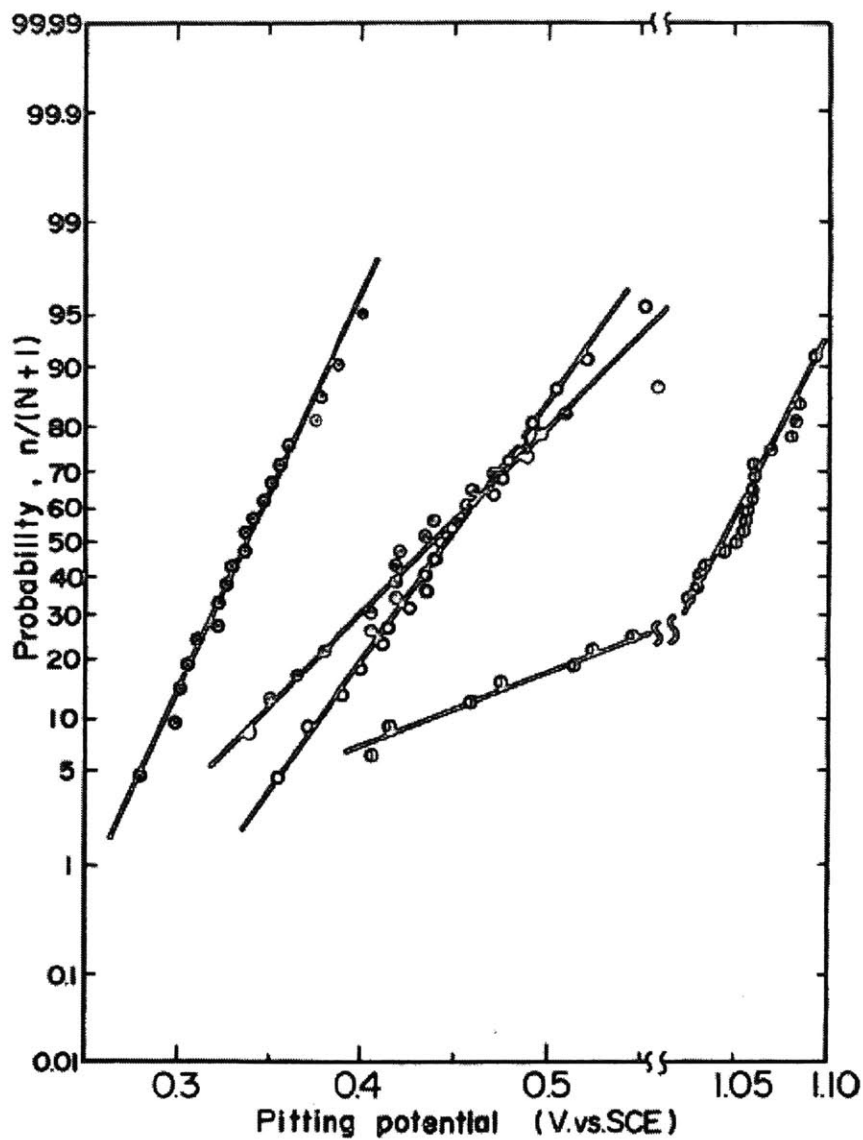


Figure 44: The normal probability plots shows how pitting probability varies with pitting potential. n indicates the number of samples in an exposure experiment that pitted, with N samples total in the experiment. From left to right: Type 304 samples with a 2/0 emery polish, Type 316 samples with a 2/0 emery polish, Type 304 samples with a chemical etch, and Type 316 samples with a chemical etch. The data falls in a straight line, indicating that the pitting potential obeys a normal distribution. [12]

$$\lambda_3 = \lambda_{30} \exp(\alpha_3 E) = 1.44 \times 10^{-19} \exp(113E) \quad (50)$$

Below E_{crit} , the pit generation rate λ becomes 0.

If the value of E is changed at a constant velocity v , such that $\lambda(t) = \lambda(E/v)$, the pitting potential cumulative damage function (CDF) can be written as:

$$P(E/v) = \exp\left(-\frac{1}{v} \int_0^E \lambda(E/v) dE\right) \quad (51)$$

$\frac{-dP(\frac{E}{v})}{dE}$ is then equivalent to the probability density function of the pitting potential. Differentiating this PDF and setting it equal to 0 allows the determination of the pitting potential most likely to be observed. The expression used for $\lambda(E/v)$ will depend on which of the three observed “stages” is assumed to control pit generation. It is asserted that the expression for λ_1 (Equation 48) controls the pitting process, since observed pitting potentials (as a function of v) were most consistent with the predictions when that expression for the pit generation rate was used. When λ_2 or λ_3 were assumed to describe the dependence of pitting on E , the resulting predictions (obtained by optimizing Equation (51)) were not consistent with observed data.

This research provides a potential framework for describing the stochastic nature of pitting on a steel surface by fitting appropriate equations to experimental data, and relating these fitted equations to cumulative and probability distribution functions that can then be used for predictive purposes.

7.4.1.1 Farmer, 1998: A model for pitting, based on the work of Shibata and Takeyama A later paper by Farmer expanded on the work of Shibata and Takeyama [45]. In this pitting model, one begins by partitioning the surface into the fractions covered by pit embryos, sites at which no pit has nucleated (vacancies), and stable pits. Variable

Table 25: Variable definitions for Farmer’s deterministic pitting model

| Variable | Definition |
|--------------------|---|
| θ_E | Fraction of metal surface covered in pit embryos (embryos) |
| θ_V | Fraction of metal surface with no corrosion (vacant) |
| θ_P | Fraction of surface covered in stable pits (pits) |
| k_{birth} | Parameter describing pit birth rate; similar to λ in other models |
| k_{pit} | Parameter describing pit growth; similar to γ in other models. |
| k_{death} | Parameter describing pit death rate; similar to μ in other models. |
| a, b | Constants |

definitions are provided in Table 25.

$$\theta_E + \theta_V + \theta_P = 1 \quad (52)$$

Next, expressions for the change of θ_E in time and θ_P in time are given as:³⁸

$$\frac{d\theta_E}{dt} = k_{\text{birth}} [Cl^-]^a (1 - \theta_E - \theta_P) - k_{\text{death}} [OH^-]^b \theta_E - k_{\text{pit}} \theta_E \quad (53)$$

$$\frac{d\theta_P}{dt} = k_{\text{pit}} \theta_E \quad (54)$$

It is stated in Reference [45] that the results (e.g. pit depth distributions in time) were consistent with those obtained by Shibata and Takeyama. This model by Farmer provides a framework for incorporating environmental parameters into the stochastic approach developed by Shibata and Takeyama. It is dependent on many parameters that must be properly fit to data, and so if this approach is taken, it will be important to determine parameters for the full range of environments that may be experienced by a used fuel canister

³⁸Henshall, Mola, and Shibata and Takeyama all use λ as a descriptor of pit initiation rates, μ as a descriptor of pit death rates, and γ as a descriptor of pit growth rate. More specifically, μ is used to describe the rate at which pits fail to reach stability. See the summary table on page 300 for an overview of these models.

in order to maximize the model's utility. Criteria for pit-to-crack transition, and a model for crack growth, would need to be determined separately.

7.4.1.2 Shibata, 1990: Later work on passivity breakdown and pitting Understanding the stochastic nature of corrosion is a major theme in Shibata's research. A 1990 paper examines several applications of probabilistic distributions to corrosion phenomena [57].

First, the Weibull distribution (used by others to describe pit distributions: see Section 7.6.2) is considered for its utility in describing time-to-failure due to SCC in Type 304 Stainless steel exposed to an aqueous chloride-containing solution. In this paper, the Weibull distribution is given as:

$$F(t) = 1 - \exp\left(-\left(\frac{t-t_0}{a}\right)^m\right) \quad (55)$$

where t is the failure time and a and m are scale and shape parameters. t_0 is the pit incubation time: before t_0 , no pitting is observed. The shape parameter m governs the slope of the distribution and is affected by chloride concentration $F(t)$ represents the CDF for time-to-failure due to SCC.

Shibata reports that for low concentrations of chlorides, an exponential distribution for time-to-crevice-initiation is appropriate.³⁹

The pitting distribution cited by Shibata is a probability of finding a number of pits (x) in a unit area that was developed by Mears and Brown [58]:

³⁹The example given by Shibata involves a 3.5% NaCl solution and Type 304 stainless steel at a temperature of 303K. The references given for the finding that time-to-crevice-initiation under these circumstances can be described by an exponential distribution are as follows:

- S. Tsujikawa, Z. Heng, and Y. Hisamatsu, *Boshuku Gijyutsu*, **32**(149), 1983, [115].
- G. Salvago and G. Fumagalli, *Corrosion Science*, **27**(927), 1987, [116].

$$P(x) = \frac{M^x e^{-M}}{x!} \quad (56)$$

where M is the mean value of x . If there is no interaction between pits, and the process of pit formation is completely random, then a simple Poisson distribution can be used instead. For a known average rate of pit generation on the surface, λ , Equation (56) becomes:

$$P(x) = \frac{(\lambda t)^x e^{-\lambda t}}{x!} \quad (57)$$

The pit distribution changes as pits appear (“birth”) and disappear (“death”). Shibata notes that birth and death processes may be modeled as occurring in parallel or in series. This choice will affect the model’s predictions and the extent to which they align with experimental observations.

When only pit birth is being considered, a “simple birth stochastic model” can be used:

$$P(t) = e^{-\lambda(t-t_0)} \quad (58)$$

This simple birth stochastic model can also be adapted as a plural combination of “simultaneous (birth) processes in series,” so that $P(t) = \prod P_i$, where P_i is given in Equation (58).

The birth stochastic model can also be expressed as a plural *series* combination, which Shibata also refers to as “simultaneous (birth) processes in parallel.” In that case, the pit distribution becomes:

$$P = 1 - \lambda \left(1 - e^{\lambda(t-t_0)} \right) \quad (59)$$

It is also possible to consider multiple independent pitting processes that are happening

in parallel. To find $P(t)$ in this case, the appropriate P_i for each independent process is then summed as $\sum f_i P_i$, where the f_i sum to one.

In other models, it is necessary to consider pit death as a result of repassivation. In these cases, μ is given as the pit death rate. If the birth and death processes are happening in parallel, which Shibata represents visually as a sample in which pit birth processes are occurring at one site while pit death processes are occurring at a separate site, then the pit distribution on the steel surface is given as follows:

$$\frac{dP}{dt} = -\lambda P \cdot \mu(1 - P) \quad (60)$$

$$P = \frac{\mu}{\lambda\mu} \cdot \frac{\lambda}{\lambda\mu} \exp(-(\lambda \cdot \mu)(t - t_0)) \quad (61)$$

The pit birth and death processes may also be occurring in series. Visually, Shibata represents this as the pit birth and pit death processes competing on the same pit site. In this case, the pit distribution on the sample surface is described as:

$$\frac{dP}{dt} = -P(\alpha\lambda \exp(-\mu\tau_c)) \quad (62)$$

$$\ln P = -\alpha\lambda(t - \tau_c)\exp(-\mu\tau_c) \quad (63)$$

These approaches can be considered when modeling the pit distribution on the surface of a sample exposed to some corrosion-inducing solution. They are easily adaptable to probabilistic simulations (Shibata's paper includes examples of using Monte Carlo simulations to model induction time), but must be chosen correctly if the results are to be representative of actual observation. In particular, it must be decided whether to consider

pit death or only pit birth, and it must be decided whether events occur in “series” or in “parallel,” as this affects the mathematical construction of the distribution model.

7.4.2 Mola, 1990: A stochastic treatment of SCC

The work of E. E. Mola was a precursor to the stochastic pitting model of Henshall (Section 7.4.3), and so it is considered here. The stochastic model developed by Mola and his colleagues was validated against experimental data from Type 316 stainless steel exposed to a sodium chloride solution [15].

Pitting is assumed to be caused primarily by loss of passivity due to the presence of aggressive ions (like $[\text{Cl}^-]$), and the pit becomes an active site. Metal dissolution occurs, causing pit growth. Mola, like others before him, notes that pitting experiments rarely result in reproducible results, even when the conditions are carefully controlled from trial to trial: pitting corrosion behaves stochastically.

With Mola’s model, pitting tends to occur at favored sites, which are here assumed to be points of reactant inclusions. However, the authors note that a larger number of factors are likely to contribute to the pitting behavior of a material, including:

- Variations in the metal bulk
- Film cracking
- More acidic pH in pits and crevices
- Transport of defects through the passive film
- Ion adsorption into the film

Mola’s model assumes that each inclusion (the number density of which are assumed to be constant for a certain material) has an equivalent chance of being at the exposed metal surface, and that the locations of inclusions are independent from one another. A

Poisson distribution gives the probability of having a certain number k of inclusions, and the average number of inclusions can be described as:

$$\langle n_0 \rangle = \sum_{k=0}^{\infty} k e^{-\alpha} \frac{\alpha^k}{k!} = \alpha \quad (64)$$

where $\alpha = n_2/n_1$, n_1 is the total number of inclusions, and n_2 is the total number of samples. Having established the likelihood that a given number of inclusions (k) is present, the following assumptions are made: the inclusions do not influence the corrosion behavior of each other, the probability of pit initiation is the same at every inclusion, the same inclusion can not be activated more than once, and the probability of pit initiation does not depend on the previous history of the inclusion site (the Markov property applies).

When τ_0 is the pit birth time (and assumed to be a continuous random variable), λ_0 is the probability density of pit births per unit time, and P_0 the probability of pit birth when $t \leq \tau_0$, it is found that:⁴⁰

$$P_0(t) = e^{-\lambda_0 t} \quad (65)$$

and:

$$\langle \tau_0 \rangle = \frac{\int_0^{\infty} t e^{-\lambda_0 t} dt}{\int_0^{\infty} e^{-\lambda_0 t} dt} = \frac{1}{\lambda_0} \quad (66)$$

The mean number of pits is found to be:

$$\langle n(t) \rangle = n_0 [1 - e^{-\lambda_0 t}] \quad (67)$$

Next, pit growth is considered. Pit size is described by the number of unit volume

⁴⁰The full derivation of Equation (65) can be found on page 11 of [15].

elements. Pits are assumed to grow in steps, with their size increases by a number of unit volume elements at each step. It is assumed that pits do not decrease in volume. The pit volume is:

$$V = k(t)dV \quad (68)$$

with k the number of volume elements that make up the pit. Consider a pit with volume $j dV$ at time $t + dt$. The pit volume has either undergone no change since the previous timestep (t), or it has grown from $(j - 1)dV$ to $j dV$. It is found that

$$\frac{dP_j}{dt} = -\lambda_j P_j(t) + \lambda_{j-1} P_{j-1}(t) \quad (69)$$

$$P_j(t) = \lambda_{j-1} \int_0^t e^{-\lambda_j(t-t')} P_{j-1}(t') dt' \quad (70)$$

where $j = 1, 2, 3 \dots$ and P_j is the probability that the pit reaches $j dV$. There are λ_j area elements at the pit surface. τ_j is chosen as a random variable, which is then assigned to the pit. δ_V is the volume of corroded material at τ_j . If δ_V has more area elements in common with λ_j , the probability of corrosion increases for the next timestep.

The probability that the pit repassivates before reaching the pit stability criterion (defined as a critical volume V_c , reached at time τ_C) is given as μ . μ depends on the conditions at hand. The other parameters in the model can be estimated from experimental observations of corroded specimens (e.g. the number of pits per unit area).

This provides another framework for a stochastic model of pit growth, and it accounts for both the probability of pit birth and pit growth at each timestep. If this model is applied to *Life Prediction of Used Fuel Canister Material*, λ_0 could be determined experimentally, or perhaps developed as a function of stress and chemistry. This model could then be used

to simulate pitting on a finite element analysis model of a representative weld. Transition to cracking, and crack growth, would need to be addressed with separate additions to the Mola framework.

7.4.3 Henshall, 1992: A stochastic approach to modeling pitting damage using phenomenological equations

G. A. Henshall of Lawrence Livermore National Laboratory carried out research concerning corrosion in high-level waste (HLW) containers that would be stored at Yucca Mountain.⁴¹ He used computer models to simulate pitting and study the manner in which parameters changed when the environment was changed. The ultimate goal was a computer model that used a stochastic approach to predict pitting behavior [35].

Because experiments used to refine such a model and fit parameters are typically accelerated (usually by making the environment purposely more aggressive to generate data in a timely manner), this work also emphasized understanding how the environment affected pitting, since (1) the canister environment of interest isn't constant in time and (2) the analysis of accelerated corrosion experiments needed to be extrapolated to the less aggressive actual environment.

Because this model predicts pit depth as a function of time, it is useful for predicting the evolution of pitting damage on a surface. At the time of the study (1992), the majority of pitting models focused instead on prediction of electrochemical quantities, such as pitting potential. Time-to-failure was defined by Henshall as the time needed for the pit to grow through the wall (note that he considered pitting, and not cracks initiated from pits, as the primary failure mode).

In the Henshall approach, the stochastic nature of pitting is driven by fluctuations in

⁴¹Note that the models were not necessarily developed for stainless steels, but the approach here could be generalized to studying pitting and cracking in other materials.

surface chemistry and variations in the surface itself. This results in local passivation and repassivation events that cause the nucleation of micropits that either become inactive or continue to grow to stability [16].

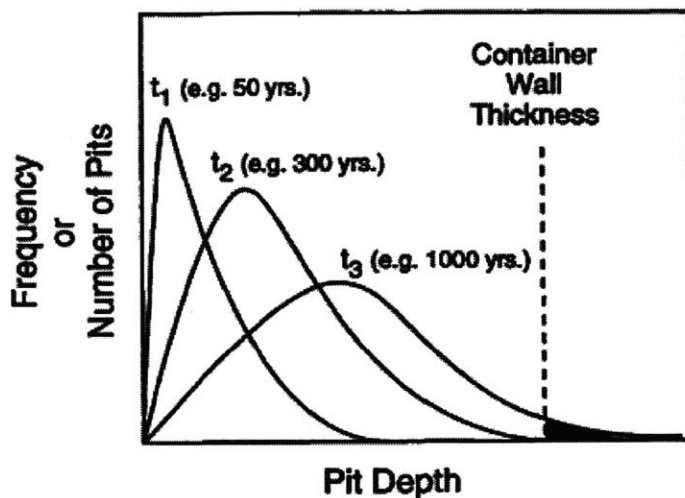


Figure 45: This is an illustrative damage function used by Henshall [17]. It shows the number of pits that have a certain depth, as calculated for several long exposure times. The area under the curve and to the right of the vertical line indicating canister depth is proportional to the number of pits that can be expected to fully penetrate the canister wall during the considered exposure time.

A damage function approach was considered because a damage function can be used to calculate, for a specific environment and a given exposure time, the number of pits expected for a certain pit depth. Several conceptual damage functions are shown in Figure 45. Damage functions can be developed using a mechanistic approach (deterministic equations that describe the damage process completely) or an experiment-informed, phenomenological approach. The latter is the most common: equations can be defined such that they are purposely consistent with experimental data. Damage mechanisms like pitting are affected by many variables - which are rarely consistent across environments of interest (e.g.

different canisters) or constant in time. Thus, a definitive, complete set of equations to describe it has yet to be developed. Some illustrative damage functions predicted with the final model (explicated below) are presented in Figure 46.

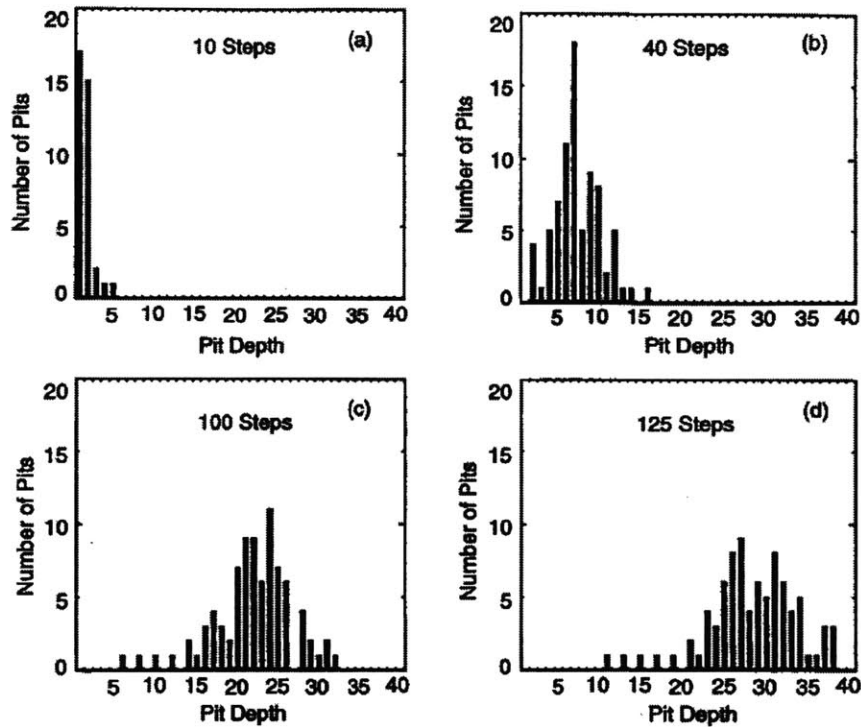


Figure 46: Example simulation results for 10, 40, 100, and 125 timesteps. The depths are in arbitrary units, as these simulations aim primarily to show how the distribution of pit depths changes in time. The growth probability γ was 0.25. Birth probability λ was assumed to be exponentially decaying. [17]

The probability that a pit will be nucleated in a defined unit area in the model (a cell⁴²) as a result of local passivity loss is given as:⁴³

⁴²In the computer model, no more than one pit can grow in a single cell [16].

⁴³Henshall cites papers by Williams et al. ([59]), for methods to experimentally determine Λ [35]. Henshall also cites the work of Williams as a key starting point for his own modeling efforts [17].

$$\lambda = \Lambda A_{\text{cell}} \Delta t \quad (71)$$

Δt is the timestep used in the model, A_{cell} is the area of a cell, and Λ is the rate at which pits are generated in a unit area.⁴⁴

This model can be modified to reflect a decaying birth probability - for example, by using the descriptions of λ developed by Shibata and Takeyama (see Section 7.4.1):

$$\lambda = \lambda_0 e^{-\alpha t} \quad (72)$$

with λ_0 and α constants. In Farmer's review of Henshall's model, it was noted that this formulation of pit birth probability is not ideal. Equation (72) was chosen because it resulted in a calculated pit depth distribution that was in better agreement with experimental results than the distribution that was calculated when a constant birth probability was assumed. Ideally, λ should be time invariant [45].

Not all of these initial pits survive. The probability that a pit will not reach its point of stability, and will thus fail to contribute to the possibility of failure, is given as

$$\mu = M \Delta t \quad (73)$$

μ is the "pit embryo death rate," and M is the experimentally measured death rate. Pits that reach a certain critical age τ_C (number of timesteps) without being "killed" are assumed to be stable.⁴⁵ Stable pits were assumed to grow linearly. However, this assumption leads to results that yield a larger number of deeper pits with increasing time

⁴⁴In the computer model, a random number is assigned to each cell. If the random number $< \lambda$, a pit is nucleated in that cell.

⁴⁵In the computer model, a random number is assigned to each previously generated pit that has not reached stability. If the random number $< \mu$, the pit is assumed to "die."

than are observed in experiments. Several possible reasons are given: the pits may cease and restart growth multiple times during their total life. Local chemistry also could change to make continued growth impossible.

To make results more consistent with observation, a growth probability γ was expressed as:

$$\gamma = \Gamma \Delta t / D \quad (74)$$

where Γ is the growth rate (cm s^{-1}) and D is the depth increase. Γ was fit to experimental data. γ is assumed to be constant.⁴⁶

In an ideal model, λ , μ , τ_c , and γ would be formulated with explicit dependence on environmental parameters. In this case, phenomenological equations that were consistent with experimentation were developed instead. The environmental parameters considered in the Henshall model were the applied potential (E_{app}), chloride concentration $[\text{Cl}^-]$, and temperature T .

λ was formulated to have a linear dependence on E_{app} , as suggested in the results of Shibata and Takeyama [12]:

$$\lambda \sim \beta(E_{\text{app}} - E_c)t \quad (75)$$

where β is a constant. E_c is the threshold potential for pitting to become possible.

The dependences of λ , μ and τ_c on T and $[\text{Cl}^-]$, as shown below, were based on data presented by Shibata and Takamiya.⁴⁷ They are as follows:

⁴⁶In the computer model, a random number was assigned to each stable pit at each timestep. If it was less than γ , the pit grew during that timestep by D .

⁴⁷See: T. Shibata and H. Takamiya, *Proceedings of the Conference on Critical Issues in Reducing the Corrosion of Steels*, (NACE, Houston, 1985), 17, [117].

$$\tau_c \sim e^{-k_1 E_{app}} \quad (76)$$

$$\lambda \sim e^{k_2 [Cl^-]} \quad (77)$$

$$\mu \sim e^{-k_3 [Cl^-]} \quad (78)$$

$$\tau_c \sim e^{-k_4 [Cl^-]} \quad (79)$$

and based on the data of Herbsleb and Engell, the growth probability γ was found to depend on chloride ion concentration as:

$$\gamma \sim [Cl^-]^a \quad (80)$$

with a constant.⁴⁸ γ was assumed to have an Arrhenius relationship with temperature T , although the author notes that this is not likely to be a truly accurate way to model $\gamma(T)$.⁴⁹ To describe how γ changes with E_{app} , Henshall used the data of Szklarska-Smialowski and Janik-Czachor, and found that:

$$\gamma \sim (E_{app} - E_{crt})^b \quad (81)$$

where E_{crt} is the threshold value for pit growth and b is a constant that depends on pit geometry (0.5 for hemispherical pits, as is assumed here).⁵⁰

The final equations for pit nucleation probability λ , pit death probability μ , critical age

⁴⁸See: G. Herbsleb and H.-J. Engell, *Werkst. Korros.* 17 (1966) 365, [118].

Broli et al. also found that γ increased with chloride concentration.

See: A. Broli, H. Holtan and T. B. Andreassen, *Werkst. Korros.* 27 (1976) 497, [119].

⁴⁹In order to propose this Arrhenius relationship, Henshall cited the data of Broli et al. See the reference above.

⁵⁰Henshall also mentioned that Herbsleb and Engell had suggested that γ is independent of E_{app} , but a linear dependence, as found in the work of Szklarska-Smialowska and Janik-Czachor, seemed more appropriate.

See: Z. Szklarska-Smialowska and M. Janik-Czachor, *Br. Corros. Journal*, 4, 1969, 138, [120].

for stability τ_c and growth probability γ are as follows:

$$\lambda = A_1(E_{\text{app}} - B_1) \cdot e^{C_1[\text{Cl}^-]} \cdot e^{-Q_A/RT} \quad (82)$$

$$\mu = A_2 \cdot e^{-C_2[\text{Cl}^-]} \cdot e^{-Q_u/RT} \quad (83)$$

$$\tau_c = A_3 \cdot e^{-B_3 E_{\text{app}}} \cdot e^{-C_3[\text{Cl}^-]} \cdot e^{+Q_\tau/RT} \quad (84)$$

$$\gamma = A_4 (E_{\text{app}} - B_4)^{B_5} [\text{Cl}^-]^{C_4} \cdot e^{+Q_\gamma/RT} \quad (85)$$

A_i , B_i , and C_i are constants.⁵¹ Next, for an environment that changes in time, the chosen environmental parameters (E_{app} , $[\text{Cl}^-]$, and T) can be described as follows:

$$E_{\text{app}} = E_0 - e^{-E_1 t} \quad (86)$$

$$[\text{Cl}^-] = K_0 e^{K_1 t} \quad (87)$$

$$T = T_\infty + T_0 e^{-T_1 t} \quad (88)$$

Henshall suggests that Equation (87) is one way to model $[\text{Cl}^-]$ on the surface of a container that is alternately wet and dry. The effects of changing chloride concentration on pit depth are shown in Figure 47.

T_∞ is the ambient temperature that a canister surface eventually tends toward as the heat production of the used fuel decays. E_0 , E_1 , K_0 , K_1 , T_0 , and T_1 are constants that are fit to experimental data. Q is the activation energy for the specified process and R is the gas constant.⁵²

⁵¹The values of these constants can be found in the original paper (see Reference [35]).

⁵²Henshall notes that it is important to select units such that the values of λ , μ , and τ_c do not exceed 1. Their values can be further limited in the code if a computer modeling approach is taken. When μ and λ are calculated in Henshall's code, they are limited to values that are ≤ 1 . However, this is seen as an additional limitation of Henshall's approach, and Farmer recommends that an SCC model should have properly normalized functions [45].

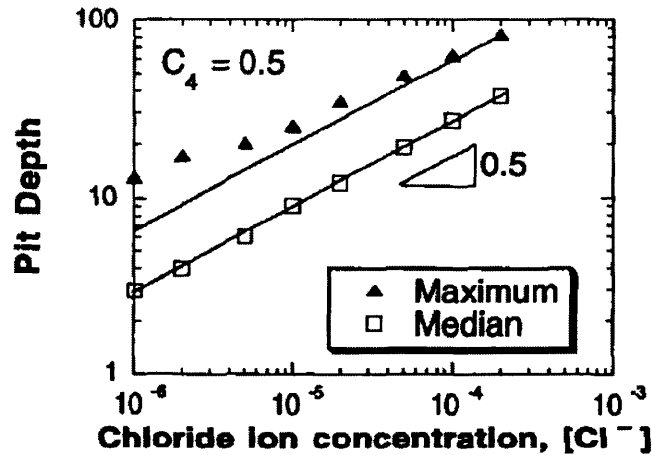


Figure 47: The graph shows the average and maximum pit depths predicted by Henshall's computer model when the chloride concentration at the surface is changed. Both pit depth and $[Cl^-]$ were calculated using arbitrary units. [16]

In carrying out simulations, the damage function generated by the model can be compared with the damage function that was validated experimentally. For example, these equations yielded a damage function that had reasonable agreement with experimental results, but which had a lower number of shallow pits and a higher number of deep pits than were observed experimentally.⁵³ This was readily seen from the data yielded by the damage function analysis approach (see Figure 46 for an example of how the predictions can be visually presented). This is an advantage of this approach: it allows for a very effective visual comparison of experimental data with predictions.

Henshall's model is more unwieldy than Mola's, but its framework includes an explicit dependence on chloride concentration, temperature, and potential. If a stochastic simulation model of pitting and cracking in canister welds is pursued, this could be a very

⁵³Henshall suggests that the best approach may be to assign a pit growth probability that varies as a function of depth in order to yield more accurate simulation results.

promising direction for establishing the pitting component of the model.

7.4.3.1 Farmer’s modifications to the Henshall model. Farmer builds on the work of Henshall in order to make the model more consistent with observed pitting behavior. The environment at each cell determines the probability that a pit will nucleate (or become inactive). Farmer intended to improve on this work by

- accounting for pH effects
- reexamining the assumption that the probability of pit birth decays exponentially
- using normalized probability expressions

Farmer suggested the following formulation for the pit birth probability λ :

$$\lambda = \lambda \left(A \theta_P^n e^{B\theta_P} \right) \quad (89)$$

n , A , and B are constants. θ_P is a shape factor that represents the percentage of the surface comprised of stable pits. The advantage of this approach is that it eliminates time as a variable, and in doing so circumvents the need to impose a decaying birth probability (which is inconsistent with experimental data) in order to get the correct pit depth distribution.⁵⁴ One then considers the time-dependent pit penetration. Farmer gives an example expression for pit penetration:

$$d = \sqrt{\underbrace{2 K_0 [\text{H}^+] (E - E_{\text{crit}})}_{=K, \text{time rate constant}} T_{\text{age}}} \quad (90)$$

with d pit penetration, K_0 constant, E the applied voltage, E_{crit} the threshold pitting potential, and T_{age} the age of the pit. Equation (90) is intended to be an illustrative, not

⁵⁴This is done in order “to obtain a reasonably shaped distribution of pit depths, the number of pits verses depth. Ideally, the birth rate (or birth probability) should be time invariant in such a mechanistic model.” [45], 160.

definitive, example of a possible form of pit depth d . Farmer also suggests that the process of “stifling” should be considered: in certain situations, a pit may grow deep enough that the current density drops, and the pit repassivates.⁵⁵

If Henshall’s model is used for *Life Prediction of Canister Material*, then Farmer’s modification should be considered for inclusion, as it is already known that Henshall’s expression for λ is inconsistent with observation.

⁵⁵Should this be identified as a possibility for the canister steel, the following references cited by Farmer may prove helpful:

- J. R. Scully, *Appendix D, Elicitation Interview Summaries, Waste Package Degradation Expert Elicitation Project final Report*, Geomatrix Consultants, August 1997, [121].
- G. P. Marsh et al., “The Kinetics of Pitting Corrosion of Carbon Steel,” SKB Technical Report 88-09, 1988, [138].

7.5 Crack initiation and propagation

These SCC models focus primarily on crack initiation and growth behavior. The majority of the models presented in this section assume that stress corrosion cracks propagate via some variation of the slip-dissolution mechanism, in which slip steps form at the crack tip, exposing unpassivated metal. This allows further corrosion, which decreases as the metal exposed by the slip process passivates, and the cycle then repeats itself.

A subset of the models covered in this section focus only on crack growth, and not crack initiation. Establishing the criteria for crack initiation from a corrosion pit is an important step toward completion of any overall model of SCC. Kondo (Section 7.3.7) and the complete SCC models (Section 7.6) also consider this process.

7.5.1 Ford and Andresen, 1982-1987: A film fracture model

Andresen and Ford also developed expressions for $\frac{da}{dt}$, and also worked within the context of SCC progressing via periodic fractures of the oxide film at the crack tip [19]. The most important input in their model is strain: the crack propagation rate is proportional to the crack-tip strain rate, and inversely proportional to the film fracture strain.

In 1984, Ford wrote [60]:

“Although fracture-mechanics parameters, such as stress intensity or crack opening displacement, are useful in design, it is not recognized that, for ductile-alloy/aqueous-environment systems, their fundamental importance lies in their effect on the oxide (or film) rupture event, the subsequent oxide (or film) rupture rate, and the ease of solution flow down the crack length.”

The crack propagation rate is found to be:

$$\frac{da}{dt} = \frac{MQ_f}{z\rho\mathbf{F}} \frac{d\epsilon_{ct}}{dt} \frac{1}{\epsilon_f} \quad (91)$$

with all variables defined in Table 26 [60, 46].

A general way to describe $\frac{da}{dt}$ in austenitic stainless steels is:

$$\frac{da}{dt} = f(n) \left(\frac{d\epsilon_{ct}}{dt} \right)^n \quad (92)$$

assuming that the crack propagates via the film rupture-slip dissolution mechanism [19]. n is a parameter that is dependent on the material and the environment. Predicting crack propagation rates then becomes a matter of determining the value of n and the expression for $f(n)$ for a given environment. The anodic current density transient that is measured following film fracture can be related to n via the following expression:

$$i_a = at^{-n} \quad (93)$$

n depends on corrosion potential, the properties of the electrolyte, and the composition of the corroding metal.

Table 26: Variable definitions for Equations (91),(92), and (93)

| Variables | Definitions |
|-----------------|--|
| $\frac{da}{dt}$ | Crack propagation rate |
| M | Atomic weight of the metal |
| z | Number of electrons exchanged when a mole of the metal is oxidized |
| ρ | Density of the metal |
| Q_f | Oxidation charge density between fracture events |
| ϵ_f | Film fracture strain |
| ϵ_{ct} | Crack tip strain |
| n | Parameter that encompasses environment and material properties |
| i_a | Anodic current density |

Ford and Andresen's model lays out the basics of the slip-dissolution-rupture (SDR) model of crack propagation in SCC processes. If the SDR model is assumed to be the valid explanation for how SCC cracks would propagate in the canister welds, then this model would likely be the starting reference for establishing an appropriate model of crack growth.

7.5.2 Buck and Ranjan, 1986: An expression for time to crack initiation

Buck and Ranjan developed a crack-tip-opening-displacement (CTOD) model for microcrack initiation [29]. Experimentally, they studied brass exposed to an ammoniacal solution. Tensile test specimens were pre-deformed in the solution to a certain constant stress level. Samples were then either partially unloaded to a lower stress or completely unloaded for a length of time t_{hold} , followed by reloading to a new stress level. The incubation time t_{inc} is the time-to-failure after the reloading to a new stress level. Experimentally, failure was indicated by a drop in applied load, which corresponds to the development of cracks.

The crack precursors are transgranular corrosion pits on the surface, whose growth is governed by potential. Pit depth as a function of time can be described as:

$$a_p = Bte^{V/V_0} \quad (94)$$

with variables defined in Table 27.

Buck and Ranjan developed an expression for the time to SCC initiation, t_{inc} :

$$t_{\text{inc}} = \frac{(K_{\text{ISCC}})^2 e^{-V_m/V_0}}{\pi B(\sigma^2 - \sigma_0^2)} \quad (95)$$

During t_{inc} , it is assumed that the material is subjected to a constant stress load.

The CTOD model assumes there is a critical pit depth, dependent on applied stress

Table 27: Variable definitions for Section 7.5.2

| Variable | Definition |
|---------------|--|
| a_p | Pit depth |
| K_{ISCC} | Stress intensity threshold |
| σ | Applied stress |
| σ_o | Threshold stress for crack initiation |
| A | Constant |
| B | Constant |
| δ | CTOD |
| δ_o | Corrosion pit opening displacement |
| δ_c | Critical CTOD |
| V | Potential |
| V_m | Electrochemical potential |
| V_0 | Reversible potential |
| K_I | Stress intensity factor |
| σ_{fl} | Flow stress of material and maximum plastic strain |
| E | Young's modulus |

σ , at which a crack will initiate, and a certain threshold stress σ_o below which cracks do not initiate. Applied stresses create plastic zones ahead of the pit and allow for crack propagation. Microcracks initiate from the base of corrosion pits and have the propagation rate, $\frac{da_m}{dt}$, which can be described as:

$$\frac{da_m}{dt} = A(\delta - \delta_o - \delta_c) \quad (96)$$

where δ is the “opening displacement” that occurs at the mouth of the pit as it grows. The propagation rate is proportional to CTOD, δ , (or, rather, is proportional to $\delta - \delta_c$). CTOD has both elastic and plastic components. δ_o is the opening displacement of the initial corrosion pits, and acts as a correction to a propagation rate expression dependent only on δ : the bluntness of the corrosion pits tends to make it more difficult to initiate a microcrack. Initiation occurs when the following condition holds:

$$\delta - (\delta_o + \delta_c) > 0 \quad (97)$$

and Buck and Ranjan make use of this condition, in conjunction with the definitions of δ , δ_o , and δ_c to develop the expression for t_{inc} given above. The definitions for the various CTOD expressions are:

$$\delta \propto \frac{K_I^2}{\sigma_{\text{fl}} E} = \frac{\sigma^2 \pi a_p}{\sigma_{\text{fl}} E} \quad (98)$$

$$\delta_o \propto \frac{\sigma_o^2 \pi a_p}{\sigma_{\text{fl}} E} \quad (99)$$

$$\delta_c \propto \frac{\sigma^2 \pi a_c}{\sigma_{\text{fl}} E} = \frac{K_{\text{ISCC}}^2}{\sigma_{\text{fl}} E} \quad (100)$$

Substitution into Equation (97) yields:

$$(\sigma^2 - \sigma_o^2) a_p - K_{\text{ISCC}}^2 / \pi > 0 \quad (101)$$

Time-dependent expressions for the elastic and plastic components of δ are given. The total equation for CTOD is given as:

$$\delta \propto \frac{1}{2} \frac{\sigma^2 \pi B e^{V/V_o}}{\sigma_{\text{fl}} E} \left[t + \left(t^2 - (t_{\text{hold}})^2 \right)^{1/2} \right] \quad (102)$$

Buck and Ranjan substitute this expression, the expressions for δ_o , δ_c , and pit depth a_p into Equation (97). When t_{hold} is assumed to be 0, and potential V is constant, this yields the estimated time-to-crack-initiation that was given in Equation (95).

Buck and Ranjan's approach to modeling the pit-to-crack transition is somewhat unique:

a microcrack initiates when the strain energy release rate is sufficiently large (instead of using the pit growth rate = crack growth rate or the threshold K_{ISCC} criteria). Furthermore, t_{inc} relates to the time required to initiate a microcrack. If this model was used for *Life Prediction of Canister Material*, it would be necessary to further develop the model to include the transition from microcrack to macrocrack, and then to model the growth of the larger crack. Since this model was developed for brass exposed to an ammonium-containing solution, it would be necessary to validate it for steel samples exposed to a chloride-containing solution. It would also be necessary to interpret t_{inc} and t_{hold} in the context of a welded steel canister that is subjected to loads due to residual stress and not active loading.

7.5.3 Nakayama and Takano, 1986: A film fracture model

Nakayama and Takano studied SCC in Type 304 stainless steel, and considered it in the context of a slip-dissolution-repassivation (SDR) model [20]. The steel was exposed to a boiling magnesium chloride solution, which is highly aggressive. The parameters of interest were strain rate, applied potential, and solution temperature. Their theories were compared with experimental results, and it was found that TGSCC propagated in the 304 stainless steel along active slip planes, in accordance with the predictions of the SDR model.

In the SDR view of SCC, a passive film forms at the crack tip. Periodically, this film ruptures along slip planes and the crack propagates. Repassivation occurs, and the process repeats. A similar mechanism has been proposed by other researchers studied here (for example, see the work of N. Saito (Section 7.5.7)).

The measured current density can be described as:

$$i(t) = J^{\circ} e^{-\beta t} \quad (103)$$

Repassivation processes cause the exponential decay behavior [46]. The crack propagate rate is:

$$\frac{da}{dt} = \frac{M\langle i \rangle}{zF\rho} \quad (104)$$

where $\langle i \rangle$, the time averaged dissolution current density, is:

$$\langle i \rangle = \frac{J^\circ}{\beta} \eta_s \left[1 - e^{-\beta/\eta_s} \right] \quad (105)$$

This was found to be consistent with experimental observation of $\frac{da}{dt}$. The relationship between the potential, n_s , and $\frac{da}{dt}$ is shown in Figure 48.

Variable definitions for all equations are found in Table 28.

Table 28: Variable definitions for the Nakayama and Takano model

| Variable | Definition |
|-----------|--|
| $i(t)$ | Dissolution current density |
| J° | Dissolution current density at the “fresh” surface exposed by film rupture |
| β | Decay constant |
| t | Time |
| n_s | Formation rate of slip steps |
| M | Molecular weight of the passive film |
| z | Number of electrons involved in metal dissolution |
| F | Faraday constant |
| ρ | Film density |

Nakayama and Takano’s model is another SDR model. If SDR is used to explain crack growth through canister welds, then all SDR models will need to be considered further. This model builds on the basic framework provided by Ford and Andresen, and suggests more explicit definitions for the constants.

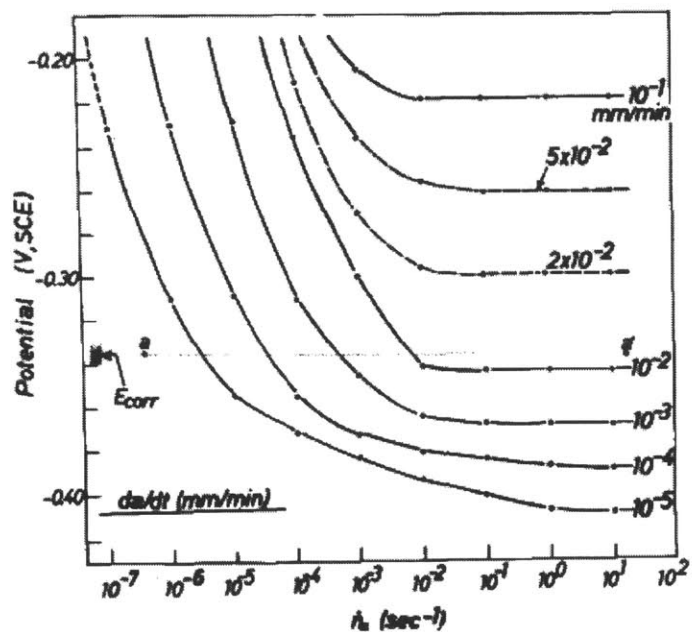


Figure 48: This figure shows the relationship between potential, slip step formation rate, and crack propagation in the slip-dissolution-repassivation model studied by Nakayama and Takano. The model was based on observed cracking behavior in Type 304 stainless steel exposed to a boiling $MgCl_2$ solution. [20]

7.5.4 Hall, 2008: Critique of the Ford-Andresen film rupture model

M. M. Hall Jr. submitted a critique of the Ford-Andresen film rupture model to *Corrosion Science* in 2008 [22]. He acknowledges that several researchers before himself have already pointed out several potential problems with the Ford-Andresen model. Macdonald claimed that Ford and Andresen's expressions for crack growth rate were not consistent with Faraday's law.⁵⁶ Gutman argued that Ford and Andresen's model did not contain explicit parameters for slip-dissolution processes, and was therefore a film-rupture model, but not necessarily a slip-dissolution model.⁵⁷

Hall points out that Ford and Andresen's assumption that $\frac{da}{dt}$ equals the rate of metal dissolution is not necessarily accurate. This implies that the instantaneous crack growth rate can be expressed as:

$$\frac{da}{dt}(t) = \frac{M}{z\rho F}i_a(t) \quad (106)$$

and that the crack "advances continuously so long as corrosion current flows from the crack tip."⁵⁸

Hall also considers the current transient that occurs during repassivation (see Equation (93)). According to Hall, this should contain a dependence on the crack tip strain rate. Since the crack is advancing during the repassivation stage, there must be a strain rate presence, and therefore, this needs to be accounted for in the model.

In Hall's view, treating film rupture and repassivation as independent events leads to inaccuracy.

Hall proposes a model in which the crack tip strain is a result of crack progression,

⁵⁶D. D. Macdonald, "On the modeling of stress corrosion cracking of iron and nickel base alloys in high temperature aqueous environments," *Corrosion Science*, **38**, 1996, 1003-1010, [122].

⁵⁷E. M. Gutman, "An inconsistency in "Film Rupture Model" of stress corrosion cracking," *Corrosion Science*, **49**, 2007, 2289-2302, [123].

⁵⁸Hall, 1104.

Table 29: Variable definitions for the Hall model

| Variable | Definitions |
|--------------------------|---|
| $\frac{da}{dt}$ | Crack growth rate |
| t | Time |
| $\dot{\varepsilon}_{ct}$ | Total strain rate at crack tip |
| M | Molecular weight of the metal |
| z | Number of electrons exchanged during dissolution reaction |
| \mathbf{F} | Faraday's constant |
| i_a | Anodic current density |
| i_a^* | Bare metal anodic current density (reference) |
| A^* | Active surface area fraction |
| k^* | Passivation rate constant for the reference metal |
| γ | Active area fraction generated per unit strain |
| $\dot{\varepsilon}_{ct}$ | Strain rate at a fixed distance ahead of crack tip |
| s | Indicates steady state |

rather than the driving force behind it [61]. Variable definitions for all equations are provided in Table 29. The instantaneous crack growth rate is derived from Faraday's law as:

$$\frac{da}{dt}(t, \varepsilon_{ct}) = \frac{M}{z\rho\mathbf{F}}i_a(t, \varepsilon_{ct}) \quad (107)$$

Current $i_a(t, \varepsilon_{ct})$ is related to the amount of active surface as:

$$i_a(t, \varepsilon_{ct}) = i_a^*A^*(t, \varepsilon_{ct}) \quad (108)$$

Equation (108) can then be substituted into Equation (107) to obtain an expression for crack growth rate. Simplified, this becomes:

$$\frac{da}{dt}(t, \varepsilon_{ct}) = \frac{da^*}{dt}(t, \varepsilon_{ct})A^*(t, \varepsilon_{ct}) \quad (109)$$

Hall points out that $A^*(t)$ can then act as a normalized crack growth rate, and the goal becomes understanding how $A^*(t)$ changes.

Next, Hall derives an expression for the crack surface activation rate. This is a combination of the effects of passivation rate and the strain-induced surface activation rate. For the surface passivation rate, a first-order passivation kinetics model is assumed, and it is found that:

$$\left(\frac{\partial A^*}{\partial t}\right)_{\varepsilon_{ct}} = -k^* A^* \quad (110)$$

The already-passive surface, represented by the fraction $1-A^*$, is activated by straining, and so:

$$\left(\frac{\partial(1-A^*)}{\partial \varepsilon_{ct}}\right)_t = -\gamma(1-A^*) \quad (111)$$

Equation (111) is the rate of passive surface activation; it can then be multiplied by the strain rate $\dot{\varepsilon}_{ct}$ to obtain the time-based surface activation rate.

Finally, the crack surface activation rate is obtained by combining Equations (110) and (111):

$$\frac{dA^*}{dt} = -k^* A^* + (1-A^*)\gamma\dot{\varepsilon}_{ct} \quad (112)$$

Hall goes on to develop an expression for $\dot{\varepsilon}_{ct}$, which is composed of the applied strain rate and strain rate caused by the advancing crack. A solution for $A^*(t)$ is then developed, a process which is described in detail in Reference [61].

An approximate solution for the steady state value of A^* can now be given:

$$A_s^* = \frac{\gamma\dot{\varepsilon}_{ct}}{k^* - \gamma\dot{\varepsilon}_{ct}} \quad (113)$$

Importantly, Hall assumes that cyclic film rupture is a driving mechanism of SCC, but rather than treating rupture and repassivation as separate events, it is assumed that the next rupture event begins while the previous rupture event is still ending. The current transients are not distinguishable in a practical sense.

This is consistent with observations that increased strain results in a saturation of current density. This saturation value increases as the applied strain increases. Saturation current density is given as:

$$i_{as} = A_s^* i_a^* = \frac{\gamma \dot{\epsilon}}{k^* + \gamma \dot{\epsilon}} i_a^* \quad (114)$$

Hall's model may be more detailed than is required for the predictive model in *Life Prediction of Used Fuel Canister Material*. However, since the SDR model is one of the major accepted theories of crack growth, this critique should be given careful attention if Ford and Andresen's theory (or any of the other SDR-based theories proposed by Nakayama and Takano, Shoji, and Saito) are used to build the crack propagation component of the predictive model for SCC in the canisters.

7.5.5 Macdonald, 1991: Crack growth rate and current at the crack tip

Macdonald and Urquidi-Macdonald considered IGSCC in sensitized Type 304 stainless steel pipes in an environment representative of a light water reactor (LWR) [23]. As is the case with the used fuel canisters, it was found that the HAZ of the pipe welds was the area most susceptible to SCC attack.⁵⁹

The Macdonald model is more descriptive of the SCC process than it is predictive of SCC damage. Furthermore, the aqueous environment of interest in the Macdonald model

⁵⁹Like the model proposed by Saito (see Section 7.5.7), this research involves a high-temperature water environment.

does not contain chlorides, the presence of which is assumed to be a requirement for SCC to be a possibility in the canister welds. However, the approach used to model SCC can still yield valuable insights.

The authors begin by considering experimental observations that pertain to SCC phenomena in Type 304 steel exposed to a high temperature water environment. The results obtained from a model of SCC in this environment must be consistent with these observations, which are as follows:

- There are threshold temperatures and potentials below which SCC is not observed to occur in the application.
- The impurity content of the solution affects the conductivity, which affects crack propagation.⁶⁰
- SCC occurs at more negative potentials when the aqueous environment is more acidic.
- Stress intensity affects the crack propagation rate.
- Dissolution at the sensitized grain boundaries is the primary cause of IGSCC.

The Macdonald model attempts to address deficiencies in other contemporary proposed models. In particular, this model includes an explicit formulation of current at the crack tip, and attempts to quantify the effects of the environment on SCC. The authors propose that this is important because of the coupled nature of the local crack environment (the occluded region) to the external bulk fluid: the latter is the primary determinant of the former.

The authors begin by stating their assumptions.

- Crack walls are parallel and inert.
- Film rupture/slip dissolution is the primary crack propagation mechanism.

⁶⁰This could be particularly important for the canister situation, in which salt films may exist, and which may contain other impurities from the atmosphere.

- Applied stresses may potentially affect crack propagation if they affect film rupture frequency.
- Cracks form in sensitized regions.
- Charge conservation applies. As the metal corrodes at the crack tip and releases oxygen, these electrons are consumed in reduction reactions on the external surface.
- The external environment is pure water.⁶¹
- Butler-Volmer equations describe charge transfer kinetics at the crack tips.

First, the electrodisolution reactions expected at the crack tip are stated. In stainless steel, one expects to observe the oxidation of iron, chromium, and nickel.

Second, equations for species fluxes are established. These are given in terms of species concentrations, species mobility, solution electrostatic potential, distance, number of electrons involved in the species reaction, and the current density at the crack tip. This current flow produces the electrons that are consumed in reduction reactions outside the crack. In total, there are seven equations: one each for Na^+ , Cl^- , H^+ , iron oxide, chromium hydroxide, nickel hydroxide, and hydroxide. These equations have the general form shown in Equation (115):

$$N_i = -D_i \frac{\partial C_i}{\partial x} - f(n_i) u_i \mathbf{F} C_i \frac{d\phi}{dx} = f(n, a) \left(\frac{i_e}{\mathbf{F}} \right) \quad (115)$$

Variable definitions for Equation (115) are given in Table 30.

Prior to solving Equation (115) to determine the values of C_i , several assumptions are made. It is assumed that dissolution behavior is stoichiometric, and that Laplace's equation and its solution ($\nabla^2 \phi = 0$) hold as a reasonable approximation for the potential inside the crack. Because there is a net flux out of the crack, the use of Laplace's equation

⁶¹This assumption would not apply for the canister model, which assumes the aqueous environment is a deliquesced salt film on the canister surface.

Table 30: Variable definitions for Equation (115)

| Variable | Definition |
|--------------|---------------------------------|
| N_i | Species i flux |
| D_i | Diffusion constant for i |
| C_i | Concentration |
| u_i | Mobility |
| ϕ | Electrostatic potential |
| \mathbf{F} | Faraday's constant |
| x | Distance |
| n | Number of electrons involved |
| i_e | Current density |
| a_i | f (atom fraction of elements) |

is not strictly accurate. If the crack is growing slowly, however, it is reasonable to assume that net flux is zero for the purposes of calculation.

Equation (115) is then solved for each of the seven species: for each concentration C_i , the ratio C_i/C_i^b is determined, where C_i^b is the concentration of species i in the external environment (the bulk). By imposing charge conservation on the system, the developed model quantitatively couples the internal (in-crack) and external (bulk) environments.

Next, a method for calculating the current at the crack tip is described. The authors begin by considering the area of metal surface that is bare, A_t at a time t after film rupture occurs. Experimental evidence indicates that A_t is given as:

$$A_t = A_t^0 \left(\frac{t}{t_0} \right)^n \quad (116)$$

where A_t^0 and t_0 is the reference time and the amount of bare metal surface area at that time. An expression for the average value of A_t by assuming that n , which has a value between 0.33 and 1, has a value of 0.5:

Table 31: Variable definitions for Equations (116) - (119)

| Variable | Definition |
|-------------|---|
| A_t | Exposed area following film fracture |
| A_t^0 | Exposed area at reference time t_0 |
| n | Parameter between 0.33 and 1 |
| i_0^0 | Standard exchange current density |
| t_f | Length of fracture-repassivation period |
| ϕ_s^L | Solution-side potential at crack tip |
| ϕ_s^0 | Standard potential for the crack tip dissolution reaction |
| L | Crack length |
| t | Time |
| \bar{M} | Composition weighted atomic weight of alloy |
| \bar{I}_0 | Average current at crack tip |
| ρ_m | Alloy density |
| F | Faraday's constant |
| W | Length of crack opening on surface |
| δ | Half-width of crack opening |
| b_a | Anodic Tafel constant |

$$\bar{A}_t = 2A_t^0 \left(\frac{t_f}{t_0} \right)^{-0.5} \quad (117)$$

Next, the authors assume that when dissolution occurs following fracture, the resulting current obeys Tafel behavior. The average dissolution current occurs when $A_t = \bar{A}_t$, and:

$$\bar{I}_0 = 2 i_0^0 A_t^0 \left(\frac{t_f}{t_0} \right)^{-0.5} e^{\frac{-\phi_s^L - \phi_s^0}{b_a}} \quad (118)$$

Crack growth rate can be calculated using the crack tip current as:

$$\frac{dL}{dt} = \frac{\bar{M}\bar{I}_0}{2\rho_m \bar{z} \bar{F} W \delta} \quad (119)$$

Variables are defined in Table 31. Parameters for the Macdonald model were determined from pre-existing data in the literature.

This model also follows the SDR approach to crack propagation, and its assumptions and methods should be reexamined if an SDR approach is selected for the crack propagation component of the predictive model for *Life Prediction of Used Fuel Canister Materials*.

7.5.6 Shoji, 1995: Crack tip strain and crack growth rate

Shoji, Suzuki, and Ballinger developed a model for SCC crack growth rate that depends on stress intensity K . Notably, this model accounts for the redistribution of strain at the crack tip as the crack grows [21]. SCC is assumed to proceed via the standard dissolution mechanism (film rupture, accelerated dissolution, repassivation) when a certain threshold stress intensity is present. Note that t_f here is the period of a rupture-dissolution-repassivation cycle.

The authors use Faraday's law to establish the dissolution rate of the bare metal, and set this equal to the crack growth rate:

$$\frac{da}{dt} = \frac{M Q_f}{\rho z \mathbf{F} t_f} \quad (120)$$

Q_f , the dissolution charge density, is equivalent to the time integral of the current $i(t)$ that is measured when the film ruptures and dissolution occurs. The current takes this form:

$$i(t) = i_0(t/t_0)^m \quad (121)$$

Shoji et al. also give an approximation of t_f : $t_f = \varepsilon_f/\varepsilon_{ct}$, the ratio of film fracture strain to crack tip strain. From these expressions, one can find the form of Equation (120) cited by Wu [27]:

$$\frac{da}{dt} = \frac{M}{z\rho\mathbf{F}} \cdot \frac{i_0(t_0)^m}{(1-m)(\varepsilon_f)^m} \cdot (\varepsilon_{ct})^m \quad (122)$$

Next, an expression for plastic strain at the crack tip was considered. The authors used expressions developed by Gao et al. that could be applied to a progressing crack in an “elastic plastic strain hardening material.”⁶² They are as follows:

$$\varepsilon_p = \beta(\sigma_y/E) \left[\ln \frac{R_p}{r} \right]^{1/1-n} \quad (123)$$

and:

$$\frac{d\varepsilon_{ct}}{dt} = \underbrace{\frac{d\varepsilon_{ct}}{da}}_{\text{}} \frac{da}{dt} \quad (124)$$

$$\frac{d\varepsilon_{ct}}{dt} = \left(\frac{\partial \varepsilon_{ct}}{\partial a} - \frac{\partial \varepsilon_{ct}}{\partial r} \right) \frac{da}{dt} \quad (125)$$

⁶²See: Y. C. Gao and K. C. Hwang, “Elastic-Plastic Fields in Steady Crack Growth in a Strain Hardening Material”, *Advances in Fracture Research* (ed. D. Francois), 5th International Conference on Fracture, Cannes, France, 2, 1981.

which yields:

$$\dot{\epsilon}_{ct} = \frac{\beta\sigma_y n}{E(n-1)} \cdot \left(2\frac{\dot{K}_I}{K_I} + \frac{\dot{a}}{r} \right) \left\{ \ln \left[\frac{\lambda}{r} \left(\frac{K_I}{\sigma_y} \right)^2 \right] \right\}^{1/(n-1)} \quad (126)$$

Substituting this result into Equation (122) yields:

$$\frac{da}{dt} = \frac{Mi_o}{z\rho F(1-m)} \left(\frac{t_0}{e_f} \right)^m \left[\frac{\beta\sigma_y n}{E(n-1)} \cdot \left(2\frac{\dot{K}_I}{K_I} + \frac{\dot{a}}{r_0} \right) \left\{ \ln \left[\frac{\lambda}{r_0} \left(\frac{K_I}{\sigma_y} \right)^2 \right] \right\}^{1/(n-1)} \right]^m \quad (127)$$

Table 32 contains variable definitions for all equations. Shoji remarks on the difficulty of comparing this model to experimental data, due to the number of parameters involved and the uncertainty associated with many of their definitions. It is also noted that the expression for crack growth rate yields plateau behavior at high K values. This indicates that crack growth rate is independent of K when K is high.

This model for crack growth could be useful because it expands even further upon Ford and Andresen's SDR model. However, it would be necessary to show that all the parameters in this model could be accurately estimated in order to avoid introducing too much uncertainty into the prediction. However, if this model was compared with experiments using canister weld material and deliquesced salt solutions and found to be accurate, and if the parameters could be accurately measured (or estimated for the canister of interest), this model's detail could actually provide an avenue for decreasing uncertainty in the crack growth stage of the model. Wu (Section 7.7.3) selected this model by Shoji et al. when he developed a predictive model for SCC in Alloy 600.

Table 32: Variable definitions for the Shoji model

| Variable | Definition |
|-----------------|--|
| a | Crack length |
| M | Atomic weight of metal |
| z | Number of electrons involved in the reaction |
| ρ | Mass density of the metal |
| \mathbf{F} | Faraday's constant |
| Q_f | Dissolution charge density |
| t_f | Time of film rupture period |
| i_0 | Current density on surface |
| m | Slope of current density curve associated with the dissolution stage |
| t_0 | Time when repassivation begins |
| ϵ_f | Film rupture strain |
| ϵ_{ct} | Crack tip strain rate |
| ϵ_f | Fracture strain of the film |
| ϵ_P | Plastic strain distribution |
| E | Young's modulus |
| σ_y | Yield stress |
| K_I | Stress intensity factor |
| \dot{K} | Change rate of K (due to load change) |
| r_0 | Distance ahead of crack tip |
| n | Strain hardening coefficient |
| β | Constant |
| λ | Constant |

7.5.7 Saito and Kuniya, 2001: Predicting SCC in Type 304 stainless steel exposed to high-temperature water

Saito and Kuniya at the Hitachi Research Laboratory in Japan developed a mechanochemical model (referred to here as the Saito model) to describe stress corrosion cracking in Type 304 stainless steel exposed to 288°C water [24]. They consider two major processes:

- The kinetics of plastic deformation in the stainless steel
- Slip dissolution and repassivation at the crack tip

and their predictive equation is a function of stress intensity factor, sensitization, strain hardening, and water chemistry. The equations presented in this section are derived in detail in their paper.

In the Saito model, SCC is driven by strain at the crack tip and the associated passivation/repassivation process. In order to characterize plastic deformation, the crack tip strain rate in this model is formulated as follows:

$$\dot{\epsilon}_{ct} = 2\rho_d b \cos\theta \underbrace{\frac{dbl\nu_D}{l_c^2} \exp\left(-\frac{2E_k^0 - bl_o d_o \beta (K - K_{ISCC})^{\frac{2}{(n'+1)}}}{k_B T}\right)}_{\dot{X}} \quad (128)$$

Variable definitions are given in Table (33).

As the crack advances through the material, dislocations are “injected” into the bulk along specific slip planes (45° to the tensile axis). Dislocation movement, described by a dislocation velocity \dot{X} , causes plastic shear deformation, and gives rise an observed strain rate at the crack tip, as described in Equation 128 above.

Next, slip dissolution processes are considered. As a crack advances, slip steps are formed at the crack tip. The formation of these slip steps exposes unpassivated metal. The newly exposed metal passivates when the crack tip conditions still support the passive

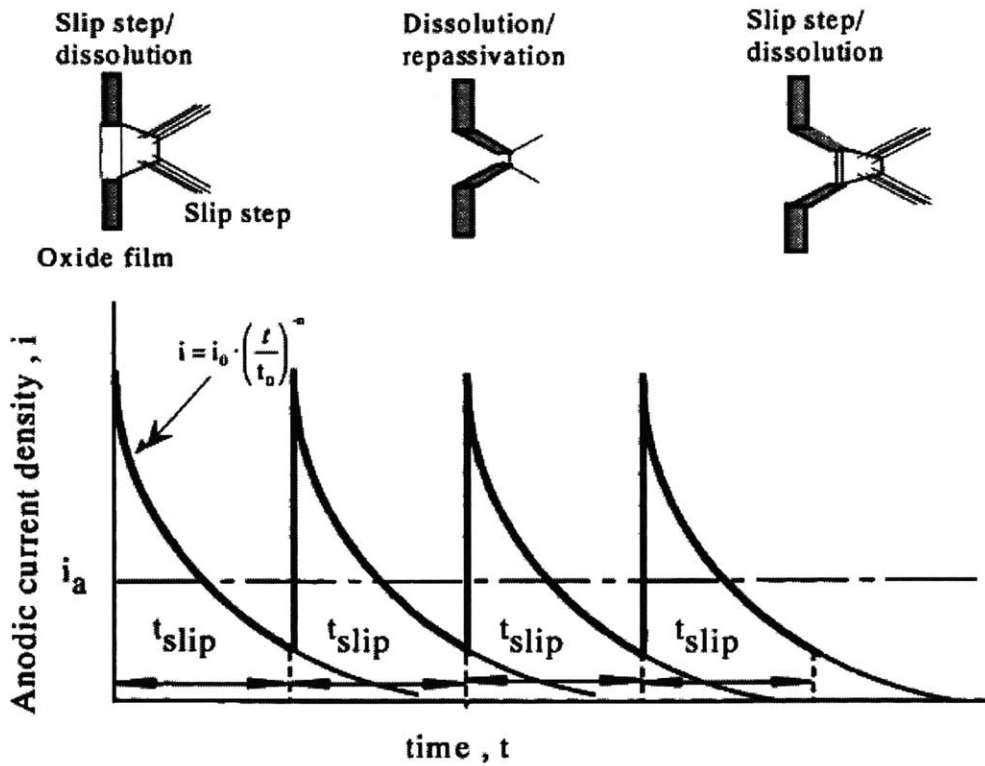


Figure 49: Above, an illustration of the slip-dissolution-repassivation mechanism by which SCC is assumed to proceed in the Saito model. Below, a general representation of the behavior observed during the slip-dissolution-repassivation process. The anodic current density jumps when film rupture occurs, and decays following power-law behavior as the newly exposed metal repassivates, impeding continued dissolution. The process then repeats itself. [24]

Table 33: Variable definitions for Equation (128)

| Variable | Definition |
|------------------|------------------------------|
| $\dot{\epsilon}$ | Crack tip strain rate |
| \dot{X} | Dislocation velocity |
| ρ_d | Dislocation density |
| b | Burgers vector |
| d | Distance dislocation travels |
| d_0 | Diameter of an obstacle |
| l | Free length of dislocation |
| ν_d | Debye frequency |
| l_c | Critical length |
| E_k^0 | Free energy of kink |
| l_o | Obstacle spacing |
| k_B | Boltzmann constant |
| T | Temperature |

state. The slip steps then begin to passivate, causing the corrosion current density to drop. This anodic current density decreases according to a power-law decay pattern as the passivating oxide layer grows and impedes metal dissolution. The current density then jumps sharply when the next slip step forms, rupturing the passive film and exposing fresh metal once again. This process is represented graphically in Figure 49. The average observed current density at the crack tip is given as:

$$i_A = \frac{i_0 t_0^n}{(1-n)} \left(\frac{\dot{X}}{N_{\text{slip}} n_d b} \right)^n \quad (129)$$

n can be approximated as:

$$n \cong -\frac{1}{3} \ln \left(\frac{i}{i_0} \right) \quad (130)$$

where i is the anodic current density. A more exact expression for n is given below In Equation (133).

Table 34: Variable definitions for Equation (129)

| Variable | Definition |
|-------------------|---|
| i_a | Average anodic current density |
| i_0 | Initial dissolution current density at bare surface |
| t_0 | Short time constant |
| n | Numerical constant in current power law relation |
| \dot{X} | Dislocation velocity |
| N_{slip} | Number of active slip bands |
| n_d | Number of dislocations that form a slipband |
| b | Burgers vector |

First, it was necessary to model the effects of slip dissolution. The anodic current density is expressed in terms of the bulk corrosion potential as follows:

$$i \cong F_{\text{EPR}} F_{\kappa} i_{(0)} \left(\frac{zF\eta_t}{RT} \right) e^{\frac{\alpha z F \eta_t}{RT}} \quad (131)$$

By expressing $\frac{zF\eta_t}{RT}$ as a linear function of ϕ_C , i can be expressed as

$$i = F_{\text{EPR}} F_{\kappa} i_{(0)} \underbrace{(C_4 \Phi_C + C_5)}_{zF\eta_t/(RT)} e^{\alpha(C_4 \Phi_C + C_5)} \quad (132)$$

The average current density from anodic dissolution, given in Equation (129), requires a value for the parameter n . A more exact expression is formulated using numerical constants by substituting Equation (132) into Equation (130).

$$n = -\frac{1}{3} \left[\underbrace{\ln(1 + C_1 \text{EPR})}_{\cong F_{\text{EPR}}} \underbrace{(C_2 \kappa + C_3)}_{F_{\kappa}} (C_4 \Phi_C + C_5) + C_6 \Phi_C + C_7 \right] \quad (133)$$

Note that F_{κ} , the influential factor of the water conductivity, is assumed by Saito to be a linear function of conductivity, and F_{EPR} , the influential factor for the degree

of sensitization, is assumed to be a linear function of the electrochemical potentiokinetic reactivation (EPR) measurement. Variable definitions are listed in Table 35.

Table 35: Variable definitions for Equations (132) and (133)

| Variable | Definition |
|------------|---|
| C_x | Numerical constants |
| EPR | Electrochemical potentiokinetic reactivation, which is used to measure the extent of sensitization |
| F_{EPR} | Influential factor of degree of sensitization, expressed as $1 + C_1 \cdot EPR$. If i_{total} represents the total anodic current density in a material with sensitized grain boundaries and an unsensitized bulk matrix such that $i_{sensitized} + i_{matrix} = i_{total}$, then $i_{total} = F_{EPR} \cdot i_{matrix}$. |
| κ | Water conductivity |
| F_κ | Influential factor of water conductivity, expressed as $C_2\kappa + C_3$ |
| $i_{(0)}$ | Exchange current density at surface-solution interface |
| Φ_C | Bulk corrosion potential |
| α | Charge transfer coefficient |

These equations account for sensitization of the Type 304 steel at the grain boundaries. Anodic current density is considered to be the weighted sum of current density from sensitized and unsensitized parts of the matrix. These equations express the anodic current density, which is a measure of metal dissolution, in terms of the corrosion potential and conductivity of the environment. This allows the prediction of the anodic current density in terms of measurable and/or predictable parameters. As an environment or material changes, the likelihood of observing SCC changes. It is important to understand how relevant quantities like anodic current, a metric for the extent of corrosion, change with environmental characteristics including conductivity or corrosion potential.

These considerations of the slip formation/dissolution mechanism allow i_a to be related to the crack growth rate $\frac{da}{dt}$ as:

$$\frac{da}{dt} = \frac{M}{z\mathbf{F}\rho_m} i_a \quad (134)$$

where M is atomic weight of the steel sample, F is Faraday's constant, ρ_m is the steel's density, z is equivalent charge, and i_a is the average current density described by Equation (129). Appropriate substitutions yield:

$$\frac{da}{dt} = \frac{M}{z\mathbf{F}\rho_m} = \frac{i_0 t_0^n}{(1-n)} \left(\frac{\dot{X}}{N_{\text{slip}} n_d b} \right)^n \quad (135)$$

$$\frac{da}{dt} = \frac{M}{z\mathbf{F}\rho_m} = \frac{i_0 t_0^n}{(1-n)} \left(\frac{\dot{\varepsilon}_{\text{ct}}}{2\rho_d \cos(\theta) N_{\text{slip}} n_d b^2} \right)^n \quad (136)$$

$$\frac{da}{dt} = \frac{M}{z\mathbf{F}\rho_m} \frac{i_0 t_0^n}{(1-n)} \left[\frac{d\nu_D}{N_{\text{slip}} n_d l_c^2} \exp \left(-\frac{2E_k^0 - b l_o d_o \beta (K - K_{\text{ISCC}})^{\frac{2}{n+1}}}{k_B T} \right) \right]^n \quad (137)$$

Next, the mechanics of crack growth are modeled. In fracture mechanics, crack growth with time is described as a power law dependent on $\dot{\varepsilon}$, which is the strain rate at the crack tip. In this model, Equation (136) is simplified as follows:

$$\frac{da}{dt} = \underbrace{\frac{M}{z\mathbf{F}\rho_m} \frac{i_0 t_0^n}{(1-n)}}_{A_0} \underbrace{\left(\frac{\dot{\varepsilon}_{\text{ct}}}{C_m} \right)^n}_{C_m = 2\rho_d \cos(\theta) N_{\text{slip}} n_d b^2} \quad (138)$$

It yields the following general expression for crack growth rate:

$$\frac{da}{dt} = A(n) (\dot{\varepsilon}_{\text{ct}})^n \quad (139)$$

A_0 and C_m are referred to as the rate coefficient and material factor constant, respectively. n is a constant for a given environment/material pair, and it accounts for sensitization, water conductivity, and corrosion potential, as given in Equation (133). Note that this formulation is the same as that developed by Ford and Andresen (see Section 7.5.1).

These constants can be determined for a specific material-environment combination. For example, in steel, A_0 can be expressed as $A(n)\epsilon_f^n$, where ϵ_f is the fracture strain of the typical oxide film. A_0 is found to be a constant. C_m can be calculated in a straightforward manner using the appropriate material constants (see Table 34 and Equation (138)).

Crack tip strain rate can be calculated from Equation (128) using the appropriate constants for the material and environment. In its general form, $\dot{\epsilon}_{ct}$ may be expressed as a function of K , since all other parameters are assumed to be constant.

The constant values for A_0 , C_m , and the expression for $\dot{\epsilon}_{ct}$ can then be substituted into (138), and this yields an expression for $\frac{da}{dt}$ in terms of K .

Finally, the authors developed an expression for n in terms of the parameters of interest. It was desired to find that calculate n as a function of

- sensitization at grain boundaries
- corrosion potential at crack mouth
- conductivity of the bulk fluid environment

In order to do this, crack experiments must be carried out and the following values recorded:

- crack growth rate
- stress intensity factor K
- EPR (sensitization)
- bulk water conductivity κ
- corrosion potential ϕ_C

Next, K is used to calculate $\dot{\epsilon}_{ct}$. n can then be calculated:

$$n = \frac{\log \left[\left(\frac{da}{dt} \right)_{\text{data}} / A_0 \right]}{\log \left[(\dot{\epsilon}_{ct})_{\text{cal}} / C_m \right]} \quad (140)$$

with C_m and A_0 determined from the properties of the given system. In the material/environment system considered by the authors, $\frac{da}{dt}_{\text{data}}$ is obtained via experiment and $\dot{\epsilon}_{ct}$ is calculated from the equations given in the footnote.⁶³

Equation (140) is then used in conjunction with Equation (133) to determine the values of the numerical constants C_1 through C_7 via multivariate analysis.⁶⁴ The result is a formula for n in terms of EPR, ϕ_C , and κ .

Saito notes that higher n values correspond to slower crack growth rates. Increasing conductivity, ϕ_C , and EPR decreases the value of n , and correspond to higher crack growth rates.

Saito and his colleagues compared the crack growth rate predictions of the model against experimental crack growth data. To do this, they used the da/dt equations proposed by their model to plot crack growth rate versus stress intensity factor. Two sets of environmental parameters were chosen: a “best case” scenario (high corrosion potential and high water conductivity) and a “worst case” scenario (low, negative corrosion potential and a low water conductivity). Experimental data was shown to lie between these curves.⁶⁵ These results are shown in Figure 50. Similar validation procedures are used to show the

⁶³Saito and Kuniya use the following equation to determine $(\dot{\epsilon}_{ct})_{\text{calc}}$, for Type 304 stainless steel in 288°C water.

$$\dot{\epsilon}_{ct} = 1.1 \times 10^7 \exp \left(-\frac{3 \times 10^{-19} - 1.5 \times 10^{-20} (K-9)^{1/3}}{7.75 \times 10^{-21}} \right)$$

⁶⁴The details of this analysis are not provided in [24].

⁶⁵This experimental data was obtained from the following two sources.

- F. P. Ford et al., EPRI NP-5064M, 1987, [137].
- L. G. Ljungberg, D. Cubicciotti, and M. Trolle. *Proceedings of the Fourth International Symposium on Environmental Degradation of Materials in Nuclear Power Systems - Water Reactors*, 1989, [131].

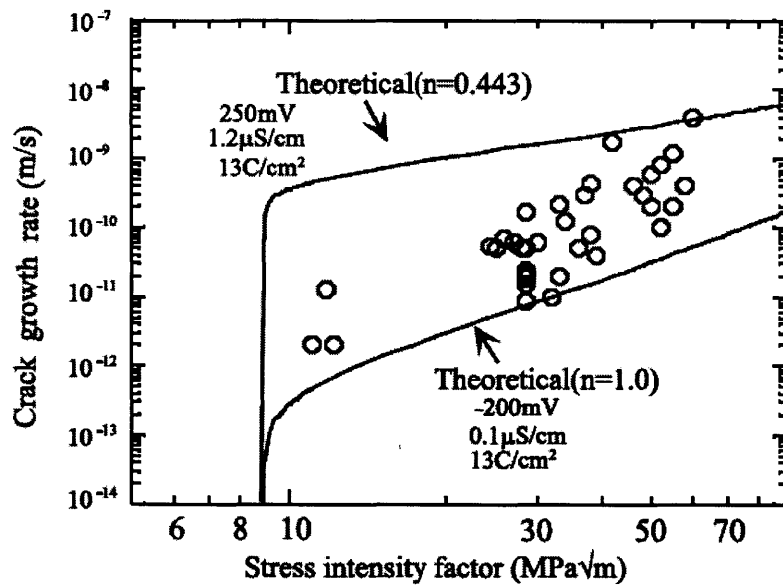


Figure 50: The Saito equations are used to plot $\frac{da}{dt}$ versus K for two sets of environmental parameters. Experimental data is shown to agree with the predicted trends. [24]

effect of ϕ_C , water conductivity, and EPR (grain boundary sensitization) on da/dt [24].

This version of modeling crack growth as a result of the SDR process is useful if it is found that including the effects of plastic deformation at the crack tip provides better accuracy. However, this model is more complex, with many parameters to determine. Since the purpose of the model in *Life Prediction of Used Fuel Canister Material* is predictive and not explanatory, the goals of the model may be attainable without introducing such explicit dependence on this many parameters. However, Saito's expression for $\frac{da}{dt}$ is effectively the same as the one originally proposed by Ford and Andresen. Saito, and the other authors who build on an SDR model of crack growth, provides a particular way of calculating strain rate at the crack tip that may prove to be useful, especially since he developed the model explicitly for Type 304 stainless steel.

7.5.8 Ihara et al., 2013: A probabilistic approach to understanding SCC crack initiation in Type 316L Steel

Ihara, Mochizuki, and Fujimoto studied the initiation of SCC in Type 316L stainless steel exposed to a boiling water reactor (BWR) environment [28]. The goal of this paper was to relate the “microcrack” stage, at which SCC begins as a transgranular SCC (TGSCC) phenomenon, to the onset of macroscopic cracking, which proceeds as intergranular SCC (IGSCC). The macroscopic stage is assumed to begin when cracks reach a depth of 1 mm. The authors assume that the “microcrack” stage plays an important role in macroscopic SCC behavior and the lifetime of the affected component.

Microcracks were induced in Type 316L samples using slow strain rate testing (SSRT) and a simulated BWR environment. The distribution of resulting crack depths was then considered. Three specimens were studied, each with a different crosshead displacement: $d=1.0$ mm, 1.5 mm, and 2.0 mm.

Experimental results are shown in Figure 51. The authors suggest that the decrease in the number of observed cracks at higher values of d indicate that microcracks have coalesced into larger cracks. The crack length probability density function was found to be consistent with a lognormal distribution, and is given as:

$$f(x) = \frac{1}{\sqrt{2\pi s^2 x}} \exp \left\{ -\frac{(\ln x - \mu)^2}{2s^2} \right\} \quad (141)$$

where x is crack length, μ is the mean crack length, and s is the standard deviation of the crack length distribution.

The average E and mode M are:

$$E = \exp \left(\mu + \frac{s^2}{2} \right) \quad (142)$$

$$M = \exp(\mu - s^2) \quad (143)$$

Crack depths were estimated by assuming a crack aspect ratio of 0.6, and calculating depth from the following relationship:

$$\text{aspect ratio} = \text{crack depth} / \text{crack length}$$

E and M can be modeled as functions of time t , where V_0 and q are materials constants and σ is the applied stress:

$$E = V_0^E e^{(q^E \sigma)t} \quad (144)$$

$$M = V_0^M e^{(q^M \sigma)t} \quad (145)$$

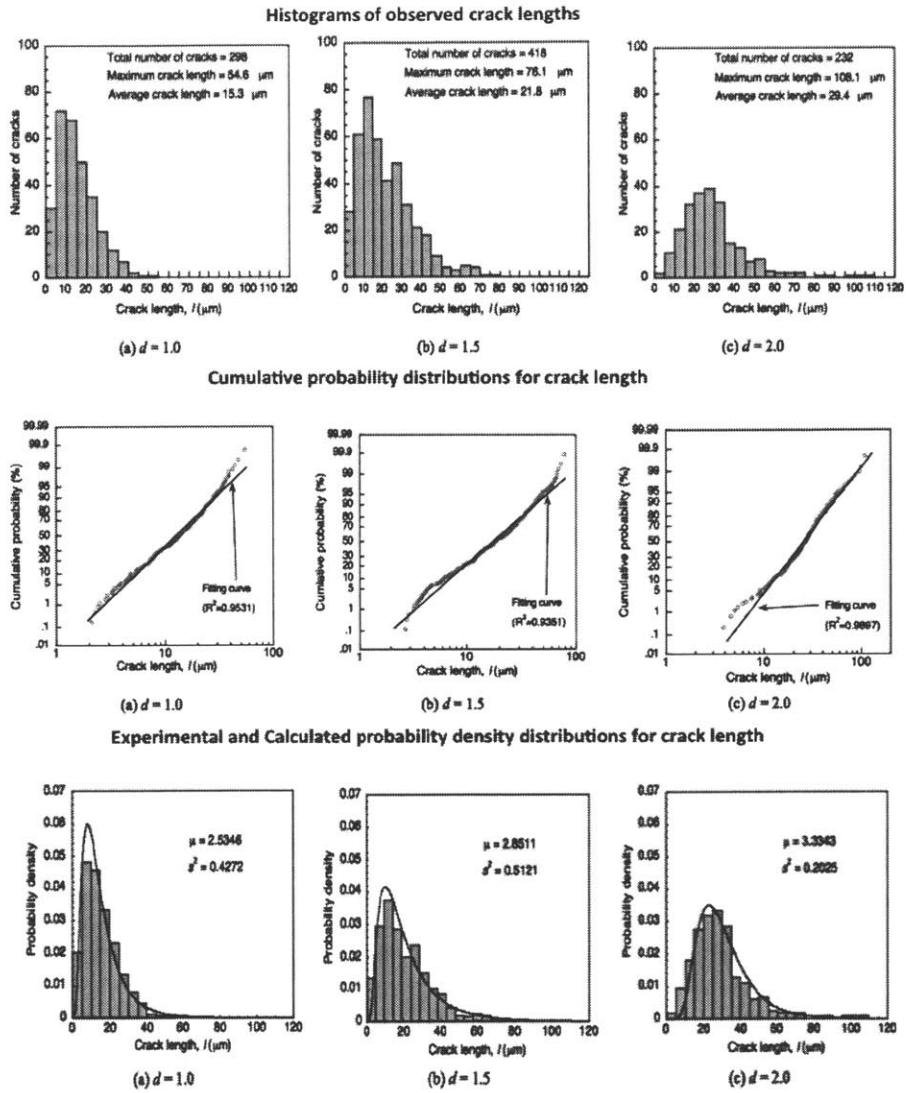


Figure 51: The experimental results of Ihara et al. are shown. For each of three SSRT specimens, with d corresponding to crosshead displacement, the distribution of observed crack lengths are plotted. [28]

Based on the assumption that SCC is assumed to have initiated when the microcracks reach a depth of 1 mm, the time to SCC initiation is calculated as a function of stress applied to or in the material. This result is shown graphically in Figure 52.

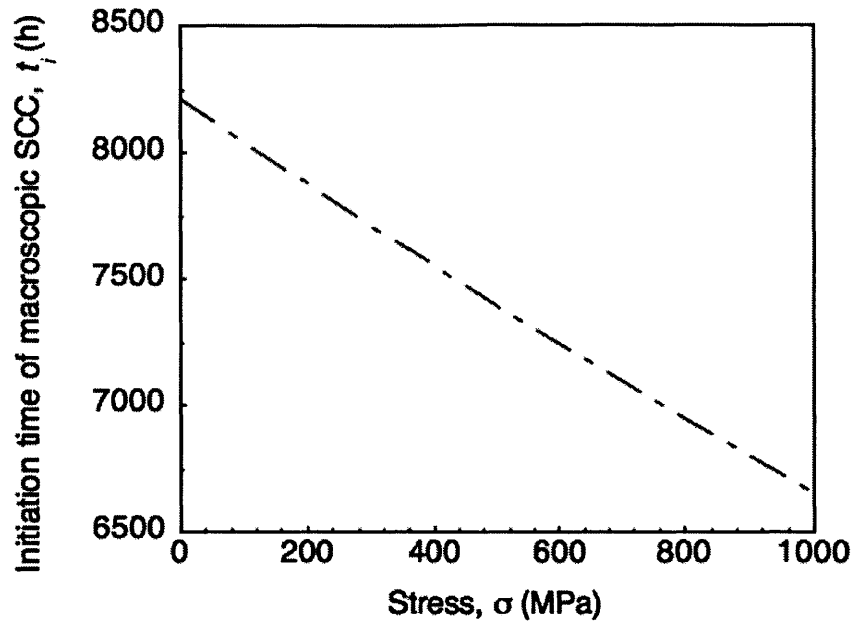


Figure 52: Time to initiation of SCC as a function of stress, as plotted in Ihara. It is assumed that microcracks “initiate” SCC when a depth of 1 mm has been reached. [28]

If an initial microcracking stage is found to play a definitive role in SCC crack development in the canister welds, Ihara’s work shows one way to develop a bridge between the microcracking stage and the initiation of macroscopic SCC cracks. However, the micro- to macro-crack transition criteria (SCC initiates when microcracks reach a depth of 1 mm) may need further refinement or experimental validation.

7.6 Pitting to Cracking: Complete SCC Models

The following two models, by Engelhardt and Turnbull, present “complete” models of SCC in steel. These models take a probabilistic approach to modeling SCC, and they account for pit growth, crack initiation, and crack growth.

Models such as these can be used to write probabilistic simulations that predict the evolution of corrosion damage on a surface. This quality is shared by the models discussed in Section 7.4, although the scope of those models is narrower than those presented here.

7.6.1 Engelhardt, 2004: A probabilistic, damage function analysis approach to modeling SCC

Engelhardt developed a model for predicting SCC damage in carbon steel and Type 316 turbine blades exposed to a chloride-containing aqueous environment [30]. He begins by noting that the prediction of SCC in industrial turbines is usually done in-situ. Pitting and crack damage is observed during turbine outages, and the amount of additional damage expected to be incurred by the next outage is extrapolated. This approach, he says, is not accurate and frequently underpredicts the amount of damage, and it is therefore not recommended for use in predicting degradation when a high degree of confidence in the quantitative results is required.⁶⁶

The author even makes an analogy between corrosion damage and the inherently probabilistic nature of quantum mechanics:

“Accordingly, the task of deterministically describing corrosion damage un-

⁶⁶It was noted by Turnbull (Section 7.6.2) that his modeling efforts were carried out more or less concurrently with those of Engelhardt. The resulting Engelhardt model is similar to that described in the Turnbull papers, but Engelhardt assumes a constant crack growth rate that does not depend on crack depth. In the Turnbull model, the crack growth rate is not prescribed, but its most probable value is indicated by a calculated distribution of crack growth rates. The growth rate for any one crack is dependent on crack depth [30], [31].

der real conditions does not reduce to the prediction of the maximum depth, $L_{\max}(t)$, but to the prediction of the probability, $P(L, t)$, that the depth of the largest corrosion events has a value between L and $L + dL$ for given observation time, t , or prediction of the probability of failure, $P_f(L, t)$, i.e. the probability that the depth of the largest corrosion events is greater than the critical dimension L for given time, t . Thus, we can see a crude analogy with the “deterministic” description of the position of a quantum particle, when only the probability of [a] particle having coordinates between x and $x + dx$ (but not the exact value of x) can be predicted.”⁶⁷

Engelhardt notes the importance of surface chemistry to predicting corrosion damage. There is a thin liquid film on the surface of the turbine blades in certain pressure and temperature regimes, and the aggressiveness of this film’s chemistry (e.g. chloride ion concentration) is correlated to the likelihood of damage. This study also notes the importance of film formation and passivity breakdown on predicting pit growth and subsequent SCC.⁶⁸

Engelhardt considers a higher degree of complexity in the role of pitting. Instead of beginning with an assumed collection of pits that grow according to appropriately distributed rates, the initiation of metastable pits on an undamaged surface is considered. Next, the evolution of these metastable pits into stable pits or inactive, repassivated pits is modeled, followed by the growth of these stable pits. These pits may eventually become

⁶⁷Reference [30], 4.

⁶⁸Modeling the formation of an aqueous film, and its subsequent effects on passivity and corrosion, is an important aspect of the *Life Prediction of Canister Material* project. The film assumed to be present on the turbine blades in the Engelhardt model is particularly damaging because it can contain chloride ions, which are the primary cause of our concern with the deliquescence of salt films on the welds.

Engelhardt notes that corrosion experiments are often set up under the assumption that films on the surface of the metal in question contain particularly high concentrations of the aggressive chemical of interest. This assumption is not always true, and there is not always an easily extrapolated relationship between highly concentrated film and a dilute one. (Frequently concentrations are increased so that corrosion is observed on a more convenient timescale.) Obviously, there is an important environmental difference between a stationary weld exposed to the outside atmosphere and a rapidly moving turbine blade, but the use of any highly concentrated films used in the experiments must be validated.

crack initiation sites.

Importantly, Engelhardt asserts that it is not possible to assume a distribution of crack growth rates that will be valid for all pits of a certain depth. Pit morphology and local material and environmental conditions affect crack growth rate, and are expected to vary across a material.⁶⁹

He uses an approach called Damage Function Analysis (DFA) to study cracking damage in the turbine blades of interest. The number of pits having depths between x_1 and x_2 during a time t is given by $\Delta N_k(x_1, x_2, t)$, which Engelhardt further expresses as:

$$\Delta N_k(x_1, x_2, t) = F_k(x_1, t) - F_k(x_2, t) \quad (146)$$

where the number of corrosion events is expressed in terms of the integral damage function (IDF) F_k . The differential with respect to depth x of F_k gives $f_k(x, t)$, known as the differential damage function. The subscript k defines the type of defect, such that the model can account for different types of defect. Engelhardt views f_k as a concentration of defect “particles” (units in number per cm^3) and j_k as the flux density of these defect particles, such that:

$$\frac{\partial f_k}{\partial t} + \frac{\partial j_k}{\partial x} = R_k \quad (147)$$

with R_k the defect source (or sink). At $x = 0$ (the surface of the material), $j_k = n_k(t)$, which is the nucleation rate of some defect of type k .

Pit nucleation can be described as:

⁶⁹If a distribution is assigned, uniform local conditions should be assumed. If the properties of the film, environment, and material vary across the surface of interest, the distinction between a global view of the pits and individual pits is important. If the assumption of uniform properties are made to model a pit, but the likelihood that a selected, single pit will initiate a crack is the desired quantity of interest, a more local view may be required.

$$N(t) = N_0 \left[1 - e^{-t/t_0} \right] \quad (148)$$

if N_0 is the total number of pits that could feasibly exist in a square centimeter of the metal surface. This equation is also based on the assumption that pit nucleation simply equals dN/dt , which requires knowledge of $N(t)$, the number of stable pits on the metal surface as a function of time, and also of t_0 , which is a sort of threshold time-to-possible-initiation.⁷⁰ A second expression for pit nucleation is presented, but pertains to situations that do not have a time threshold that must be considered in the overall prediction.

Engelhardt presents several options for treating pit growth, using v throughout for pit propagation rate. One can express the flux density of the defect particles (with a corresponding to “active pits”) as:

$$j_a(x, t) = f_a(x, t)v(x) \quad (149)$$

if it can be assumed that v is dependent only on pit depth x .

One can also proceed by assuming that pit size L is proportional to some kt^m , with k and m empirical constants: this is consistent with pitting experiments, and is similar to expressions used elsewhere (such as in Turnbull [31]). However, m is typically less than 1, and this means that its limit (the limit being, of course, $dL/dt = v$) is nonphysical for small times. Engelhardt suggests using:

$$v = \frac{dL}{dt} = v_0(1 + t/t_0)^{m-1} \quad (150)$$

⁷⁰This t_0 concept is of importance to this project, as the time that the canister welds have been exposed to the environment is a very important parameter in determining their susceptibility to SCC. For example, it takes a certain amount of time following the placement of the canister on the concrete pad for the surface temperature to drop below the required temperature to even sustain an aqueous film: presumably, if this time is t_0 , then an observation period from $t = 0$ to $t_1 < t_0$ will result in zero initiated pits.

instead of $L = kt^m$.

Depending on the situation, it may also be appropriate to assume that v is constant, and can thus be expressed as v_0 at all times. Or, it may be best to express v as:

$$v = \frac{dL}{dt} = v_0 \zeta(x) \quad (151)$$

where $\zeta(x)$ is used to ensure that the appropriate boundary conditions hold at the surface ($x = 0$).⁷¹

In the Engelhardt view, the total propagation rate V is the sum of electrochemical and mechanical processes that lead to increased corrosion and crack propagation. The mechanical contribution to crack propagation can be expressed as:

$$V_{\text{mec}} = C(\Delta K)^n \quad (152)$$

with C and n alloy specific parameters and ΔK the expected range of stress intensity.⁷²

In adapting these equations to a real situation, Engelhardt acknowledges that there will likely be a distribution in pit growth rates. As mentioned previously, in real applications, conditions across a component are rarely uniform. It is assumed that the distribution in propagation rates is not time dependent. Pits in the Engelhardt model, propagating at an initial rate v_0 , are represented by the following equation:

$$n(t) = \int_0^\infty \lambda(t, v_0) dv_0 \quad (153)$$

⁷¹Engelhardt's paper includes a particular expression for $\zeta(x)$ that can be used when Equation 150 holds, in addition to an explicit formulation for the parameter m . These details are omitted here, but should this form of a model be followed, this detailed information can be found in Reference [30].

⁷²There are also explicit relationships for V_{mec} in terms of temperature and yield strength, although these are specific to disc materials. Engelhardt refers to the relationships explained in T. H. McCloskey et al., "Turbine Steam Path Damage: Theory and Practice, Vols 1 and 2," EPRI, Palo Alto, CA, 1999, [134].

where $n(t) = dN(t)/dt$, or the rate at which pits nucleate. ($N(t)$ was given as the number of stable pits that nucleate per cm^2 between 0 and t seconds.)

If the rate distribution isn't time dependent, the variable dependence in $\lambda(t, v)$ can be separated as:

$$\lambda(t, v) = n(t)\Psi(v_0) \quad (154)$$

An appropriate distribution must be chosen for $\Psi(v_0)$. Engelhardt uses Laplace's distribution function to describe the pit propagation rates.⁷³ The distribution governing pit growth rate is selected differently by different researchers (for example, see Section 7.6.2), but characterizing these differently growing pit rates correctly is a crucial part of model development. In general, it is necessary to conduct proper experimentation to validate the selection of the distributions chosen to govern the different stages of the SCC model and to calculate the values of any fitting parameters. This is especially true when adapting an existing model to a new situation, since the SCC process varies so much across materials, system types, and environments.

Having considered the rates at which pits grow, it is next important to consider how pits repassivate or initiate a crack. Engelhardt assumes that repassivation is described as:

$$R_a(x, t) = -\gamma f_a(x, t) \quad (155)$$

with γ a constant that characterizes the repassivation of pits that were previously stable, referred to by Engelhardt as the "delayed repassivation" constant.⁷⁴ It is specific to the material-environmental system, and may also be specific to the pit itself (as an example, pit

⁷³This looks like $\Psi(v_0) = \frac{1}{2\beta} \exp(-|v_0 - V_0|/\beta)$, where V_0 = mean initial pit propagation rate.

⁷⁴ γ is a function of potential, temperature, solution chemistry, and pit depth, but an explicit formulation is not given in [30].

potential and chemistry changes with pit depth, so γ is not necessarily constant throughout the pit's lifetime).

Whether or not to consider repassivation rates as constant is an assumption that must be made (and justified) when determining the form of a SCC model. For example, one might calculate the critical potential at which passivation occurs, and from there the depth at which the pit's potential would reach this value. It would be necessary to show experimentally that this calculation worked well for each pit, and that it was valid to assume that every pit reaching this critical depth repassivated and ceased contributing to corrosion damage. This type of assumption can be difficult for certain systems - such as the cask-and-deliquested-salt-solution that is the concern of this project - if a wide variability in local conditions is expected. A time-dependent, local salt film is different from a uniform bulk liquid.

Conditions for crack initiation in the Engelhardt model are

- $K_I > K_{ISCC}$
- Crack propagation rate $>$ pit propagation rate

Engelhardt goes on to solve three differential damage functions: f_a (active pits), f_p (passive pits), and f_{cr} (cracks). These expressions depend on γ , $g(x)$, v_0 , $\zeta(x)$, $\Psi(v_0)$, $N(t)$, V_{cr} , and other parameters. These expressions, which are derived from solutions of Equation 147, are presented in Table 36. The percentage of pits of a certain depth which have initiated a crack may be found from the ratio of f_{cr} to f_{total} . Figure 53 shows how the predictions of the equations in Table 36 compare with experimental results. The solid lines show the likelihood of a crack developing from a pit (expressed as the percentage of pits that have an associated crack) as a function of pit depth, as calculated by the equations in Table 36. The individual points correspond to experimental results.

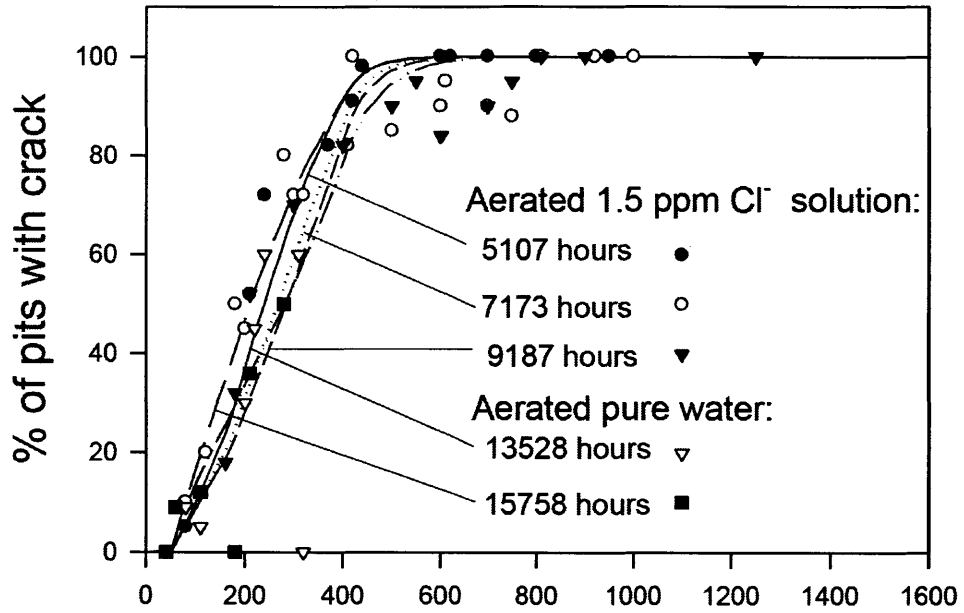


Figure 53: Engelhardt calculated the percentage of pits that were expected to initiate a crack as a function of pit depth using the equations in Table 36. Experimental results are also plotted. The scenarios of interest were 3NiCrMoV disk steel exposed to aerated 1.5 ppm Cl⁻ solution and aerated pure water for different periods of time. It can be seen that the equations accurately predict the expected cracking behavior of the disk steel. [30]

Table 36: Differential damage functions in the Engelhardt model

| |
|---|
| f_a, the differential damage function for active pits |
| $f_a = \int_0^{\infty} dv_0 \Psi(v_0) \left(\frac{1}{v_0 \zeta(x)} \cdot e^{-\gamma g(x)/v_0} \cdot n(t - g(x)/v_0) \cdot U[\max(x_{tr}, x_{v0}) - x] \right)$ |
| f_p, the differential damage function for passive pits |
| $f_p = \gamma U(x_{tr} - x) \int_0^{\infty} dv_0 \Psi(v_0) \left(\frac{1}{v_0 \zeta(x)} \gamma e^{-\gamma g(x)/v_0} N(t - g(x)/v_0) \right)$ |
| f_{cr}, the differential damage function for cracks |
| $f_{cr} = U(x - x_{tr}) \times \int_0^{\infty} dv_0 \Psi(v_0) \left(U(x_{tr} - x_{v0}) A(x, x_{tr}, t) + U(x_{tr} - x_{v0}) U(x_{v0} - x) B(x, t) \right. \\ \left. + U(x_{tr} - x_{v0}) U(x - x_{v0}) [B(x_{v0}, t - \theta(x, x_{v0})) + A(x, x_{v0}, t)] \right)$ |
| $A(x, y, t) = e^{-\gamma g(y)/v_0} n[t - g(y)/v_0 - \theta_{cr}(x, y)] \times \frac{1}{V_{cr}(x)}$ |
| $B(x, t) = \frac{\gamma}{V_{cr}(x)} \times \int_{x_{tr}}^x \frac{1}{v_0 \zeta(x')} e^{-\gamma g(x')/v_0} n[t - g(x')/v_0 - \theta(x, x')] dx'$ |

Table 37: Variable definitions for the Engelhardt model

| Variable | Definition |
|-------------|--|
| x | Depth |
| t | Time |
| k | Index |
| K | Total number of different defects in the system |
| N | Number of corrosion events per cm^2 |
| $F_k(x, t)$ | Integral damage function |
| $f_k(x, t)$ | Differential damage function |
| j_k | Flux density |
| R_k | Bulk source of particle k |
| n_k | Nucleation rate of defect k |
| f_{k0} | Initial distribution of defect k |
| N_0 | Maximum number of stable pits |
| t_0 | Characteristic time |
| t_s | Service life of component |
| a, b | Parameters reflecting halide activity, pH, and potential |
| v | Pit propagation rate |
| v_0 | Initial, finite pit propagation rate |

Continued on next page

Table 37 – continued from previous page

| Variable | Definition |
|-------------------|---|
| f_a | Damage function for active pits |
| f_p | Damage function for passive pits |
| f_{cr} | Damage function for cracks |
| f | $f_a + f_p + f_{cr}$ |
| L | Depth |
| k | Constant in depth law ($L = kt^m$) |
| m | Constant, usually ≤ 1 |
| $\zeta(x)$ | Function used to satisfy boundary conditions |
| α_{eff} | Anodic transfer coefficient for the alloy of interest |
| V | Total rate of corrosion crevice propagation |
| V_{el} | The electrochemical component of V |
| V_{mec} | The mechanical component of fatigue/creep |
| C, n | Alloy dependent constants in $V_{mec} = C(\Delta K)^n$ |
| ΔK | Stress intensity range |
| T | Temperature |
| σ_y | Yield stress |
| $\lambda(t, v_0)$ | Used in $n(t)$ to describe the number of pits nucleating between t and $t + dt$ with and a propagation rate between v and v_0 |
| γ | Constant describing pit death rate |
| $g(x)$ | $\int_0^x ds/\zeta(x')$ |
| $\Psi(v_0)$ | Pit growth rate distribution |
| E | Potential |
| E_{cr}, x_{cr} | For E and x below these values, the pit is not active |
| U | Unit function |
| θ | Age of defect |
| θ_{cr} | Age of defect with corresponding propagation rate V_{cr} |
| x_{tr} | Depth at which $K_I = K_{ISCC}$ and cracking can occur |
| ε | Percentage of pits with cracks at a given pit depth |
| β | Constant that characterizes the Laplace distribution for defect growth rate |
| $\Phi(x, t)$ | CDF: probability that a random pit has depth $\leq x$ at an observation time t |
| S | Area |
| $N(t)$ | Number of nucleated pits per cm^2 |

The damage function approach is useful because it ties in naturally to extreme value statistics. Extreme value statistics allow the researcher to use the data obtained from a

small laboratory sample to extrapolate a meaningful prediction for the larger, real component. In Engelhardt's case, the real component is a turbine blade; in the case of the *Life Prediction of Canister Material* project, the real component is the weld and heat-affected zones of an actual used nuclear fuel storage canister. The cumulative distribution function for the system can be expressed as:

$$\Phi(x, t) = \frac{S[N(t) - F(x, t)]}{SN(t)} = 1 - \frac{F(x, t)}{N(t)} \quad (156)$$

Engelhardt points out that this is especially useful for characterizing the likelihood of failure due to SCC: if $F(x, t)$, S , and $N(t)$ are known, then $\Phi(x_{\text{fail}}, t)$, the probability of no failure, can be calculated, with x_{fail} being the pit depth at which component failure is assumed to occur. The probability of failure can be expressed as:

$$P_f(x, t) = 1 - e^{(-SF(x,t))} \quad (157)$$

Solving $F(x, t)$ as detailed in Reference [30] and assuming that the initial nucleation of the pits occurred at $t = 0$ yields the final CDF:

$$\Phi(x, t) = 1 - \int_{x/t}^{\infty} e^{-\gamma g(x)/v_0} \Psi(v_0) dv_0 \quad (158)$$

This approach outlines one possible way to bridge deterministic models (damage function analytics) with probabilistic methods in order to predict the effects of SCC in a component or material of interest. Engelhardt provides a nearly complete view of SCC, from pit growth to crack growth. Each step of this model would require experimental validation if it were to be used to describe SCC in stainless steel canister weld material exposed to deliquesced salt solutions, since some of the mathematical expressions might need to be changed or adapted in order to be accurate for the new material-environment combination.

7.6.2 Turnbull, 2006: A probabilistic model for pitting and cracking

Turnbull's work focuses on developing a statistical model of SCC in steam turbine disc steel. It is of particular interest because it takes an explicitly probabilistic approach to modeling (1) initial pitting, (2) pit growth, (3) pit-to-crack transition, and (4) crack growth.⁷⁵

The Turnbull model first establishes a distribution of pit locations. Note that this model begins with the assumption that a pit distribution exists, but does not predict the initiation of the pits using environmental parameters as an input.

After the distribution of pitting locations on the metal surface has been determined, an additional distribution is developed to describe the initial depths of these pits. Typically, this starting point is informed by experimental observations of the relevant material. However, the characterization of this distribution should be done carefully. Small experimental samples whose distribution of pits following an exposure test may not truly be representative of the actual distribution expected to be present on a full-sized operational component [31].

These two distributions must account for the expected areal density of pits and the assumed starting depths of pits. Minimum and maximum values for areal density of pits and pit depths were prescribed.⁷⁶ A model should also account for inactive pits (often referred to as "dead" pits) which are too shallow to develop into cracks, and be able to dynamically account for pit nucleation and deactivation as the simulation proceeds if this behavior is relevant to the material-environment couple at hand.

First, it is assumed that all initial pit depths lie in a range from x_0 to x_{\max} . Turnbull applies Weibull statistics to the study of the pit distribution.⁷⁷ The Weibull distribution

⁷⁵The mathematical techniques used in this work will likely provide the starting point for construction of the predictive model for SCC in the used fuel canister welds.

⁷⁶More ideally, the initial pit depths do not vary evenly between the prescribed minimum and maximum values, but instead vary in accordance with an expected distribution (e.g., if more shallow pits are expected, or more deep pits, and so on.)

⁷⁷Weibull distributions have long been familiar to industrial materials scientists. A common practical use

yields a cumulative distribution function (CDF) that can be used to calculate the percentage of pits that are smaller than some given size x [62]. The standard Weibull distribution is as follows⁷⁸ [62]:

$$f(x; k, \lambda, \theta) = \frac{k}{\lambda} \left(\frac{x - \theta}{\lambda} \right)^{k-1} \exp \left(-\frac{x - \theta}{\lambda} \right)^k \quad (159)$$

Here, x is the pit depth; λ is the average pit diameter; and k characterizes the spread of the observed pit diameters. θ , the location parameter, is typically equivalent to zero in materials science applications, thus reducing the Weibull distribution to its “two-parameter” form [62]. This distribution can be used to characterize pitting on a metallic surface. Environmental SCC is a regular, uniform process (assuming equal exposure of all parts of the sample) that does not result in a perfectly uniform collection of equally sized corrosion pits, and the Weibull distribution can be used to describe the expected range of pit sizes.

To find the probability that a pit lies in a size range of 0 to x , the following expression is used [31], [63]:

$$F(x) = \int_0^x p(\zeta) d\zeta = 1 - e^{-a_1(x-x_0)^{a_2}} \quad (160)$$

where a_1 and a_2 are fitting parameters, and x_0 is the minimum observed pit depth (or the minimum prescribed pit depth, if carrying out a simulation). If one is modeling pitting, it is possible to solve this distribution for x as follows:

$$x = x_0 + \left[\frac{1}{a_1} \ln \left(\frac{1}{1 - F(x')} \right) \right]^{1/a_2} \quad (161)$$

of these distributions is the characterization of the sizes of particles that are created when a solid material is ground up. An example would be stone being crushed into gravel: the Weibull distribution can be used to accurately describe the size range and size distribution of the gravel particles.

⁷⁸In Equation 159, x is the pit diameter, λ is the average pit diameter, and k characterizes the spread of the observed pit diameters. θ , the location parameter, is typically equivalent to zero in materials science applications, thus reducing the Weibull distribution to its “two-parameter” form [62].

and use a random number generator (RNG) to assign a value to x' , thus finding $F(x')$ and calculating an initial pit depth.⁷⁹ Note that prior to using the RNG, a value x_{\max} must be determined, such that values of x' that are not realistic are rejected. Turnbull suggests that the validity of the distribution is not especially sensitive to the selection of x_{\max} . It is important to be sure that x_{\max} is not too small, or else the distribution will be unnaturally truncated [31].

Turnbull also describes two approaches for working with this initial pit distribution. In the first approach, the pit distribution on an exposed sample is determined experimentally. The pit distribution is then modeled using Weibull statistics, and refined by fitting the parameters a_1 and a_2 to experimental data. The second approach involves arbitrarily assigning values to a_1 and a_2 given a range of appropriate possible values: clearly, this approach is more accessible than carrying out exposure tests and carefully determining the distribution of pits on the sample surface. It is contended by Turnbull that this second approach is valid for the purposes of modeling and prediction because the mechanisms that govern the growth of pits and cracks are far more important to the final state of the sample than is the initial distribution of shallow pits.

It is then necessary to describe how the pits evolve in time. If $P(x, t)$ is the pit size distribution function, then its time rate of change can be described as:

$$\frac{\partial P(x, t)}{\partial t} = -\frac{\partial}{\partial x}[g(x)P(x, t)] + S(P(x, t)x, t) \quad (162)$$

with g the pit growth rate and S a source/sink term that can be ignored if a stable pit size distribution is assumed [31].

The pit's depth x is given as:

⁷⁹Turnbull does not distinguish between x and x' in the cited paper; this is my addition to make the process more clear.

$$x = \alpha t^\beta \quad (163)$$

with α a normally distributed variable and β a parameter that must be fit to applicable experimental data. It is possible to divide the pits into groups governed by different values of α : this allows more refinement of the model, and increased agreement with observed behavior [31]. The pit's growth rate can be described as:

$$\frac{dx}{dt} = g(x) = \beta \alpha^{1/\beta} x^{(1-1/\beta)} \quad (164)$$

Qualitatively, this describes a distribution in which shallower pits grow more quickly.

Experimental validation of proposed distributions for initial pitting and subsequent pit growth is a key step for the development of a new SCC model. Turnbull proposes two ways to go about this, but the second “quick fit” method- while tempting - is not likely to be an option for an endeavor like the canister-weld SCC modeling project. Because one of the objectives of that project is to quantify and also minimize uncertainty, experimental validation of every step of the model will be required.

Once the mathematical models of pit distribution and pit growth is in place, it is necessary to consider the transition from pit to crack. Not all pits will yield a crack: while these flaws do act as local stress concentrators, if they never yield a crack, they will not contribute to the possibility of failure in SCC (assuming that material thickness \gg the maximum pit depth). Cracks do not initiate from a non-pitted surface in the Turnbull model.

The transition occurs when the pit reaches a critical depth, indicating that the threshold mechanical driving force has been reached. Turnbull argues that while this depth does depend on the input of applied stress and environment, it should be found experimentally.

Due to the complex interactions of factors leading to SCC, it is difficult to accurately predict pit depth as a function of environmental and material conditions theoretically. After this pit depth has been reached, flaw growth is governed by an appropriate crack growth rate model [31].

Turnbull takes a similar view to that of Kondo (Section 7.3.7) as to how best to model the pit-to-crack transition, and also that he similarly acknowledges that any model for a given application will likely rely heavily on experimental data to fit any proposed governing equations. As Kondo did, Turnbull suggests using experimental results to verify threshold pit sizes (under the assumption that pit depth is static following the pit-to-crack transition). Experimental data is also used in SCC models to fit parameters and constants, thus taking into account the interactive effects of many environmental and material factors without having to explicitly account for each one.

It is also interesting to note that the model includes an additional requirement for crack initiation, that of a minimum pit depth that is less than or equal to the depth at which the crack growth rate first exceeds the pit growth rate. In a later paper, Turnbull explains that this is because some pits will have extremely small growth rates, and thus, if one only imposes the condition that crack growth rate must exceed pit growth rate for a crack to grow, these pits will always yield cracks [63]. In reality, however, these extremely slow-growing pits would effectively be inactive (or “dead”) pits that do not contribute significantly to the possibility of materials failure [63].

The crack growth rate is described and used to establish an expression for the critical pit depth that leads to crack initiation.

The growth of the flaw immediately following the pit-to-crack transition can be described as:

$$\frac{dx}{dt} = C\sigma^p x^q \quad (165)$$

where p and q are fit to experimental data, and C is randomly selected from an appropriate normal distribution when carrying out a simulation, or measured explicitly from observation of a sample for a specific pit-crack system [31].

One can now solve explicitly for the critical pit depth x_{crit} by setting the crack growth rate equal to the pit growth rate:

$$x_{\text{crit}} = \left(\frac{\beta\alpha^{1/\beta}}{C\sigma^p} \right)^{\beta/(1+\beta(q-1))} \quad (166)$$

This model allows the simulation of pit size distribution, and a prediction of the number of pits that will eventually yield cracks. Overall, the model agreed well with experimentally observed pit depth distribution evolution, and it also sufficiently reproduced the variability of the experimental measurements [31]. Predictions for crack-depth distribution using this model are shown in Figure 54. The model is generally in good agreement with experimental observations, although it somewhat overpredicts the number of deep cracks. However, if the purpose of an SCC model is to provide a conservative prediction of failure, this may not be an undesirable feature.

In a subsequent paper, Turnbull gave further consideration is given to Equation 165 [63]. It is noted that this particular crack growth law indicates that this formulation of the crack growth rate would accelerate as its depth increased. This is not in accordance with experiment: after a certain depth, crack growth is observed to proceed at a constant rate. The value of this constant, “deep crack” growth rate is dependent on the environment (but not on the applied stress), and can be determined experimentally. In the Turnbull model, then, after the pit-to-crack transition occurs, the crack grows according to Equation 165

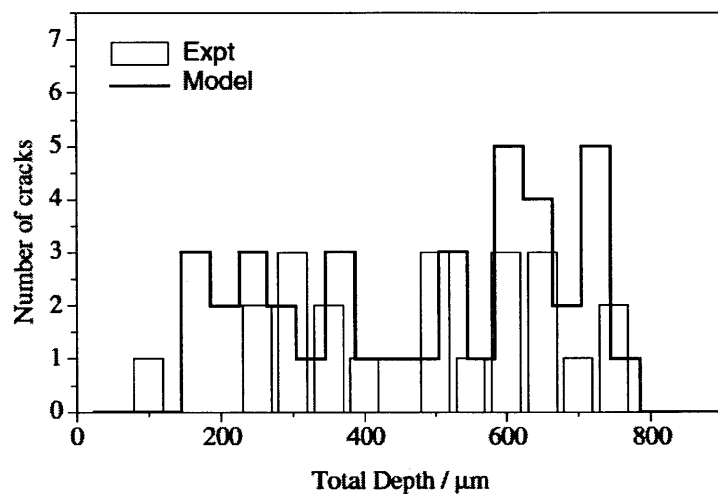


Figure 54: The results of a crack-depth distribution prediction using the Turnbull model are shown and compared with experimental results. The steel of interest was a turbine disc steel exposed to 1.5ppm Cl^- at 90°C for 9187 hours. Deep cracks are somewhat over-predicted, but this may not be a major issue in an intentionally conservative model. [63]

until a critical crack depth is reached.⁸⁰ At this point, the crack growth transitions to the “deep crack” regime, and its depth increases at a constant rate.

Turnbull et al. constructed the model knowing that the cracks would transition from the short-crack regime (characterized by the growth rate described by Equation 165) to the long-crack regime, but they did not proceed with any definitive knowledge of when this transition occurred. As a result, in their model, a critical depth is assumed at which the growth rate switches regimes.⁸¹ Ultimately, this results in a reasonable approximation of ultimate corrosion damage, but is obviously not an exact representation of how cracks propagate through material. For example, real cracks do not suddenly drop down to the same constant crack growth rate once some threshold depth is reached. Here, the critical crack depth was chosen such that the model’s predictions had a good fit with experimentally observed data when the simulation was run.

It was also noted by Turnbull that two of the major assumptions of Kondo’s model (see [18]) and his own prior model (see [31]) were not actually correct. First, it is not always true that pits simply stop changing once the pit-to-crack transition occurs. Second, cracks do not always initiate at the base of the pit (where stress and strain were assumed to be the most concentrated) [64].

Importantly, the researchers observed different pit-and-crack configurations in the experimental samples: when a pit initiated a crack, the crack only grew from the pit base 43% of the time [64]. For example, in a 3Ni-Cr-Mo-V steel exposed to an aerated 1.5 ppm chloride solution, the researchers also observed pits with cracks that broke the surface on

⁸⁰Other researchers, such as Engelhardt and Macdonald, have approached SCC modeling in a manner that is largely similar to that of Turnbull. However, they assert that the crack growth rates are not statistically distributed [30]. Turnbull claims that his approach, with the statistically distributed short crack growth rates, is more accurate (at least for the situation he is modeling) [31].

⁸¹This critical depth may be chosen retroactively, by picking the depth that causes the model to have the best agreement with experimental results, or it may be chosen proactively, in which cracks in a sample are monitored in order to empirically determine a depth at which the crack growth rate transition occurs.

either side of the pit and extended beneath the pit. They observed cracks that did not extend beneath the pit but which grew outward from the pit walls; and they observed cracks which extended below the pit but which did not break the surface of the material [64]. A thorough model should explain and predict these differences in crack type.

Turnbull suggests that configurations in which the cracks break the surface on the sides of the pit but do not extend beneath the pit can be accounted for in a properly formulated pit and crack growth rate distribution. In some cases, pit growth rate may in fact exceed crack growth rate, in particular as the crack transitions to the slower deep-crack growth rate: this may correspond to the pit-and-crack configurations in which the cracks initiate from the pit sides and not the pit bottom. Turnbull noted that his model did predict that a certain fraction of pits would grow faster than the cracks emanating from them, and that these pairs might manifest as cracks that grew from the sides of the pit. However, the percentage of experimentally observed pit-and-crack systems displaying this behavior (50%) actually exceeded the percentage predicted by the Turnbull model (12%) [63].

More recently, Horner, Turnbull, Connolly, Zhou, and Crocker carried out finite element analyses of the stress and strain fields around prototypical pits in order to gain insight into the different crack morphologies that were observed in experiments [51]. Stress is localized near the bottom of the pit. Strain was localized toward the mouth of the pit, meaning the material is more susceptible to plastic flow there. Importantly, this research shows that one cannot simply assume that the strain field parallels the stress field, because the assumption of pure elastic strain is not necessarily correct [64]. This means that the crack is not always expected to initiate from the bottom of the pit, as is commonly assumed. The finite element analysis suggests a possible explanation for the large percentage of observed cracks that emanate from the pit walls and not from pit base. This research effort is also

covered in additional detail in Section 7.9.4.^{82,83}

Turnbull concludes that the model described in this sections has merit, but that it is not entirely capable of predicting the different pit-and-crack morphologies that are observed in experiment. Models (for certain situations) may also need to account for the generation of multiple cracks from a single pit, and for the interaction between pits and cracks.

7.7 Modeling SCC in Alloy 600 exposed to primary water environments

Stress corrosion cracking is a major degradation mechanism for Alloy 600 (75Ni-15Cr-9Fe) components exposed to the primary water system in pressurized water reactors. A significant amount of work on modeling this process has been reported. The approaches considered here have been selected because they aimed to develop a predictive model. Even though the material and environment considered in these models is different, aspects of the modeling approaches presented here could be applicable to the development of a predictive model for SCC in used nuclear fuel canisters.

7.7.1 Aly, 2007: SCC in Alloy 600 components used in PWRs

Aly et al. also attempted to model the initiation and propagation of SCC in Inconel Alloy 600 in a high pressure, high temperature water environment characteristic of a PWR pri-

⁸²Crack tip chemistry, in addition to the stress and strain field at the pit walls, is also a key input to the where-and-when of crack nucleation. This chemistry is typically most aggressive at the pit base [64], but as this chemistry is highly localized, it is not necessarily the same in every pit present on a sample surface. This further influences the variation of crack initiation location relative to the pit geometry, and adds another layer of complexity to any complete model of SCC.

⁸³Turnbull and his associated researchers utilized x-ray microtomography technology in a 2011 paper to gain further insight into the crack-pit configurations characteristic of the material and environment being studied. This technique allows high-resolution 3D imaging of pits and their associated cracks based on radiation attenuation at many points in a sample with a very fine mesh [51]. This technique is of particular interest for the canister weld SCC project, since it will be important to establish the expected crack-pit morphologies for the canister weld/salt-environment situation. Turnbull's work shows that these morphologies can vary significantly, even in the same sample. Any SCC model should account for these differences, should they be found to exist.

mary system [25]. This is a different environment than the one of concern to the canisters, but many of the same questions are appropriate: how will temperature, surface chemistry, surface stress, and component fabrication affect the probability of SCC failure?

Important factors that were considered include [25]:

- microchemistry of the grain boundaries (segregation and other factors can weaken grain boundaries)
- thermal treatment of the component material
- carbide distribution (weakening of grain boundaries)
- grain size
- plastic deformation undergone by the component
- material yield stress
- residual stress of the material
- applied stress on the material
- strain on the material
- temperature
- pH
- chemistry of environment and solution on surface
- partial pressures of gases

Aly also notes many micro-scale events that serve to increase the likelihood of SCC, per R. W. Staehle [49]. These are illustrated in Figure 55, and include:

- Ejection of passivating species or attraction of depassivating species at the surface enhance corrosion vulnerability.
- Catalytically active precipitates at the surface or near flaws accelerate corrosion.
- Anions at the grain boundaries due to solute dissolution
- Hydrogen embrittlement

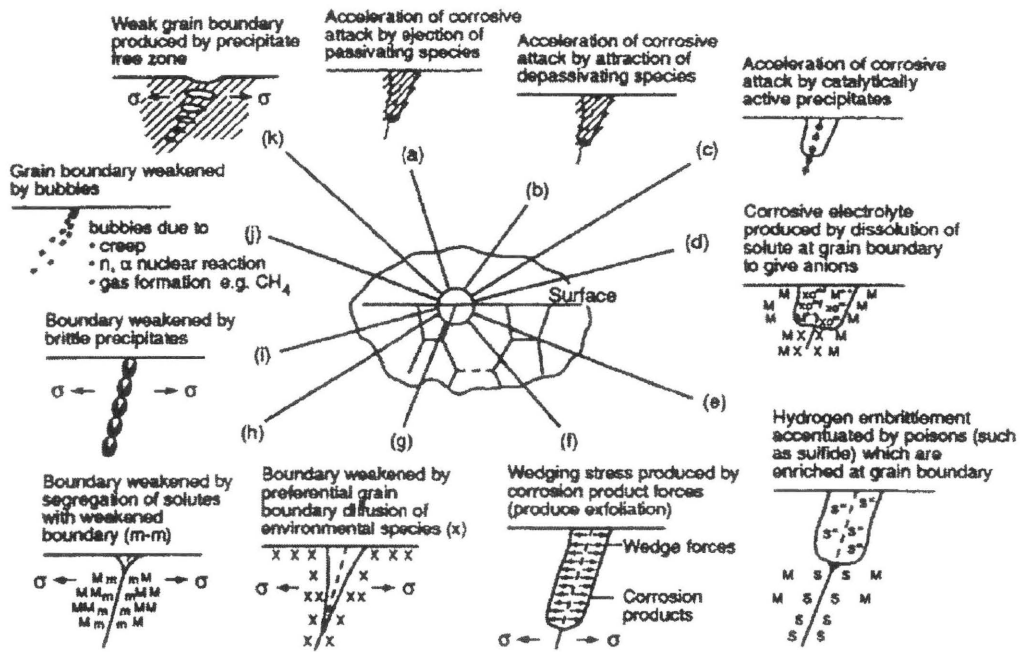


Figure 55: Processes that can affect stress corrosion cracking behavior in steels. [49]

- Wedging forces from corrosion products in the material
- Precipitates on the surface
- Bubbles along the grain boundary

Aly proposes a general phenomenological expression that describes the depth of a stress corrosion crack. This model is based on the work of Staehle [25]. Each term in the equation describes a particular aspect of the environment/material combination, as described in Table 38. This equation for depth is as follows:

$$x = A[\text{H}^+]^n [x]^p K^m e^{\frac{E-E_0}{b}} e^{\frac{Q}{RT}} t^q \quad (167)$$

Table 38: Variable definitions for Equation (167)

| Term | Definition |
|-----------------------|-------------------------------|
| x | SCC penetration depth |
| A | Constant |
| $[\text{H}^+]^n$ | pH |
| $[x]^p$ | Environmental species |
| K^m | Stress intensity |
| $e^{\frac{E-E_0}{b}}$ | Potential, alloy, environment |
| α | Crack growth amplitude |
| T | Temperature |
| t^q | Time |

In order to develop their model, Aly et al. begin by considering two existing kinetic models. The first is an empirical-probabilistic model expressed as:

$$t_f = A t_{\text{ref}} \left(\frac{\sigma}{\sigma_{\text{ref}}} \right)^n \exp \left[\left(\frac{Q}{R} \right) \left(\frac{1}{T} - \frac{1}{T_{\text{ref}}} \right) \right] \quad (168)$$

A is a constant that changes for different materials. t_{ref} is the time elapsed since the reference state existed, in which a predetermined number of components have undergone

PWSCC. Q is an activation energy, n is a stress exponent, and R is the gas constant. Equation (168) is simplified from a pH dependent expression for t_f (time-to-failure) proposed in a 1994 EPRI report on the topic.⁸⁴

A Weibull distribution is then used to describe the number of components that have undergone PWSCC since t_{ref} .⁸⁵

The second model considered by Aly is mainly dependent on strain rate, and is semi-empirical. If D , which has units of length, is a “damage parameter” that gives information regarding the extent to which cracks have initiated and propagated, then

$$D = \int_0^t A \underbrace{[\dot{\epsilon}(t)]^p}_{\dot{\epsilon} = \dot{\epsilon}_e + \dot{\epsilon}_n} dt \quad (169)$$

Total strain is a summation of elastic and nonelastic components.⁸⁶ A and p depend on the environment and the material.⁸⁷

One particularly interesting technique that Aly et al. use in their consideration of PWSCC is a three-dimensional diagram that combines a Pourbaix diagram (pH and potential) with useful strength, and then superimposes the submodes of corrosion for Alloy 600 (shown as a function of pH and potential in Figure 56). The corrosion submodes are determined from data in the literature. By seeing how strength changes with pH and potential, and then determining which corrosion submodes are possible where, it can be shown

⁸⁴See J. A. Gorman et al., “PWSCC Prediction Guidelines,” EPRI Final Report TR-104030 Project 2812-15, July 1994, [136].

⁸⁵If F is the fraction of components that have experienced PWSCC at the given time, then $F = 1 - \exp\left[-\left(\frac{t}{\theta}\right)^b\right]$. b is the Weibull slope which is fitted for a given set of data, and t is in units of effective full power years (these units are only appropriate for reactor applications). θ is a Weibull characteristic time, and it is a reference value for a certain situation: here, at $t = \theta$, 63.32% of the components of interest have experienced PWSCC. See: [25], 146. Note also that “components” is not formally defined: it is not clarified whether each reactor component composed of Alloy 600 is counted as one component, regardless of size, or whether “component” refers to a unit area of Alloy 600 that is exposed to the primary water environment.

⁸⁶Nonelastic and elastic strain are time dependent. Equations and methods for establishing expressions for $\epsilon(t)$ are given in more detail in Reference [25].

⁸⁷pp.146-147 give more detailed information as to how these two constants might be determined.

what degradation mechanisms are likely to be problematic in a known environment.⁸⁸ The boundaries of these submode regions are determined from the data in the literature.⁸⁹

This plot is used to determine the length of time a plant has operated under conditions that allow the development SCC. This information, coupled with the previously developed equations, is then used to estimate the fraction of all Alloy 600 components that are susceptible to SCC.

In 2009, Aly et al. outlined the primary challenges to refining and validating a proposed predictive model for SCC. One major challenge was designing and carrying out tests in order to get better values for the parameters in the model (and to show that experimental results are in good agreement with the model's predictions) [65].⁹⁰

In 2011, further work was presented at the Brazilian Congress of Mechanical Engineering. Three additional models were presented as being likely to be useful for modeling SCC in high-temperature water environments. Aly notes that the validity of most SCC models is debatable, and that further refinements and experimental validations must be made [66].

These models are as follows:

1. Andresen and Ford, 1988

Crack growth rate V_{scc} is given as:

$$V_{scc} = (7.8 \times 10^{-3} n^{3.6})(5.1 \times 10^{-14} K^4)^n \quad (170)$$

where n is a parameter encompassing the environment and the chemistry and K is stress

⁸⁸This diagram was originally developed by Staehle.

⁸⁹This sort of data visualization could be very valuable to our application, as it makes the conditions under which different corrosion-related mechanisms (for example: passivation, initial pitting, pit growth, crack initiation, crack growth in its various regimes) are able to proceed very clear.

⁹⁰Aly also points out a helpful reference for evaluating crack growth rates in SCC tests: B. Alexandreanu, O. K. Chopra, and W. J. Shack, "Crack Growth Rates and Metallographic Examinations of Alloy 600 and Alloy 82/182 from Field Components and Laboratory Materials Tested in PWR Environments," USNRC: Argonne, IL, 2008 (NUREG/CR-6964; ANL-07/12), [132].

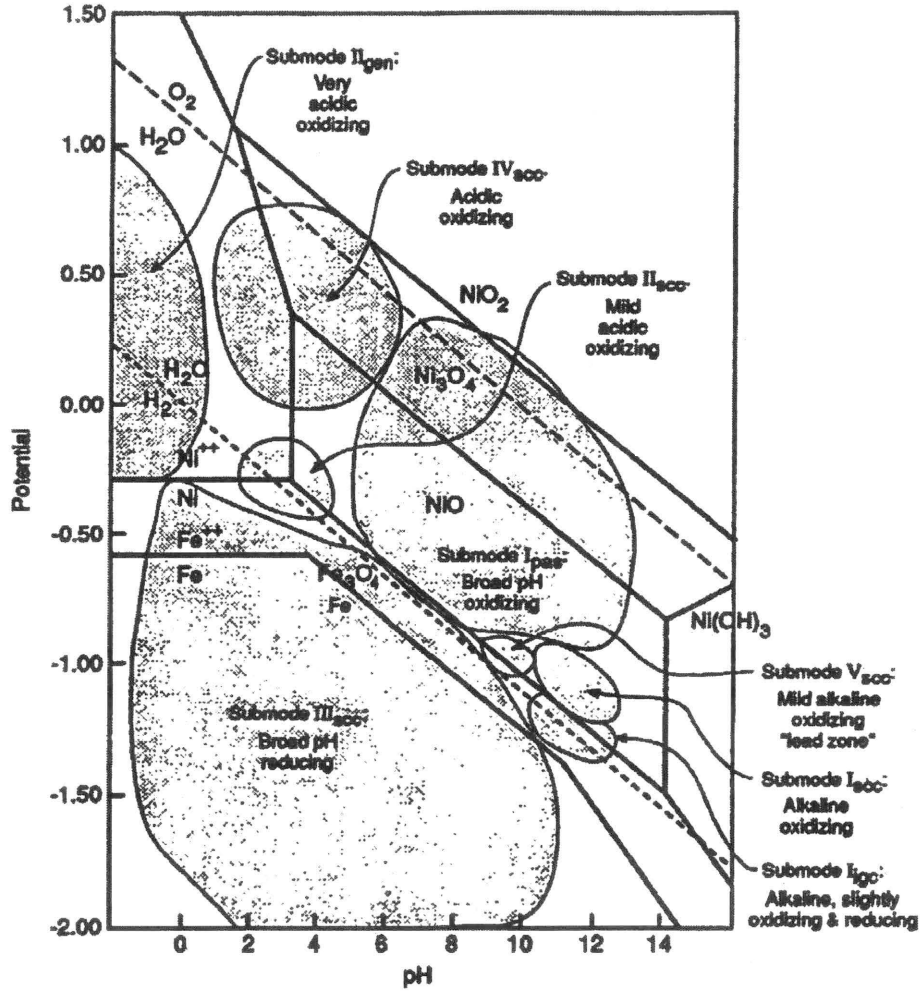


Figure 56: This Pourbaix diagram for Alloy 600 at a temperature of 300°C was used as the base diagram for the 3D diagram that combines potential and pH (shown here) with useful strength in a third dimension ([25], adapted from Staehle [49]). The corrosion submodes are based on experimental data from the literature. It is suggested by Staehle that crack velocity could replace useful strength.

intensity (units of $\text{MPa}\cdot\text{m}^{0.5}$). Transient creep results in strain, which ruptures the oxide film on the metal surface, and SCC propagates along vulnerable paths (for example, a grain boundary) [66], [19]. This model is not generally applicable to SCC in *Life Prediction of Canister Material*, as it was developed specifically for predicting crack growth rates in light water reactor environments, in which the steel components being studied are exposed to a continuous aqueous environment with well-characterized properties. This model is cited as a generally accepted model for SCC crack growth rates in boiling water reactor environments.⁹¹

2. Rice, 1981

Rice proposed the following equation for crack opening in an SCC situation:

$$\delta_{cat} = \alpha[(\sigma_{\infty} - \sigma)/\sigma_{\infty}] \times \epsilon_{avg} \times d \quad (171)$$

δ is an average crack opening - here, grain boundary separation - in the material, σ_{∞} is a remotely applied stress, σ is the stress at the grain boundary, ϵ is the average strain in the material resulting from creep, and d is grain diameter [66]. The objective of this model is to predict how creep (or, the strain induced by creep) affects the propagation of intergranular SCC. Aly mentions that this model gives reasonably good fits with data.

Rice also proposed a model in which time to rupture is proportional to the creep rate of the material:

$$t_f \times (d\epsilon_{CRP}/dt) = c \quad (172)$$

where c is a constant.

⁹¹See: F. P. Ford, D. F. Taylor, P. L. Andresen, and R. G. Ballinger. "Environmentally controlled cracking of stainless and low alloy steels in light water reactor environments," EPRI Final Report, NP-5064M, Electric Power Research Institute, 1987, [126].

7.7.2 Hickling, 2002: The Materials Reliability Program (MRP) model for PWSCC in Alloy 600

The objective of this EPRI research project was to model crack growth rates (CGR) due to primary water SCC of certain Alloy 600 components. The components of concern were “thick-wall” components, such as reactor vessel head and in-core instrument nozzles. Existing CGR data was combined with data from fracture tests carried out explicitly for this project.

The authors begin with the following equation, which shows a power-law dependence of CGR on the stress intensity factor and an Arrhenius temperature relationship. Equation 173 is stated to be a commonly accepted model for crack growth in Alloy 600 components exposed to a primary water environment [26]. Variable definitions are given in Table 39.

$$\frac{da}{dt} = \alpha \cdot \exp \left[-\frac{Q}{R} \left(\frac{1}{T} - \frac{1}{T_{\text{ref}}} \right) \right] (K - K_{\text{th}})^{\beta} \quad (173)$$

Table 39: Variable definitions for the Hickling model

| Variable | Definition |
|------------------|--|
| a | Crack length |
| t | Time |
| Q | Thermal activation energy for crack growth |
| R | Universal gas constant |
| T | Absolute temperature at the crack |
| T_{ref} | Reference temperature for data normalization |
| α | Crack growth amplitude |
| K | Crack tip stress intensity factor |
| K_{th} | Crack tip stress intensity factor threshold |
| β | Exponent |

The power-law dependence on stress intensity was derived from CGR data for steam

generator tubes.⁹² The authors note that there is not sufficient experimental data for CGR in thick-walled components, and that the dependence of CGR on stress intensity may plateau at high K values.

Twenty-six test specimens, each with a different heat treatment, were studied in order to better understand the relationship between CGR and microstructural differences. A mean power-law constant β was determined for each of the twenty-six heat treatments. The mean of twenty-six values of α were used to fit a single log-normal distribution.⁹³

Figure 57 shows the resulting curve from this research effort, known as the MRP curve. It plots $\frac{da}{dt}$ as a function of K .

7.7.3 Wu, 2011: Combining previous models to predict SCC damage

This master's thesis from the mechanical engineering department at the University of Maryland focused on modeling SCC in Alloy 600, particularly as it applies to steam generator tubes in nuclear power plants [27]. This is a different alloy and a different environment, but the goals of this paper were very similar to those of the canister project:

- Model crack incubation
- Model crack initiation
- Model crack propagation
- Consider associated uncertainties

To model SCC, Wu started with an existing empirical model and expanded upon it to develop a model for crack propagation rates in Alloy 600 in PWR steam generator

⁹²P. M. Scott carried out this work on thin-walled Alloy 600 components in the early 1990s, and the curve he developed is shown alongside the MRP curve in Figure 57. See:

P. M. Scott, "An Analysis of Primary Water Stress Corrosion Cracking in PWR Steam Generators," Presented at NEA/CSNI Specialist Meeting on Operating Experience with Steam Generators, Brussels, Belgium, 1991.

⁹³The reference temperature was 598.15 K, α was calculated to be 2.67×10^{-12} at 325°C when SI units are being used, B to be 1.16, and K_{th} was taken to be 9 MPa \sqrt{m} .

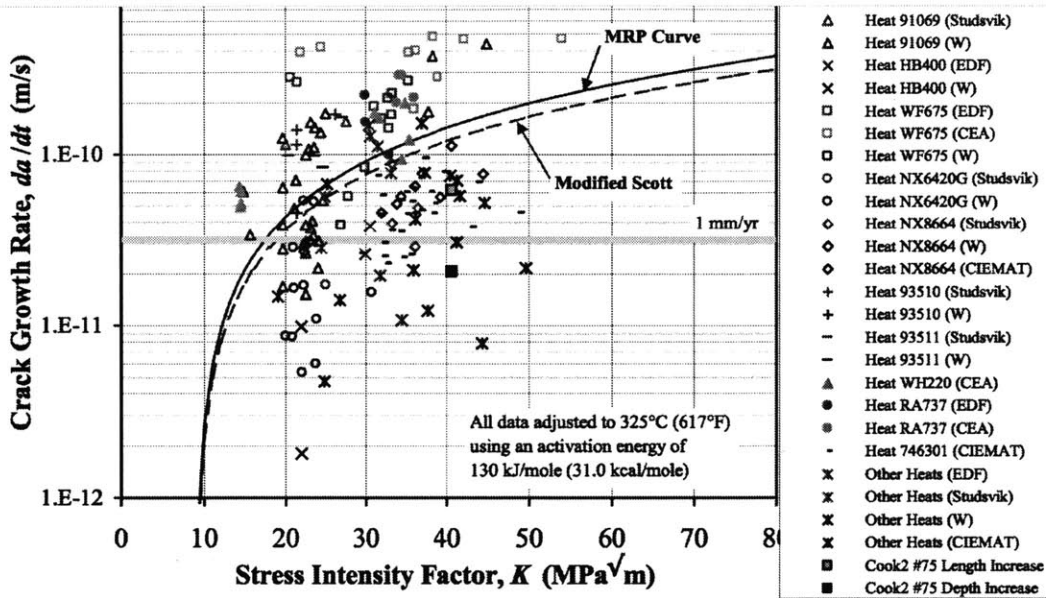


Figure 57: This graph shows the MRP curve (solid black line) for expected crack growth rates as a function of K in Alloy 600 thick-walled components. The modified Scott curve is the dashed blue line. Experimental data for the different heat treatments is plotted next to both curves. [26]

tubing. He used Hickling's model (see Section 7.7.2) as an initial method for describing the propagation rate of a stress corrosion crack in Alloy 600 [27].

It was then desired to account for pH and yield strength in the model. It was proposed that:

$$\frac{da}{dt} \propto \text{pH}^\beta \quad (174)$$

where the pH is that of the bulk electrolyte and β is the power relationship parameter.

Wu noted that Alloy 600 crack growth occurred in three distinct stages. In the initial stage of crack propagation, there is a strong dependence on the stress intensity. In the second stage of crack propagation, this dependence becomes much weaker. In the third stage, the crack growth rate increases sharply, and failure is likely to occur. A comparison of the power law given in Equation (174) with $\frac{da}{dt}$ versus pH data determined that Equation (174) applied best to the second stage of crack propagation.

To describe the dependence of $\frac{da}{dt}$ on yield strength, the following equation was proposed:

$$\frac{da}{dt} \propto [\sigma_{ys}]^m \quad (175)$$

where σ_{ys} is the yield strength of Alloy 600, and m is the power relationship parameter.⁹⁴ Cold work was not selected as a variable to consider due to its tendency to vary too much across components. This power law applied to SCC data in all stages of crack propagation.

⁹⁴Equation (175) was based on the work of Rebak et al. and Speidel, in which a power-law dependence of crack growth rate on yield strength and percent cold work was proposed. See:

- R. B. Rebak, Z. Xia, and Z. Szklarska-Smialowska, "Effect of Temperature and Cold Work on the Crack Growth Rate of Alloy 600 in Primary Water," *Corrosion*, 51(9), 1995, 689-697, [130].
- M. O. Speidel and R. Magdowski, "Stress Corrosion Crack Growth in Alloy 600 Exposed to PWR and BWR Environments," *Corrosion*, 2000, [127].

The final model proposed by Wu combines the model proposed by Hickling (Section 7.7.2) with the two power law relationships given in Equations (174) and (175). Expressions for crack propagation rate are given below, one for each of the two proposed stages of SCC propagation. The second stage includes a pH dependence.

$$\left(\frac{da}{dt}\right)_I = C_I \cdot \exp\left[\frac{Q}{R}\left(\frac{1}{T} - \frac{1}{T_{\text{ref}}}\right)\right] \cdot [\sigma_{\text{ys}}]^{m_I} \cdot [K - K_{\text{th}}]^{n_I} \quad (176)$$

$$\left(\frac{da}{dt}\right)_{II} = C_{II} \cdot \exp\left[\frac{Q}{R}\left(\frac{1}{T} - \frac{1}{T_{\text{ref}}}\right)\right] \cdot [\text{pH}]^{\beta_{II}} \cdot [\sigma_{\text{ys}}]^{m_{II}} \cdot [K - K_{\text{th}}]^{n_{II}} \quad (177)$$

The rapid third stage of SCC is not modeled. In order to link the two stages, the following formulation is proposed:

$$\frac{da}{dt} = \begin{cases} \left(\frac{da}{dt}\right)_I & \text{for } K < K_{\text{trs}}, \\ \left(\frac{da}{dt}\right)_I (1-x) + \left(\frac{da}{dt}\right)_{II} (x) & \text{for } K < K_{\text{tre}}, \\ \left(\frac{da}{dt}\right)_{II} & \text{for } K \geq K_{\text{tre}}. \end{cases} \quad (178)$$

where x is the transition ratio, and is described by:

$$x = \frac{K - K_{\text{trs}}}{K_{\text{tre}} - K_{\text{trs}}} \quad (179)$$

All variable definitions are provided in Table 40.

Fitting parameters were estimated from experimental data. Bayesian techniques were used to analyze the experimental data and understand the uncertainty associated with each calculated parameter value.

Table 40: Variable definitions for Hickling and Wu models

| Variable | Definition |
|----------------------|--|
| a | Crack length |
| t | Time |
| α | Crack growth amplitude parameter |
| Q | Activation energy for propagation |
| R | Universal gas constant |
| T | Temperature |
| T_{ref} | Reference temperature |
| K | Stress intensity factor |
| K_{th} | Threshold stress intensity factor |
| β | Fitting parameter |
| pH | Bulk electrolyte pH |
| σ_{ys} | Yield strength of the material |
| x | Transition ratio (Equation (179)) |
| K_{trs} | Stress intensity factor at beginning of Stage I to II transition |
| K_{tre} | Stress intensity factor at end of Stage I to II transition |
| m, n | Fitting parameters |

The model parameters were fit to experimental data, and Bayesian analysis techniques were used to understand the uncertainty associated with those calculations. The aim was to develop a joint probability density function that estimates the values of the parameters and which also gives information about the actual observed data spread.

In this model, the parameters were C , n , m , and β , with separate values for each of the two crack growth rate regimes. Their estimated values were obtained from data collected on $\frac{da}{dt}$, K , pH, T , and σ_{ys} . The output of the Bayesian analysis - the estimated probability distribution that describes the likely parameter values - is called the posterior distribution. Wu defines the set of parameters as $\underline{\theta}$, and refers to the set of collected data as $Data$.

Then, the posterior distribution, π , is given as:

$$\pi(\underline{\theta} | Data) = \frac{L(Data | \underline{\theta})\pi_o(\underline{\theta})}{\int L(Data | \underline{\theta})\pi_o(\underline{\theta})d\underline{\theta}} \quad (180)$$

Table 41: Variable definitions for Equation (180)

| Expression | Definition |
|--|--|
| $\underline{\theta}$ | C, n, m, b, s |
| $Data$ | $CPR, K, T, \sigma_{ys}, pH$ |
| $\pi(\underline{\theta} Data)$ | Posterior distribution |
| $L(Data \underline{\theta})$ | Likelihood function for regression |
| $\pi_o(\underline{\theta})$ | Prior beliefs for parameters |
| N | Number of data points |
| s | Standard deviation of the error |
| $\frac{da}{dt}_{exp}(i)$ | i^{th} experimental $\frac{da}{dt}$ value |
| $\frac{da}{dt}_{exp}(i, \underline{\theta})$ | i^{th} experimental value for $\frac{da}{dt}$ given $\underline{\theta}$ |

$L(Data | \underline{\theta})$ is an expression for the error distribution in the model, where the error distribution describes the difference between the data and the best-fit model. Ideally, the error associated with the model can be described by a normal distribution with a mean of 0.

To find the likelihood function associated with his model and data, Wu used the following expression:

$$L(Data | \underline{\theta}) = \prod_{i=1}^N \frac{1}{s\sqrt{2\pi}} \exp \left[-\frac{1}{2} \left(\frac{\frac{da}{dt}_{exp}(i) - \frac{da}{dt}_{calc}(i, \underline{\theta})}{s} \right)^2 \right] \quad (181)$$

All variables are defined in Table 41. The process for calculating the distribution of values for each parameter is described in Reference [27]. An example of the results is given in Figure 58. It shows the posterior joint distribution calculations for each parameter for the Stage II model given in Equation (177). The calculated parameter values can then be used in the model proposed in Equation (178), as shown in Figure 59.

This work provides one possible framework for developing a model for stress corrosion crack growth rate in the canisters, especially with regard to incorporating a probabilistic approach into existing deterministic or semiempirical models.

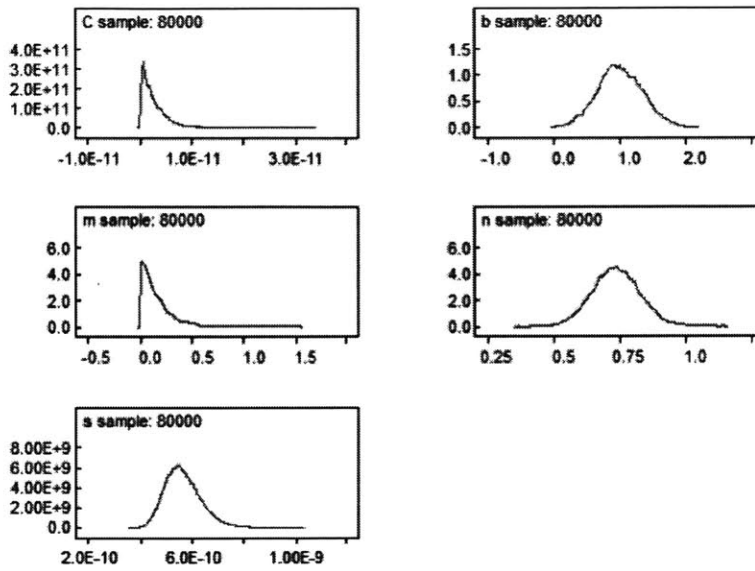


Figure 58: Posterior joint distribution calculations for the parameters C , β , m , n , and s in Equation (177). These were calculated in accordance with Equation (180). The calculations were carried out with the WinBUGS software for Bayesian analysis. [27]

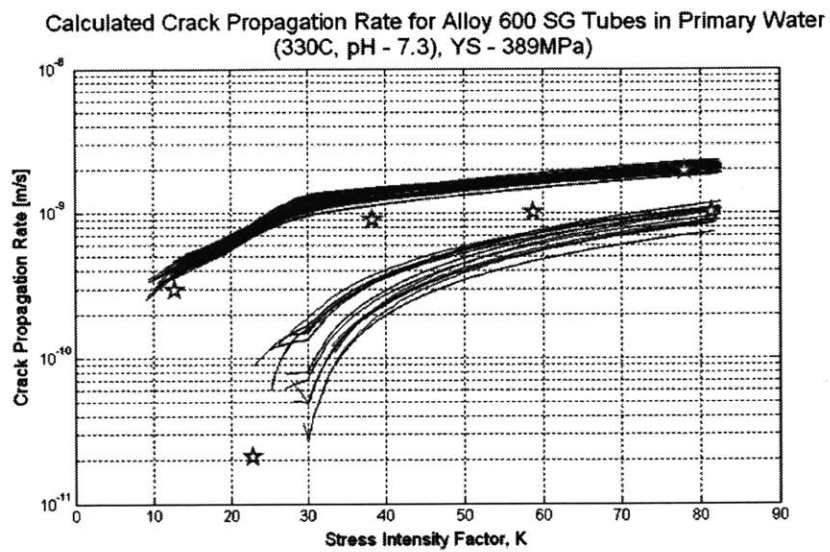


Figure 59: Experimental data for observed $\frac{da}{dt}$ given a stress intensity factor K for Alloy 600 exposed to 330°C water with pH 7.3 is plotted with red stars. This is compared to the results of the model (blue lines) proposed in Equation (178). Two sets of parameter values were used: 97.5% and 2.5%. [27]

7.8 Selected computer models for stress corrosion cracking

In this section, several other SCC studies are considered. These models did not include a mathematical formulation of SCC, but incorporated interesting and potentially useful methods that may be useful in the development of a predictive SCC model.

7.9 Wells et al., 1989: Using percolation theory to study SCC

D. B. Wells et al. used percolation theory to study intergranular SCC in austenitic stainless steels. Sensitization is considered a necessary prerequisite for this to occur: the crack propagates through continuous, sensitized grain boundaries. Unsensitized grain boundaries, or slightly sensitized grain boundaries with incomplete carbide precipitation, may cause crack arrest and prevent IGSCC failure. The criterion for SCC given by the authors is that at least 23% of the grain boundaries must be sensitized [67].

Under these assumptions, percolation theory was a useful tool for studying SCC, and the manner in which the locations of sensitized and unsensitized grain boundaries impact SCC behavior. This method accounts for the way in which a crack may progress from sensitized boundary to grain boundary, or to a plane of sensitized grain boundaries, or how existing propagating cracks may link together.

The authors developed a computer simulation that used the percolation model to study SCC in a representative material. They also experimentally evaluated sensitization in stainless steel samples.

In the simulation, a network of linked points is modeled. The links are either active (sensitized; SCC will propagate) or inactive (unsensitized; SCC will not propagate). The ratio of sensitized to unsensitized grain boundaries is determined at the beginning of the simulation.⁹⁵ Figure 60 shows the results of simulations on a 2D lattice where the probabil-

⁹⁵To decide whether an individual grain boundary is sensitized or unsensitized, a random number generator can be used to pick a value from 0 to 1. If the value is less than the preset percentage of sensitized

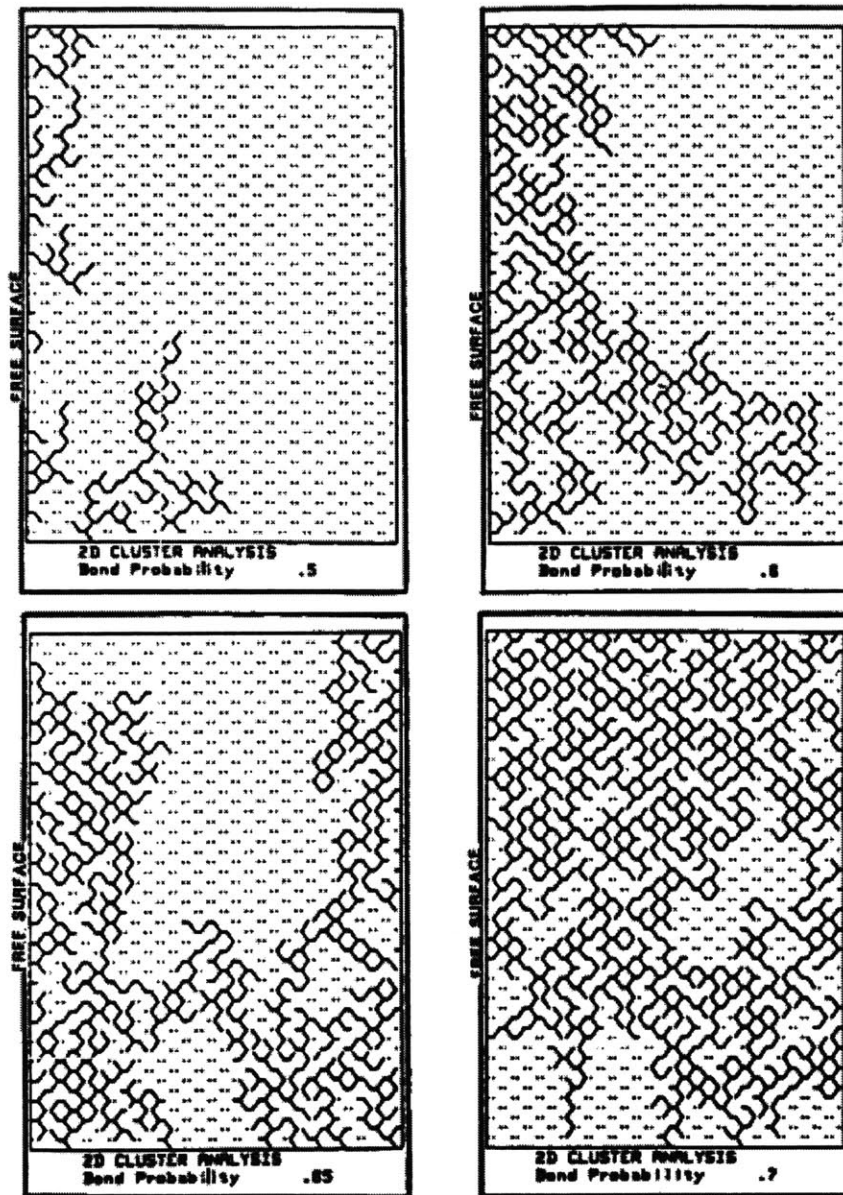


Figure 60: These four simulations on a 2D lattice model a crack progressing across active (sensitized) grain boundaries. In the top row, the probability of a link between two points being sensitized was 0.5 on the left and 0.6 on the right. In the bottom row, the probability is .65 on the left and 0.7 on the right. The authors found that the percolation threshold for failure (defined as a crack progressing across the lattice) was 0.6527. [67]

ity for a “grain boundary” to be sensitized and allow the progression of a crack was varied. The critical percentage of sensitized bonds - at which a through-sample crack is certain - was found to be 0.6527. The simulation was expanded to 3 dimensions by using a unit cell containing a tetrakaidecahedron structure with eight hexagonal faces and six square faces, and simulations using 16,000 to 54,000 “grains” were run. In the three dimensional case, the percolation threshold - the critical probability - was found to be 0.23 ± 0.01 . Above this threshold, the material will fail via mixed ductile and brittle failure. When the percentage of sensitized grain boundaries is increased to 89%, the material will show entirely brittle intergranular failure.

This approach provides one way to model how cracks may progress along grain boundaries in IGSCC situations, how crack clusters may link, and a way to predict the degree of sensitization that results in component failure or the occurrence of a certain failure mechanism.

7.9.1 Kamaya and Kitamura, 2004: A Monte Carlo study of SCC

Kamaya and Kitamura developed a Monte Carlo simulation technique that accounted for microstructural effects in SCC behavior. A given material can be characterized by its bulk properties, but at the microscopic level, the material is rarely homogeneous. The stress field at the microscopic level is usually variable and can impact the growth of small cracks. The presence of grain boundaries will also impact the crack’s growth, especially in IGSCC scenarios. Finally, if multiple cracks are present, the stress fields induced by each crack can impact the growth of the cracks around it [69].

The authors describe these microstructural effects using three terms: the polycrystal effect (local variations in stress), the kink effect (caused by the presence of grain boundaries), grain boundaries, the grain boundary is assigned a sensitized status.

and the interaction effect.

First, single-crack simulations were carried out. An expression for the stress intensity factor K was developed that encompassed the polycrystal and kink effects in terms of the correction factors F_{ani} and F_{kink} :

$$K_s = CF_{\text{ani}}F_{\text{kink}}\sigma_o\sqrt{\pi a} \quad (182)$$

where C is a constant, a is the crack size, and σ_o is the stress applied to the sample.

The authors developed expressions for F_{ani} and F_{kink} in previous work:

$$F_{\text{ani}} = \frac{1}{\pi a} \int \left(\frac{K_I}{\sigma_o\sqrt{\pi a}} \right) d\Gamma \quad (183)$$

$$F_{\text{kink}} = \frac{1}{N_g} \sum_{n=1}^{N_g} \cos^3 \left(\frac{\alpha^{(n)}}{2} \right) \quad (184)$$

K is the stress intensity factor and Γ represents the crack's path through the material. N_g is the number of grain boundaries that are present along the front of the crack and α is the deflection angle. In the simulation, this deflection angle is generated randomly. Mean values for F_{ani} and F_{kink} are calculated using known properties for the material of interest (here, Alloy 600).

Next, the authors define a parameter D , which describes the resistance of an individual grain boundary to cracking:

$$D = zD_o \quad (185)$$

D_o is a constant, and z is a random variable in the simulation. Variations in this resistance are due to microstructural factors, such as the concentration of carbide precipitates.

Next, the simulation for a single crack is carried out. A crack is “initiated” by assigning it an initial depth a_o . The length of a_o is equivalent to the length of a single grain boundary.⁹⁶ At each time interval Δt , the increase in crack length Δa is calculated:

$$\Delta a = DK_s^m \Delta t = \underbrace{H_o}_{D_o C^m} Z_p (F_{\text{ani}} F_{\text{kink}} \sigma_o \sqrt{\pi a})^m \Delta t \quad (186)$$

H_o and m are parameters that were set to make the equation consistent with the observed growth rates of macroscopic cracks in Alloy 600. Z_p is the average value of D for the bulk sample. The results of the single-crack simulation are shown in Figure 61. The solid black line shows the macroscopic crack growth rate predicted by the simulation. The dotted lines showed the variation in crack growth rate at a given crack depth, as calculated for 200 crack simulations. The solid blue lines show individual crack growth rates, while the dotted lines graph the maximum and minimum values of da/dt for 200 simulated cracks.

The authors next included the interaction effect between multiple cracks. Previous work indicated that when multiple cracks were present, crack growth rate was accelerated.

The stress intensity for the multiple crack simulation is given as:

$$Kd = \frac{K_{\text{BFM}}}{\underbrace{\sigma_o \sqrt{\pi a}}_{F_{\text{mut}}}} K_s \quad (187)$$

F_{mut} is the correction factor that accounts for the interaction effects of multiple cracks. K_{BFM} is the stress intensity factor evaluated for a 2D crack using the body force method.⁹⁷

A flow chart depicting the simulation procedure is given in Figure 62.

Equation (186) can then be modified to accommodate the interaction of multiple cracks.

⁹⁶Because there is variation in the length of grain boundaries in a material, a_o is actually selected from a distribution of appropriate grain boundary lengths. This distribution is culled from experimental data - in this case, the material considered was Alloy 600.

⁹⁷See: Nishitani, H., and Y. Murakami. “Stress intensity factors for elliptical and semi-elliptical cracks.” Transactions of the Japan Society of Mechanical Engineers 40 (1974): 31-40, [128].

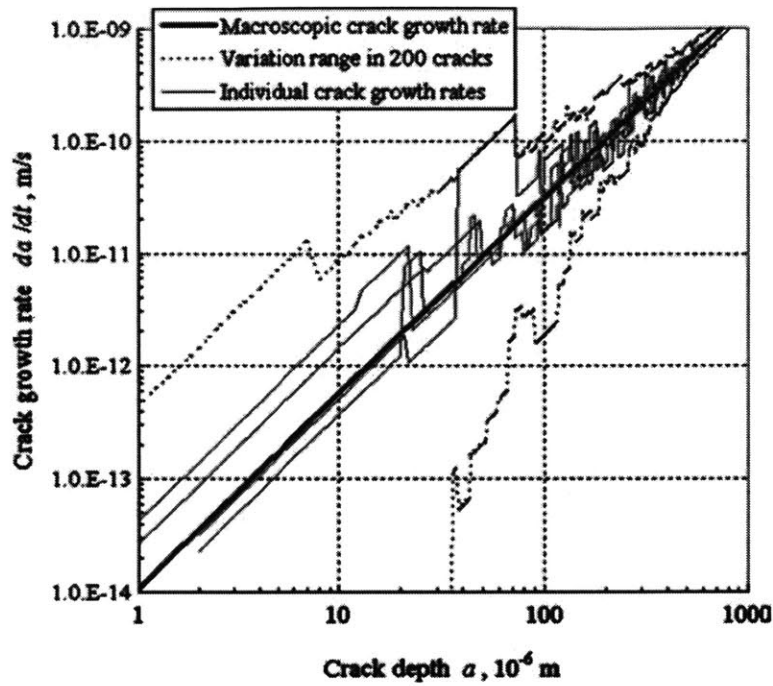


Figure 61: The result of single-crack simulations by Kamaya and Kitamura is plotted. The solid black line shows the macroscopic crack growth rate predicted by the simulation. The dotted lines showed the variation in crack growth rate at a given crack depth, as calculated for 200 crack simulations. The solid blue lines show individual crack growth rates, while the dotted lines graph the maximum and minimum values of da/dt for 200 simulated cracks.

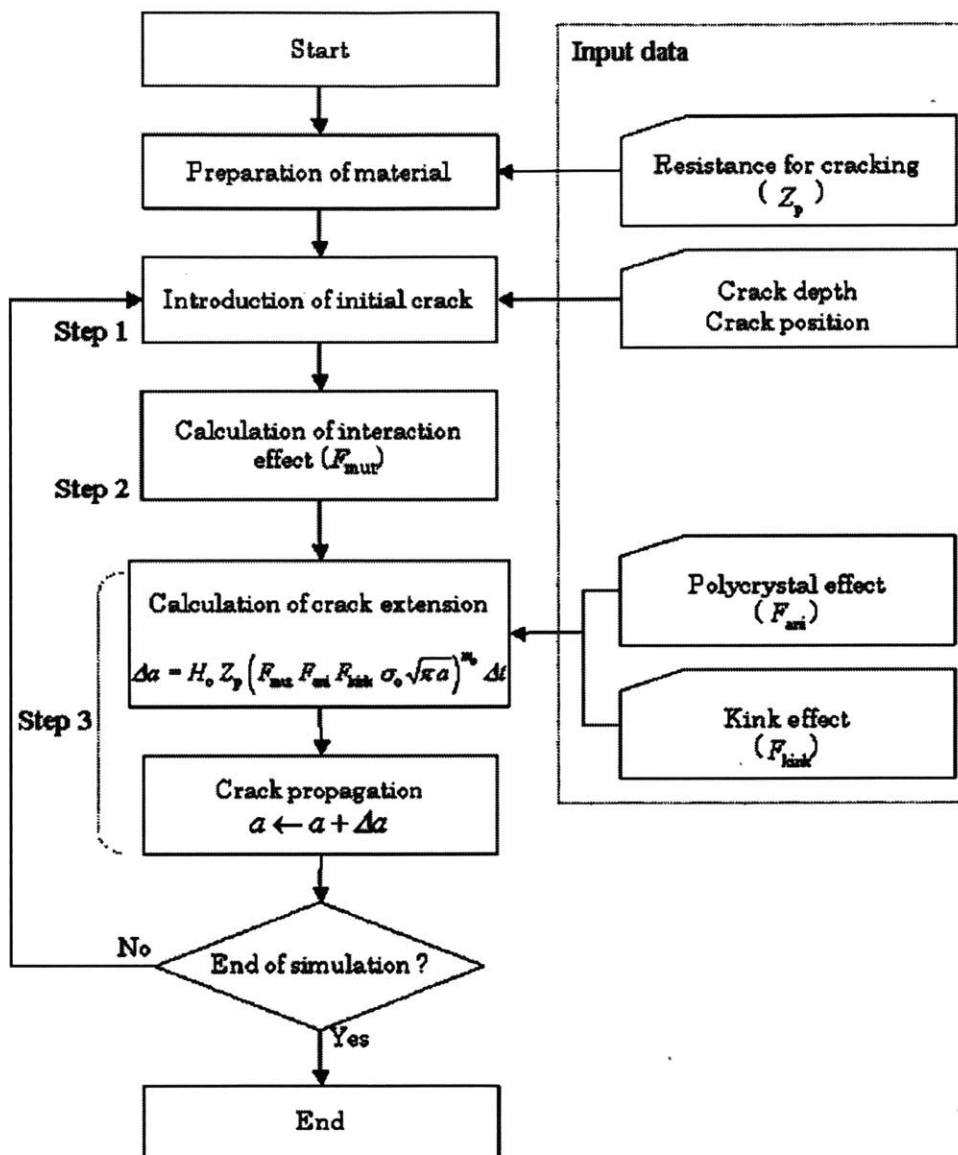


Figure 62: The simulation begins by setting the material characteristics. The initial depth of a crack is set to be the length of a grain boundary. This length is selected randomly from a distribution of grain boundary sizes appropriate for the material. The interaction effect is calculated, followed by the calculation of Δa . [69]

The result is Equation (188).

$$\Delta a = DK_s^m \Delta t = \underbrace{H_o}_{D_o C^m} Z_p (F_{\text{mut}} F_{\text{ani}} F_{\text{kink}} \sigma_o \sqrt{\pi a})_p^m \Delta t \quad (188)$$

It was found that a Gumbel distribution could be used to accurately describe the distribution of maximum crack depths obtained by the simulation. The authors suggest that Gumbel statistics could therefore be useful to predict the largest crack expected to be observed in a component undergoing SCC.

The authors drew several conclusions from these simulations. First, they found that in order for a large crack to form, the initial crack must have undergone continuous fast growth while it was still shallow (less than 100 μm). For this reason, it was important to quantify the fluctuations in observed crack growth rates in the early stages of propagation, in order to better predict the occurrence of large cracks. It was also found that the presence of multiple cracks tended to increase the growth rate of large cracks.

7.9.2 Wenman, 2007: A finite element approach to studying SCC

M. R. Wenman et al. used finite element analysis to investigate chloride-assisted transgranular SCC (Cl-TGSCC) in Type 304 stainless steel piping [77].

An ABAQUS finite element model (FEM) was made to match the exact dimensions of a machined Type 304L pipe sample that was used for the experiments associated with this research project. The authors describe the inputs and subroutines they started with to carry out this research [77]. This work outlines a method for modeling TGSCC in an arbitrary geometry with a complex residual stress field using finite element techniques.

A residual stress field was imposed on a FEM of a pipe pipe during a loading phase by constraining the bottom half while compressing the top half by 2 mm. When the FEM of the pipe was unloaded, plastic deformation remained. Misfit between the plastically

deformed elements and the unaffected, still-elastic elements caused a residual stress state.

To simulate pitting, certain elements in the mesh were removed. To simulate the chemistry and material variations that change the likelihood of pitting across a surface, a random number was assigned to each element. Numbers closer to 1 indicated that the element was more susceptible to pitting. Only elements in the two element rows adjacent to the surface were able to “pit,” i.e. be removed.

The criteria for pitting was as follows:

- The random number associated with the element is greater than 0.8
- The plastic strain at the element is greater than 10^{-4}
- The element is load bearing

Next, stress was redistributed. Cracking was assumed to occur if high stress elements were concentrated around deep pits. Cracks grew via the deletion of adjacent elements. The residual stress field in the model influenced the way in which the crack grows. It was found that if the ratio of actual stress to yield stress did not exceed 0.65, cracking did not occur. In a real situation, the authors suggest that this ratio would relate to the stress required to fracture the oxide film at the crack tip. For the purposes of modeling, it is also noted that changing the mesh size affects the calculation of the stress field.⁹⁸

The criteria for cracking was as follows:

- $\sigma_{\text{eq}}/\sigma_y > 0.65$. σ_{eq} was the current equivalent stress, and σ_y is the new yield stress.
- The element is near a deleted finite element.
- Resultant stress normal to the possible path was positive and > 120 MPa. Negative stresses impede crack growth.

⁹⁸Here, the finer mesh elements had a size of 20–40 μm , which is much larger than the average crack tip size, which is on the order of 1 μm . However, the mesh elements were suitable for modeling crack growth, as the elements were on the same order of size as actual grains. The “macrostress gradients” are the primary driver of crack growth behavior.

The authors note that this is in accordance with the corrosion-enhanced plasticity model proposed by T. Magnin et al.⁹⁹

A partial view of the inner diameter of the FEM pipe at two timesteps, showing the progression of pits and cracks and the associated stress maps, is shown in Figure 63.

Additional results are shown in Figure 64. (a), (b), (c), and (d) represent the 10 o'clock position on the FEM pipe at increasing timesteps. Cracks are shown to propagate through the material, and their direction is influenced by local stress fields, which are changed in time by the cracks themselves. A local plastic zone is created in the vicinity of the point at which two cracks combine.

In the view of the authors, a tensile triaxial stress is required for SCC propagation. SCC retardation may occur if any of the three principal stresses is compressive.

⁹⁹In this view of transgranular SCC, dislocation mobility is enhanced at the crack tip due to the dissolution processes occurring there. The increased mobility of the dislocations leads to an increase in plasticity. In steels (Type 316 is an example cited by the authors), the dislocations pile up, and brittle fracture is possible. See:

- T. Magnin, R. Chieragatti, and R. Oltra, "Mechanism of brittle fracture in a ductile 316 alloy during stress corrosion," *Acta Materiala*, **38**(7), 1990, 1313-1319, [124].
- T. Magnin, A. Chambreuil, and B. Bayle, "The corrosion-enhanced plasticity model for stress corrosion cracking in ductile fcc alloys," *Acta Materiala*, **44**(4), 1996, 1457-1470, [125].

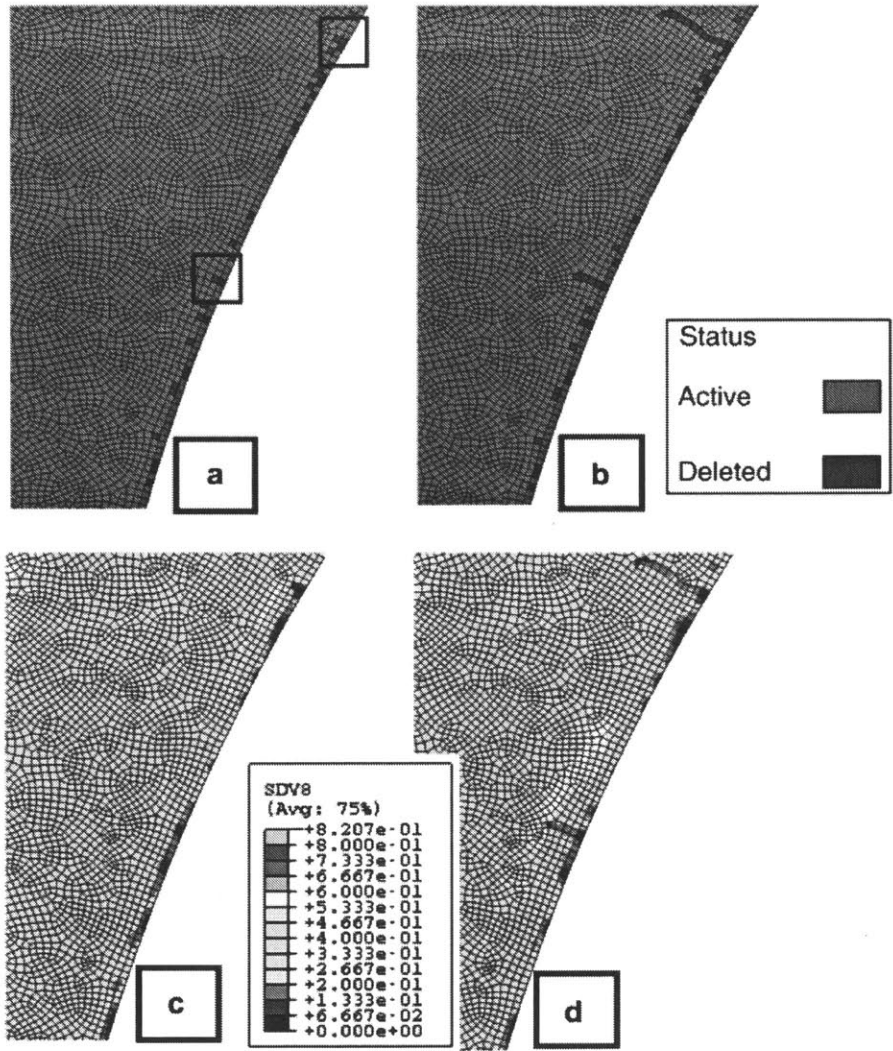


Figure 63: In (a), elements were randomly deleted from the first two rows. (b) shows the model after several timesteps have passed and cracks have begun to progress. (c) and (d) show the model at the same timesteps as (a) and (b), only this time, mapping the elements based on ratio of their calculated stress to the yield stress. [77]

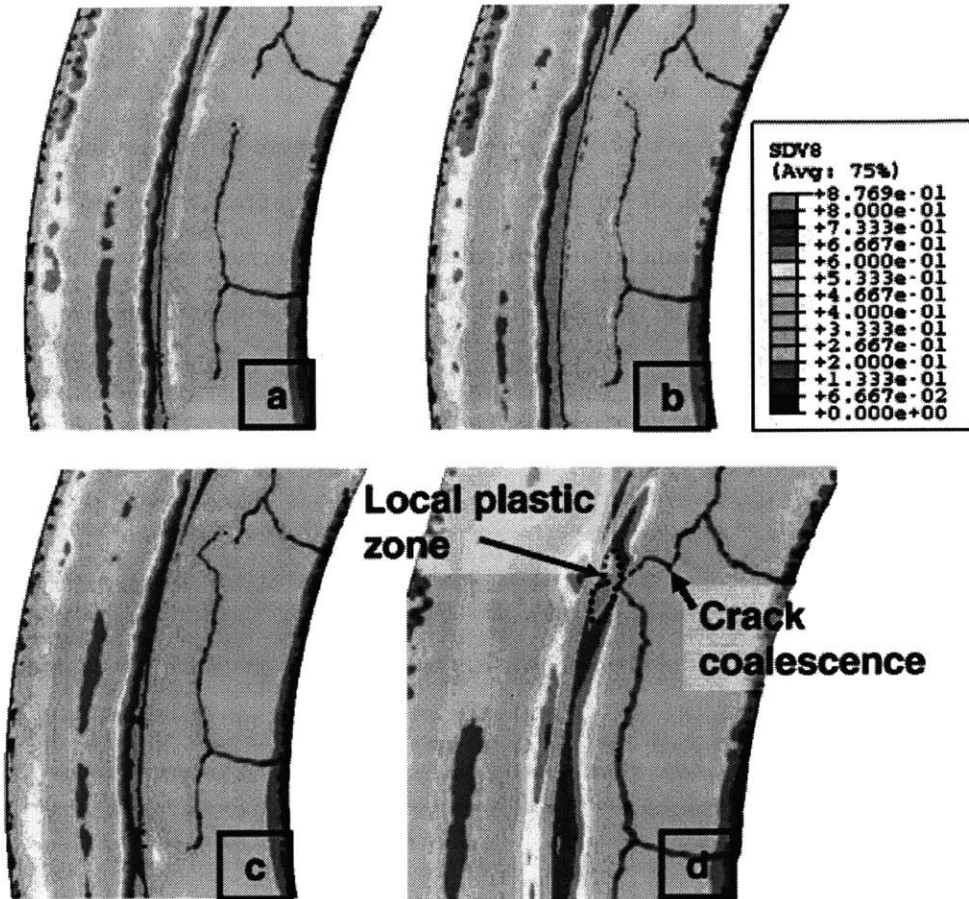


Figure 64: Increasing timesteps at the 10 o'clock section of the FEM pipe. Cracks progress, and their local stress fields influence each other's growth. Local plastic zones may be created. [77]

7.9.3 Zhang et al., 2009: Simulating surface corrosion damage

This paper used Monte Carlo techniques to simulate surface corrosion in aluminum alloys. Simulation results were compared with experimental results [78].

In the experiments, aluminum alloy samples were exposed to EXCO solution at various temperatures and time durations. Observation of the corroded surfaces allowed a calculation of the “corrosion damage ratio,” which is the ratio of corroded surface area to total surface area (see Table 42 for all pertinent equations and definitions for this section).

Equations were then determined to model the evolution of surface corrosion in a simulation. Assuming that the volume of each corrosion pit grew according to the usual Arrhenius and Faraday behavior (see Table 42), it was found that the pit depth at the i^{th} timestep in the simulation, c_i , could be expressed as:

$$c_i^3 = c_0^3 + \frac{3}{2\pi\phi^2} \frac{MI_{P_0}(k)}{n\mathbf{F}\rho} \exp\left(-\frac{E_a}{RT}\right) t \quad (189)$$

Variable definitions are provided in Table 42. Pitting current constant I_{P_0} is a random parameter, and is the cause of variation in c_{itp} , which is the pit depth at a target time period. The corrosion ratio can then be expressed as a function of these pit depths:

$$\alpha = \frac{\pi\phi^2}{A} \sum_{i=1}^N c_i^2 \times 100\% \quad (190)$$

To incorporate this into a Monte Carlo simulation, pit depth was reframed as a cumulative distribution function:

$$F(c_i) = P(c_i \geq c_{itp}) \quad (191)$$

$F(c_i)$ is the probability that c_{itp} is less than or equal to the pit depth calculated by Equation (189). The pit depths follow a normal distribution if each pit is assumed to grow

Table 42: Equations and variable definitions of the Zhang model (Section 7.9.3)

| | |
|-------------------------------|---|
| Corrosion damage ratio, v.1 | $\alpha = \frac{1}{A} \sum_{i=1}^n A_{pi} \times 100\%$ |
| Surface area of i^{th} pit | $A_{pi} = \pi a^2$ |
| a | Corrosion pit radius |
| n | Number of pits |
| Pit growth rate | $\frac{dV}{dt} = \frac{MI_{P_0}(k)}{nF\rho} \exp\left(-\frac{E_a}{RT}\right)$ |
| V | Pit volume |
| M | Molecular weight |
| I_{P_0} | Pitting current constant |
| F | Faraday's constant |
| n | Valence |
| ρ | Alloy mass density |
| Pit volume | $V = \frac{2}{3}\pi a^2 c$ |
| c | Pit depth |
| ϕ | Aspect ratio; $= \frac{a}{c}$ |
| Pit depth | $c_i^3 = c_0^3 + \frac{3}{2\pi\phi^2} \frac{MI_{P_0}(k)}{nF\rho} \exp\left(-\frac{E_a}{RT}\right) t$ |
| Corrosion damage ratio, v.2 | $\alpha = \frac{\pi\phi^2}{A} \sum_{i=1}^N c_i^2 \times 100\%$ |
| Corrosion damage ratio, v.3 | $\alpha = \frac{\pi\phi^2}{A} \left\{ \sigma^2 \sum_{i=1}^N \left[\left(\frac{c_i - \mu}{\sigma} \right)^2 \right] + 2\mu \sum_{i=1}^N c_i - N \cdot \mu^2 \right\} \times 100\%$ |
| N | Number of pits per unit area |
| σ | Standard deviation, when normal distribution describes pit depths |
| μ | Mean pit depth, when normal distribution describes pit depths |
| CDF of pit depth | $F(c_i) = P(c_i \geq c_{itp})$ |
| $F(c_i)$ | Probability of a pit depth at $t =$ target period (tp) |
| CDF of corrosion damage ratio | $F(\alpha) = P(\alpha \geq \alpha_{itp})$ |

independently of the others. If μ and σ^2 are the mean and standard deviation of this distribution, respectively, then the corrosion ratio of the metal surface at timestep i can be described as:

$$\alpha = \frac{\pi\phi^2}{A} \left\{ \sigma^2 \sum_{i=1}^N \left[\left(\frac{c_i - \mu}{\sigma} \right)^2 \right] + 2\mu \sum_{i=1}^N c_i - N \cdot \mu^2 \right\} \times 100\% \quad (192)$$

When material and environmental parameters in the simulation were matched to those used in the experiments, it was found that the simulation produced corrosion damage results that were consistent with those observed in the experiments.

7.9.4 Horner et al., 2011: Finite element analysis of corrosion pits

This study is focused on turbine disc steels (3 NiCrMoV) that experience SCC, which initiate from corrosion pits. The authors used finite element analysis to understand the strain distribution near pits [51]. Two geometries were studied: a 100 μm deep pit and a 500 μm deep pit. Loading was varied for each, between 50%, 70%, and 90% of $\sigma_{0.2\text{YS}}$. These analyses allowed the authors to examine where plastic strain and maximum stresses were localized, in order to better understand the pit-to-crack mechanism of SCC.

Experimental exposure tests (in aerated 1.5 ppm chloride solution at a temperature of 90°C) had been carried out on disk steel at various exposure times and loads. Pits and cracks were quantified and measured. Finite element analyses (FEA) of the pits (Figures 65, 66) showed a localization of maximum strain near the pit walls, especially at higher stress levels. Interestingly, a majority of the cracks were found to emanate from the walls of the pits and not the bottom, as models commonly assume to be the case. Figure 67 shows tomographic scans and an SEM image of two pits with wall cracks.¹⁰⁰ The material

¹⁰⁰The turbine disc steel sample in the images of Figure 67 was exposed to 1.5 ppm chloride solution at 90°C for 2204 hours.

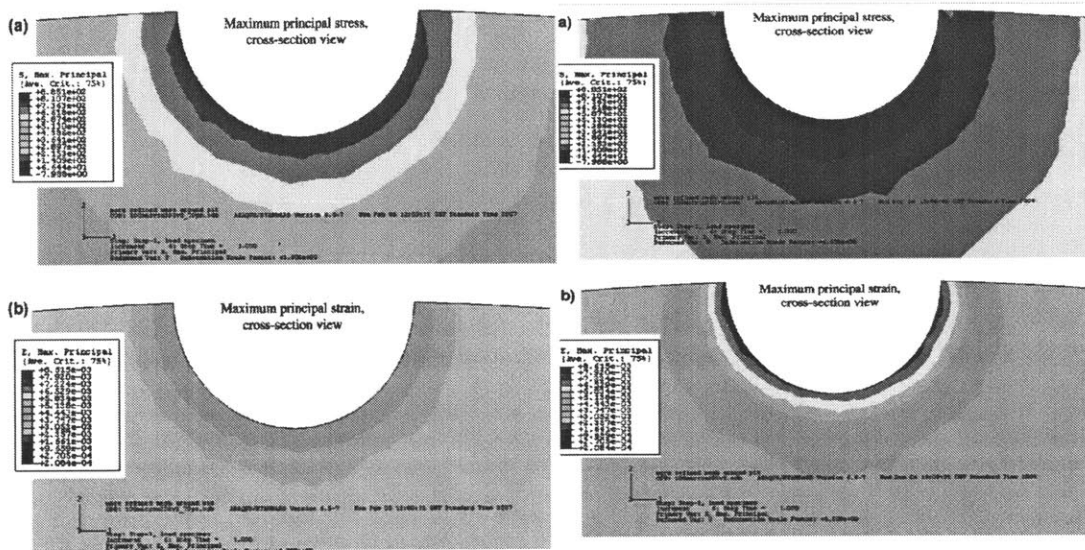


Figure 65: On the left, maximum principal stress and maximum principal strain distributions are shown for the 100 μm pit loaded to 70% $\sigma_{0.2YS}$. On the right, the same distributions are shown on the same pit, but this time, the pit has been loaded to 90% $\sigma_{0.2YS}$. Localization of maximum strain near the sides of the pit is apparent. [51]

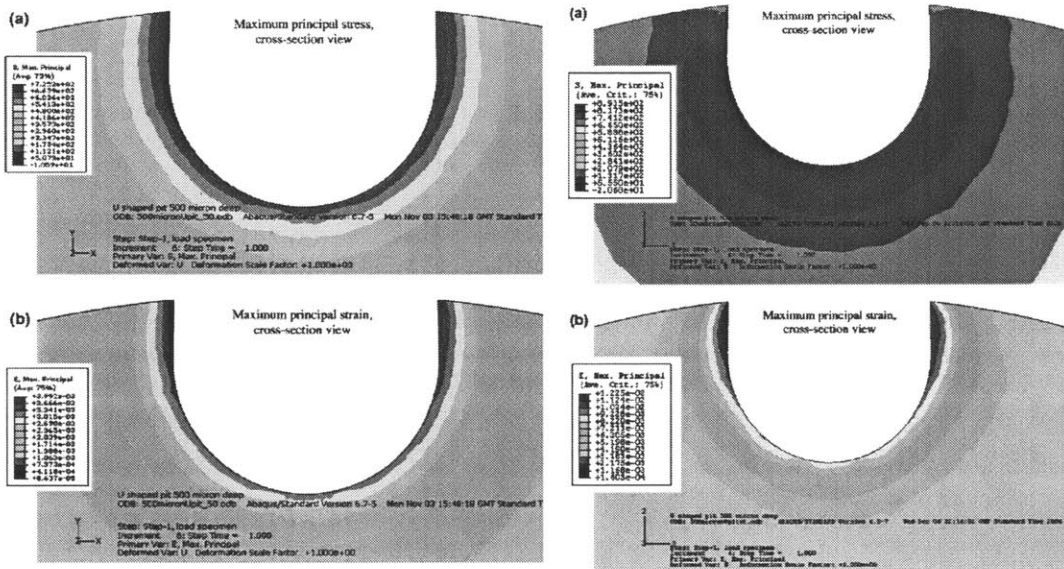


Figure 66: On the left, maximum principal stress and maximum principal strain distributions are shown for the 500 μm pit loaded to 50% $\sigma_{0.2YS}$. On the right, the same distributions are shown on the same pit, but this time, the pit has been loaded to 90% $\sigma_{0.2YS}$. Localization of maximum strain near the sides of the pit is apparent at the low and high strain levels. [51]

is expected to yield at the point of least constraint, and the maximum strains found at the pit walls in the FEA is consistent with the observation that cracks initiated from pit walls and not pit bases [51].

These findings are considered here because they raise an important point for any attempt to model SCC in a system where the cracks initiate from pits and not directly from the surface: is the common modeling assumption that the cracks develop at the pit base and propagate through the material normal to the surface always accurate? If a percentage of cracks grow parallel to the surface, this must be taken into account in the model. Models that assume every crack that develops grows straight through the material may significantly overestimate the likelihood of component failure.

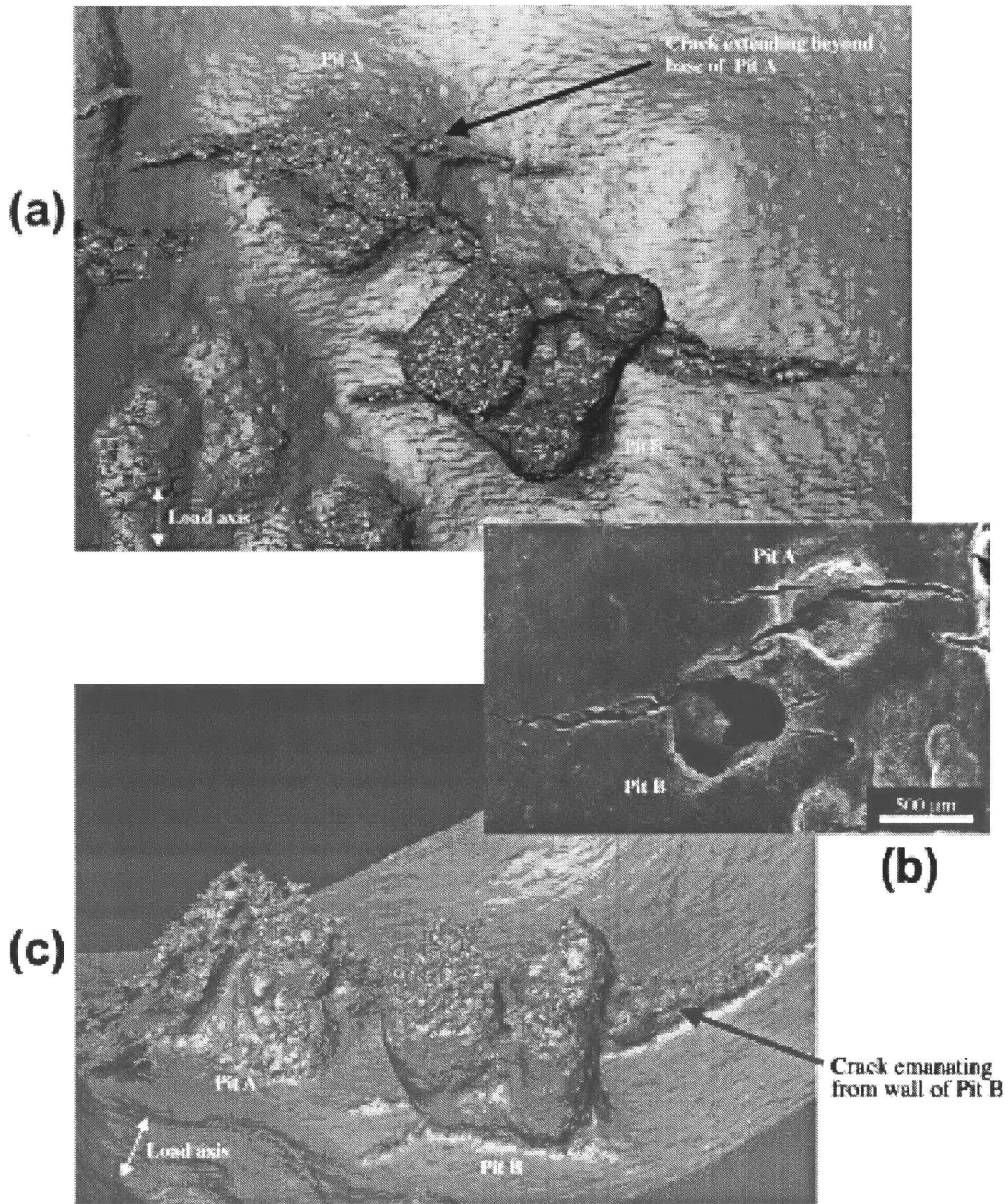


Figure 67: (a) Tomographic reconstruction of a crack through a pit. (b) SEM image of the pits in (a). (c) Tomographic reconstruction of pits with three wall cracks. [51]

7.10 Modeling SCC in other systems

The following models are concerned with a predictive, and in some cases probabilistic, treatment of SCC. Ahn [99] considers the theoretical maximum opening of SCC cracks in a canister after a seismic event imparts a large force to the canister. Harlow and Weir [79] developed a probabilistic model for SCC in aluminum. Hoch et al. [80] developed a useful set of assumptions for modeling pit growth in carbon steel waste containment. Cote et al. [81] and Jain et al. [82] developed a probabilistic method for predicting SCC in underground pipelines. Papakonstantinou and Shinozuka [83] adapted existing models and probabilistic techniques to modeling SCC in concrete/rebar systems. While these models are not directly applicable to the situation of concern in the *Life Prediction of Canister Material* project, their insights may still be adaptable to the modeling of SCC in the canister walls.

7.10.1 Ahn, 2013: The Sandia National Laboratory Model for SCC damage following a seismic event

The Sandia National Laboratory (SNL) model aims to predict the extent of crack opening that could occur in a canister that has undergone SCC precursor corrosion (such as pitting), and is then subjected to a seismic event [99].

Corrosion pits and manufacturing flaws are prerequisites for the development of SCC in this model. The SNL model does not provide a definitive model of pitting.¹⁰¹ Ahn also considers the effect of flaws from the canister manufacturing process, especially welding. Microscopic cracks may form at these flaws.

Ahn also considered the corrosion data from coastal environment exposure tests at Kure

¹⁰¹Instead, Ahn refers to the existing pitting models by Shibata (Section 7.4.1) and Macdonald et al. (Section 7.3.5). It is also mentioned that pitting is limited by repassivation of the metal. Pitting density may also be limited by the cathodic behavior of the pit walls when the pit base is anodic.

Beach.¹⁰² Expected pit sizes in sensitized Type 304 stainless steel were between 10 and 100 μm . Residual stresses in canister welds were assumed to be in a range of 0 to 600 MPa.¹⁰³ Ahn then used GoldSim Version 10.11 to determine the cumulative probability of finding a particular stress intensity factor (K) in a canister. These results are shown in Table 43. SCC was found to occur in the literature at K values between 0.5 and 7.0 $\text{MPa}\sqrt{\text{m}}$.¹⁰⁴

Table 43: Results of GoldSim study to determine probability of finding a given K in canister material [99]

| K | Probability |
|----------------------------------|-------------|
| 0.43 $\text{MPa}\sqrt{\text{m}}$ | 0.001 |
| 1.57 $\text{MPa}\sqrt{\text{m}}$ | 0.05 |
| 2.59 $\text{MPa}\sqrt{\text{m}}$ | 0.25 |
| 4.57 $\text{MPa}\sqrt{\text{m}}$ | 0.75 |
| 6.94 $\text{MPa}\sqrt{\text{m}}$ | 0.95 |

Crack propagation rates are expected to decrease as the crack progresses away from the weld area, where highest residual stresses occur. In a seismic event, the imposed stress would be strongest at the surface of the canister, so a crack propagating through-wall would undergo slower growth as it progressed toward the inner canister wall.

Ahn outlines a method for predicting the maximum opening area of existing cracks in a canister during a seismic event. First, it is noted that any existing cracks must be separated

¹⁰²See: Electric Power Research Institute (EPRI), "Effects of Marine Environments on Stress Corrosion Cracking Austenitic Stainless Steels," EPRI 1011820, Palo Alto, CA, 2005, [133].

¹⁰³This was based on CRIEPI research. See: K. Shirai et al., "SCC Evaluation of Multi-Purpose Canister," *Proceedings of 2011 International Radioactive Waste Management Conference (IIHLRWMC)*, Albuquerque, New Mexico, April 10-14, Paper No. 3333, 2011, [135].

¹⁰⁴See the following references for this data:

- Electric Power Research Institute (EPRI), "Effects of Marine Environments on Stress Corrosion Cracking of Austenitic Stainless Steels, EPRI 1011820, Palo Alto, California, 2005, [133].
- K. Shirai, J. Tani, T. Arai, M. Wataru, H. Takeda, and T. Saegusa., "SCC Evaluation of Multi-Purpose Canister" *Proceedings of 2011 International Radioactive Waste Management Conference (IIHLRWMC)*, Albuquerque, New Mexico, April 10-14, Paper No. 3333, 2011, [135].
- Kosaki, A., "Evaluation Method of Corrosion Lifetime of Conventional Stainless Steel Canister under Oceanic Air Environment" *Nuclear Engineering and Design*, 238, 1233-1240, 2008. (Reference [84])

by a minimum distance (in Ahn's work, this is considered to be approximately equal to the thickness of the canister), because as cracks grow and relieve the existing stress in the material near the crack, there is no longer sufficient stress to drive another crack nearby.

The width of an existing crack is described as:

$$w(t) = C\sigma a(t)/E \quad (193)$$

where σ is stress, E is Young's modulus, C is a geometric constant, and t is time. The crack area, which is equivalent to the product of crack length and crack width, is then summed across all cracks in order to calculate the total crack opening. The maximum possible crack opening is limited by the maximum possible density of cracks, which is limited by stress relaxation around each crack. For stainless steels, Ahn calculated that the expected maximum possible ratio of the opening area of multiple cracks to unit area in the weld and HAZ was 1.2×10^{-3} , given 170-310 MPa of applied stress.

This model is intended to predict maximum possible damage due to SCC, and does not predict whether SCC will occur at a specific place or how it will develop and progress. In practice, its main utility would likely be in assessing the maximum (worst-case scenario) possible release of radionuclides and fill gas from a canister if it was susceptible to SCC.

7.10.2 Harlow and Wei, 1998: A probabilistic model for corrosion pits in aluminum alloys

Harlow and Wei developed a probabilistic model for the growth of corrosion pits that initiate at constituent particles in aluminum alloys [79]. They analyze SEM images of aluminum samples to develop their model for SCC, and to model the clustering of these constituent particles.

In the Harlow and Wei model, pits nucleate on the bare surface in the vicinity of

exposed constituent particles. Particles may be anodic or cathodic with respect to the aluminum matrix, but anodic particles initiate self-terminating pits (dissolution of the particle tends to terminate pit growth). The authors therefore focus on cathodic constituent particles. These cathodic particles promote dissolution of the surrounding matrix and promote pitting. Models for pit growth are discussed in the context of existing work on the topic, such as Kondo [18], Turnbull [31], and Engelhardt [30].

A key part of this model involved modeling the distribution of the particles and how they clustered. This may not be relevant to *Life Prediction of Canister Models*, unless it is decided that pits nucleate primarily at flaws in the material. If that is the case, this model will be revisited.

Harlow and Wei assume that pits in the aluminum grow at a constant rate governed by the pitting current, $\frac{dV}{dt} = \frac{MI_{\text{pit}}}{nF\rho}$, which in turn has an Arrhenius dependence on temperature. The pits are not assumed to hemispherical, but prolate spheroids, with $V = \frac{2}{3}\pi ab^2$, where a and b are half the length of the major and minor axes. Three methods are considered in order to determine the behavior of a and b in time.

In the first method, the aspect ratio is held constant: $b/a = \phi_k$ (where $\phi_k = 1$ would correspond to a hemispherical pit). Then, it is found that:

$$\frac{2}{3}\pi\phi_k^2(a^3 - aa_o^3) = \frac{MI_{P_0}(k)}{nF\rho} \exp\left[-\frac{\Delta H}{RT}\right] t \quad (194)$$

in which a_o is the original half-length of the pit's major axis. Pit depth is assumed to be equivalent to half the value of a . a is then expressed as:

$$a = C_1 + C_2 t^{1/3} \quad (195)$$

where C_1 and C_2 encompass material and environmental effects.

In the second method, the interaction of the growing pit with constituent particles embedded in the matrix is considered. As the pit grows, it interacts with more and more of these particles, which in turn affect its aspect ratio in a discrete manner as they are encountered by the pit.¹⁰⁵

The third method attempts to smooth the discontinuous volumetric growth rate in the second model, but is defined to be outside the scope of the author's work, and is only treated symbolically.

The authors then use their probabilistic pit nucleation model coupled to the historical growth models selected to create cumulative distribution functions for pit depth based on different values of the deterministic and random variables in the model. Sensitivity of the results to selection of the values and to choice of either of the first two methods is demonstrated. The authors mention that their results, and associated trends, are qualitatively consistent with typical observations, but this correlation is treated only anecdotally.

The size of particle clusters and the pitting current are then modeled as random variables.

7.10.3 Hoch et al., 1997: Mathematical models for predicting corrosion in carbon steel used fuel overpacks

Hoch et al. investigated the prediction of carbon steel corrosion using mathematical models [80]. The carbon steel in question was intended for the use of underground HLW disposal in Japan. A computer model is utilized to model pit growth. Many simplifying assumptions are made in order to carry this calculation, and the ones which could be relevant to corrosion modeling on the surface of the canister are listed here:

- The electrolyte solution is static.

¹⁰⁵The equations corresponding to this second method can be found on p.312 of [79], but are omitted here since this type of interaction is not expected to be relevant to the canister project.

- The “moving boundary” of the growing pit can be ignored because the pit growth rate is so much slower than the movement of ions within the pit.
- Only two dimensions are considered for ion migration.
- Geometry is simplified so that the pit is cylindrically symmetric.
- Cathodic reactions occur on the bulk surface only. Anodic reactions occur in the pit only.
- The electrolyte solution in the pit is in equilibrium with any solid phases in the pit.
- Metal potential remains fixed, and can be determined from balancing charges between the anode and cathode of the pit/bulk surface corrosion cell.

Efforts were also made to minimize the chemical species and reactions considered in order to simplify computation. Hoch et al. describe three timescales that are relevant to the modeling of corrosion pits. On the first timescale, chemical reactions are of concern. On the second, the transport of species in the pit matter. On the third and longest timescale, the movement of the pit walls are considered.

The program CAMLE (Corrosion and Migration in Localized Environments) was used to solve for the concentration of species in the pit and the potential. Pit growth rate is calculated by determining i_{corr} on the wall. The processes modeled in the simulation is shown in Figure 68. The anodic current was found to be highest on the pit walls, and lowest at the pit base. The authors also carried out simulations to understand how pitting behavior changed when various input parameters were changed, and found that the pit growth rate increased with cathode size and the diffusion constants of the species involved in the anodic and cathodic reactions.

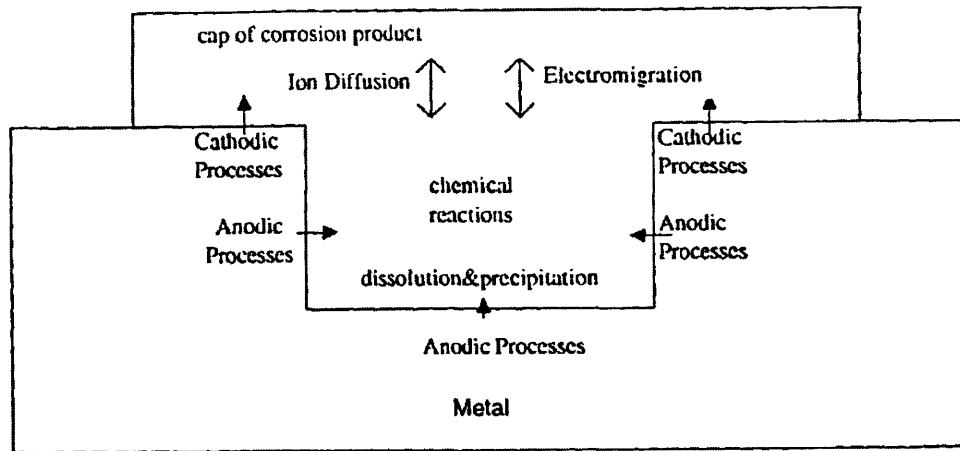


Figure 68: This figure depicts a simplified pit, and the processes being modeled by Hoch and Honda's CAMLE simulation. [80]

Their results were compared to experimental pitting data, and it was found that the CAMLE model underpredicted observed pit depths. However, with proper parameter input, this is one tool that could be useful for modeling the local electrochemical environment around pits, and the effects of that environment on pit behavior.

7.10.4 Probabilistic approaches to predicting TGSCC in underground pipelines

Cote, Ferguson, and Tehsin considered pipelines that could undergo TGSCC if exposed to the right combination of environment and residual and applied tensile stress [81]. The goal of the statistical predictive model (SPM) is to relate the stress, environment, and operational factors to the likelihood of SCC developing in the pipelines.¹⁰⁶ This informs which sites are selected for inspection for SCC damage. Multiple input variables (predictor variables) were considered, and determined experimentally at pipeline sites. Most of

¹⁰⁶The statistical predictive model was developed by CIMARON Engineering Limited and the Statistical Consulting and Research Laboratory at the University of Calgary.

these variables were specific to pipeline technology, although some (such as potential) are applicable to SCC in the canisters.

Experimental data was collected from selected pipelines (environmental and material data, in addition to the presence and extent of SCC). Linear regression was performed with the goal of understanding the correlation between input variables (like pipeline geometry and local environment) and the presence of SCC. The probability of occurrence (PoO) of SCC was then calculated as follows:

$$\text{PoO} = \frac{e^{g(x_1, x_2, \dots, x_n)}}{1 + e^{g(x_1, x_2, \dots, x_n)}} \quad (196)$$

where x_n are the values of the predictor variables and:

$$g(x_1, x_2, \dots, x_n) = \beta_0 + \beta_1 x_1 + \beta_2 x_2 + \dots + \beta_n x_n \quad (197)$$

with β_n coefficients determined during statistical analysis using logistic regression. The goal of this approach is to determine the dependence of the SCC response variable, which is binary (SCC occurs or SCC does not occur) on various inputs. This approach could be useful for understanding the relative importance of different material and environmental parameters in experimental SCC tests.

In 2013, Jain et al. presented a method for using a Bayesian model to predict the likelihood of SCC in pipeline steel [82]. This model allows for the updating of probability as real observations of SCC are made. It is also noted that the Bayesian approach accounts for uncertainty in the input parameters. Unquantified uncertainties represent a significant limitation to the utility of probabilistic SCC models. The authors develop a Bayesian network using the Bayes rule, which is given in this paper as:¹⁰⁷

¹⁰⁷The original source variable definitions are kept here for ease of cross-referencing.

$$P(H|e) = \frac{P(e|H) \cdot P(H)}{P(e)} \quad (198)$$

The terms in Equation (198) are defined in Table 44.

Table 44: Bayesian terms used by Jain et al. (Equation (198))

| term | definition |
|-------------|---|
| e | Outcome with probability $P(e)$ |
| H | Hypothesis |
| $p(H)$ | The posterior probability distribution |
| $P(H e)$ | Probability of H occurring given that observation e is true |
| $P(e H)$ | Probability of H given e , or “likelihood function” |

In the Bayesian network approach taken by Jain et al., variables (or “nodes”) are represented by a probability density function (pdf) instead of a single quantity. Importantly, when a quantity is unknown, a flat pdf can be used in the calculation, allowing greater ability to study SCC behavior when only some quantities are known. Another advantage of this approach is the ability to run the model in “two directions,” namely, from the cause to the consequence, and from the consequence to the cause. This allows the prediction of behavior from input parameters, but also the ability to study known behavior and determine which parameters had the most influence. The two major steps of building a Bayesian network model for SCC involve establishing the relationships between inputs and outcomes, and determining the pdf at each node.

Bayesian networks were developed for both the environment and the stress. These networks were used as inputs in a crack growth rate model, which was then used to predict SCC failure. The Bayesian network used by the authors to predict maximum stress in a pipeline is shown in Figure 69.

As is the case with the canisters, stresses are one of the primary inputs to the SCC

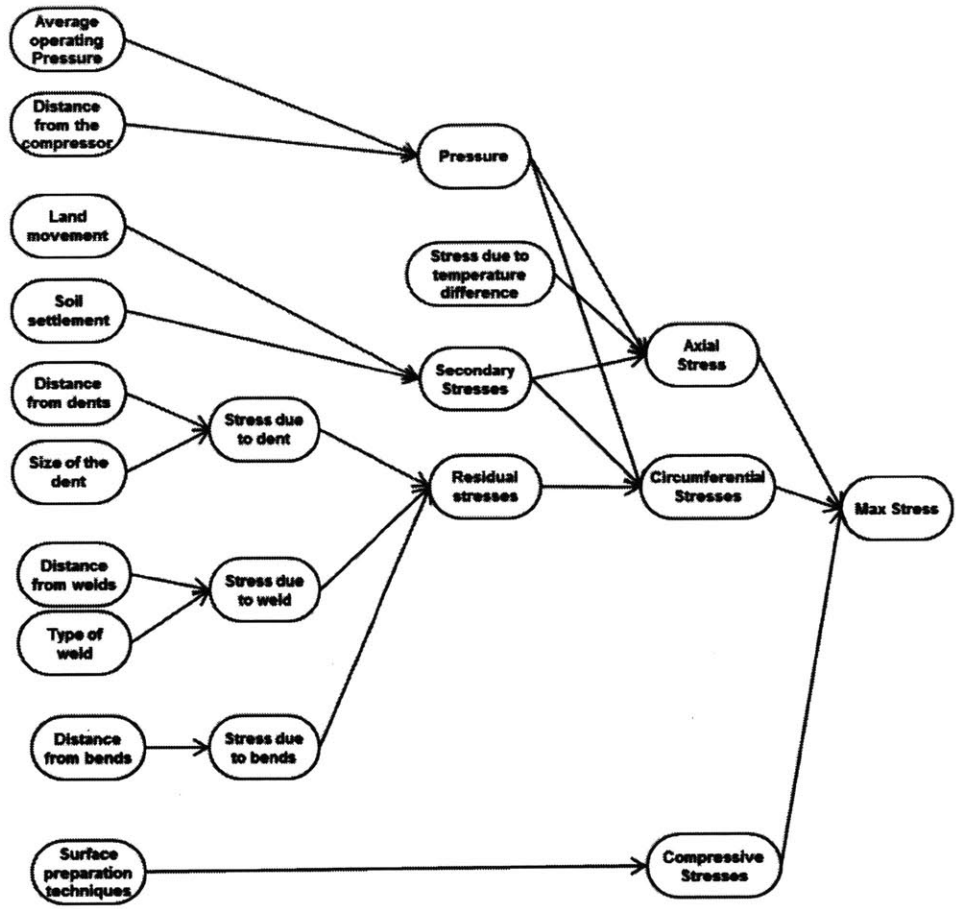


Figure 69: This is the subset of the Bayesian network developed by Jain et al. that pertained to the estimation of the maximum stress in the pipeline wall. A distribution or range can be determined for each input, or node. The computer program HuginExpert was used to carry out this analysis. [82]

model, although the causes of the stress are quite different in a pipeline. Stresses can be input as a distribution or a range. The primary environmental inputs are potential and the pH and carbonate concentration of the solution in contact with the pipeline steel.

SCC was assumed to progress in four stages: initiation, initial crack growth to a critical size, slow crack growth as work hardening or film formation occurs (plus possible coalescence of cracks), and rapid crack growth, leading to SCC failure.

The authors also provide a method for determining the pdf to be used for crack growth rates (CGR) in the environment of interest (high pH environment at a buried pipeline). In the first two stages of SCC described above, the growth rate is zero in Stage 1 and negligible in Stage 2 (Stage 2 is very short, so the authors progress directly to Stage 3 following crack initiation). In Stage 3, CGR was assumed to be dependent on temperature, maximum possible current, and stress. These three inputs determined the upper bound of the Stage III CGR, which is expressed as:

$$\log_{10}(\text{CGR}) = a \log_{10}(i_{\text{corr}}) + b\sigma^n + cT \quad (199)$$

where the constants (a, b, n, c) are fit to experimental data from slow strain rate tests.

In the final stage, Equation (199) was used as the lower bound of the CGR, and the Faraday limit was used as the upper bound. As more specific CGR distributions become available, they can simply be updated in the computer model. The program used by the authors was HuginExpert.

This approach is capable of accounting for the multiple interconnected input parameters that affect SCC behavior. It can accommodate unknown input parameters and the uncertainty associated with input parameters that are known to have a range of possible values. When implemented as a computer model, the pdf associated with each node can be updated as more information becomes known.

7.10.5 Papakonstantinou and Shinozuka, 2013: A probabilistic model for corrosion-assisted cracking in reinforced concrete structures

Papakonstantinou and Shinozuka proposed a probabilistic model for the occurrence of chloride-induced SCC in the reinforcing steel of concrete structures [83]. Rapid, localized corrosion of the reinforcing steel occurs when the rebar loses passivation due to carbonation or the presence of chlorides that enter into the concrete from the surrounding environment.

As with the canisters, the first question to address is the length of time it takes for a sufficient concentration of chlorides to be present at the surface of the steel rebar. However, this is governed by the diffusion of chlorides through concrete, which is quite a different situation than the deposition of chlorides onto the canister surface. Multiple models for corrosion current in rebar are considered, and the authors move forward using one proposed by Liu and Weyers.¹⁰⁸ Their empirical model for i_{corr} was fit to experimental data and depends on chloride content as a function of rebar depth, temperature, ohmic resistance of the concrete over the rebar, and time. i_{corr} and the ohmic resistance are found to be lognormally distributed. The authors suggest that a truly comprehensive model for i_{corr} would include the effects of oxygen availability, and be valid for a wider range of environments. The specifics of their formulation are only partially applicable to the canister project, as they are concerned more with the volumetric change associated with the iron in the steel corroding into various iron oxides and iron hydroxides, and the pressure exerted on the concrete from this expansion, causing cracking in concrete. These cracks, in turn, affect the transport of chlorides, oxygen, and other species to corrosion surfaces.

However, due to the large amount of uncertainty encountered in both processes due to

¹⁰⁸The Liu and Weyers correlation for corrosion current is one of many possible models. In this situation, the corrosion current is dependent on variables unique to the rebar-in-concrete situation. The authors note that this model does not account for the effect of oxygen availability on the surface of the rebar, and that ohmic resistance is a function of chloride content and temperature. The reference for Liu and Weyers is: T. Liu and R. W. Weyers, "Modeling the dynamic corrosion process in chloride contaminated concrete structures," *Cement and Concrete Research*, **28**, 1998, 365 - 379, [91].

the many material and environmental parameters involved, the large variability in these parameters, and the difficulty in measuring them accurately, the attraction of stochastic models is common to both processes. In this paper, the authors recognize that many of the parameters being used as inputs to the model meant to predict corrosion behavior do not follow simple normal distributions. The authors recognize, therefore, that a generalized linear model (GLIM) may be more appropriate for incorporating the scatter of input parameters. GLIM is similar to ordinary linear regression, but is more robust in that it allows for the response variable to have variance that changes with the value of the prediction. It is appropriate, for example, when trying to model a process that is known to produce skewed results, such as crack width predictions, wherein no values below zero are possible, and there may be many cracks of small size, but few of larger sizes.

GLIM will be considered for the canister project, after taking into account the distributions of input parameters and an analysis of initial results is available.

7.11 Other corrosion prediction techniques

The following sections describe additional corrosion prediction techniques. In the first, Strutt, Nichols, and Barbier develop a method for predicting future corrosion behavior from observed corrosion profiles, using a combination of standard distributions and extreme value statistical distributions [92]. In the second, the quantification of uncertainty is considered as it pertains to corrosion predictions [93]. They are included here because these techniques may prove insightful during the development of the SCC model for the canister material.

7.11.1 Strutt, Nicholls, and Barbier, 1985: Predicting corrosion from corrosion profiles

Strutt, Nicholls, and Barbier developed a method to predict the risk of exceeding a certain corrosion penetration depth in a sample through analysis of that sample's corrosion profile [92]. It is also demonstrated how an extreme value distribution can be used in conjunction with a more standard distribution to accurately describe the corrosion behavior of samples that corrode by multiple mechanisms and/or exhibit corrosion damage that is not entirely at surface level. This method was validated via analysis of carbon manganese steel samples exposed to CO₂-acidified seawater. A statistical analysis of the corrosion profiles of these samples enabled a prediction of their future corrosion behavior.

This analysis is important when corrosion is not uniform. For example, observation of a pitted surface may reveal that the pits have variable depths. If time-to-failure is a function of the deepest pit, it is necessary to predict the depth of the deepest pit at a future time. This information may be obscured by simply estimating an average corrosion rate (as a function of metal weight lost per unit time) and using that quantity to predict failure.

The volume of corroded metal over a sample area A_o can be expressed as:

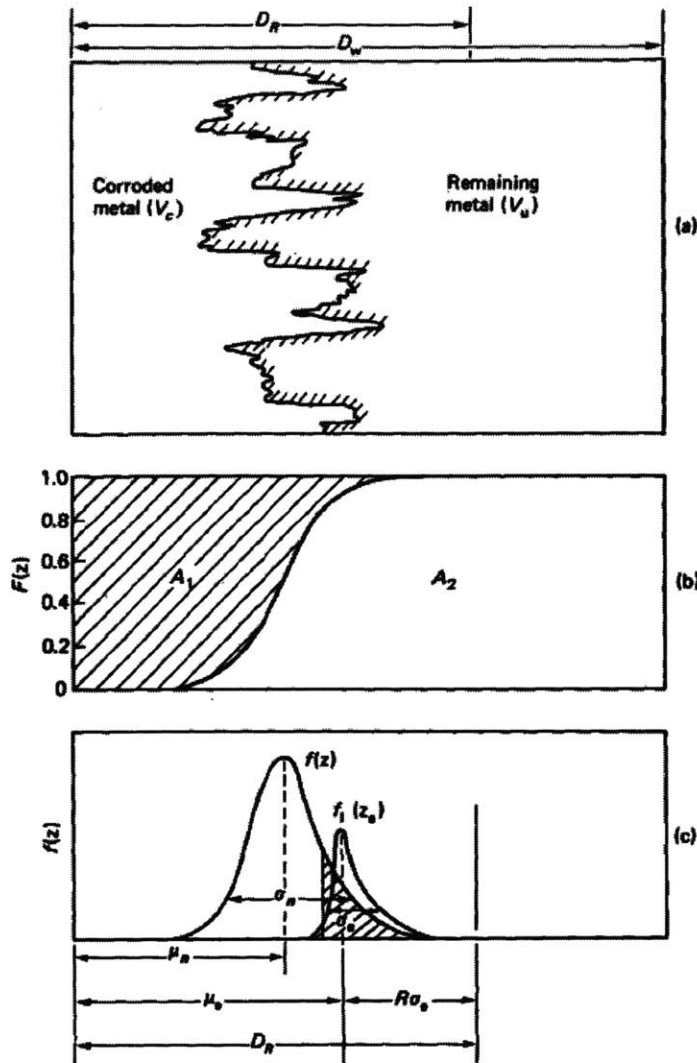


Figure 70: An example corrosion profile is shown in the top image. V_c is the volume of corroded metal and V_u is the volume of uncorroded metal. D_w represents the original thickness of the sample before corrosion began. D_R is the maximum penetration depth for a given risk value α . (b) shows the cumulative distribution function $F(z)$, where z is the depth variable. It is obtained by plotting corrosion depths from lowest to highest against $i/(n + 1)$, with n the total number of depths sampled. In (c), $f(z)$ shows the probability density function (pdf), and $f_I(z_e)$ shows the extreme value probability density function. [92]

$$V_c = \int_{A_o} z(A)dA = A_o \left[D_w - \int_{z=0}^{z=D_w} F(z) \cdot dz \right] \quad (200)$$

where $z(A)$ is the corrosion depth and D_w is the original, uncorroded sample thickness. $F(z)$ is the cumulative distribution function (CDF). The volume of uncorroded metal remaining, V_u , in the sample can be expressed as:

$$V_u = A_o \int_0^{D_w} F(z)dz \quad (201)$$

An example cumulative distribution function and probability distribution function for a corroded surface are shown in Figure 70.

The authors point out that this type of analysis is not capable of accurately describing corrosion profiles which include “subsurface lateral attack” (such as IGSCC) instead of, or in addition to, an open-pit, generally uniform surface corrosion profile. Another limitation is the failure of typical statistical models (examples given include normal, log normal, and Weibull distributions) to accurately describe the observed corrosion profile in many real-world applications, especially when more than one corrosion mechanism is operating.

A more accurate distribution is developed here. The maximum tail of the pdf is fit to a type I extreme value function, which has the CDF F_I :

$$F_I(z_e; \mu_e, \sigma_e) = \exp \left(-\exp - \frac{(z_e - \mu_e)}{\sigma_e} \right) \quad (202)$$

where μ_e is the location parameter, σ_e is the scale parameter for the distribution, and z_e is the extreme depth value. The authors describe the significance of $F_I(z_e)$ thusly: The value of $1 - F_I(z_e)$ is the risk α of taking some z_e as the maximum allowable penetration in a component, because it is the likelihood of observing a maximum depth that is greater than z_e .

For a given risk value α , the maximum penetration depth D_R is:¹⁰⁹

$$D_R = \mu_e + \sigma_e(-\ln(-\ln(1 - \alpha))) \quad (203)$$

These methods could be utilized in the *Life Prediction of Canister Material* project as a way to estimate maximum expected pitting depth from the corrosion profiles of experimental samples. The maximum depth predicted by this method could also be compared to the maximum depth predicted by a mathematical model.

7.11.2 King et al., 2012: Uncertainty in performance predictions based on experimental data

King et al. consider the uncertainty that arises when researchers use small experimental data sets to predict material performance, particularly in the context of nuclear materials work [93]. The uncertainty in such predictions increases as the extrapolation becomes further removed from the conditions particular to the original data, and methods of uncertainty quantification are not especially well-developed. This paper is especially relevant to this project, because there is not an extensive set of data for canister material exposed for long times to representative environments, and yet there is a need to predict the canister's corrosion behavior out to tens and hundreds of years.

In one example, the authors consider predictions of components with long service lives. In order to do material testing for these components, researchers must typically carry out accelerated testing, since it is impractical to test the material for the duration of the component service life. However, the methods associated with accelerated testing (for example, increasing the temperature of the environment, or increasing frequency loading

¹⁰⁹The authors give an example of how to obtain the expression for D_R when the initial pdf can be described a standard normal distribution [92], 308.

in a fatigue test) might lead to results that aren't representative of material behavior in the unaccelerated conditions. This is the example provided that is likely the most relevant to this project, but the authors also consider issues like the validity of using high-dose-rate ion irradiation to simulate lower-dose-rate neutron irradiation, as well as situations in which continual approximations compound uncertainty in undefined ways.

If the physics are well characterized, the researchers can use a physics-based approach and incorporate well-defined uncertainties. They can then better quantify the uncertainties of their predictions. However, it is not always possible to know and quantify every uncertainty that could affect a model's predictions. The authors consider a simple example of a ballistic trajectory, and show that for a small testing domain, there are many possible models that could be found to reasonably fit the data (see Figure 71).

Other recommendations of the authors include peer review procedures for addressing uncertainties. One suggestion is to have different groups develop models independently, in order to compare the physics considered and the predictions that result. Ideally, it would be possible to build models that allow for the assimilation of additional data as it becomes available.

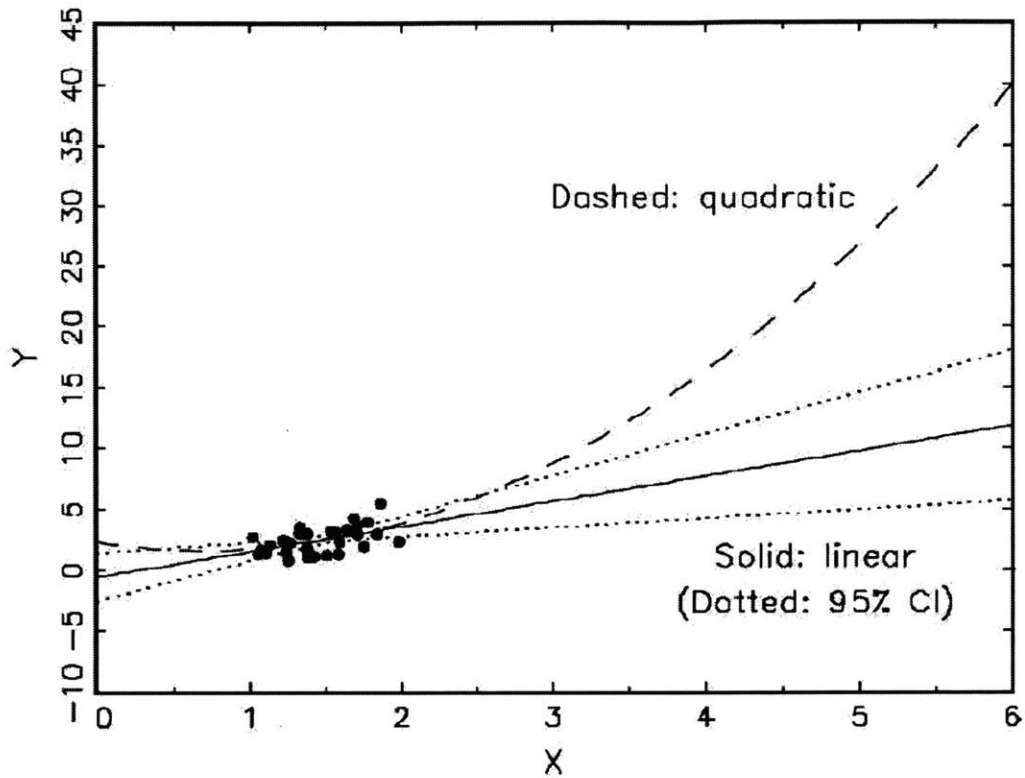


Figure 71: In this example, an example of a narrow data set (the clustered black dots) are fit to a quadratic and a linear model. In the range of the data set, both models look like equally good approximations. As the range is expanded, however, it is clear that the models predict very different behavior. In the case of a ballistic trajectory, the linear model would lead to erroneous predictions. The relevant physics should be carefully considered to constrain the model and inform the extrapolation, especially when there are multiple mathematical models that are consistent with the available data. [93]

7.12 Conclusions

The objective of this document is to understand and critically consider the major research efforts to model stress corrosion cracking, with particular attention given to models that emphasize the stochastic nature of this phenomenon. The ultimate goal of the *Life Prediction of Used Fuel Canister Material* research project is the development of a probabilistic model to predict the likelihood of SCC damage in canister welds and HAZ.

Accounting for the many factors that affect pitting and crack growth during the SCC is a significant challenge. It is one thing to create a semi-empirical model and fit parameters using experimental data for each different environment-material couple. However, it is quite another to be able to isolate each variable that affects pitting and crack growth and create a predictive model that allows an understanding of how SCC is affected when each individual variable is changed. The interactions between all the possible relevant factors - temperature, environment, local chemistry, microstructure, stresses, and so on - in SCC are highly complex.

The literature shows that there are many approaches to modeling SCC. First, many researchers focus solely on modeling one stage of SCC, such as pit growth or crack growth. If these models are selected for adaptation into the model for *Life Prediction of Used Fuel Canister Material*, they cannot stand alone. Additional models must be selected so that pit initiation, pit growth, crack initiation, and crack growth can be predicted. Which model is selected will depend on the model's consistency with relevant experimental data. The theory on which the model is based must be shown to be consistent with manner in which SCC is known to proceed in stainless steel: for example, if a slip-dissolution-rupture (SDR) model is used to describe crack growth in the weld material, it must be possible to show that the SDR model is consistent with what is known to happen in a cracking weld sample at the relevant scale. Importantly, many of these "individual-stage" models are primarily

deterministic. They would need to be adapted into a probabilistic model in order to fulfill the objectives of this project.

The advantage of such a piecemeal approach is that each stage of the model could be tailored exactly to the way that SCC is observed to proceed in canister weld material exposed to a chloride-containing solution representative of a deliquesced salt film. The disadvantage, though, comes in linking the separate models and reconciling their assumptions with each other and with the material-environment combination at hand. Assumptions would need to be consistent, and criteria for transitioning to the next “stage” (e.g. pits to cracks) would need to be established and validated. Furthermore, an objective of the *Life Prediction of Used Fuel Canister Material* project is to minimize the uncertainties associated with the model. Combining multiple models could increase the uncertainty, especially at points of transition, and especially if the model was not originally developed for stainless steel exposed to a chloride-containing aqueous solution.

The more probabilistic models are likely to be more straightforward to work with. A disadvantage of these models is that they often obscure the fundamental physics of how SCC is occurring, and so for the purposes of understanding SCC in canister material at a fundamental level, they may not be ideal. However, for the purposes of developing a useful predictive model, this approach is likely to be more desirable. Parameters can be fit to the situation of interest using experimental data. Propagation and quantification of uncertainty is straightforward, since one is dealing with probability distributions that can be fit to data instead of multiple deterministic equations that rely on simplifying assumptions that must be validated for the situation of interest, and whose effects on uncertainty must be quantified.

7.13 Future work

These challenges will be considered extensively as the project to model SCC in used fuel canister welds moves forward. It is necessary to consider the many research efforts to model SCC in a variety of situations, and determine their shortcomings and successes, in order to decide the best first approach to the problem. Many questions remain to be addressed.

For example:

- What pit-and-crack configurations can be expected in the weld material or HAZ? How do different configurations of pits and cracks affect the likelihood of wall breach due to SCC?
- Can an initial pit distribution and pit growth rate distribution model like that proposed by Turnbull be adapted to fit experimental data for the HAZ?
- Salt deliquescence will significantly affect the likelihood of SCC in this particular situation. Therefore, a full predictive model will need to have an environmental component that accounts for the likelihood of salt deliquescence developing. Is it possible to account for a dynamically changing environment and varying canister geometries in a single model? Or, will it be necessary to develop a different SCC model for each fuel storage site?
- What is the best strategy for calculating uncertainties, and how can experiments be strategically designed to yield results that can be used to refine the model and reduce these uncertainties?

There will be a detailed experimental component of this research project. The first objective of the experiments will be to obtain the data necessary to properly construct the predictive model. The experiments are to include high-resolution imaging of pits and cracks, in addition to monitoring of crack growth. Therefore, it is hoped that the overall research endeavor will yield interesting and new information about how SCC proceeds in welded stainless steels, in addition to the development of the probabilistic model itself.

Additional work is being carried out to understand: (1) residual stress and (2) environment development. The residual stresses in the welds will be measured, and it is hoped

that this research will yield further insight into the role that these stresses play in the onset of pitting and the rate of crack propagation. The first residual stress measurements of weld samples were made in the fall of 2014 at the Canadian Institute for Neutron Scattering facilities in Chalk River, Ontario. Preliminary results may be found in Appendix C.

Understanding the development of a sufficiently aggressive environment is the next key step for the project. Without the threshold environment, SCC will not proceed, but an understanding of how the aggressiveness threshold varies with surface conditions (residual stress at surface, temperature) and how the environment develops in time are still knowledge gaps that need to be addressed.

The questions to be addressed in this regard are as follows. For the known range of residual stresses in the canister material, what is threshold chemistry for an aqueous film on the canister surface that could result in the initiation of the SCC process? What is the intersection of that threshold chemistry with the canister temperature (new canisters are too hot to sustain an aqueous film) and with external temperature and humidity conditions? What is the probability of an aqueous film being sustained on the canister for a sufficiently long time that pits and cracks develop? If the threshold chloride concentration for SCC is known, what is the probability that a sufficient amount of chloride would be deposited on the canister for that to occur? Understanding the environment in which SCC can occur, and how it develops, may prove to be as much of a challenge as developing the SCC model itself.

Ultimately, the *Life Prediction of Used Fuel Canister Material* project will provide a probabilistic model for SCC in the canister material, as well as knowledge of the threshold environment for SCC to initiate and the likelihood that this environment could be present at current ISFSI sites. This model will be used to help predict which used fuel canisters in the United States are most likely to suffer SCC damage, and when wall breach might be

expected to occur following postulated SCC initiation. The project will also provide novel insight into SCC in stainless steel welds, and into the residual stresses that are present in used nuclear fuel canisters in the United States. It is hoped that the efforts of this project will be useful both for maintaining the integrity of used fuel storage in the United States, and for further understanding how stress corrosion cracking proceeds in welded stainless steels.

7.14 SCC modeling approaches summary table

A summary of the models considered in this document are listed in order of appearance in the table on the following page. The source citation number is given, along with the page number on which the discussion of each model can be found. Variable definitions are omitted here for brevity, but are given in the relevant paper section. In nearly all cases, the original variables used by the authors have been retained to make cross-referencing with original sources more straightforward. As a result, however, some models apply the same variable to different quantities.

Table 45: Modeling approaches: a summary

| Model | Environment | Equations | Assumptions |
|---|--|--|---|
| Pitting | | | |
| <p>Sato Electrostriction model of pit initiation 1971 [7] <i>Page 141</i></p> | <p>Aluminum, Stainless steel in salt-containing solutions Metals that form an anodic oxide film</p> | <p>Film pressure: $P - P_0 = \underbrace{\frac{\epsilon(\epsilon - 1)e^2}{8\pi}}_{\text{Electrostriction}} - \underbrace{\frac{\gamma}{L}}_{\text{Interfacial tension}}$</p> <p>Relationship between breakdown potential and ion concentration: $\frac{d\phi^*}{d \ln(a_{KA})} = -\frac{8\pi k T \Gamma_A^*}{\epsilon(\epsilon+1)E}$</p> | <p>Interfacial tension and electrostriction pressure are the only effects considered in this model. Other factors, like impurities in the film, should be considered in applications (or their negligibility validated).</p> <p>Smaller dielectric constants and higher breakdown stresses promoted film stability.</p> <p>Films break down via brittle crack (anhydrous, rigid film), plastic slip (hydrous and viscoplastic film), or plastic flow (pores form on the film surface, developing a porous oxide layer, resulting in a dual-layer film).</p> |
| <p>Pickering & Frankenthal Active pit base model of pit growth 1972 [13] <i>Page 144</i></p> | <p>Iron and stainless steel Electrolyte solution Specific materials and solutions that were used in testing are listed in the paper.</p> | <p>Flux of the metal ion: $j_{M^+} = -D_{M^+} \left(\frac{dc_{M^+}}{dx} + c_{M^+} + \frac{F}{RT} \frac{d\phi}{dx} \right) = -\frac{i_M}{F}$</p> <p>Concentration of the metal ion: $c_{M^+} = \frac{4D_{M^+} F c^{\circ} i_{M^+} x + (i_{M^+})^2}{2D_{M^+} F (2D_{M^+} F c^{\circ} + i_{M^+} x)}$</p> | <p>Only metal dissolution is considered.</p> <p>The walls of the pits are ignored; only the base undergoes dissolution.</p> <p>The ions of the salt are non-complexing.</p> <p>Interactions between ion species are neglected.</p> |
| Continued on next page | | | |

Table 45 – continued from previous page

| Model | Environment | Equations | Assumptions |
|---|--|--|--|
| <p>Galvele Modifications to Pickering and Frankenthal 1976 [55] Page 149</p> | <p>Susceptible metal Salt containing solution</p> | <p>Pit potential as a function of salt concentration $[\Phi - \Phi'] = A - \frac{RT}{F} \ln(C)$</p> | <p>Metal dissolution is followed by a hydrolysis reaction that comes into equilibrium rapidly.</p> <p>The walls of the pits are ignored; only the base undergoes dissolution.</p> <p>The hydrolysis reaction may result in pH suppression that prevents passivation.</p> <p>The bulk solution is the supporting electrolyte, and only ion transport via diffusion processes needs to be considered. This allows simplification of the transport equations.</p> <p>The ions of the salt are non-complexing.</p> |
| <p>Beck & Alkire Salt film limits pit growth 1979 [14] Page 149</p> | <p>Passivating metals Salt-containing electrolyte</p> | <p>Flux associated with dissolution of salt film: $j = D(C_s - C_b) \left[\frac{1}{r} + \frac{1}{\sqrt{\pi Dt}} \right]$ Pit radius as function of time $r = \sqrt{r_1^2 + \frac{2DC_s Mt}{\rho}}$ Salt film thickness: $t_f = \beta \eta_f / \ln \left(\frac{zFDC_s}{i_0 r} \right)$</p> | <p>There is a poreless salt film adjacent to the metal surface that causes electrical resistance within the pit.</p> <p>Corrosion rates inside the pit are controlled by the behavior of the salt film.</p> <p>In calculations, pits are hemispherical. Salt film is uniform.</p> <p>Salt concentration in the bulk electrolyte is negligible.</p> |

Continued on next page

Table 45 – continued from previous page

| Model | Environment | Equations | Assumptions |
|---|--|---|--|
| <p>Chao, Lin, & McDonald Point defect model of pit initiation 1981 [8] <i>Page 153</i></p> | <p>Stainless steel, Nickel Chloride containing solution</p> | <p>Film growth: $\exp(2KL) - 2KL - 1 = 2KA(B-1)t$</p> <p>Form of critical pitting potential: $V_c = A - B \log a_{[Cl^-]}$</p> <p>Threshold number of vacancies forming a void: $(J_{ca} - J_m) \times (t - \tau) \geq \zeta$</p> <p>Pit initiation conditions: $J^{\circ}u^{-x/2} \exp\left(\frac{xF\alpha V_{app}}{2RT}\right) (a_{[Cl^-]})^{-x/2} < J_m$</p> <p>Derived critical pitting potential: $V_c = \frac{4.606RT}{\alpha F} \log\left(\frac{J_m}{J^{\circ}u^{-x/2}}\right) - \frac{2.303RT}{\alpha F} \log(a_{[Cl^-]})$</p> | <p>Oxygen anions promote film growth. Chloride anions promote film breakdown.</p> <p>Voids form at the interface when vacancies pile up at the metal/film interface.</p> <p>When voids grow to a certain size, local film breakdown results and pit formation becomes likely.</p> <p>If vacancies pile up at the metal/film interface faster than they are subsumed into the bulk, film breakdown becomes likely.</p> <p>Chloride ions are incorporated into the lattice at oxygen vacancy sites.</p> <p>Metal cation diffusion rate increases as more chloride ions are incorporated into the film.</p> |
| <p>Okada Halide nuclide theory of pit initiation 1984 [10] <i>Page 159</i></p> | <p>Passivating metal Halide-containing solution</p> | <p>Critical pitting potential: $E_c = C - \frac{RT}{\xi F} \ln[X^-]$</p> <p>Time to pit initiation: $\ln(\tau) = C - 2n \ln[X^-] \frac{2\xi FE}{RT}$</p> <p>Critical pitting potential, general: $E_c = f([Cl^-], pH, T)$</p> | <p>Aqueous halide solution breaches the oxide film.</p> |
| <p>Kondo Identifying the pit-to-crack transition 1989 [18] <i>Page 162</i></p> | <p>Deionized water Low carbon steel</p> | <p>Pit growth rate: $\frac{2}{3}\pi r^3 = Bt$</p> <p>Pit-to-crack transition criterion: $c = C_p t^{1/3} = C_p (N/f)^{1/3}$</p> <p>Critical pit diameter: $2c_{cr} = \frac{2Q}{\pi\alpha} \left[\frac{(\Delta K)_p}{2.24\sigma_a} \right]^2 r^2$</p> | <p>Pits are hemispherical.</p> <p>Pits stop growing after crack initiation.</p> <p>Cracks initiate when CGR = PGR.</p> <p>Pit is a sharp crack from fracture mechanics standpoint.</p> |

Continued on next page

Table 45 – continued from previous page

| Model | Environment | Equations | Assumptions |
|---|--|--|--|
| <p>Shibata & Takeyama Stochastic description of pitting 1977 [12] Page 166</p> | <p>Type 304, 316 steel 3.5% NaCl solution</p> | <p>Transition probability: generate pit in dt $\lambda(t)dt = -dP(t)/P(t)$</p> <p>Survival probability: $P(t) = \exp\left(-\int_0^t \lambda(t)dt\right)$</p> <p>$\lambda_i$ expressed as a function of E, fit to data ($i = 1, 2, 3$)</p> <p>Pitting potential CDF if E changed at a constant sweeping velocity $P(E/v) = \exp\left(-\frac{1}{v} \int_0^E \lambda(E/v)dE\right)$</p> | <p>Film is modeled as a 2D film; film thickness effects are neglected.</p> <p>Variations in the film are the cause of variations in pitting potential when all other conditions are held the same.</p> |
| <p>Farmer: Pitting Model Deterministic Model of Pitting, after Shibata & Takeyama 1998 [45] Page 170</p> | <p>Stainless steel</p> | <p>Partitioning of metal surface: $\theta_E + \theta_P + \theta_V$</p> <p>Pit embryos covering surface over time: $\frac{d\theta_E}{dt} = k_{\text{birth}} [\text{Cl}^-]^a (1 - \theta_E - \theta_P) - k_{\text{death}} [\text{OH}^-]^b \theta_E - k_{\text{pit}} \theta_E$</p> <p>Stable pits covering surface over time: $\frac{d\theta_P}{dt} = k_{\text{pit}} \theta_E$</p> | <p>Pit embryos and stable pits are the only relevant indicators of corrosion.</p> <p>$[\text{Cl}^-]$ and $[\text{OH}^-]$ undergo competitive adsorption.</p> <p>Higher chloride concentrations yield more embryos.</p> <p>Higher hydroxide concentration results in more embryo death.</p> <p>One embryo nucleates a pit. The effect of pit formation from multiple embryos is assumed negligible.</p> |

Continued on next page

Table 45 – continued from previous page

| Model | Environment | Equations | Assumptions |
|---|--|--|---|
| <p>E. E. Mola Stochastic pitting and pit growth</p> <p>1990 [15]</p> <p>Page 175</p> | <p>Type 316 stainless steel</p> <p>Solution containing aggressive ions</p> | <p>Average number of inclusions per unit area:</p> $\langle n_0 \rangle = \sum_{k=0}^{\infty} k e^{-\alpha} \frac{\alpha^k}{k!} = \alpha$ <p>Probability of pit birth when $t \leq \tau_0$:</p> $P_0(t) = e^{-\lambda_0 t}$ <p>Average time to pit nucleation:</p> $\langle \tau_0 \rangle = \int_0^{\infty} t e^{-\lambda_0 t} dt / \int_0^{\infty} e^{-\lambda_0 t} dt = 1/\lambda_0$ <p>Mean number of pits:</p> $\langle n(t) \rangle = n_0 [1 - e^{-\lambda_0 t}]$ <p>Probability that pit grows to volume $j dV$:</p> $P_j(t) = \lambda_{j-1} \int_0^t e^{-\lambda_j(t-t')} P_{j-1}(t') dt'$ <p>Time rate of change for pit growth probability:</p> $\frac{dP_j}{dt} = -\lambda_j P_j(t) + \lambda_{j-1} P_{j-1}(t)$ | <p>Pitting is a stochastic process.</p> <p>Pitting occurs at inclusion sites.</p> <p>Inclusions are independent of each other; the presence of one does not influence the location or behavior of another inclusion.</p> <p>The Markov property applies to the pit birth process.</p> <p>Pit birth always happens if exposure time is long enough.</p> <p>The probability densities for pit birth and pit death per unit time depend on the corrosion conditions.</p> <p>Pit volume decrease does not occur.</p> <p>Pit growth can be treated as a stepwise process.</p> <p>Pit overlap effects can be ignored.</p> <p>The growth rate depends on the active area.</p> <p>Pits are unstable until they reach a certain critical size. Before then, they are subject to death probability μ.</p> <p>Below a certain E_c corrosion is driven by local electrochemical reactions. Above it, diffusion-controlled processes dominate and a stable pitting limit is reached.</p> |
| | | | Continued on next page |

Table 45 – continued from previous page

| Model | Environment | Equations | Assumptions |
|---|--|--|---|
| <p>Henshall</p> <p>A stochastic approach to pitting and pit growth using phenomenological equations</p> <p>1992 [35]</p> <p>Page 178</p> | <p>Considered alloys likely to be used in HLW containment at Yucca mountain</p> <p>Data from Alloy 825 exposed to 5 % NaCl solution, pH 2.57, T = 90°C</p> | <p>Probability that a pit will be nucleated in a unit area:</p> $\lambda = \Lambda A_{\text{cell}} \Delta t$ <p>If a decaying birth probability is assumed:</p> $\lambda = \lambda_0 e^{-\alpha t}$ <p>Pit death probability:</p> $\mu = M \Delta t$ <p>Pit growth probability:</p> $\gamma = \Gamma \Delta t / D$ <p>The dependence of the stochastic parameters on $[\text{Cl}^-]$:</p> $\tau_c \sim e^{-k_1 E_{\text{app}}}$ $\lambda \sim e^{k_2 [\text{Cl}^-]}$ $\mu \sim e^{-k_3 [\text{Cl}^-]}$ $\tau_c \sim e^{-k_4 [\text{Cl}^-]}$ <p>Dependence on potential:</p> $\gamma \sim (E_{\text{app}} - E_{\text{crt}})^b$ $\lambda \sim \beta (E_{\text{app}} - E_c) t$ <p>Final set of equations:</p> $\lambda = A_1 (E_{\text{app}} - B_1) e^{C_1 [\text{Cl}^-]} e^{Q_A / RT}$ $\mu = A_2 e^{-C_2 [\text{Cl}^-]} e^{-Q_u / RT}$ $\tau_c = A_3 e^{-B_3 E_{\text{app}}} e^{-C_3 [\text{Cl}^-]} e^{Q_\tau / RT}$ $\gamma = A_4 (E_{\text{app}} - B_4)^{B_5} ([\text{Cl}^-])^{C_4} e^{Q_\gamma / RT}$ <p>Time dependence of environmental inputs:</p> $E_{\text{app}} = E_0 - e^{-E_1 t}$ $[\text{Cl}^-] = K_0 e^{K_1 t}$ $T = T_\infty + T_0 e^{-T_1 t}$ | <p>Metastable pits initiate as a result of fluctuations in the local environment.</p> <p>If the metastable pit reaches a certain critical size, it becomes stable.</p> <p>Pits are hemispherical.</p> <p>Stable pits grow in a “start/stop” manner that can be modeled using RNG techniques.</p> <p>pH, $[\text{O}_2]$, and ions other than chloride are neglected in this treatment.</p> <p>γ has an Arrhenius dependence on T.</p> <p>T, E_{app}, and $[\text{Cl}^-]$ have no feedback effects on each other, so proportionalities can be combined.</p> |
| | | | Continued on next page |

Table 45 – continued from previous page

| Model | Environment | Equations | Assumptions |
|--|---|--|--|
| Farmer Modifications to Henshall 1998 [45] Page 186 | Canister surface | Pit birth probability modification: $\lambda = \lambda(A\theta_P^n \exp[B\theta_P])$ Time-dependent pit penetration: $d = \sqrt{\frac{2 K_0 [H^+] (E - E_{crit}) T_{age}}{=K, \text{ time rate constant}}}$ | Birth probability λ is time invariant. Pit growth can be modeled as a function of pit age. Penetration rate is limited by diffusion or by electromigration, and expression is modified according to the assumption made. $d \propto t^{1/2}$ for both. |
| Crack Propagation | | | |
| Ford & Andresen Film fracture at crack tip 1980s [19] Page 188 | Stainless steel (Types 304, 316L) Low alloy steel (A533B, A508) Inconel (600, 182) 288°C water | Crack propagation rate: $\frac{da}{dt} = \frac{MQ_f}{z\rho F} \frac{d\epsilon_{ct}}{dt} \frac{1}{\epsilon_f}$ General form of $\frac{da}{dt}$: $\frac{da}{dt} = f(n) \left(\frac{d\epsilon_{ct}}{dt}\right)^n$ Anodic current density transient following film rupture: $i_a = at^{-n}$ | The slip dissolution/film rupture mechanism is responsible for the propagation of SCC. The crack growth rate is equal to the metal dissolution rate. |
| Buck & Ranjan Crack tip opening displacement model 1986 [29] Page 190 | Brass Ammoniacal solution | Time to SCC: $t_{inc} = \frac{(K_{ISCC})^2 e^{-V_m/V_0}}{\pi B(\sigma^2 - \sigma_0^2)}$ Crack tip opening displacement: $\delta \propto \frac{1}{2} \frac{\sigma^2 \pi B e^{V/V_0}}{\sigma_n E} [t + (t^2 - (t_{hold})^2)^{1/2}]$ | Crack propagation rate at pit base is \propto displacement at the pit mouth. Crack initiates from micro-crack when displacement at mouth exceeds a threshold value. Dissolution is uniform at pit walls. |

Continued on next page

Table 45 – continued from previous page

| Model | Environment | Equations | Assumptions |
|--|--|---|--|
| <p>Nakayama & Takano Slip dissolution repassivation model 1986 [20] Page 193</p> | <p>Type 304 stainless steel Boiling 42% MgCl₂ solution</p> | <p>Current density: $i(t) = J^0 e^{-\beta t}$</p> <p>Crack propagation rate: $\frac{da}{dt} = \frac{M \langle i \rangle}{z F \rho}$</p> <p>Time averaged dissolution current density: $\langle i \rangle = \frac{J^0}{\beta} \eta_s [1 - e^{-\beta/\eta_s}]$</p> | <p>SCC occurs via the slip-dissolution repassivation mechanism.</p> <p>Film rupture occurs at every instance of slip step formation.</p> |
| <p>T. Shoji et. al Additions to Ford & Andresen 1995 [21] Page 204</p> | <p>Passivating metal</p> | <p>Crack propagation rate: $\frac{da}{dt} = \frac{M}{z \rho F} \frac{i_0(t_0)^m}{(1-m)(\epsilon_f)^m} (\epsilon_{ct})^m$</p> <p>Strain rate at crack-tip: $\epsilon_{ct} = \frac{\beta \sigma_y n}{E(n-1)} \left(2 \frac{K_I}{K_I} + \frac{\dot{a}}{r_0} \right)$ $\cdot \left\{ \ln \left[\frac{\lambda}{r_0} \left(\frac{K_I}{\sigma_y} \right)^2 \right] \right\}^{1/(n-1)}$</p> | <p>SCC proceeds via a dissolution mechanism.</p> <p>The authors note that many assumptions are typically made when calculating the strain rate at the crack tip, and that this is a large source of uncertainty.</p> |

Continued on next page

Table 45 – continued from previous page

| Model | Environment | Equations | Assumptions |
|---|--|---|---|
| <p>M. M. Hall A critique of the Ford-Andresen model 2009 [22, 61] Page 196</p> | <p>Passivating metal Aqueous solution</p> | <p>Crack growth rate as a function of current: $\frac{da}{dt}(t) = \frac{M}{z\rho F} i_a(t)$ $\frac{da}{dt}(t, \dot{\epsilon}_{ct}) = \frac{M}{z\rho F} i_a(t, \dot{\epsilon}_{ct})$</p> <p>Relating current to the active surface fraction: $i_a(t, \dot{\epsilon}_{ct}) = i_a^* A^*(t, \dot{\epsilon}_{ct})$</p> <p>Relating crack growth rate to active surface fraction: $\frac{da}{dt}(t, \dot{\epsilon}_{ct}) = \frac{da^*}{dt}(t, \dot{\epsilon}_{ct}) A^*(t, \dot{\epsilon}_{ct})$</p> <p>Surface activation rate: $\left(\frac{\partial A^*}{\partial t}\right)_{\dot{\epsilon}_{ct}} = -k^* A^*$ $\left(\frac{\partial(1-A^*)}{\partial \dot{\epsilon}_{ct}}\right)_t = -\gamma(1-A^*)$ $\frac{dA^*}{dt} = -k^* A^* + (1-A^*)$</p> <p>Activated surface fraction at steady-state: $A_s^* = \frac{\gamma \dot{\epsilon}_{ct}}{k^* - \gamma \dot{\epsilon}_{ct}}$</p> <p>Current density at steady-state: $i_{as} = A_s^* i_a^* = \frac{\gamma \dot{\epsilon}}{k^* + \gamma \dot{\epsilon}} i_a^*$</p> | <p>The Ford-Andresen model is mathematically inconsistent.</p> <p>Current is affected by strain rate at the crack tip.</p> <p>Discrete crack segments contribute to i_a, and these contributions are accounted for by including the active surface fraction in calculations.</p> <p>The reference current i_a^* is independent of strain rate.</p> <p>Temperature and environment are constant.</p> <p>The rate of surface passivation is linearly proportional to the fraction of active surface.</p> <p>The rate of passive surface activation is linearly proportional to the fraction of passive surface.</p> <p>When applied strain is held constant, $\dot{\epsilon}_{ct}$ quickly approaches an asymptotic value. $\dot{\epsilon}_{ct}$ is a linear combination of strain rate and the rate of change of applied strain.</p> |

Continued on next page

Table 45 – continued from previous page

| Model | Environment | Equations | Assumptions |
|---|---|---|--|
| <p>Macdonald Coupled environment model for SCC in sensitized steel 1991 [23] Page 199</p> | <p>Sensitized Type 304 (HAZ) LWR environment</p> | <p>Expected electro-dissolution reactions are determined. Determine species concentrations: $N_i = -D_i \frac{\partial C_i}{\partial x} - f(n_i) u_i F C_i \frac{d\phi}{dx} = f(n, a) \left(\frac{i_c}{F} \right)$ Calculate CGR: $\frac{dL}{dt} = \frac{M I_0}{2 \rho_m z F W \delta}$ Average dissolution current: $\bar{I}_0 = 2 i_0^0 A_0^0 \left(\frac{t_f}{t_0} \right)^{-0.5} e^{(-\phi_s^L - \phi_s^0)/b_a}$</p> | <p>Parallel, inert crack walls The mechanism is SDR. Cracks form in sensitized regions. Charge conservation applies. The water is pure. Butler-Volmer equations apply for charge transfer kinetics.</p> |
| <p>Saito SCC CGR as a function of chemistry, stress, and sensitization 2001 [24] Page 208</p> | <p>Type 304 stainless steel 288° C water</p> | <p>Plastic deformation strain rate: $\dot{\epsilon}_{ct} = 2 \rho_d b \cos \theta \frac{db l v_D}{l_c^2} \dot{X}$ Avg current density at crack tip due to slip dissolution: $i_A = \frac{i_0 t_0^n}{(1-n)} \left(\frac{\dot{X}}{N_{slip} n_d b} \right)^n$ Anodic current density: $i = F_{EPR} F_{\kappa} i_0 (C_4 \Phi_C + C_5) \times e^{\alpha(C_4 \Phi_C + C_5)}$ Crack growth rate, simplified: $\frac{da}{dt} = \frac{M}{z F \rho_m} i_a$ $\frac{da}{dt} = A(n) (\dot{\epsilon}_{ct})^n$ Expression for n: $\frac{\log \left[\left(\frac{da}{dt} \right)_{data} / A_0 \right]}{\log \left[(\dot{\epsilon}_{ct})_{cal} / C_m \right]}$</p> | <p>A combination of plastic deformation at the crack tip (mechanical) and the slip dissolution mechanism (environmental) drives SCC propagation.</p> |

Continued on next page

Table 45 – continued from previous page

| Model | Environment | Equations | Assumptions |
|--|---|---|---|
| <p>Ihara Probabilistic crack initiation 2013 [28] Page 217</p> | <p>Type 316L stainless steel</p> <p>BWR environ- ment</p> | <p>Crack length probability den- sity function:</p> $f(x) = \frac{1}{\sqrt{2\pi s^2} x} \exp \left\{ -\frac{(\ln x - \mu)^2}{2s^2} \right\}$ <p>Average crack length:</p> $E = V_0^E e^{(q^E \sigma)_t}$ <p>Crack length mode:</p> $M = V_0^M e^{(q^M \sigma)_t}$ | <p>Microcracks develop before SCC occurs. Microcracks coalesce into larger cracks.</p> <p>A crack aspect ratio of 0.6 is assumed.</p> <p>It is appropriate to model the crack length pdf with a lognor- mal distribution.</p> <p>A macroscopic crack initiates from the microcracks when the microcracks reach a depth of 1 mm.</p> |
| | | | Continued on next page |

Table 45 – continued from previous page

| Model | Environment | Equations | Assumptions |
|--|---|--|--|
| <i>Complete SCC Models</i> | | | |
| <p>Engelhardt A deterministic SCC model 2004 [30] Page 221</p> | <p>Turbine blades and an aqueous chloride- containing film</p> <p>Carbon steel and Type 316 stainless steel data used</p> | <p>Pit growth rate: $v = \frac{dL}{dt} = v_0(1 + t/t_0)^{m-1}$</p> <p>Pits propagating at an initial rate v_0 agree with $n(t) = \int_0^\infty \lambda(t, v_0) dv_0$ Information on expressing λ is included in [30].</p> <p>Pit repassivation: $R_a(x, t) = -\gamma f_a(x, t)$</p> <p>Differential damage function for Active Pits: $f_a = \int_0^\infty \left\{ \frac{1}{v_0 \zeta(x)} e^{-\gamma g(x)/v_0} n \left(t - \frac{g(x)}{v_0} \right) \cdot U[\max(x_{tr}, x_{v0}) - x] \Psi(v_0) dv_0 \right\}$</p> <p>Differential damage function for passive pits: $f_p = \gamma U(x_{tr} - x) \int_0^\infty \left\{ \frac{1}{v_0 \zeta(x)} \gamma e^{-\gamma g(x)/v_0} \cdot N \left(t - \frac{g(x)}{v_0} \right) \Psi(v_0) dv_0 \right\}$</p> <p>Differential damage function for cracks: $f_{cr} = U(x - x_{tr}) \times \int_0^\infty \Psi(v_0) dv_0 \left\{ U(x_{tr} - x_{v0}) A(x, x_{tr}, t) + U(x_{tr} - x_{v0}) U(x_{v0} - x) B(x, t) + U(x_{tr} - x_{v0}) U(x - x_{v0}) \times [B(x_{v0}, t - \theta(x, x_{v0})) + A(x, x_{v0}, t)] \right\}$</p> | <p>Electrochemical parameters for Type 316 SS and carbon steel are considered to be good approximations for Type 403 SS and 3NiCrMoV disk steel.</p> <p>The common assumption that the film is highly concentrated in chlorides may only be true in restricted regions, and should be avoided when considering the total blade surface.</p> <p>Pit repassivation is statistical in nature and can be described with a first order decay law.</p> |
| Continued on next page | | | |

Table 45 – continued from previous page

| Model | Environment | Equations | Assumptions |
|---|---|---|--|
| <p>Turnbull</p> <p>Statistical modeling of SCC</p> <p>2006-present</p> <p>[31, 63, 64, 51]</p> <p>Page 232</p> | <p>Steam turbine disc steel</p> <p>3NiCrMoV composition</p> <p>Exposed to specific discrete environments</p> <p>Model intended to be applied to power plant turbines.</p> | <p>Weibull distribution for pit size:</p> $f(x; k, \lambda, \theta) = \frac{k}{\lambda} \left(\frac{x-\theta}{\lambda}\right)^{k-1} \exp\left(-\frac{x-\theta}{\lambda}\right)^k$ <p>Find P (pit has size in range 0 to x):</p> $F(x) = \int_0^x p(\zeta) d\zeta = 1 - e^{-a_1(x-x_0)^{a_2}}$ <p>Pit size x:</p> $x = x_0 + \left[\frac{1}{a_1} \ln\left(\frac{1}{1-F(x')}\right)\right]^{1/a_2}$ <p>Pit size distribution time-rate-of-change:</p> $\frac{\partial P(x,t)}{\partial t} = -\frac{\partial}{\partial x} [g(x)P(x,t)] + S(P(x,t), x, t)$ <p>Pit depth as a function of time:</p> $x = \alpha t^\beta$ <p>“Groups” of pits may be governed by different values of α.</p> <p>Pit growth rate:</p> $\frac{dx}{dt} = g(x) = \beta \alpha^{1/\beta} x^{(1-1/\beta)}$ <p>Flaw growth following transition to cracking:</p> $\frac{dx}{dt} = C \sigma^p x^q$ <p>Critical pit depth:</p> $x_{crit} = \left(\frac{\beta \alpha^{1/\beta}}{C \sigma^p}\right)^{\beta/(1+\beta(q-1))}$ | <p>The Weibull distribution is appropriate for describing pit sizes.</p> <p>The chosen fitting parameters are accurate for the environment at hand.</p> <p>Pit geometry is assumed to be regular and symmetric. Geometry variations do not affect pit behavior.</p> <p>An initial pit distribution is assumed. Imperfect surface at $t = 0$.</p> <p>Pits cease to grow when crack is initiated (known to be untrue).</p> <p>Cracks occur from pit base (known to be untrue).</p> <p>Transition to crack occurs when $CGR > PGR$. An additional constraint is imposed (that of minimum pit depth).</p> <p>There are two regimes of crack growth (short- and long-crack). Regime transition chosen to agree with experimental data.</p> |

Continued on next page

Table 45 – continued from previous page

| Model | Environment | Equations | Assumptions |
|---|---|---|---|
| <i>Models for SCC in Alloy 600</i> | | | |
| O. F. Aly PWR PWSCC 2000s [25] Page 241 | Alloy 600 PWR environ- ment | Time-to-failure $t_f =$ $At_{ref} \left(\frac{\sigma}{\sigma_{ref}} \right)^n \exp \left[\left(\frac{Q}{R} \right) \left(\frac{1}{T} - \frac{1}{T_{ref}} \right) \right]$ Crack length $D = \int_0^t A[\dot{\epsilon}(t)]^p dt$ | |
| Hickling et. al MRP Model 2002 [26] Page 249 | Thick-walled Alloy 600 components Primary water environment | Crack growth rate $\frac{da}{dt} = \alpha \cdot \exp \left[-\frac{Q}{R} \left(\frac{1}{T} - \frac{1}{T_{ref}} \right) \right]$ $\cdot (K - K_{th})^\beta$ | There is a power law depen- dence of CGR on stress inten- sity. |
| | | | Continued on next page |

Table 45 – continued from previous page

| Model | Environment | Equations | Assumptions |
|--|---|--|--|
| <p>G. Wu A probabilistic-mechanistic SCC model 2011 [27] Page 250</p> | <p>Alloy 600 Primary Water</p> | <p>Additions to Hickling model: $\frac{da}{dt} \propto [\text{pH}]^\beta$ $\frac{da}{dt} \propto [\sigma_{ys}]^m$ Proposed Model: $\left(\frac{da}{dt}\right)_I = C_I \cdot \exp\left[\frac{Q}{R} \left(\frac{1}{T} - \frac{1}{T_{ref}}\right)\right] \cdot [\sigma_{ys}]^{m_I} \cdot [K - K_{th}]^{n_I}$ $\left(\frac{da}{dt}\right)_{II} = C_{II} \cdot \exp\left[\frac{Q}{R} \left(\frac{1}{T} - \frac{1}{T_{ref}}\right)\right] \cdot [\text{pH}]^{\beta_{II}} \cdot [\sigma_{ys}]^{m_{II}} \cdot [K - K_{th}]^{n_{II}}$ Use Bayesian analysis to determine parameter values: $\pi(\theta \text{Data}) = \frac{L(\text{Data} \theta)\pi_o(\theta)}{\int L(\text{Data} \theta)\pi_o(\theta)d\theta}$ $L(\text{Data} \theta) = \prod_{i=1}^N \frac{1}{s\sqrt{2\pi}} \cdot \exp\left[-\frac{1}{2} \left(\frac{\frac{da}{dt} \text{exp}(i) - \frac{da}{dt} \text{calc}(i,\theta)}{s}\right)^2\right]$</p> | <p>Cracks initiate from pits. A set of assumptions were made to model the components in question, including material characterization properties and the number of flaws on an affected component. Crack aspect ratios are uniformly distributed, so the initial crack depth distribution can be randomly generated.</p> |
| Continued on next page | | | |

Table 45 – continued from previous page


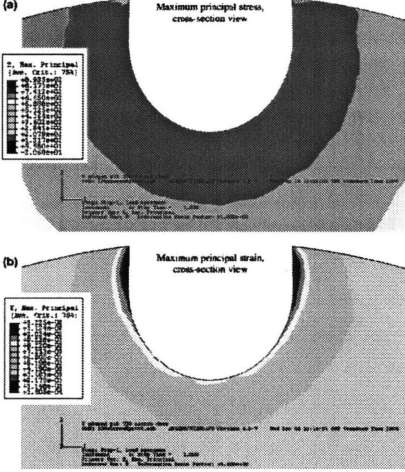
| Model | Environment | Equations | Assumptions |
|--|---|--|--|
| <i>Computer Modeling Techniques for Investigating SCC</i> | | | |
| <p>Wells et al. Percolation theory for IGSCC 1989 [67] Page 258</p> | <p>Sensitized austenitic steel</p> <p>Aggressive environment (thiosulphate, tetrathionate known to cause IGSCC in particular)</p> |  | <p>Sensitized bonds are modeled as a random occurrence in the lattice.</p> <p>Each bond is either active (sensitized) or inactive (unsensitized), blocks crack propagation). There is no range of sensitization for an individual bond.</p> <p>Only crack clusters that initiated at the surface were considered to be significant.</p> |
| <p>Horner et al. FEA of corrosion pits 2008 [77] Page 265</p> | <p>3 NiCrMoV disk steel</p> <p>1.5 ppm Cl aerated water at 90°C</p> |  | <p>Pits studied in the FEA model were hemispherical and symmetric.</p> <p>The Von Mises model was applied to the material.</p> <p>A uniform stress was imposed at one end of the FEA specimen.</p> <p>As with any FEA study, simplifying assumptions are made, and it is assumed that the imposed boundary conditions are an accurate reflection of reality.</p> |
| Continued on next page | | | |

Table 45 – continued from previous page

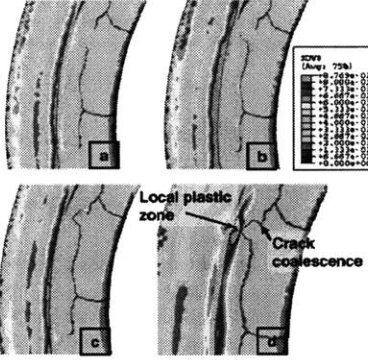
| Model | Environment | Equations | Assumptions |
|---|---|---|---|
| <p>Wenman et al. A finite element model of Cl-TGSCC 2011 [51] Page 272</p> | <p>Type 304L stainless steel pipe Chloride containing environment</p> |  | <p>The corrosion enhanced plasticity model developed by Magnin is consistent with the findings. The work hardening gradient for Type 304L steel was developed by fitting a line to tensile test data in the literature. Pitting precedes cracking. Crack growth occurred when the calculated stress perpendicular to the propagation path exceeded a threshold tensile stress.</p> |
| Film Formation | | | |
| <p>Gdowski & Bullen Oxidation rates 1988 [96] Page 319</p> | <p>Degradation modes in multiple potential canister materials and environments were considered.</p> | <p>Oxide thickness: $m^3 = k_1 t$ $m^2 = k_2 t$ Rate constants (Arrhenius): $k_i = A_i \exp\left(\frac{E_i}{RT}\right)$</p> | <p>Farmer identifies these equations as being the most applicable to a canister exposed to atmospheric conditions.</p> |
| Modeling Species Concentrations | | | |
| <p>Turnbull & Thomas Ion transport 1982 [97] Page 321</p> | <p>Structural steel NaCl in solution</p> | <p>Concentration gradients: $\frac{\partial C_i}{\partial t} + v \nabla C_i = \underbrace{D_i \nabla^2 C_i}_{\text{diffusion}} + z_i \underbrace{\left(\frac{F}{RT}\right) D_i \nabla (C_i \Phi)}_{\text{electromigration}} + \underbrace{R_i}_{\text{consumption/generation}}$</p> | <p>SCC is being driven by anodic dissolution at crack walls. Convection is negligible. Time-dependent terms are negligible. Ion concentration in bulk provides one boundary condition. Current density from dissolution reactions provides another boundary condition.</p> |
| Continued on next page | | | |

Table 45 – continued from previous page

| Model | Environment | Equations | Assumptions |
|--|---|---|--|
| <p>Farmer et al. Crevice corrosion 1998 [45] Page 322</p> | <p>Candidate materials for Yucca Mountain canisters (Alloy 625, Alloy C-22) Salt-containing solution</p> | <p>Ion fluxes in crevice (Nernst-Planck): $\vec{N}_i = -z_i u_i \mathbf{F} c_i \bar{\nabla} \Phi - D_i \bar{\nabla} c_i + \bar{v}$</p> <p>Current density: $\bar{i} = -\mathbf{F}^2 \bar{\nabla} \Phi \sum_i z_i^2 u_i c_i - \mathbf{F} \sum_i z_i D_i \bar{\nabla} c_i$</p> <p>Express transients as: $\frac{\partial c_i}{\partial t} = -\bar{\nabla} \cdot \vec{N}_i + R_i$</p> | <p>Anodic dissolution reactions are depolarized by cathodic reduction of O₂ or generation of H₂.</p> <p>Electroneutrality is assumed when determining $d[\text{H}^+]/dt$.</p> <p>Crevice is initially symmetric.</p> <p>H⁺ and O₂ concentrations at crevice mouth form boundary conditions.</p> <p>$c_i = 0$ at crevice mouth.</p> |

7.15 Additional notes

The following sections provide additional information that may prove insightful to the development of the probabilistic model of SCC for used nuclear fuel canister material.

7.15.1 SCC in the vapor-phase environment

Farmer et al. considered SCC in the “vapor-phase” and “aqueous-phase” environments, the latter of which is the environment assumed to be relevant to the situation at hand.¹¹⁰ However, should SCC occur in a “vapor-phase” environment, it was suggested that the equations used to describe the rates of spontaneous oxidation processes in copper and austenitic stainless steels would be useful. These equations were outlined by Gdowski and Bullen [96], and are described in Table 46 on page 320.

In order to adapt an SCC model intended for a metal exposed to an aqueous environment to a vapor-phase situation, Farmer suggested that the rates of anodic oxidation at the crack tip in the original model could be substituted for the appropriate rate of spontaneous oxidation k_i . Five common spontaneous oxidation rate laws are given in Table 46 [48].

The equations most relevant to a stainless steel canister would be:

$$m^1 = k_1 t \quad (204)$$

$$m^2 = k_2 t \quad (205)$$

with m as oxide thickness, t as time, and k_i as rate constants that follow Arrhenius behavior:

¹¹⁰Both copper alloys and steel were expected to be used in Yucca Mountain. While vapor-phase corrosion was not expected to be problematic for stainless steel containment systems, Farmer et al. suggested that it could be a life-limiting process for those utilizing copper alloys. The authors calculated that a copper-nickel canister exposed to moisture-containing air at 95°C could undergo 60% oxidation after 1000 years [48]. Therefore, vapor-phase corrosion processes were of concern to the Yucca Mountain project, but are not expected to be a major issue for canisters at ISFSI sites.

Table 46: Oxidation rates in stainless steels, as outlined in Gdowski and Bullen [96]

| Rate law | Type | Applicable conditions |
|-----------------------------------|---------------------|---|
| $m^1 = k_1 t$ | Linear | The alloy does not develop a protective film, such that no film impedes the reaction of oxygen with the bulk metal. |
| $m^2 = k_2 t$ | Parabolic | The alloy develops a film that acts as a barrier to ion diffusion. Thicker films impede oxide growth. Oxide growth rate will depend on the diffusional properties of the film and reactant molecules. |
| $m^3 = k_3 t$ | Cubic | Cubic film growth is observed in certain alloys. Specific resistance to mass transport is proportional to the thickness of the film that has developed on the surface. Integrated resistance is the square of the film thickness, and it is found that $\frac{dm}{dt} = \frac{k_3}{m^2}$. Integrating to find film thickness m yields cubic behavior [94]. |
| $m^{-1} = k_4 \log(t/\tau_1 + 1)$ | Inverse logarithmic | This behavior is induced by electric-field-driven ion transport through the oxide film [95]. |
| $m^{+1} = k_5 \log(t/\tau_2 + 1)$ | Direct logarithmic | There are multiple theories for logarithmic oxide film growth which are dependent on the situation at hand [95]. |

$$k_i = A_i \exp\left(\frac{E_i}{RT}\right) \quad (206)$$

with A_i a constant, T temperature, R the Boltzmann constant, and E_i the activation energy for the oxidation reaction.

Oxidation processes follow the rate behavior described by Equation (205) when a passive film is present. This film protects the bulk material from oxidation by limiting the diffusion of ions to and from the metal. Under normal conditions, the stainless steel canisters are expected to retain their passive film.

7.15.2 Modeling species concentrations in pits and crevices

Modeling the concentrations of important species inside the pit or crevice is important to understanding localized corrosion. Localized corrosion processes are heavily influenced by oxygen and chloride concentrations in particular. The two models in this section present two methods for modeling species concentration in a crevice or pit.

7.15.2.1 Turnbull and Thomas, 1982: Ion transport and anodic dissolution

When stress is low, and intergranular attack is likely (as it is in sensitized steel), SCC may be governed by the rate at which ions are transported along the crack. Farmer refers to work done by Turnbull and Thomas to model this process in stainless steels. In this view, H^+ ions and water are reduced, Fe^{2+} ions are hydrolyzed, and the metal undergoes anodic dissolution along the crack walls and at the crack tip. The concentration gradients were determined using conservation of species theory:

$$\frac{\partial C_i}{\partial t} + v \nabla C_i = \underbrace{D_i \nabla^2 C_i}_{\text{diffusion}} + \underbrace{z_i \left(\frac{\mathbf{F}}{RT} \right) D_i \nabla (C_i \Phi)}_{\text{electromigration}} + \underbrace{R_i}_{\text{consumption/generation}} \quad (207)$$

The boundary conditions and assumptions were as follows:

- Convection is negligible, such that the $v \nabla C_i$ term drops out
- Quasi-steady state, such that the time-dependent term drops out
- The ion concentration in the bulk electrolyte provides a boundary condition
- Current density due to the anodic and cathodic reactions give additional boundary conditions

Solutions to Equation (207) are detailed in Reference [97]. They were used to model the concentration profiles as a function of distance-from-crack-tip for the relevant species in the dissolution of BS 4360 steel immersed in a sodium chloride solution.

7.15.2.2 Farmer and McCright, 1998: Modeling species concentrations during crevice corrosion Farmer and McCright modeled the concentrations of chemical species inside a corrosion pit or crevice [45].¹¹¹

To define the expected chemical reactions, the authors begin by:

¹¹¹Farmer and McCright were particularly concerned with the waste storage system that was to be used at Yucca Mountain. This Engineered Barrier System (EBS) consisted of an inner barrier of Alloy 825, 625, or C-22 (materials chosen for their corrosion resistance) while the outer barrier was constructed from A416 or Monel 400, and was not corrosion resistant. Humidity in the air or groundwater, coupled with EBS surface temperatures that dropped in time, meant that the development of an aqueous solution on the EBS surface could be possible. Since the outer barrier was not corrosion resistant, it was possible that this solution could lead to the localized breach of the outer barrier, exposing the corrosion resistant inner barrier. Since this corrosion was expected to be highly localized if it occurred, a crevice corrosion scenario could result, and the the corrosion resistant inner barrier could be exposed to an especially aggressive environment. The concern, then, was that the inner barrier could corrode in certain scenarios - leading to the need to model the concentrations of species in a theoretical crevice that formed due to localized breach of the outer barrier.

- listing the possible hydrolysis reactions involving iron ions, nickel ions, and chromium ions.
- defining equilibrium constants for each hydrolysis reaction
- defining the possible precipitation reactions that occur when solubility limits for dissolved metal species are exceeded
- defining the corresponding solubility products

Next, the hydrogen ion generation rate is considered. This is important because the hydrogen ion concentration determines pH. By considering all the reactions that consume and produce hydrogen ions, an expression for $\frac{d[\text{H}^+]}{dt}$ is determined in terms of solubility products, equilibrium products, and the rate of change in the concentration of each relevant reactant and product species. This expression is unwieldy, so the authors also suggest that $\frac{d[\text{H}^+]}{dt}$ can be estimated by determining $[\text{Cl}^-]$, assuming electroneutrality, and determining the resulting $[\text{H}^+]$.

The next goal of this model, then, was to describe the fluxes in the crevice between the two barrier layers, assuming a breach of the outer barrier. These fluxes are given by the Nernst-Planck equation:

$$\bar{N}_i = -z_i u_i \mathbf{F} c_i \bar{\nabla} \Phi - D_i \bar{\nabla} c_i + \bar{v} \quad (208)$$

and the current density is given as:

$$\bar{i} = -\mathbf{F}^2 \bar{\nabla} \Phi \sum_i z_i^2 u_i c_i - \mathbf{F} \sum_i z_i D_i \bar{\nabla} c_i \quad (209)$$

Finally, transients are described with the following equation:

$$\frac{\partial c_i}{\partial t} = -\bar{\nabla} \cdot \bar{N}_i + R_i \quad (210)$$

The boundary conditions are as follows:

- $c_i = 0$ at crevice mouth
- Symmetric crevice when flux is zero
- H^+ and O_2 concentration can be assigned at the crevice mouth

Table 47: Variable definitions for Section 7.15.2.2

| Variable | Definition |
|----------|---------------------------|
| N | Flux |
| i | Ion species index |
| z | Charge |
| u | Mobility |
| c | Concentration |
| Φ | Electrolyte potential |
| D | Diffusivity |
| R | Apparent homogeneous rate |

To solve these equations, an explicit solution method was used, in addition to the implicit Crank-Nicolson method.¹¹²

Axial current density i_x is then found by integrating wall current density i_y along the crack length L and dividing by the distance h that separates the two crevice walls in Equation (211). Potential in the crevice is found by integrating the calculated axial current with the solution resistivity ρ over distance in Equation (212).¹¹³

¹¹²The original reference for the Crank-Nicolson method is as follows:

- J. Crank and P. Nicolson, "A practical method for numerical evaluation of solutions of partial differential equations of the heat-conduction type," *Mathematical Proceedings of the Cambridge Philosophical Society*, **1**, 1947, 50-67, [87].

The references cited by Farmer and McCright for the numerical methods they utilized were:

- V. G. Jenson, G. V. Jeffreys, *Mathematical Methods in Chemical Engineering*, Academic Press, New York, NY, 1963, 410-422, [86]. (Crank-Nicolson method)
- D. D. McCracken, W. S. Dom, *Numerical Methods and Fortran Programming with Applications in Science and Engineering*, John Wiley and Sons, New York, NY, 1964, 377-385, [85]. (explicit method)

¹¹³The following references are cited by Farmer as additional resources for modeling the electrochemical phenomena associated with crevice corrosion, and may be helpful in future modeling efforts. It is stated

8 Appendix B

8.1 Breakdown of the $F_{\text{parameters}}$ calculation by model

The parameters for each model were separated into categories and used to calculate $F_{\text{parameters}}$, which is one component of the figure-of-merit used to pick which models were best suited for use in this thesis. $F_{\text{parameters}}$ is described on page 46.

- Table 48: Pit initiation models
- Table 49: Pit growth models
- Table 50: Pit growth models
- Table 51: Transition models
- Table 52: Complete models

that the methods presented in these references are very similar to those suggested by Farmer and McCright here.

$$i_x(x) = \frac{\int_x^L i_y(x) dx}{h(x)} \quad (211)$$

$$E(x) = \int_0^x \rho(x) i_x(x) dx \quad (212)$$

- P. O. Gartland, "A Simple Model of Crevice Corrosion Propagation for Stainless Steels in Sea Water," *Corrosion* 97, Paper No. 417, National Association of Corrosion Engineers, Houston, TX, 1997, [90].
- Y. Xu, H. W. Pickering, "The Initial Potential and Current Distributions of the Crevice Corrosion Process," *J. Electrochemical Society*, 140(3), 1993, 658-668, [89].
- E. A. Nystrom, J. B. Lee, A. A. Sagues, H. W. Pickering, "An Approach for Estimating Anodic Current Distributions in Crevice Corrosion from Potential Measurements," *Journal of the Electrochemical Society*, 141(2), 1994, 358-361, [88].

Table 48: Calculating F parameters for the pit initiation models

| Model Name | Macroscopic Parameters | Microscopic Parameters | Atomic-scale Parameters | Characterizing Parameters | Fitting Parameters | FOM |
|-----------------------------------|------------------------------------|-----------------------------------|-------------------------|--|--|------|
| Sato | P_0 L φ T | P_{film} γ | | ϵ Γ^* a_{KA} | | 0.21 |
| Chao, Lin, & Macdonald | T pH $a_{[\text{Cl}^-]}$ | $\phi_{(f/s)}^\circ$ J° | J_m | χ Ω ΔG_{A-1}° α | β | 0.12 |
| Okada | T X^- E | | | n | C ξ | 0.17 |
| Shibata & Takeyama | | | | | $\lambda(E)$ N n | 0.17 |
| Farmer (after Shibata & Takeyama) | $[\text{Cl}^-]$ $[\text{OH}^-]$ | | | θ_E θ_P θ_V | k_b k_{death} k_{pit} | 0.13 |
| Mola | | | | | n_1 n_2 λ_0 λ_j ΣP_j | 0.10 |

Table 49: Calculating $F_{\text{parameters}}$ for the pitting models

| Model Name | Macroscopic Parameters | Microscopic Parameters | Atomic-scale Parameters | Characterizing Parameters | Fitting Parameters | FOM |
|---|--|------------------------|-------------------------|---------------------------|--|------|
| Pickering & Frankenthal | T ϕ | i_M c° | $C_{M^+}(x)$ | D_{M^+} | | 0.19 |
| Galvele | ϕ T | C | | ϕ' A | | 0.40 |
| Beck & Alkire | | r_1 | | C_s M, ρ D | | 0.57 |
| Henshall <i>Parameters specific to Farmer's Henshall modifications are listed in parentheses</i> | E_{app} [Cl ⁻] T E_1 | | | | Λ λ_0 α M Γ D k_1, k_2, k_3, k_4 E_{crt} a b A_1, A_2, A_3, A_4 B_1, B_2, B_3, B_4 C_1, C_2, C_3, C_4 Q_Λ Q_μ Q_τ Q_γ K_0 K_1 E_0 T_0 T_1 (A, B, n, θ_P) | 0.01 |

Table 50: Calculating F parameters for the crack growth models

| Model Name | Macroscopic Parameters | Microscopic Parameters | Atomic-scale Parameters | Characterizing Parameters | Fitting Parameters | FOM |
|-------------------|------------------------|---|-------------------------|--|---|------|
| Ford & Andresen | | ϵ_{ct} ϵ_f | | M, z, ρ | Q_f | 0.24 |
| Nakayama & Takano | | J_0 | | M, z, ρ | β η_s | 0.19 |
| Shoji | E σ_y | ϵ_f K_I \dot{K}_I | | M, z, ρ i_0 t_0 t_0 r_0 | m n β λ | 0.08 |
| Hall | | i_a^* A^* $\dot{\epsilon}_{ct}$ | | M, z, ρ | k^* γ | 0.14 |
| Macdonald | T | I_0 ϕ_s^L | | M, z, ρ W, δ i_0^0 A_t^0 t_f ϕ_s^0 α | | 0.22 |
| Saito | | | X | M, z, ρ ρ_d b d l ν_D l_c n_d | n | 0.17 |
| Aly | | $\dot{\epsilon}_e$ $\dot{\epsilon}_n$ | | | A p | 0.17 |
| Hickling | T σ | | | T_{ref} σ_{ref} t_{ref} | α n | 0.17 |
| Wu | T pH | K | | T_{ref} K_{th} σ_{ys} | C_I, C_{II} m_I, m_{II} n_I, n_{II} β_{II} | 0.06 |
| Ihara | | σ | | V_0^E, V_0^M q^E, q^M | μ s | 0.17 |

Table 51: Calculating $F_{\text{parameters}}$ for the transition models

| Model Name | Macroscopic Parameters | Microscopic Parameters | Atomic-scale Parameters | Characterizing Parameters | Fitting Parameters | FOM |
|---------------|--------------------------------|--|-------------------------|---------------------------|--------------------------|------|
| Buck & Ranjan | V_m σ_{app} | K_{ISCC} V_0 σ_0 | | | B | 0.17 |
| Kondo | N F | K σ_a | | | α B C_p | 0.11 |

Table 52: Calculating $F_{\text{parameters}}$ for the complete models

| Model Name | Macroscopic Parameters | Microscopic Parameters | Atomic-scale Parameters | Characterizing Parameters | Fitting Parameters | FOM |
|------------|------------------------|------------------------|-------------------------|---------------------------|--|------|
| Engelhardt | | K V_{cr} | | K_{ISCC} | m ζ β A, B v_0 t_0 $\lambda(t, v_0)$ γ $\zeta(x)$ $\Psi(v_0)$ n_a, n_p, n_{cr} | 0.09 |
| Turnbull | | σ | | | k, λ a_1, a_2 α β p, q C | 0.05 |

8.2 Code

The following sections include the MATLAB® code used in the implementation of the stress corrosion cracking models discussed in this thesis.

8.2.1 Residual stress and stress intensity functions

The data used to fit the residual stress functions is presented in Table 53. The data used to fit the stress intensity functions is presented in Table 54. An explanation of these residual stress functions can be found on page 57.

Figures 72 - 74 show the fourth-order Fourier fits for the residual stress functions made in the MATLAB® Curve-Fitting Toolbox. Note that the Curve-Fitting Toolbox extrapolates the end behavior. The code is scaled to the thickness of the theoretical canister used to make these data estimates. However, if these functions are used for other purposes, it should be noted that K is an extrapolation of the data for depths greater than 0.0127 m.

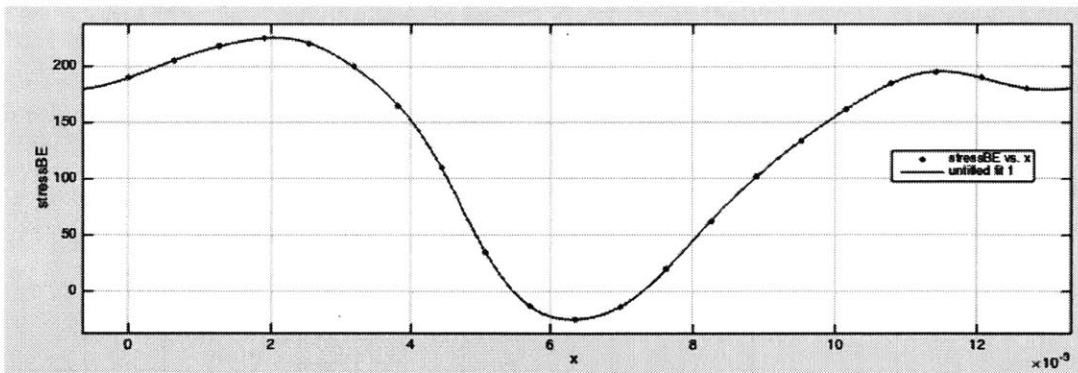


Figure 72: This is the fourth-order Fourier fit to the data used in [32] to determine the best-estimate case residual stress through a prototypical canister wall in the hoop direction. The fit was performed in the MATLAB® Curve-Fitting Toolbox in order to determine a continuous expression for stress σ as a function of depth x . R^2 for this fit = 0.994.

Table 53: This is the data used in [32] and used in this project to estimate the residual stress profile through the canister wall in the hoop direction. Depth is measured from the canister surface. Depth here is listed in inches, but meters were used to fit the data to enable the use of SI units throughout the code.

| Depth m | Best Estimate MPa | Barely above $K_{\text{threshold}}$ MPa | Highly Tensile MPa |
|------------|----------------------|--|-----------------------|
| 0.025 | 100 | 240 | 340 |
| 0.05 | 150 | 290 | 390 |
| 0.075 | 186 | 326 | 426 |
| 0.1 | 200 | 340 | 440 |
| 0.125 | 186 | 326 | 426 |
| 0.15 | 140 | 280 | 380 |
| 0.175 | 50 | 190 | 290 |
| 0.2 | -50 | 90 | 190 |
| 0.225 | -126 | 14 | 114 |
| 0.25 | -166 | -26 | 74 |
| 0.275 | -178 | -38 | 62 |
| 0.3 | -166 | -26 | 74 |
| 0.325 | -126 | 14 | 114 |
| 0.35 | -50 | 90 | 190 |
| 0.375 | 44 | 184 | 284 |
| 0.4 | 110 | 250 | 350 |
| 0.425 | 130 | 270 | 370 |
| 0.45 | 116 | 256 | 356 |
| 0.475 | 80 | 220 | 320 |
| 0.5 | 30 | 170 | 270 |

Table 54: This is the data used in [32] and used in this project to estimate the stress intensity through the canister wall in the hoop direction. Depth is measured from the canister surface. Depth here is listed in inches, but meters were used to fit the data to enable the use of SI units throughout the code.

| Depth [m] | Best Estimate [MPa√m] | Barely above $K_{\text{threshold}}$ [MPa√m] | Highly Tensile [MPa√m] |
|--------------|--------------------------|--|---------------------------|
| 0.025 | 6.118863943 | 7.051617593 | 7.051617593 |
| 0.05 | 9.202131325 | 10.43893154 | 10.43893154 |
| 0.075 | 11.63215233 | 13.09263368 | 13.09263368 |
| 0.1 | 13.13317139 | 14.86436216 | 14.86436216 |
| 0.125 | 13.34848363 | 15.48424101 | 15.48424101 |
| 0.15 | 12.21308932 | 14.97028676 | 14.97028676 |
| 0.175 | 8.794429447 | 12.43212526 | 12.43212526 |
| 0.2 | 2.991431082 | 7.841822908 | 7.841822908 |
| 0.225 | -1.178502671 | 4.618823928 | 4.618823928 |
| 0.25 | -2.490170459 | 4.058977849 | 4.058977849 |
| 0.275 | -1.462559174 | 5.233872473 | 5.233872473 |
| 0.3 | 2.182276052 | 8.619990406 | 8.619990406 |
| 0.325 | 7.041293281 | 13.02639257 | 13.02639257 |
| 0.35 | 12.07564742 | 17.60439972 | 17.60439972 |
| 0.375 | 16.42088889 | 21.55548026 | 21.55548026 |
| 0.4 | 20.50318075 | 25.27459998 | 25.27459998 |
| 0.425 | 24.13472883 | 28.60291511 | 28.60291511 |
| 0.45 | 26.17683276 | 30.57319827 | 30.57319827 |
| 0.475 | 26.20454576 | 30.82482094 | 30.82482094 |
| 0.5 | 25.47028106 | 30.42283572 | 30.42283572 |

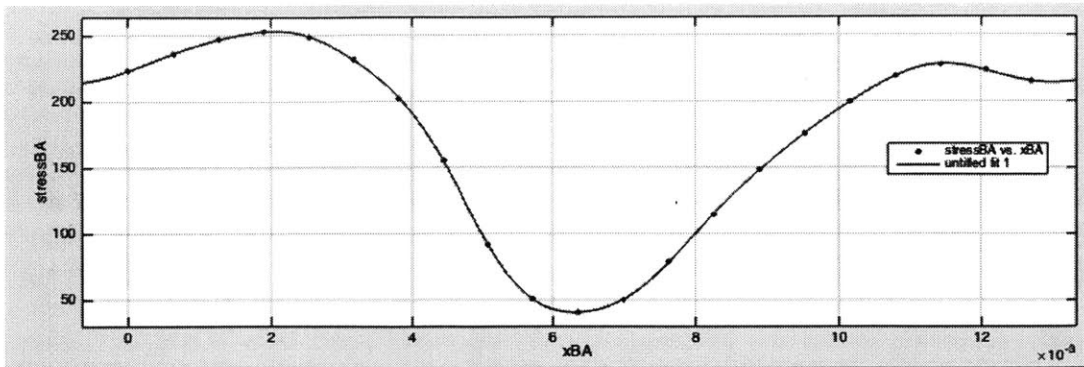


Figure 73: This is the fourth-order Fourier fit to the data used in [32] to determine the barely-above- $K_{\text{threshold}}$ case residual stress through a prototypical canister wall in the hoop direction. The fit was performed in the MATLAB® Curve-Fitting Toolbox in order to determine a continuous expression for stress σ as a function of depth x . R^2 for this fit = 0.994.

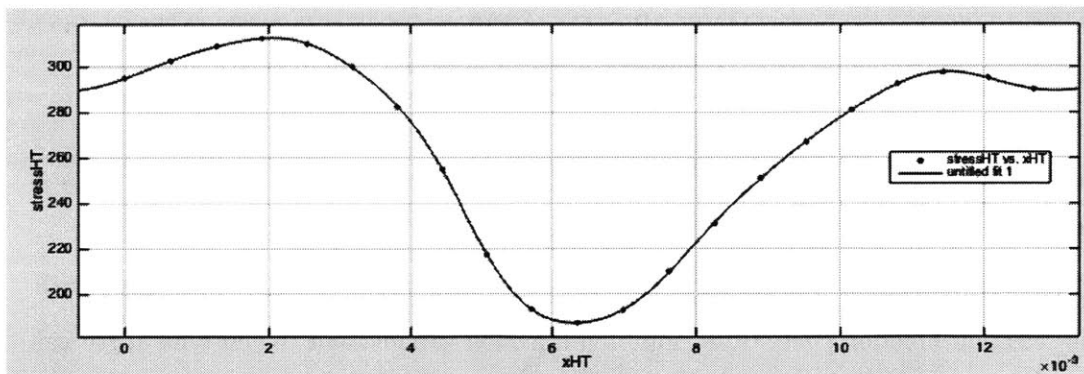


Figure 74: This is the fourth-order Fourier fit to the data used in [32] to determine the highly-tensile case residual stress through a prototypical canister wall in the hoop direction. The fit was performed in the MATLAB® Curve-Fitting Toolbox in order to determine a continuous expression for stress σ as a function of depth x . R^2 for this fit = 0.994.

Figures 75 - 77 show the eighth-order Fourier fits made for the stress intensity functions in the MATLAB® Curve-Fitting Toolbox. Note that the Curve-Fitting Toolbox extrapolates the end behavior. The code is scaled to the thickness of the theoretical canister used to make these data estimates. However, if these functions are used for other purposes, it should be noted that K is an extrapolation of the data for depths greater than 0.0127 m.

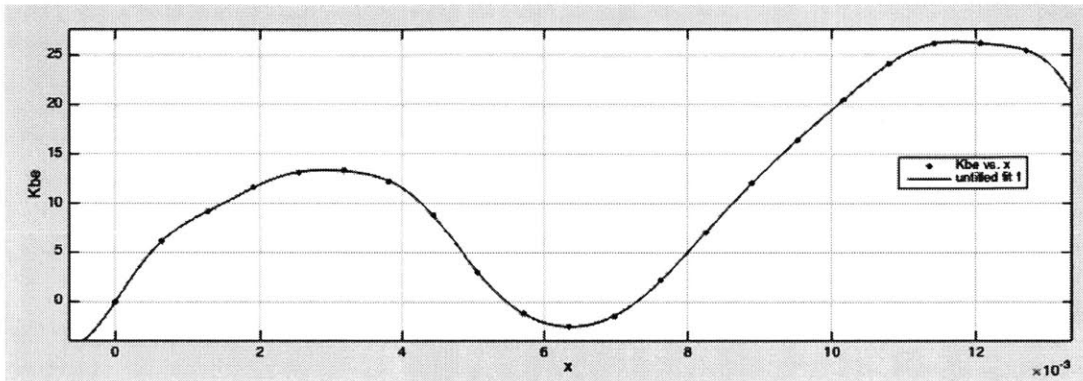


Figure 75: This is the eighth-order Fourier fit to the data used in [32] to determine the best-estimate case stress intensity through a prototypical canister wall in the hoop direction. The fit was performed in the MATLAB® Curve-Fitting Toolbox in order to determine a continuous expression for K as a function of depth x . R^2 for this fit = 1.

The process for obtaining these Fourier fits was described in Section 3.1.4. The original data is from [32].

The following functions return stress and stress intensity as a function of flaw depth. The selection function “get_stress” inputs a selection variable and the current depth calculated by the flaw growth loop of whatever model is being implemented. The selection variable has an integer value of 1, 2, or 3. These correspond (in order) to the three cases considered in [32]: best-estimate (this is the least conservative case, and the only case for which the stresses become compressive), barely-above-K-threshold, and highly-tensile. Given the selected case and the depth, the “get_stress” function will then return the ap-

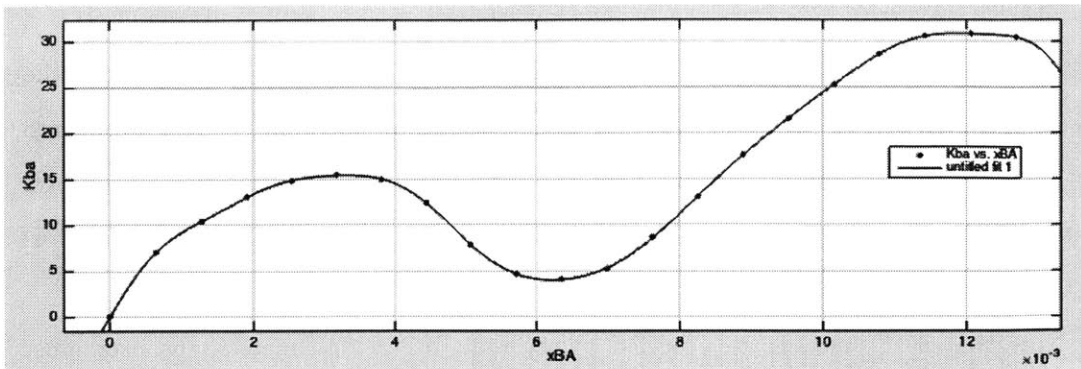


Figure 76: This is the eighth-order Fourier fit to the data used in [32] to determine the barely-above- $K_{\text{threshold}}$ case stress intensity through a prototypical canister wall in the hoop direction. The fit was performed in the MATLAB® Curve-Fitting Toolbox in order to determine a continuous expression for K as a function of depth x . R^2 for this fit = 1.

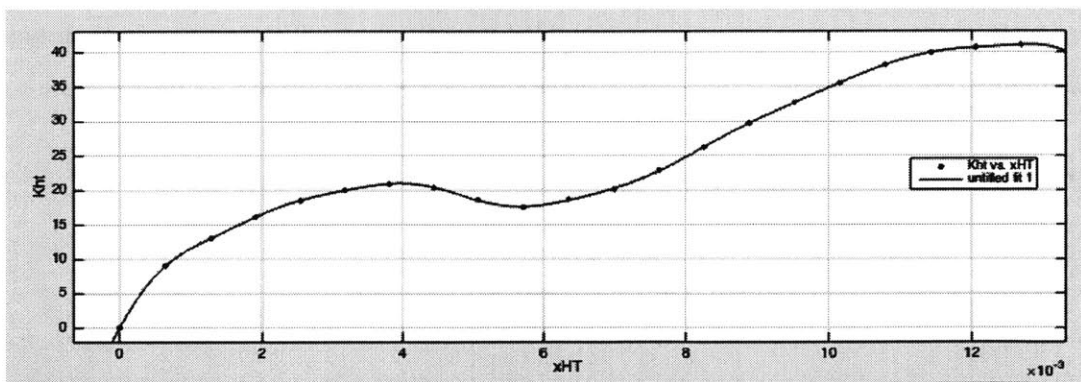


Figure 77: This is the eighth-order Fourier fit to the data used in [32] to determine the highly-tensile case stress intensity through a prototypical canister wall in the hoop direction. The fit was performed in the MATLAB® Curve-Fitting Toolbox in order to determine a continuous expression for K as a function of depth x . R^2 for this fit = 1.

appropriate $\sigma(x)$ and $K(x)$ values.

8.2.1.1 Implementation notes In each of the models considered in this project, the user inputs 1, 2, or 3 as the value of the variable “select_stress_function.” This is input into the “get_stress” function in order to select $\sigma(x)$ and $K(x)$ from the correct distributions. Note that the Henshall model is not dependent on $\sigma(x)$ or $K(x)$ when it is being used as a stand-alone pitting model.

Note that if the models are rescaled to use units other than meters, the user must modify either the flaw growth loop or the “get_stress” function to ensure that the depth called by the $\sigma(x)$ and $K(x)$ functions is in the correct units. All stress and stress intensity distributions use units of meters. For example, in a code that is optimized to calculate flaw depth in units of μm , like the Turnbull model, a conversion factor is applied to the flaw depth before it is imported into the stress and stress intensity functions. This can be done either in the Turnbull growth loop itself, or in the first lines of the “get_stress” function. Obviously, these conversions should not be added in both places: if the user is frequently modifying units, it is useful to check that the model isn’t doubly-converting length units.

8.2.1.2 Code for residual stress functions

```
function [sigma,K] = get_stress(select_stress_eqn, FD, thickness)

%FD = FD/10^6; %Convert to meters for use in the stress function
%thickness=thickness/10^6;

CD=FD;

if select_stress_eqn==1
    sigma=best_estimate_stress_4(thickness,FD);
    K=K_best_estimate(CD,thickness);
end
if select_stress_eqn==2
    sigma = barely_above_stress_4(thickness,FD);
    K=K_barely_above(CD,thickness);
end
if select_stress_eqn==3
    sigma = highly_tensile_stress_4(thickness,FD);
    K=K_high(CD,thickness);
end

end
```

```

function [ sigma ] = best_estimate_stress_4( thickness,FD )

    a0 =      134;    %(130.2, 137.8)
    a1 =      99.7;    %(85.39, 114)
    b1 =     -10.01;    %(-36.02, 16)
    a2 =     -44.87;    %(-53.61, -36.13)
    b2 =      33.18;    %(4.283, 62.07)
    a3 =     -2.254;    %(-6.964, 2.456)
    b3 =     -7.955;    %(-10.04, -5.865)
    a4 =      3.444;    %(-4.062, 10.95)
    b4 =      5.454;    %(1.841, 9.066)
    w =      438 ;    %(393.8, 482.2)

x=FD;

    sigma = a0 + a1*cos(x*w*0.0127/thickness) +
b1*sin(x*w*0.0127/thickness) + ...
          a2*cos(2*x*w*0.0127/thickness) +
b2*sin(2*x*w*0.0127/thickness) + ...
          a3*cos(3*x*w*0.0127/thickness) +
b3*sin(3*x*w*0.0127/thickness) + ...
          a4*cos(4*x*w*0.0127/thickness) +
b4*sin(4*x*w*0.0127/thickness);
end

```

```

function [ K_best] = K_best_estimate( CD,thickness)

    a0 =      10.52    ;%(9.472, 11.57)
    a1 =      0.7325    ;%(-4.573, 6.038)
    b1 =     -7.623    ;%(-8.482, -6.763)
    a2 =     -9.044    ;%(-9.977, -8.112)
    b2 =      4.497    ;%(-1.531, 10.53)
    a3 =     -2.836    ;%(-3.25, -2.422)
    b3 =      0.8395    ;%(-1.721, 3.4)
    a4 =     -0.3214    ;%(-2.329, 1.686)
    b4 =      2.113    ;%(1.076, 3.15)
    a5 =     -0.1261    ;%(-1.806, 1.554)
    b5 =      1.517    ;%(0.9829, 2.05)
    a6 =      0.2964    ;%(-0.9662, 1.559)
    b6 =      0.7951    ;%(0.4144, 1.176)
    a7 =      0.552    ;%(0.1402, 0.9639)
    b7 =      0.2279    ;%(-0.7169, 1.173)
    a8 =      0.2278    ;%(0.06492, 0.3907)
    b8 =      0.1059    ;%(-0.3062, 0.5181)
    w =      403.5    ;%(361.4, 445.5)

    x=CD;
    t0=0.0127;

    K_best = a0 + a1*cos(x*w*t0/thickness) + b1*sin(x*w*t0/thickness) +
    ...
            a2*cos(2*x*w*t0/thickness) + b2*sin(2*x*w*t0/thickness)
+ a3*cos(3*x*w*t0/thickness) + b3*sin(3*x*w*t0/thickness) +...
            a4*cos(4*x*w*t0/thickness) + b4*sin(4*x*w*t0/thickness)
+ a5*cos(5*x*w*t0/thickness) + b5*sin(5*x*w*t0/thickness) +...
            a6*cos(6*x*w*t0/thickness) + b6*sin(6*x*w*t0/thickness)
+ a7*cos(7*x*w*t0/thickness) + b7*sin(7*x*w*t0/thickness) +...
            a8*cos(8*x*w*t0/thickness) + b8*sin(8*x*w*t0/thickness);
end

```

```

function [ sigma ] =barely_above_stress_4(thickness, FD)
%take out thickness eventually (works for now because it cancels out)
a0 =      175.9   ;%(172.7, 179.1)
a1 =      84.74   ;%(72.59, 96.9)
b1 =     -8.509   ;%(-30.61, 13.6)
a2 =    -38.14   ;%(-45.57, -30.71)
b2 =      28.2    ;%(3.641, 52.76)
a3 =     -1.916   ;%(-5.919, 2.088)
b3 =     -6.762   ;%(-8.538, -4.986)
a4 =      2.928   ;%(-3.453, 9.308)
b4 =      4.636   ;%(1.565, 7.706)
w =       438     ;%(393.8, 482.2)

x=FD;
sigma = a0 + a1*cos(x*w*0.0127/thickness) +
b1*sin(x*w*0.0127/thickness) + ...
      a2*cos(2*x*w*0.0127/thickness) +
b2*sin(2*x*w*0.0127/thickness) + ...
      a3*cos(3*x*w*0.0127/thickness) +
b3*sin(3*x*w*0.0127/thickness) + ...
      a4*cos(4*x*w*0.0127/thickness) +
b4*sin(4*x*w*0.0127/thickness);
end

```

```

function [ K_barely ] = K_barely_above( CD, thickness)

    a0 =      13.98    ;%(12.32, 15.63)
    a1 =     -3.015    ;%(-9.765, 3.735)
    b1 =     -7.957    ;%(-9.7, -6.215)
    a2 =     -9.341    ;%(-10.39, -8.292)
    b2 =       4.99    ;%(-2.279, 12.26)
    a3 =     -3.259    ;%(-4.278, -2.24)
    b3 =       1.922    ;%(-1.711, 5.556)
    a4 =     -0.1845   ;%(-2.997, 2.628)
    b4 =       2.692    ;%(1.404, 3.98)
    a5 =       0.2946   ;%(-2.13, 2.719)
    b5 =       1.874    ;%(1.536, 2.212)
    a6 =       0.6274   ;%(-0.8344, 2.089)
    b6 =       0.8192   ;%(-0.03893, 1.677)
    a7 =       0.6546   ;%(0.3929, 0.9164)
    b7 =       0.08902  ;%(-1.078, 1.256)
    a8 =       0.2489   ;%(0.08128, 0.4165)
    b8 =       0.04357  ;%(-0.381, 0.4682)
    w =      396.5     ;%(348.2, 444.7)

x=CD;
    t0=0.0127;

    K_barely = a0 + a1*cos(x*w*t0/thickness) + b1*sin(x*w*t0/thickness) +
...
                a2*cos(2*x*w*t0/thickness) + b2*sin(2*x*w*t0/thickness)
+ a3*cos(3*x*w*t0/thickness) + b3*sin(3*x*w*t0/thickness) +...
                a4*cos(4*x*w*t0/thickness) + b4*sin(4*x*w*t0/thickness)
+ a5*cos(5*x*w*t0/thickness) + b5*sin(5*x*w*t0/thickness) +...
                a6*cos(6*x*w*t0/thickness) + b6*sin(6*x*w*t0/thickness)
+ a7*cos(7*x*w*t0/thickness) + b7*sin(7*x*w*t0/thickness) +...
                a8*cos(8*x*w*t0/thickness) + b8*sin(8*x*w*t0/thickness);
end

```

```
function [ sigma] = highly_tensile_stress_4( thickness,FD)
```

```
    a0 =      267;  %(265.1, 268.9)
    a1 =      49.85; %(42.7, 57)
    b1 =     -5.005; %(-18.01, 7.998)
    a2 =     -22.44; %(-26.81, -18.06)
    b2 =      16.59; %(2.142, 31.03)
    a3 =     -1.127; %(-3.482, 1.228)
    b3 =     -3.977; %(-5.022, -2.933)
    a4 =       1.722; %(-2.031, 5.475)
    b4 =       2.727; %(0.9207, 4.533)
    w =      438 ; %(393.8, 482.2)
```

```
x=FD;
```

```
    sigma = a0 + a1*cos(x*w*0.0127/thickness) +
    b1*sin(x*w*0.0127/thickness) + ...
            a2*cos(2*x*w*0.0127/thickness) +
    b2*sin(2*x*w*0.0127/thickness) + ...
            a3*cos(3*x*w*0.0127/thickness) +
    b3*sin(3*x*w*0.0127/thickness) + ...
            a4*cos(4*x*w*0.0127/thickness) +
    b4*sin(4*x*w*0.0127/thickness);
end
```

```

function [ K_highly_tensile ] = K_high( CD,thickness )
    a0 =      20.7   ;%(12.48, 28.92)
    a1 =     -13.27 ;%(-34.14, 7.605)
    b1 =     -6.783 ;%(-18.46, 4.89)
    a2 =    -10.17 ;%(-12.32, -8.023)
    b2 =      7.757 ;%(-12.27, 27.78)
    a3 =     -3.167 ;%(-11.21, 4.877)
    b3 =      5.857 ;%(-6.505, 18.22)
    a4 =      1.325 ;%(-8.748, 11.4)
    b4 =      4.333 ;%(0.08851, 8.577)
    a5 =      2.152 ;%(-5.925, 10.23)
    b5 =      2.131 ;%(-2.088, 6.35)
    a6 =      1.518 ;%(-2.305, 5.34)
    b6 =      0.2935 ;%(-3.821, 4.408)
    a7 =      0.6665 ;%(-0.5928, 1.926)
    b7 =     -0.4182 ;%(-2.784, 1.948)
    a8 =      0.2448 ;%(-0.4815, 0.9712)
    b8 =     -0.1388 ;%(-1.637, 1.359)
    w =      372.9   ;%(200.7, 545.1)

    x=CD;
    t0=0.0127;

    K_highly_tensile = a0 + a1*cos(x*w*t0/thickness) +
    b1*sin(x*w*t0/thickness) + ...
        a2*cos(2*x*w*t0/thickness) + b2*sin(2*x*w*t0/thickness)
    + a3*cos(3*x*w*t0/thickness) + b3*sin(3*x*w*t0/thickness) +...
        a4*cos(4*x*w*t0/thickness) + b4*sin(4*x*w*t0/thickness)
    + a5*cos(5*x*w*t0/thickness) + b5*sin(5*x*w*t0/thickness) +...
        a6*cos(6*x*w*t0/thickness) + b6*sin(6*x*w*t0/thickness)
    + a7*cos(7*x*w*t0/thickness) + b7*sin(7*x*w*t0/thickness) +...
        a8*cos(8*x*w*t0/thickness) + b8*sin(8*x*w*t0/thickness);
end

```


8.2.2 The Turnbull model

8.2.2.1 MATLAB® code The following is the code used for the Turnbull model. First, the main m-file growth loop is given. The only functions called by the Turnbull model are the `get_stress` selection function for residual stress $\sigma(x)$ and residual stress intensity $K(x)$, which are given in Section 8.2.1.

8.2.2.2 Implementation notes In the case given here, the growth rates (pit and crack) have been scaled to give yearly growth rates in order to get results more quickly. This can be modified as needed by removing or changing the conversion factors found after the growth rate (here, the conversion of $24 \times 365.25 \times 3600$ is used to convert a growth rate in length-per-second to length-per-year).

In order to calculate the statistics of interest, additional lines of code can be added to obtain the average time-to-failure, the minimum time-to-failure, the standard deviation of failure times, the median of failure times, and so on. The total time spent pitting and the total time spent cracking are also of interest.

In the MATLAB® program, these quantities can be written as

```
ttf_avg=mean(mean(counter_vector))
ttf_min=min(min(counter_vector))
std_dev=mean(std(counter_vector))
median=mean(median(counter_vector))
pit_time=mean(mean(pit_matrix))
crack_time=mean(mean(crack_matrix))
```

A histogram of the failure times may be obtained by adding the line `hist(counter_vector)`.

When running this code on a cluster, it is generally more convenient to write all quantities of interest to a single text file. In this case, the code above was kept in the file,

and these quantities were collected in one text file using the “dlmwrite” and “-append” commands. For example:

```
dlmwrite('filename', ttf_avg);  
dlmwrite('filename', std_dev, '-append')
```

The total matrix of times to failures was also written to a separate text file in case further analysis was required.

It may also be of interest to monitor the code's progress. To do this when running MATLAB® on the cluster, the group index was copied to a third text file. Each successive group index was appended to this third text file, which could be opened while the program was still running. For example, just before the end of the outermost loop, the following lines were added:

```
test=j;  
dlmwrite('filename', test ,'-append');
```

When large numbers of groups and flaws per group are being simulated, it can be very helpful to know how far the program is from completion using this technique.

```

clear all
clc

%%%%%%%%%%%%%%%%%%%%%%%%%%%%%%%%%%%%%%%%%%%%%%%%%%%%%%%%%%%%%%%%%%%%%%%%
%Initialize fundamental parameters%
%that apply to whole simulation %
%%%%%%%%%%%%%%%%%%%%%%%%%%%%%%%%%%%%%%%%%%%%%%%%%%%%%%%%%%%%%%%%%%%%%%%%

N_batch      =5;
N_pits       =5;
thickness    = 0.0127;      %meters
thickness_um =0.0127*10^6;

%%%%%%%%%%%%%%%%%%%%%%%%%%%%%%%%%%%%%%%%%%%%%%%%%%%%%%%%%%%%%%%%%%%%%%%%
% Select residual stress function %
% 1 = best estimate RS           %
% 2 = barely above K threshold RS %
% 3 = highly tensile case       %
%%%%%%%%%%%%%%%%%%%%%%%%%%%%%%%%%%%%%%%%%%%%%%%%%%%%%%%%%%%%%%%%%%%%%%%%

select_stress_eqn =2;
K_threshold       =3.9999999 ;

%*****%
%   parameter means   %
%*****%

s          = 0.10;
mean_C     = 2.6*10^-18*(10^6)^2;
s_C        = 3.8*10^-18*(10^6)^2;
mean_q     = 3.0;
mean_beta  = 0.37;
mean_alpha = 0.0;
s_alpha    = 0.76;

%*****%
% growth loop        %
%*****%

tff_vector   =zeros(N_batch,1);
counter_vector=zeros(N_pits,N_batch);
C_matrix     =zeros(N_pits,N_batch);
beta_matrix  =zeros(N_pits,N_batch);
alpha_matrix =zeros(N_pits,N_batch);
q_vector     =zeros(N_batch,1);
p_vector     =zeros(N_batch,1);
flaw_depth   =ones(N_pits,N_batch);
pit_matrix   =zeros(N_pits,N_batch);
crack_matrix =zeros(N_pits,N_batch);

for j=1:N_batch
    q=-1;
    while q<0
        q=normrnd(mean_q,s*mean_q);
    end
    q_vector(j)=q;

```

```

    p_vector(j)=2*q_vector(j);
end
for j=1:N_batch
    for i=1:N_pits
        beta=-1;
        while beta <0;
            beta = normrnd(mean_beta,s*mean_beta);
        end
        beta_matrix(i,j)=beta;
        C=-1;
        while C<0
            C = normrnd(mean_C,s_C);
        end
        C_matrix(i,j)=C;
        alpha=-1;
        while alpha<0
            alpha=normrnd(mean_alpha,s_alpha);
        end
        alpha_matrix(i,j)=alpha;
    end
end

for j=1:N_batch
    p=p_vector(j);
    q=q_vector(j);
    for i=1:N_pits
        C=C_matrix(i,j);
        beta=beta_matrix(i,j);
        alpha=alpha_matrix(i,j);
        while flaw_depth(i,j)<thickness_um;
            FD=flaw_depth(i,j)*10^-6;
            [sigma,K]=get_stress(select_stress_eqn, FD,thickness) ;
            if sigma < 0
                break
            end
            CM=counter_vector(i,j);
            if CM>10000
                break
            end
            top=beta*alpha^(1/beta) ;
            bottom=C*sigma^p;
            exponent=beta/(1+beta*(q-1));
            x_crit=(top/bottom)^exponent;
            if flaw_depth(i,j)>x_crit && K>=K_threshold
                flaw_depth(i,j)=flaw_depth(i,j)+(C*sigma^p*flaw_depth(i,j)^
                q)*24*3600*365.25;
                crack_matrix(i,j)=crack_matrix(i,j)+1;
            else
                flaw_depth(i,j)=flaw_depth(i,j)+(beta*alpha^(1/beta)*
                flaw_depth(i,j)^(1-1/beta))*24*3600*365.25;
                pit_matrix(i,j)=pit_matrix(i,j)+1;
            end
            counter_vector(i,j)=counter_vector(i,j)+1
        end
    end
end
end

```

8.2.2.3 Graphs of the Gaussian distributions used to calculate constants in the Turnbull model Figures 78 - 81 show the normal distributions used to calculate the constants in the Turnbull model. α and C are selected from normal distributions with means and standard deviations prescribed in [31] for an aerated chloride environment. The means of β and q are taken from the prescribed values in Turnbull, but normal distributions have been assigned to induce more variability and represent the uncertainty in the applicability of these values for the canister environment. One calculated value of q is assigned to a group of flaws, whereas the set of values of the other 3 constants are unique to each flaw.

The Gaussian distributions are plotted here to show the effects of constraining the selection to allow only positive values. For all constants except α , this effect is minimal. For α , the skew in the distribution is significant, but the standard deviation and mean were fitted under this constraint, so the effects of the skew are not expected to be detrimental to the simulation.

For constants that are characterized by a normal distribution with a standard deviation s - the global standard deviation assigned by the user at the beginning of the simulation - it should be noted that this not the absolute standard deviation, but rather the percentage of the mean which is equivalent to the standard deviation, i.e., for a value of s , the standard deviation of a normal distribution with mean μ is $s \cdot \mu$.

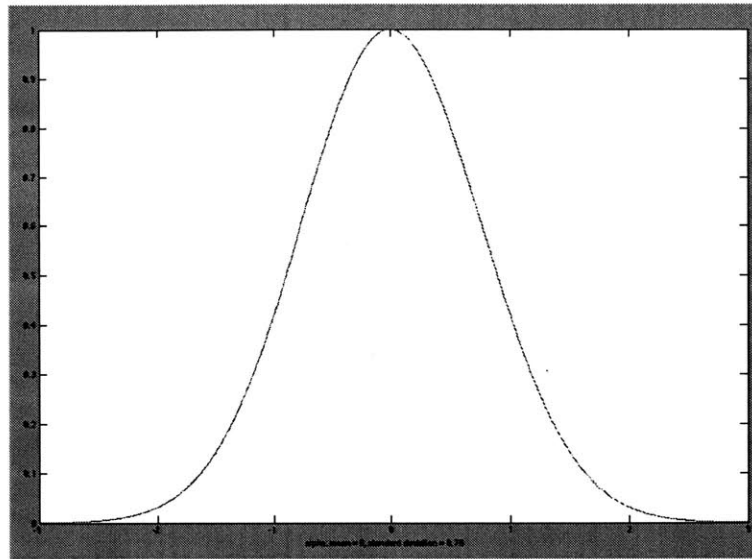


Figure 78: α , used in the pit growth equations in the Turnbull model, has a mean value of 0 and a standard deviation of 0.76. The constraints placed on α ensure that only positive values are picked, significantly skewing this distribution. However, this is the value of mean and standard deviation that the authors in [31] fit to data while also operating under this constraint.

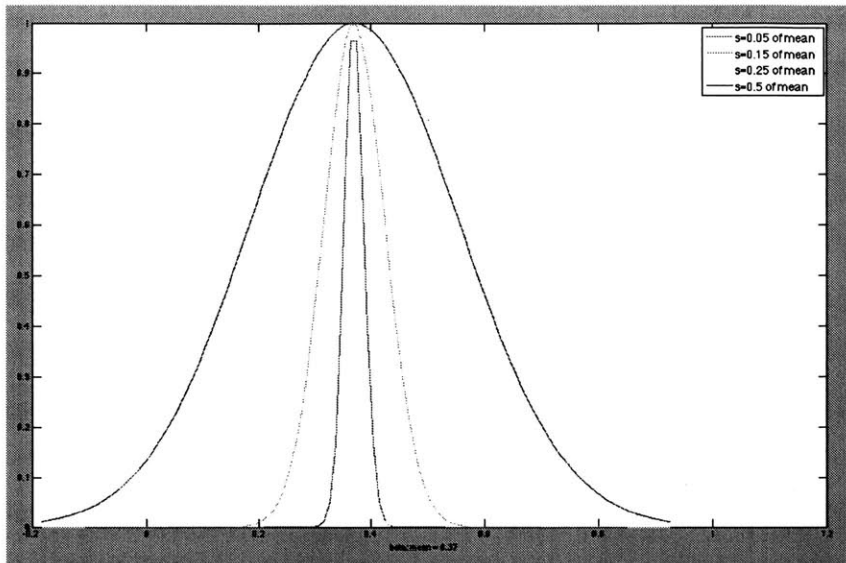


Figure 79: β , used in the pit growth equations in the Turnbull model, has a mean value of 0.37 and a standard set by the user (a standard deviation “set” to 0.15 means that the standard deviation will be $0.15 \times \beta$).

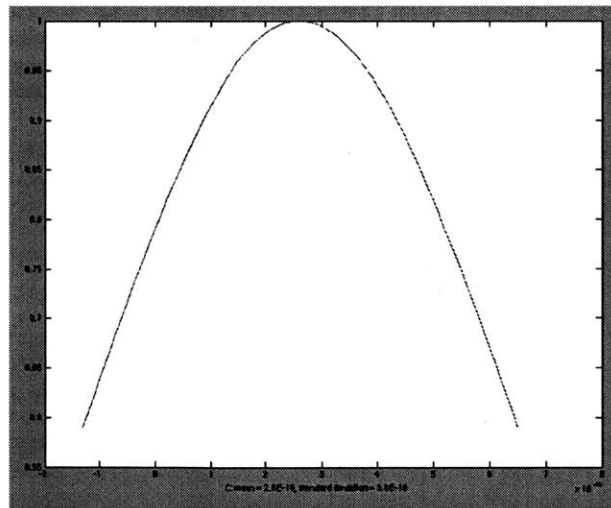


Figure 80: C , used in the crack growth equations in the Turnbull model, has a mean value of 2.6×10^{-18} and a standard deviation of 3.8×10^{-18} .

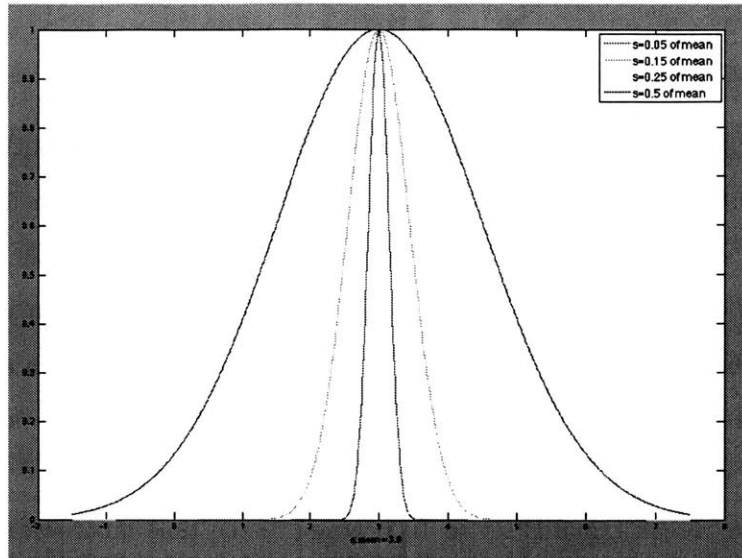


Figure 81: q , used in the crack growth equations in the Turnbull model, has a mean value of 3 and a standard deviation set by the user.

8.2.3 Pit growth: The Henshall model

8.2.3.1 MATLAB® code for the Henshall model The following is the code used for the Henshall model. First, the main m-file growth loop is given. The Henshall model does not require knowledge of the stress or stress intensity as a function of depth in the canister.

There are four functions associated with the Henshall model. These are the “get_growth_prob” function, which calculates the probability that the pit will grow at each iteration, and the environment-related functions that the “get_growth_prob” function calls. These environment-related functions are “get_cl”, “get_potential”, and “get_temperature”, which calculate the chloride concentration, the electric potential, and the temperature at the canister surface respectively as a function of time.

8.2.3.2 Implementation notes The Henshall model is scaled to years in this implementation. The code can be modified by changing the appropriate growth rate (from the growth rate in length-per-year to length-per-desired-time-unit) D at the beginning of the code. If this is changed, it is important to make sure that the three environmental functions are also changed so that their units are consistent with the main body of the code.

For example, the temperature function is written assuming that t is in years. If t as imported from the main body of the code is in a different time unit, then a line should be added to the beginning of the temperature function that converts the imported time to time in years.

Note that the “break” time is set to 1000 years. If the time units are rescaled, this should also be updated, especially if the rescaling is to a shorter unit of time.

```

clear all
clc

%*****%
% simulation parameters %
%*****%

N_batch=5;
N_pits=5;
pit_depth=zeros(N_pits,N_batch);
break_matrix=zeros(N_pits,N_batch);
thickness=0.0127; %m
ttf_vector =zeros(N_batch,1);
counter=zeros(N_pits,N_batch);
%D=3E-11; %mm/s
D=0.001;
act_E=14; %kJ/mol

%*****%
% parameter calculation %
%*****%

s=0.0 ;
mean_E0=1.4;
mean_E1=0.047;
mean_K0=3;
mean_K1=0.0465;
mean_A4=10^-7;
mean_B4=0.4;
mean_B5=0.3;
mean_C4=0.2;

A4_vector=zeros(N_batch,1);
E0_vector=zeros(N_batch,1);
E1_vector=zeros(N_batch,1);
K0_vector=zeros(N_batch,1);
K1_vector=zeros(N_batch,1);
B4_vector=zeros(N_batch,1);
B5_vector=zeros(N_batch,1);
C4_vector=zeros(N_batch,1);

for j=1:N_batch
    while A4_vector(j)<=0
        A4_vector(j)=normrnd(mean_A4,s*mean_A4);
    end
    while E0_vector(j)<=0
        E0_vector(j)=normrnd(mean_E0,0);
    end
    while E1_vector(j)<=0
        E1_vector(j)=normrnd(mean_E1,0);
    end
    while B4_vector(j)<=0
        B4_vector(j)=normrnd(mean_B4,s*mean_B4);
    end
    while B5_vector(j)<=0
        B5_vector(j)=normrnd(mean_B5,s*mean_B5);
    end
end

```

```

while C4_vector(j)<=0
    C4_vector(j)=normrnd(mean_C4,s*mean_C4);
end
while K0_vector(j)<=0
    K0_vector(j)=(normrnd(mean_K0,s*mean_K0));
end
while K1_vector(j)<=0
    K1_vector(j)=(normrnd(mean_K1,s*mean_K1));
end
end

%*****%
% growth loop %
%*****%

for j=1:N_batch
    A_4=A4_vector(j);
    B_4=B4_vector(j);
    B_5=B5_vector(j);
    C_4=C4_vector(j);
    E_0=E0_vector(j);
    E_1=E1_vector(j);
    K_0=K0_vector(j);
    K_1=K1_vector(j);
    for i=1:N_pits
        while pit_depth(i,j)<thickness
            t=counter(i,j);

gamma=get_growth_prob(act_E,t,s,A_4,B_4,mean_B4,B_5,C_4,K_0,K_1,E_0,E_1
);
            if rand<gamma
                pit_depth(i,j)=pit_depth(i,j)+rand*D;
            end
            counter(i,j)=counter(i,j)+1
            if counter(i,j)>200
                break_matrix(i,j)=1;
                break
            end
        end
    end
    check=j;
end
end

```

```

function gamma =
get_growth_prob(act_E,t,s,A_4,B_4,mean_B4,B_5,C_4,K_0,K_1,E_0,E_1)

Q=act_E*1000;

T=get_temp(t);
chloride_conc=get_cl(t,K_0,K_1);
E_app=get_potential(t,E_0,E_1);

R=8.3144521;
RT=R*T;

if B_4==E_app
    E_app=B_4+0.001;
end
% when s=0, B4 will always = E_app on the first iteration, so create an
inequality artificially

gamma=-1;
while gamma<0
gamma=A_4*(E_app-B_4)^B_5*chloride_conc^C_4*exp(Q/RT) ;
end

end

```

```
function Cl = get_cl(t,K_0,K_1)
```

```
t_years=t;
```

```
Cl=K_0-exp(-K_1*t_years);
```

```
end
```

```
function E_app = get_potential(t,E_0,E_1)
```

```
t_years=t;
```

```
E_app=E_0-exp(-E_1*t_years);
```

```
end
```

```
function temp = get_temp(t)
```

```
t_years=t;
```

```
temp=71.74*exp(-0.1126*t_years) +107.3*exp(-0.005747*t_years);
```

```
end
```

8.2.3.3 Graphs of the Gaussian distributions used to calculate constants in the Henshall model In Henshall [35], multiple sets of values are given for the constants used in the model's equations. One set was chosen for use in this work, and these values became the average values for each constant. At each iteration of the pit growth loop in the code, the parameter's value was selected from a Gaussian distribution with that value and a standard deviation (expressed as a percentage of the average value) selected by the user. To prevent unphysical results, negative values of the constants were rejected. In practice, this artificially skews the Gaussian distribution to the right, but for typical values of the standard deviation, this should have a minimal effect on the results. The Gaussian distributions for the constants E_0 , E_1 , A_4 , B_4 , B_5 , and C_5 are shown here, with standard deviations equivalent to 5, 15, 25, and 50% of the parameter's mean value. The area under the curves that represents negative parameter values is small compared to the overall area.

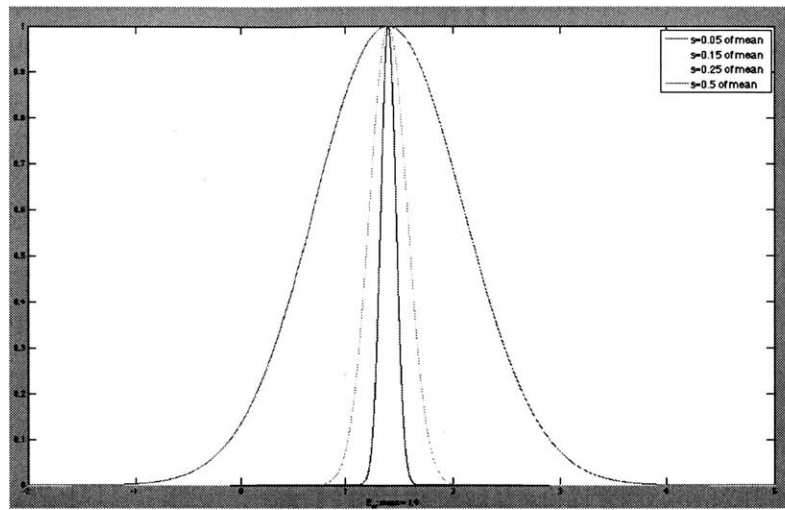


Figure 82: E_0 , used in the equation describing potential in the flaw, has an average value of 1.4.

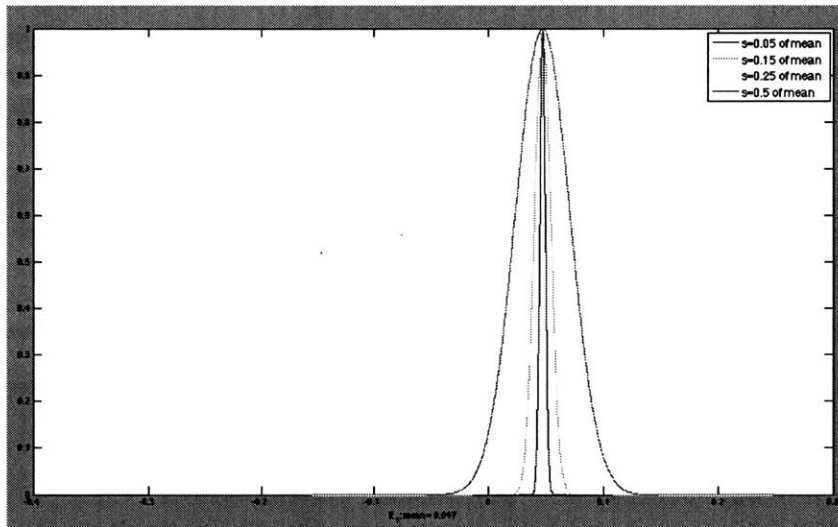


Figure 83: E_1 , used in the equation describing potential in the flaw, has an average value of 0.047.

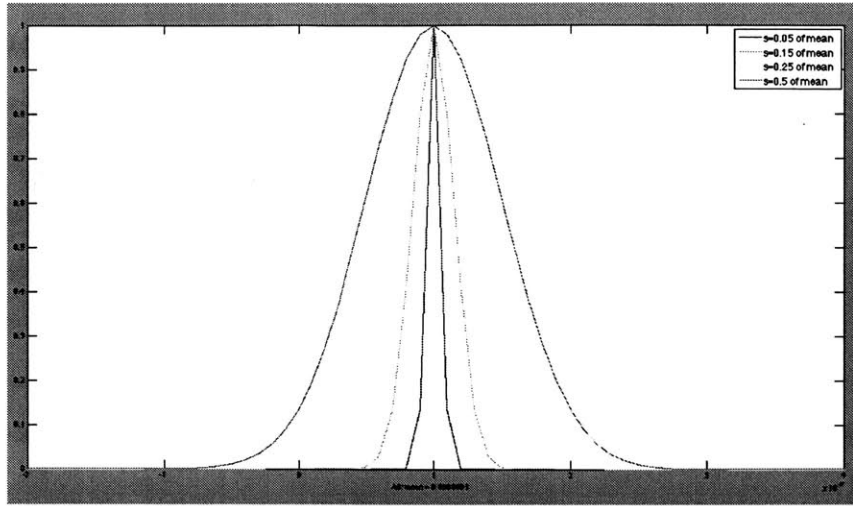


Figure 84: A_4 , used in the equation describing pit growth probability, has an average value of 10^{-7} .

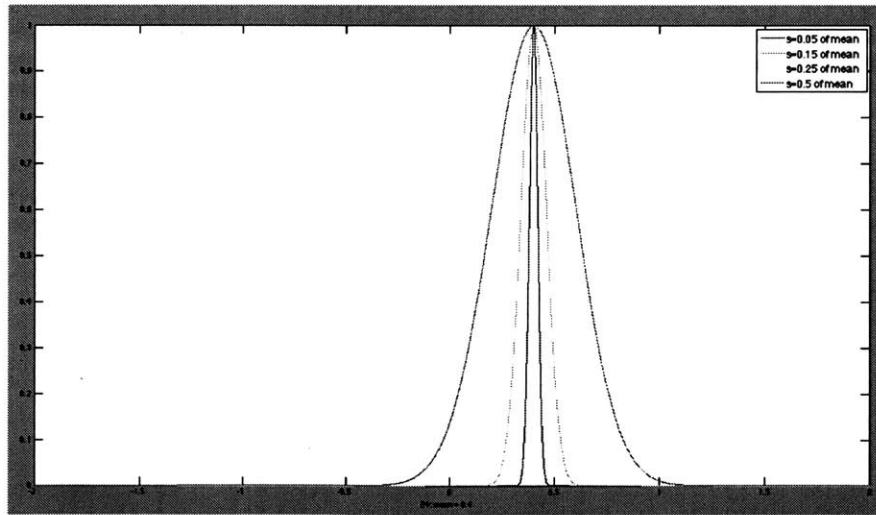


Figure 85: B_4 , used in the equation describing pit growth probability, has an average value of 0.4.

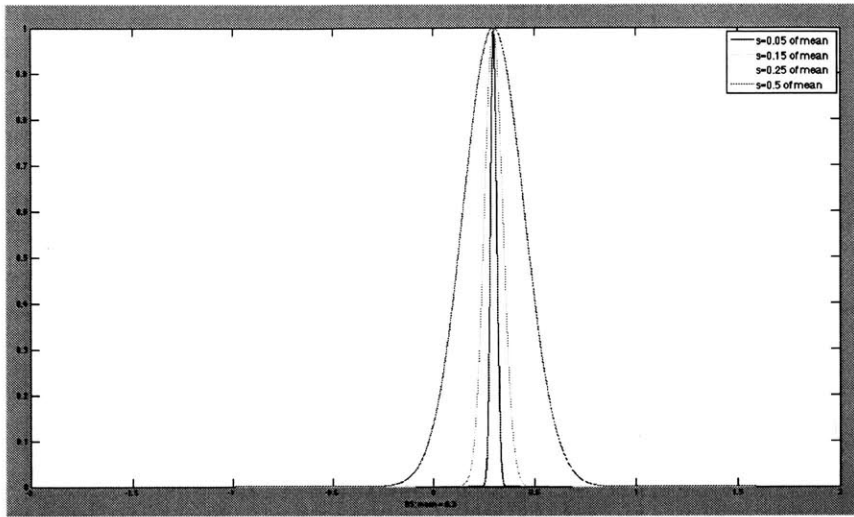


Figure 86: B_5 , used in the equation describing pit growth probability, has an average value of 0.3.

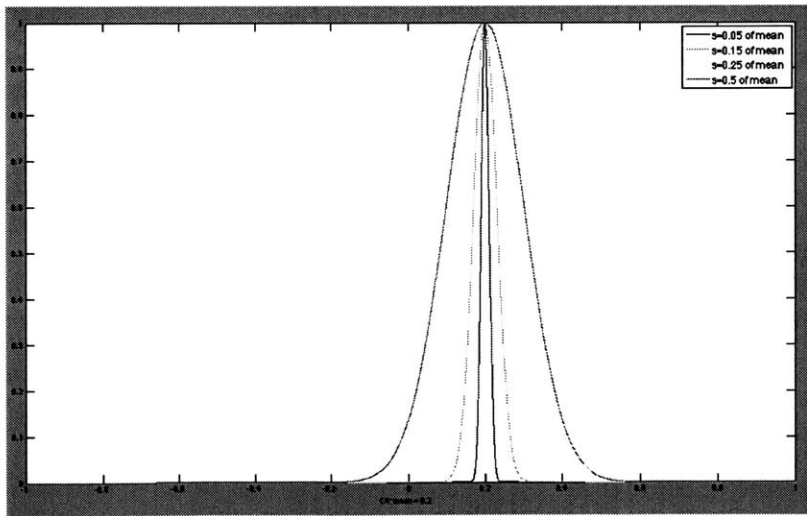


Figure 87: C_4 , used in the equation describing pit growth probability, has an average value of 0.2.

8.2.4 Pit-to-crack growth: The combined Henshall/Shoji model

8.2.4.1 MATLAB® code for the Henshall/Shoji model The following is the code used for the combined Henshall (pits) - Shoji (cracks) model. First, the main m-file growth loop is given. Note that functions particular to the Henshall model are not given here, as they are given in the previous section. The functions particular to the Shoji cracking model are “CGR_Shoji” (crack growth rate calculator), “get_K” and “get_K_dot.” The Shoji model also requires knowledge of the stress intensity as a function of depth. As explained in Section 8.2.1, there are three possible cases (best-estimate, barely-above the threshold for cracking, and highly tensile) derived from the work in [32]. The desired case is set by the user at the beginning of the simulation, and this information is passed through the “get_K” function in order to update $K(x)$ at each iteration step. The residual stress intensity functions themselves are not repeated here.

8.2.4.2 Implementation notes The growth loop is set to break after 1000 years to optimize calculation speed. Breaks are tallied so the user can estimate the extent to which the statistics were affected by this break.

```

clear all
clc

N_batch          =2;
N_flaws          =3;
flaw_depth      =zeros(N_flaws,N_batch);
counter         =zeros(N_flaws,N_batch);
pitcount        =zeros(N_flaws,N_batch);
crackcount      =zeros(N_flaws,N_batch);
select_K_function =2;
%1 = best estimate; 2 = highly tensile; 3 = barely above K threshold
thickness       =0.0127;
D               =0.001;
act_E           =14;
K_th            =4;
f               =0.64;
K_IC            =1.4*10^6;
E_ox            =208*10^9;
b=D;

%SHOJI CRACK MODEL CONSTANTS
s               =0.0;
mean_beta      =5.08;
mean_lambda    =0.11;
mean_m         =0.567;
mean_n         =1.36;
%HENSHALL PIT MODEL CONSTANTS
mean_E0        =1.4;
mean_E1        =0.047;
mean_K0        =3;
mean_K1        =0.0465;
mean_A4        =10^-7;
mean_B4        =0.4;
mean_B5        =0.3;
mean_C4        =0.2;

A4_vector=zeros(N_batch,1);
E0_vector=zeros(N_batch,1);
E1_vector=zeros(N_batch,1);
K0_vector=zeros(N_batch,1);
K1_vector=zeros(N_batch,1);
B4_vector=zeros(N_batch,1);
B5_vector=zeros(N_batch,1);
C4_vector=zeros(N_batch,1);

for j=1:N_batch
    while A4_vector(j)<=0
        A4_vector(j)=normrnd(mean_A4,s*mean_A4);
    end
    while E0_vector(j)<=0
        E0_vector(j)=normrnd(mean_E0,0);
    end
    while E1_vector(j)<=0
        E1_vector(j)=normrnd(mean_E1,0);
    end
    while B4_vector(j)<=0
        B4_vector(j)=normrnd(mean_B4,s*mean_B4);
    end
end

```

```

end
while B5_vector(j)<=0
    B5_vector(j)=normrnd(mean_B5,s*mean_B5);
end
while C4_vector(j)<=0
    C4_vector(j)=normrnd(mean_C4,s*mean_C4);
end
while K0_vector(j)<=0
    K0_vector(j)=(normrnd(mean_K0,s*mean_K0));
end
while K1_vector(j)<=0
    K1_vector(j)=(normrnd(mean_K1,s*mean_K1));
end
end

lambda_vector=zeros(N_batch,1);
beta_vector=zeros(N_batch,1);
m_vector=zeros(N_batch,1);
n_vector=zeros(N_batch,1);

for j=1:N_batch
    lambda_vector(j)=normrnd(mean_lambda,0);
    while beta_vector(j)<= 0
        beta_vector(j)=normrnd(mean_beta,mean_beta*s);
    end
    while m_vector(j)<= 0
        m_vector(j)=normrnd(mean_m,mean_m*s);
    end
    while n_vector(j)<= 0
        n_vector(j)=normrnd(mean_n,mean_n*s);
    end
end

%*****%
% Growth loop      %
%*****%

for j=1:N_batch
    A_4=A4_vector(j);
    B_4=B4_vector(j);
    B_5=B5_vector(j);
    C_4=C4_vector(j);
    E_0=E0_vector(j);
    E_1=E1_vector(j);
    K_0=K0_vector(j);
    K_1=K1_vector(j);
    lambda=lambda_vector(j);
    beta=beta_vector(j);
    m=m_vector(j);
    n=n_vector(j);
    for i=1:N_flaws
        while flaw_depth(i,j)<thickness
            FD= flaw_depth(i,j);
            K=get_K(FD,select_K_function,thickness);
            t=counter(i,j);
            if K < 0
                break
            end
        end
    end
end

```

```

end
if K<K_th
    pitcount(i,j)=pitcount(i,j)+1;
gamma=get_growth_prob(act_E,t,s,A_4,B_4,mean_B4,B_5,C_4,K_0,K_1,E_0,E_1
);
    if rand<gamma
        flaw_depth(i,j)=flaw_depth(i,j)+rand*D;
    end
end
if K >= K_th;
    crackcount(i,j)=crackcount(i,j)+1;
    c=flaw_depth(i,j);
    fracture_strain=K_IC/(f*E_ox*(pi*c)^0.5);
    eps_f=fracture_strain;
    old_FD=flaw_depth(i,j);
    if counter(i,j)>1
        a=old_FD;
        K_dot=get_K_dot(K,a,select_K_function,thickness);
    else
        K_dot=0.1;
    end
    count=counter(i,j);

flaw_depth(i,j)=flaw_depth(i,j)+CGR_Shoji(K,K_dot,b,mean_m,mean_n,mean_
beta,mean_lambda,s,eps_f,count);

b=CGR_Shoji(K,K_dot,b,mean_m,mean_n,mean_beta,mean_lambda,s,eps_f,count
);
    end
    counter(i,j)=counter(i,j)+1
end
end
test=j;
dlmwrite('HS_0t_jcheck',test,'-append');
end

```

```

function crackgrowth_shoji =
CGR_Shoji(K,K_dot,b,mean_m,mean_n,mean_beta,mean_lambda,s,eps_f,count)

M      =47.9886733/1000;
i_0    =0.5;
z      =2;
rho    =8.03/1000*100^2;
r      =10*10^-6;
F      =9.64853399*10^-4;
t_0    =54.02;

sigma_ys=205 ;
E=193000;

beta=-1;
n=-1;
m=-1;
lambda=-1;

while beta<0
beta=normrnd(mean_beta,s*mean_beta);
end
while n<=1
n=normrnd(mean_n,s*mean_n);
end
while m<0
m=normrnd(mean_m,s*mean_m);
end
while lambda<0
lambda=normrnd(mean_lambda,s*mean_lambda);
end

electro=(M*i_0)/(z*rho*F*(1-m));
time=(t_0/eps_f)^m ;
beta_term = (beta*sigma_ys*n)/(E*(n-1));
K_term=2*K_dot/K;
a_dot_term=b/r;
n_exp=1/(n-1);
lambda_term=lambda/r*(K/sigma_ys)^2;
log_lambda=log(lambda/r*(K/sigma_ys)^2);

crackgrowth_shoji=electro*time^m*(beta_term*(K_term+a_dot_term)*log_lambda^
n_exp)^m;

end

```

```
function [K]=get_K(FD,select_K_function,thickness)
```

```
if select_K_function==1  
    [K]=K_best_estimate(FD,thickness);  
end
```

```
if select_K_function==2  
    [K]=K_barely_above(FD,thickness);  
end
```

```
if select_K_function==3  
    [K]=K_high(FD,thickness);  
end  
end
```

```
function [Kdot] = get_K_dot(K,a,select_K_function,thickness)
```

```
K_new=K;  
FD=a;  
K_old=get_K(FD,select_K_function,thickness);  
Kdot=K_new-K_old;
```

```
end
```

8.2.4.3 Graphs of the Gaussian distributions used to calculate constants in the Shoji model .

The Gaussian distributions for the constants m , n , β , and λ are shown here, with standard deviations equivalent to 5, 15, 25, and 50% of the parameter's mean value. The area under the curves that represents negative parameter values is small compared to the overall area. Further explanation of the selection of the mean values of these parameters can be found on page 81.

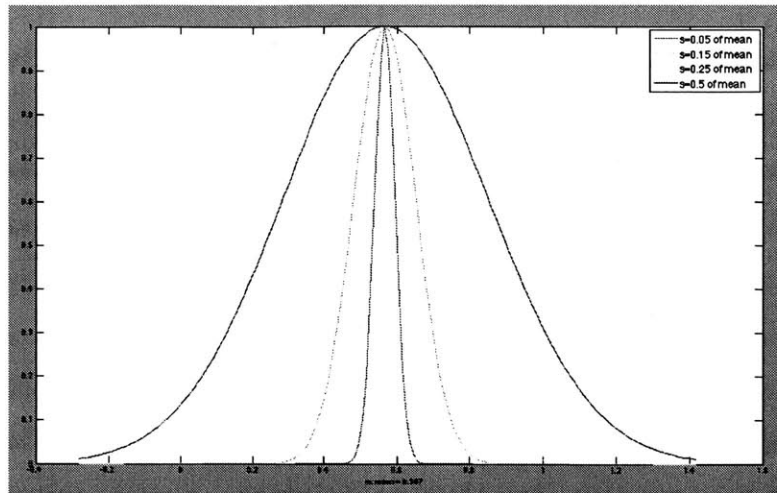


Figure 88: m , the slope of the oxidation rate decay curve used in the Shoji model, has a mean value of 0.567.

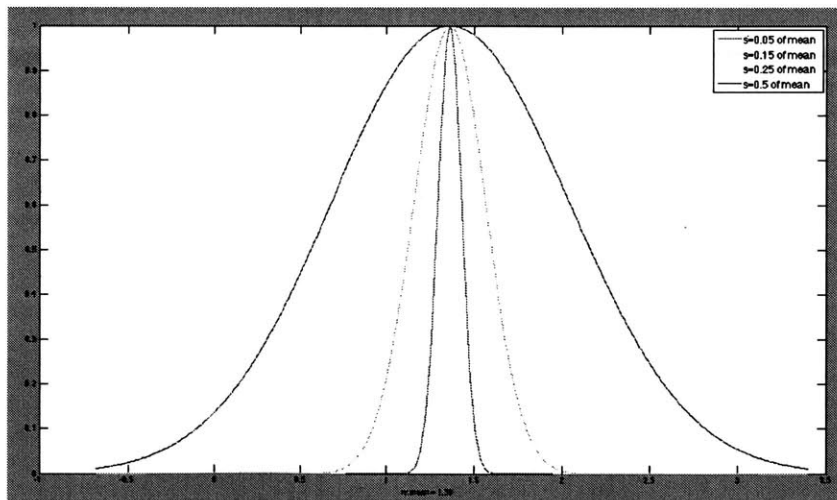


Figure 89: n , the strain hardening exponent used in the Shoji model, has a mean value of 1.36.

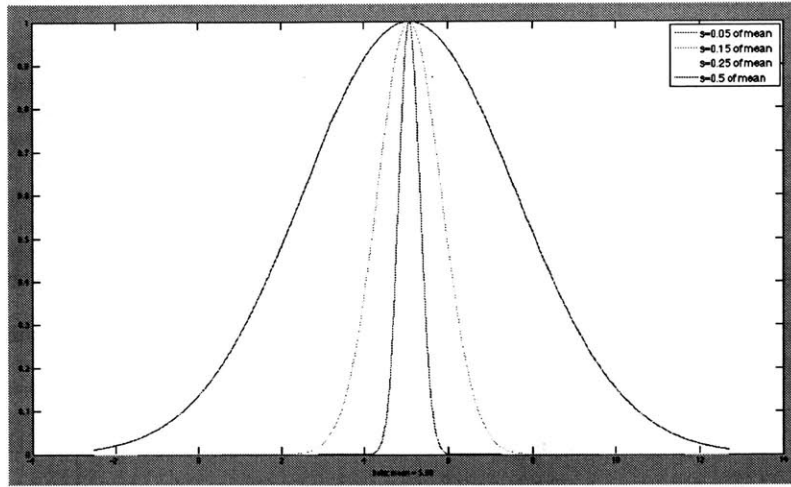


Figure 90: β , a fitting constant in the Shoji model, has a mean value of 5.08.

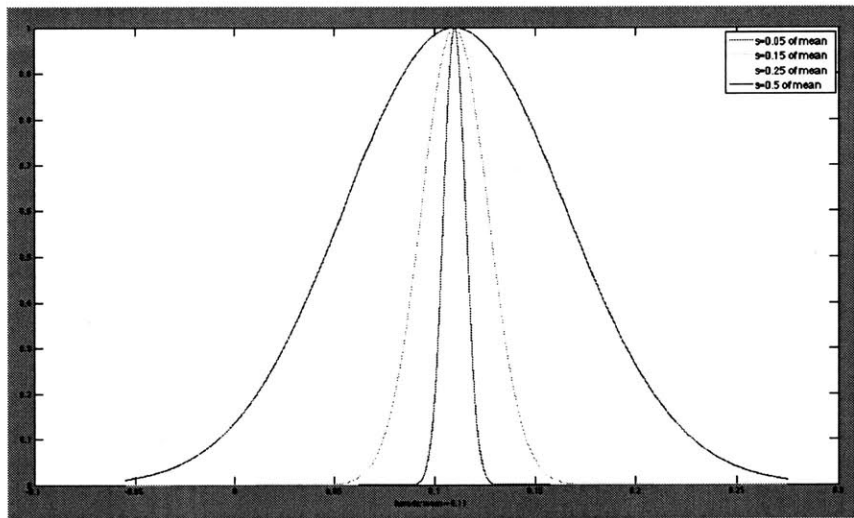


Figure 91: λ , a fitting constant in the Shoji model, has a mean value of 0.11.

8.2.5 Pit-to-crack growth: The combined Henshall/Wu model

8.2.5.1 MATLAB® code for the Wu model The following is the code used for the combined Henshall (pits) - Wu (cracks) model. First, the main m-file growth loop is given. Note that functions particular to the Henshall model are not given here, as they are given in Section 8.2.3. The functions particular to the Wu cracking model are the three crack growth rate functions (“CGR_1”, “CGR_12”, and “CGR_2”) and the function to calculate pH (“get_pH”). Note that the Wu model, like the Henshall model, also requires the calculation of the temperature; in this case, the same temperature function used in the Henshall model was also used in the Wu cracking model portion of the simulation.

8.2.5.2 Implementation notes The growth loop is set to break after 1000 years to optimize calculation speed. Breaks are tallied so the user can estimate the extent to which the statistics were affected by this break.

```

clear all
clc
tic
%*****%
%Wu Crack Growth %
%*****%

N_batch      = 20      ;
N_flaws      = 100     ;
flaw_depth   = zeros(N_flaws,N_batch) ;
K_at_depth   = zeros(N_flaws,N_batch) ;
counter      = zeros(N_flaws,N_batch) ;
counter_pits = zeros(N_flaws,N_batch);
counter_cracks = zeros(N_flaws,N_batch);
breaktally=0;

thickness=0.0127;
D=0.001;
act_E=14;

select_K_function = 2;
%1 = best estimate; 2= barely above K threshold; 3=highly tensile
t_conv=365.25*24*3600;

K_trs      = 15;
K_tre      = 25;
K_th       = 4;
sigma_ys   = 290;
R          = 0.008314;
Q          = 29;
Q_s        = 0.414;
T_ref      = 180+273.15;

s          = 0.50;
mean_C1    = 9.7*10^-12;
mean_C2    = 2.86*10^-12;
mean_m1    = 0.2286;
mean_m2    = 0.1836;
mean_n1    = 0.8982;
mean_n2    = 0.736;
mean_b2    = 0.3418;
mean_K0    = 3;
mean_K1    = 0.0465;

C1_vector=zeros(N_batch,1);
C2_vector=zeros(N_batch,1);
m1_vector=zeros(N_batch,1);
m2_vector=zeros(N_batch,1);
n1_vector=zeros(N_batch,1);
n2_vector=zeros(N_batch,1);
b2_vector=zeros(N_batch,1);
Q_vector =zeros(N_batch,1);

for j=1:N_batch
    while C1_vector(j)<=0
        C1_vector(j)=normrnd(mean_C1,s*mean_C1);
    end
end

```

```

while C2_vector(j)<=0
    C2_vector(j)=normrnd(mean_C2,s*mean_C2);
end
while m1_vector(j)<=0;
    m1_vector(j)=normrnd(mean_m1,s*mean_m1);
end
while n1_vector(j)<=0
    n1_vector(j)=normrnd(mean_n1,s*mean_n1);
end
while m2_vector(j)<=0
    m2_vector(j)=normrnd(mean_m2,s*mean_m2);
end
while n2_vector(j)<=0
    n2_vector(j)=normrnd(mean_n2,s*mean_n2);
end
while b2_vector(j)<=0
    b2_vector(j)=normrnd(mean_b2,s*mean_b2);
end
while Q_vector(j)<=0
    Q_vector(j)=normrnd(Q,Q_s*Q);
end
end
end

```

```

mean_E0=1.4;
mean_E1=0.047;
mean_A4=10^-7;
mean_B4=0.4;
mean_B5=0.3;
mean_C4=0.2;

```

```

A4_vector=zeros(N_batch,1);
E0_vector=zeros(N_batch,1);
E1_vector=zeros(N_batch,1);
K0_vector=zeros(N_batch,1);
K1_vector=zeros(N_batch,1);
B4_vector=zeros(N_batch,1);
B5_vector=zeros(N_batch,1);
C4_vector=zeros(N_batch,1);

```

```

for j=1:N_batch
    while A4_vector(j)<=0
        A4_vector(j)=normrnd(mean_A4,s*mean_A4);
    end
    while E0_vector(j)<=0
        E0_vector(j)=normrnd(mean_E0,0);
    end
    while E1_vector(j)<=0
        E1_vector(j)=normrnd(mean_E1,0);
    end
    while B4_vector(j)<=0
        B4_vector(j)=normrnd(mean_B4,s*mean_B4);
    end
    while B5_vector(j)<=0
        B5_vector(j)=normrnd(mean_B5,s*mean_B5);
    end
    while C4_vector(j)<=0
        C4_vector(j)=normrnd(mean_C4,s*mean_C4);
    end
end

```

```

while K0_vector(j)<=0
    K0_vector(j)=normrnd(mean_K0,s*mean_K0);
end
while K1_vector(j)<=0
    K1_vector(j)=normrnd(mean_K1,s*mean_K1);
end
end

%initialize depth of flaws
for j=1:N_batch
    C1=C1_vector(j);
    C2=C2_vector(j);
    m1=m1_vector(j);
    m2=m2_vector(j);
    n1=n1_vector(j);
    n2=n2_vector(j);
    b2=b2_vector(j);
    Q_= Q_vector(j);
    A4=A4_vector(j);
    B4=B4_vector(j);
    B5=B5_vector(j);
    C4=C4_vector(j);
    E0=E0_vector(j);
    E1=E1_vector(j);
    K0=K0_vector(j);
    K1=K1_vector(j);
    for i=1:N_flaws
        while flaw_depth(i,j)<thickness
            t=counter(i,j);
            FD= flaw_depth(i,j);
            K_at_depth(i,j)=get_K(FD,select_K_function,thickness);
            if K_at_depth(i,j)<0
                break
            end
            if K_at_depth(i,j) <K_th
                counter_pits(i,j)=counter_pits(i,j)+1;
            end
        end
        gamma=get_growth_prob(act_E,t,s,A4,B4,mean_B4,B5,C4,K0,K1,E0,E1);
        if rand<gamma
            flaw_depth(i,j)=flaw_depth(i,j)+rand*D;
            K_at_depth(i,j)=get_K(FD,select_K_function,thickness);
        end
        if K_at_depth(i,j) >=K_th && K_at_depth(i,j)<= K_tr;
            K=K_at_depth(i,j);
            t=counter_pits(i,j)+counter_cracks(i,j)/t_conv;
            g1=CGR_1(K,K_th,R,Q_,T_ref,sigma_ys,C1,m1,n1,t)*t_conv;
            flaw_depth(i,j)=flaw_depth(i,j)+g1;
            counter_cracks(i,j)=counter_cracks(i,j)+1;
            FD=flaw_depth(i,j);
            K_at_depth(i,j)=get_K(FD,select_K_function,thickness);
        end
        if K_at_depth(i,j)>K_tr && K_at_depth(i,j) < K_tre;
            K=K_at_depth(i,j);
            t=counter_pits(i,j)+counter_cracks(i,j)/t_conv;
        end
    end
end

g12=CGR_12(K,K_th,K_tr,K_tre,sigma_ys,R,Q_,T_ref,m1,m2,n1,n2,C1,C2,b2,
K0,K1,t)*t_conv;

```

```

        flaw_depth(i,j)=flaw_depth(i,j)+g12;
        counter_cracks(i,j)=counter_cracks(i,j)+1;
        FD=flaw_depth(i,j);
        K_at_depth(i,j)=get_K(FD,select_K_function,thickness);
    end
    if K_at_depth(i,j) >= K_tre;
        t=counter_pits(i,j)+counter_cracks(i,j)/t_conv;
g2=CGR_2(K,R,Q,T_ref,sigma_ys,C2,n2,m2,b2,K_th,t,mean_K0,mean_K1)*t_co
nv;
        flaw_depth(i,j)=flaw_depth(i,j)+g2;
        FD=flaw_depth(i,j);
        K_at_depth(i,j)=get_K(FD,select_K_function,thickness);
        counter_cracks(i,j)=counter_cracks(i,j)+1;
    end
    counter(i,j)=counter(i,j)+1;
    if counter(i,j)>=1000
        breaktally=breaktally+1;
        break
    end
end
end
check=j
end

final_counter=zeros(N_flaws,N_batch);
for j=1:N_batch
    for i=1:N_flaws
        final_counter(i,j)=counter_pits(i,j)+counter_cracks(i,j);
    end
end
end

```

```

function crack_growth_1 = CGR_1(K,K_th,R,Q_,T_ref,sigma_ys,C1,m1,n1,t)
T=get_T_wu(t);
if K>K_th
crack_growth_1=C1*exp(Q_/R*(1/T-1/T_ref))*sigma_ys^m1*(K-K_th)^n1;
else
crack_growth_1=C1*exp(Q_/R*(1/T-1/T_ref))*sigma_ys^m1;
end
end

```

```

function
crack_growth_2=CGR_2(K,R,Q_,T_ref,sigma_ys,C2,n2,m2,b2,K_th,t,K0,K1)
T = get_T_wu(t);
pH = get_pH_wu(t,K0,K1);
if K>K_th
    crack_growth_2=C2*exp(Q_/R*(1/T-1/T_ref))*pH^b2*sigma_ys^m2*(K-
K_th)^n2;
else
    crack_growth_2=C2*exp(Q_/R*(1/T-1/T_ref))*pH^b2*sigma_ys^m2;
end
end

```

```

function [ crack_growth_12 ] =
CGR_12(K,K_th,K_trs,K_tre,sigma_ys,R,Q_,T_ref,m1,m2,n1,n2,C1,C2,b2,K0,K
1,t)
T =get_T_wu(t);
pH =get_pH_wu(t,K0,K1) ;
if K>K_th
crack_growth_1 = C1*exp(Q_/R*(1/T-1/T_ref))*sigma_ys^m1*(K-K_th)^n1;
crack_growth_2 = C2*exp(Q_/R*(1/T-1/T_ref))*pH^b2*sigma_ys^m2*(K-
K_th)^n2;
x = (K-K_trs)/(K_tre-K_trs);
crack_growth_12=crack_growth_1*(1-x)+crack_growth_2*x;
else
crack_growth_1 = C1*exp(Q_/R*(1/T-1/T_ref))*sigma_ys^m1;
crack_growth_2 = C2*exp(Q_/R*(1/T-1/T_ref))*pH^b2*sigma_ys^m2;
x = (K-K_trs)/(K_tre-K_trs);
crack_growth_12=crack_growth_1*(1-x)+crack_growth_2*x;
end
end

```

```

function pH=get_pH_wu(t,K0,K1)
C1=K0-exp(-K1*t);
pH = 14 + log10(sqrt(7.7*10^-21*C1));
end

```


8.2.5.3 Graphs of the Gaussian distributions used to calculate constants in the Wu model The Gaussian distributions for the constants C_1 , C_2 , m_1 , m_2 , n_1 , n_2 , and β_2 are shown here, with standard deviations equivalent to 5, 15, 25, and 50% of the parameter's mean value. The area under the curves that represents negative parameter values is small compared to the overall area. Further explanation of the selection of the mean values of these parameters can be found on page 90.

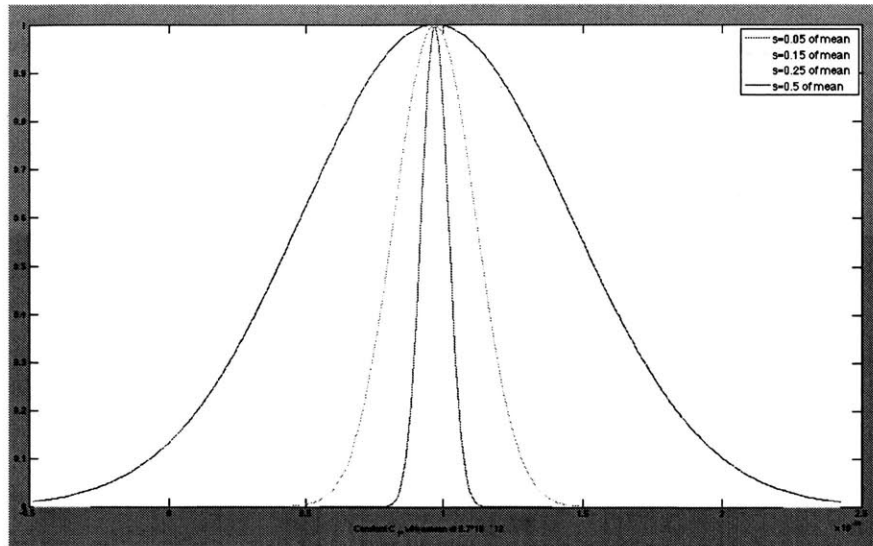


Figure 92: C_1 , a fitting constant in the Wu model, has a mean value of 9.7×10^{-12} .

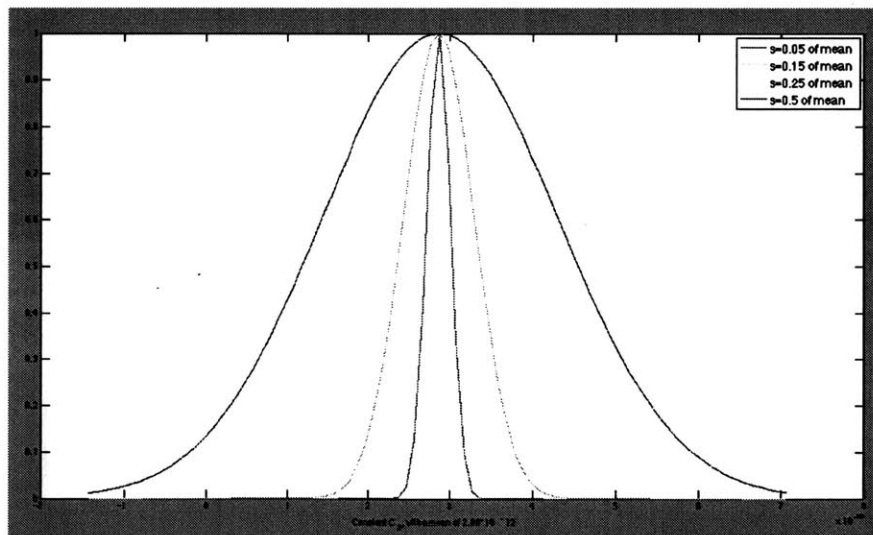


Figure 93: C_2 , a fitting constant in the Wu model, has a mean value of 2.86×10^{-12} .

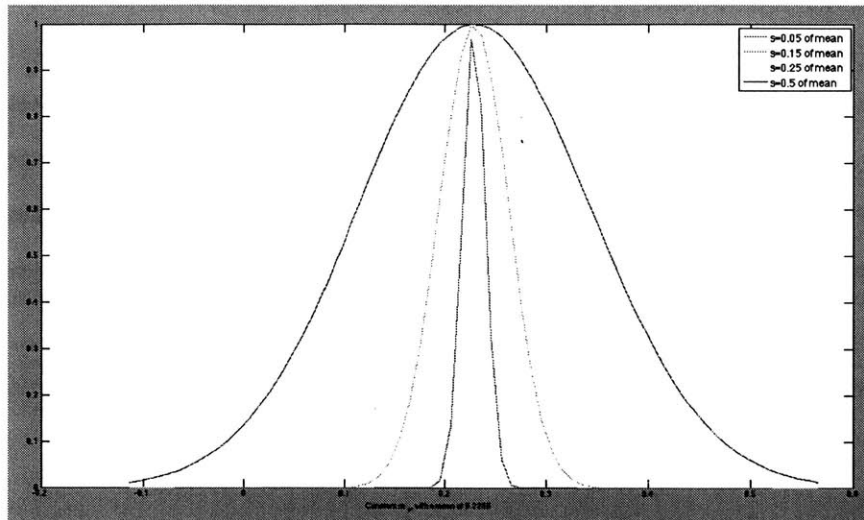


Figure 94: m_1 , an exponent on yield stress in the Wu model, has a mean value of 0.2286.

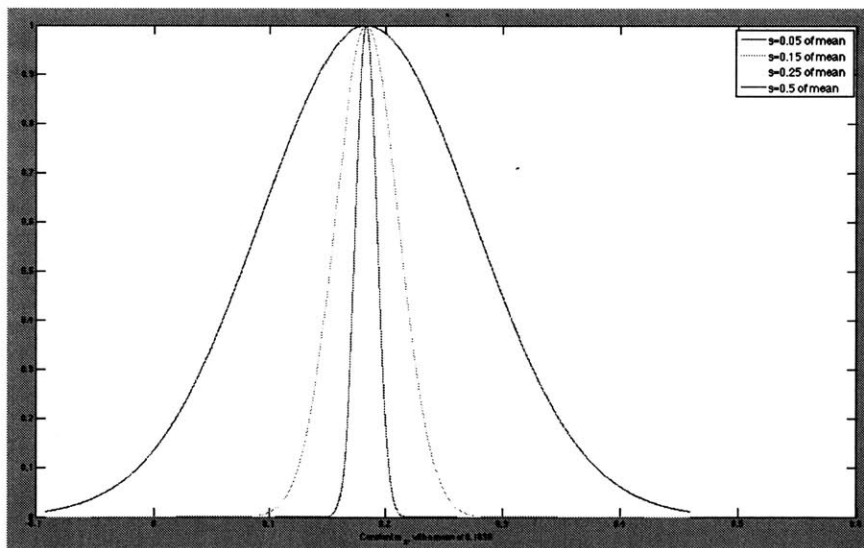


Figure 95: m_2 , an exponent on yield stress in the Wu model, has a mean value of 0.1836.

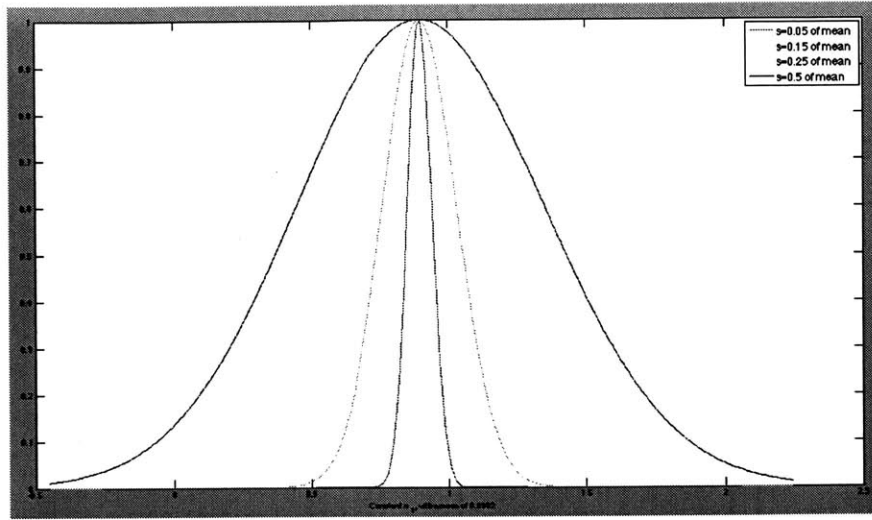


Figure 96: n_1 , an exponent on stress intensity in the Wu model, has a mean value of 0.8982.

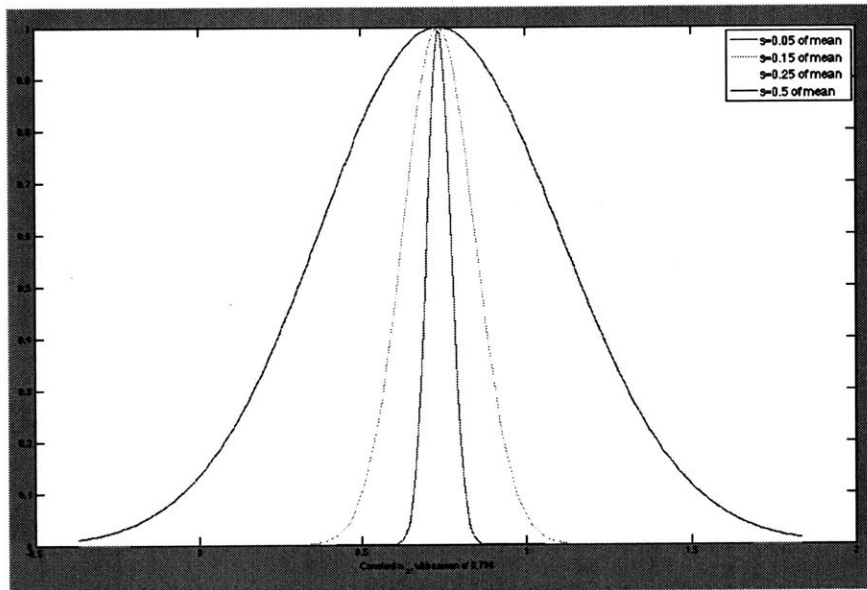


Figure 97: n_2 , an exponent on stress intensity in the Wu model, has a mean value of 0.7360.

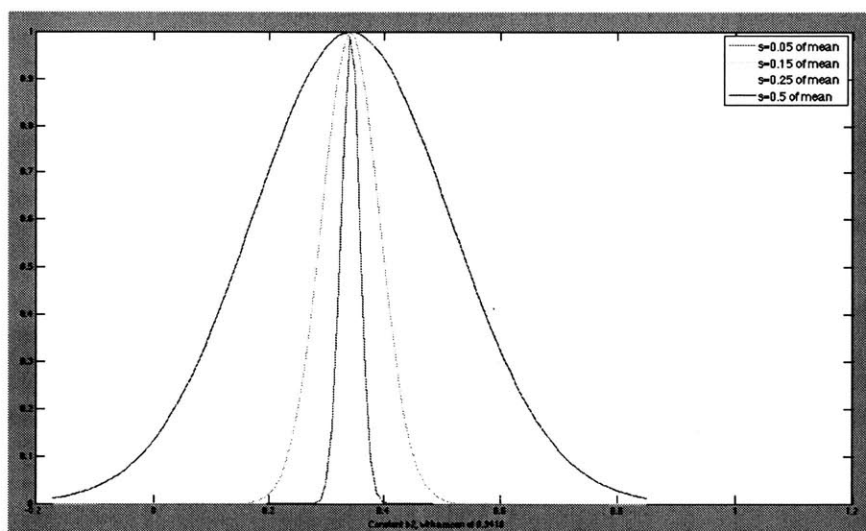


Figure 98: β_2 , an exponent on pH in the Wu model, has a mean value of 0.3418.

9 Appendix C: Weld samples

This appendix contains information about research carried out on weld samples from prototypical canister material. Images of the weld and its metallographs are provided, in addition to the results of a hardness test carried out on a weld sample. Finally, select preliminary results of neutron diffraction measurements carried out to measure residual stresses inside the weld are included here for the reference and interest of the reader.

9.1 Prototypical weld samples

Prototypical weld samples were obtained for characterization, environmental testing, and measurement of residual stresses. These flat-plate Type 304 stainless steel welds were intended to be a good approximation of an average spent fuel canister. Figure 99 shows the section of the weld plate that was used in these characterization studies. Figure 100 shows a polished cross section of this sample. The weld is of the “double-vee” type. Figure 101 shows a composite micrograph that depicts the edge of one of the “vees.” The fusion line where the weld material meets the bulk material is small, possibly indicating that the heat-affected zone (HAZ) next to the weld is small as well. The HAZ is the area most likely to experience sensitization during the welding process itself, and is one of the areas of greatest concern with regard to corrosion problems that may occur in the canisters. Figure 102 shows a close up micrograph of the intersection of two of the weld “vees.”

The documentation available for this weld sample includes the metallurgical report, the radiographic testing report, the liquid penetrant exam report, the visual inspection reports, and statements of compliance from the relevant providers. These documents have been redacted from the final version of this thesis, but can be made available upon request.¹¹⁴

¹¹⁴Contact information: seferry@mit.edu

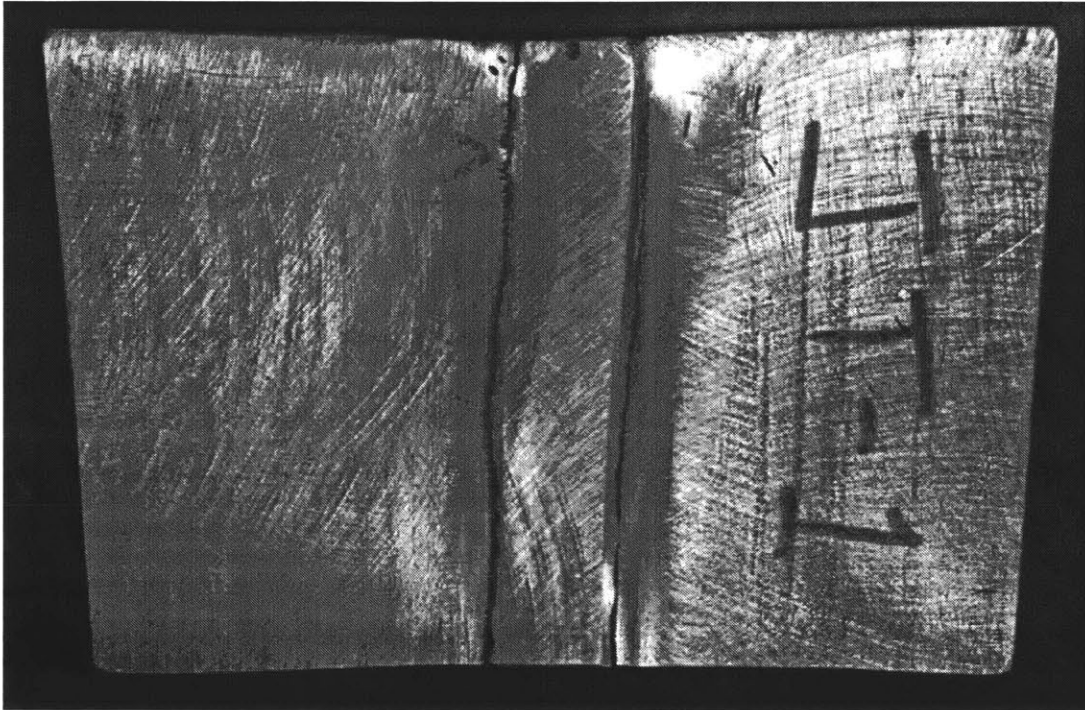


Figure 99: A section of the weld plate that was cut away and used for micrography and hardness testing. An identical section was sent to Sebastien Tesseyre at Idaho National Laboratory.

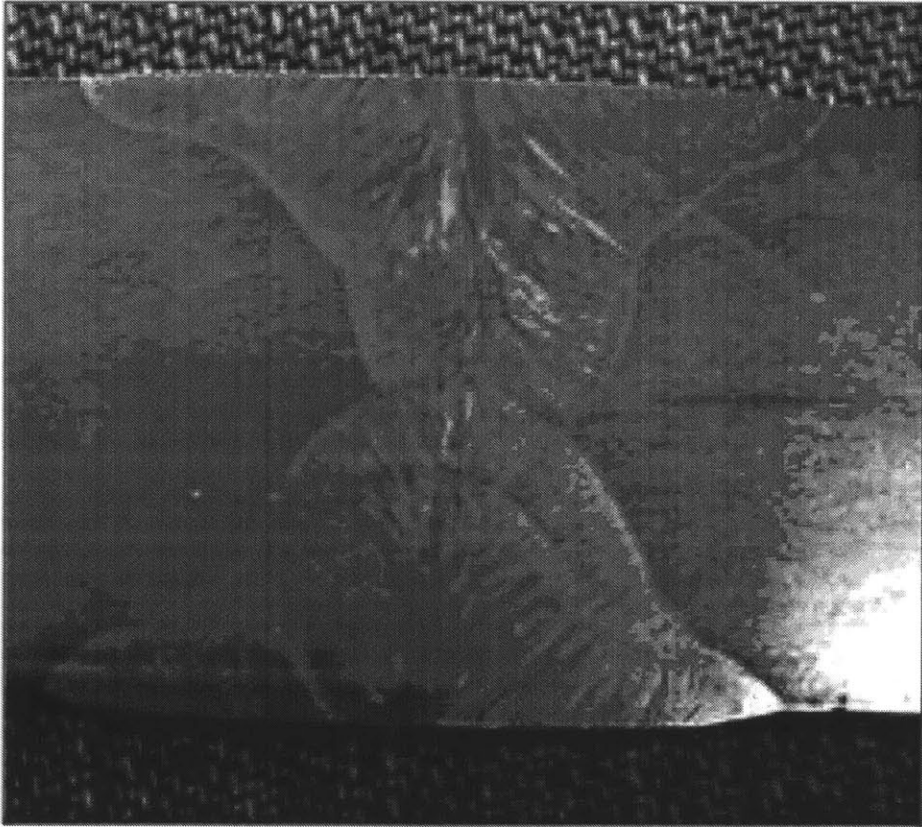


Figure 100: A polished weld specimen showing the geometry of the weld

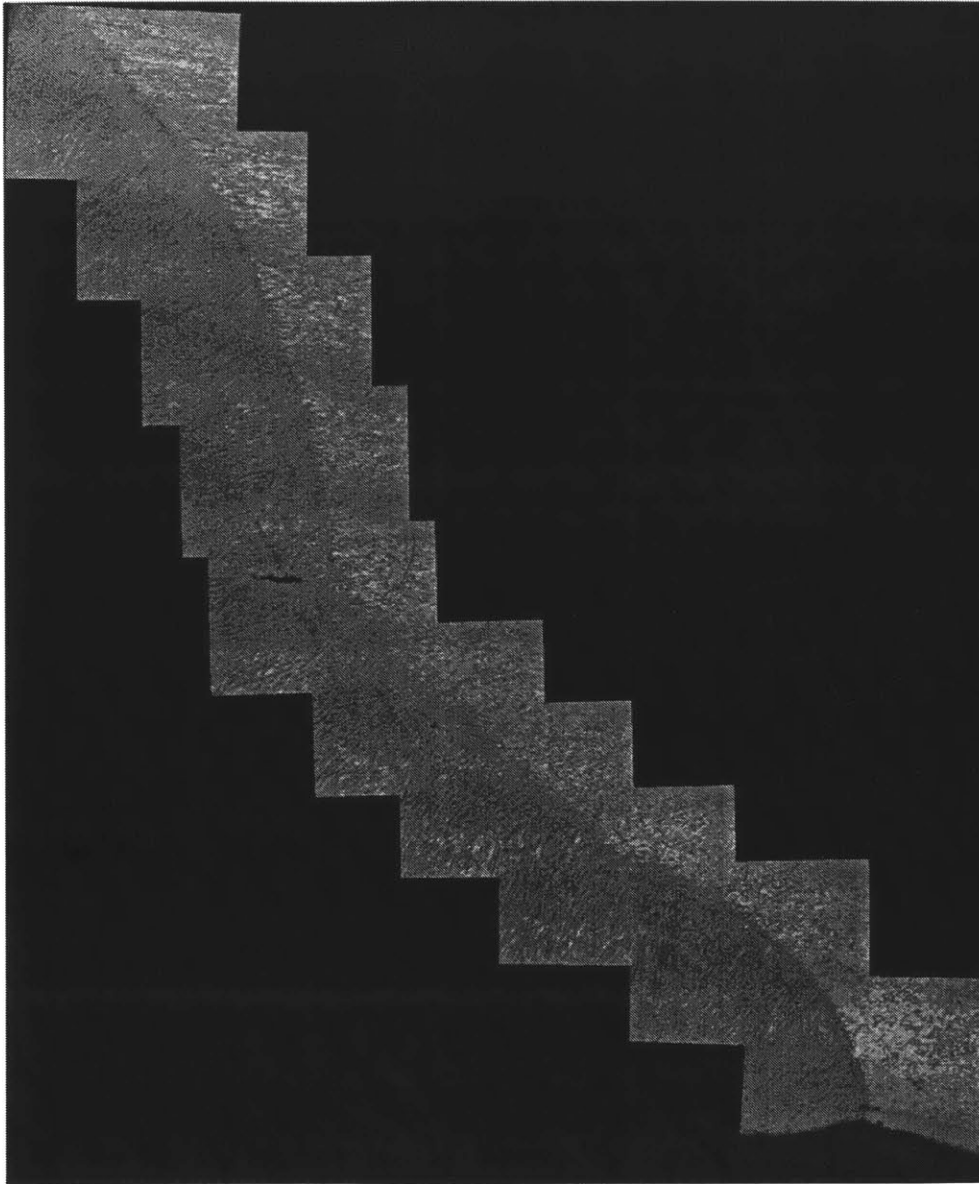


Figure 101: A composite micrograph showing the border of one of the "vees." The fusion line, where the weld material meets the the bulk material, is visibly small.

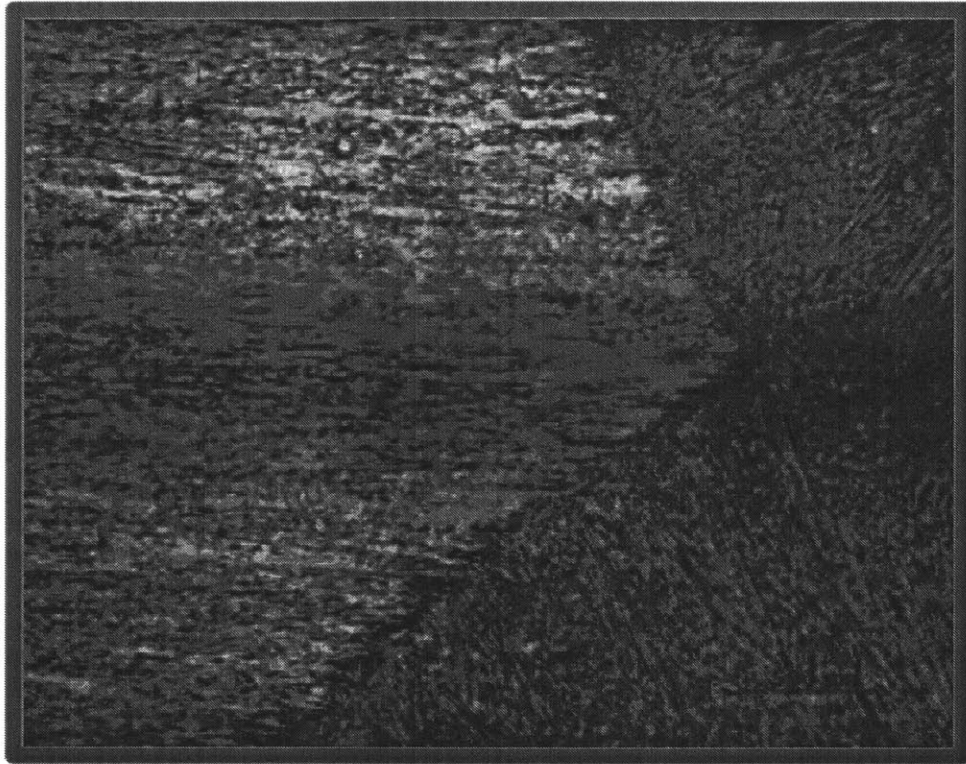


Figure 102: An etched and polished micrograph showing the intersection of the “vees” of the weld. This image was obtained by Y. Maruno, a visiting scientist at the H. H. Uhlig Corrosion Laboratory.

9.1.1 Results of hardness tests

Figure 103 gives the results of a standard Vickers hardness test carried out on a polished weld sample. The red line represents the location of the border between the weld material and the bulk material. The hardness was measured in a straight light, starting on one side of the weld and going straight across to the other side of the weld, across the fusion line, and into the bulk. A symmetric hardness distribution is visible between 0 and 6000 μm . The hardness is low (around 145), rises to approximately 166, and then drops again before rising back to the 166-168 range. This hardness value is constant through the fusion line, before rising to above 180 in the bulk material.

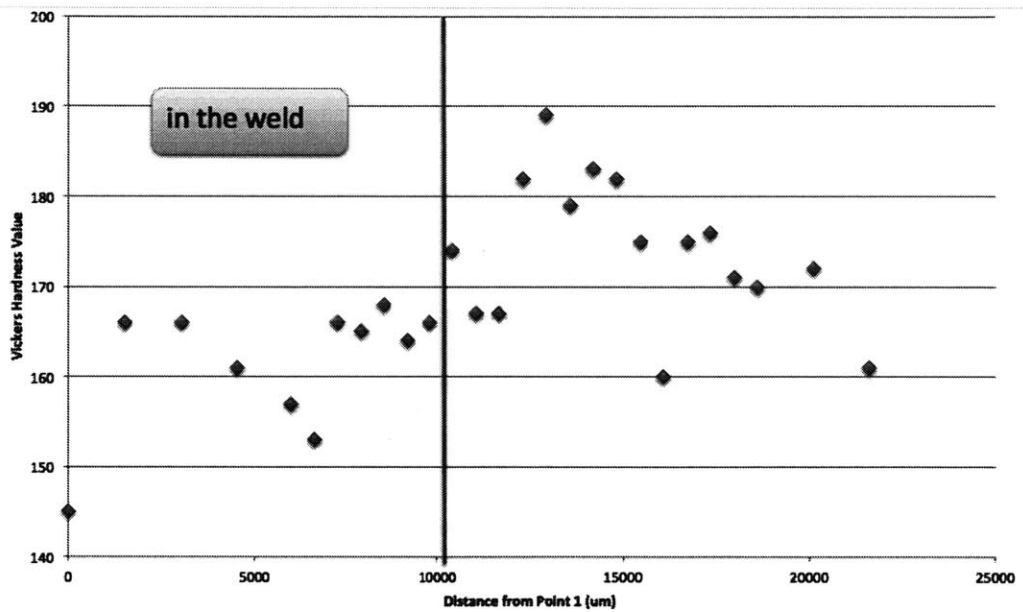


Figure 103: The results of a hardness test of the weld specimen. The hardness test consisted of a horizontal linescan that spanned the weld and entered approximately 10 mm into the bulk material.

9.2 Neutron diffraction testing

Neutron diffraction allows the measurement of lattice spacing in a metal sample in three dimensions. By comparing variations in the lattice spacing to the known, unstressed lattice spacing, the residual stresses present in the material can be determined.¹¹⁵ Therefore, neutron diffraction measurements of the prototypical weld material will result in experimental measurements of the residual stresses present in the sample, both in and near the weld, using a well-validated experimental method [106].

A proposal was submitted to the Canadian Institute for Neutron Scattering in order to obtain beamtime to perform neutron diffraction measurements at Chalk River Laboratories (CRL) of the National Research Council of Canada. These measurements were carried out by Dr. Ronald Rogge of CRL in fall of 2014. Douglas Jonart of MIT attended the measurements.¹¹⁶

Figures 104, 105, and 106 show preliminary strain measurements on a sample of the weld.¹¹⁷ These measurements were carried out on a sample similar to the one that can be seen in Figure 99. The measurements begin approximately 35 mm to the left of the weld centerline, continue across the weld in a straight line, and end approximately 35 mm to the right of the weld centerline. The measurements were carried out near the center of the

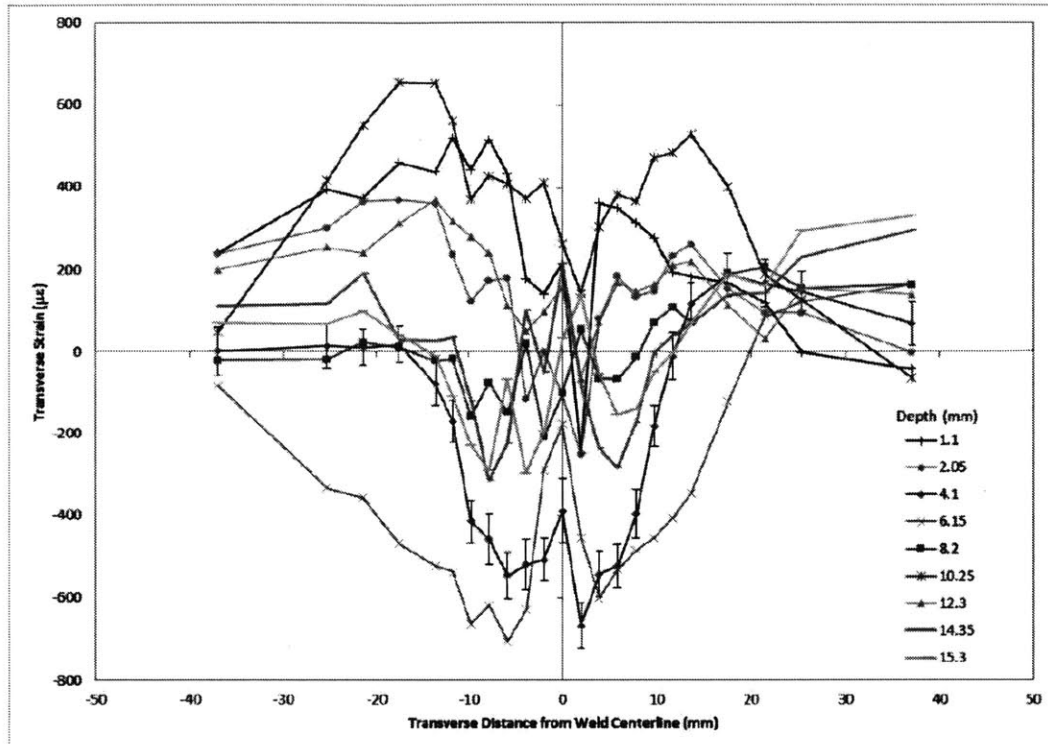
¹¹⁵Neutron diffraction has been used to measure residual stresses in steel welds before. Some examples in the literature include:

- M. Mochizuki, M. Hayashi, and T. Hattori, “Numerical analysis of welding residual stress and its verification using neutron diffraction measurement,” *Journal of Engineering Materials and Technology*, **122**(1), 2000, [107].
- S. Pratihari, M. Turski, L. Edwards, P. J. Bouchard, “Neutron diffraction residual stress measurements in a 316L stainless steel bead-on-plate weld specimen,” *International Journal of Pressure Vessels and Piping*, **86**(1), 2009, [108].
- A. P. Reynolds, W. Tang, T. Gnaupel-Herold, and H. Prask, “Structure, properties, and residual stress of 304L stainless steel friction stir welds,” *Scripta Materiala*, **48**(9), 2003, [109].

¹¹⁶I was the main author on the proposal, but I no longer officially worked for this project in fall 2014, when our beamtime was scheduled.

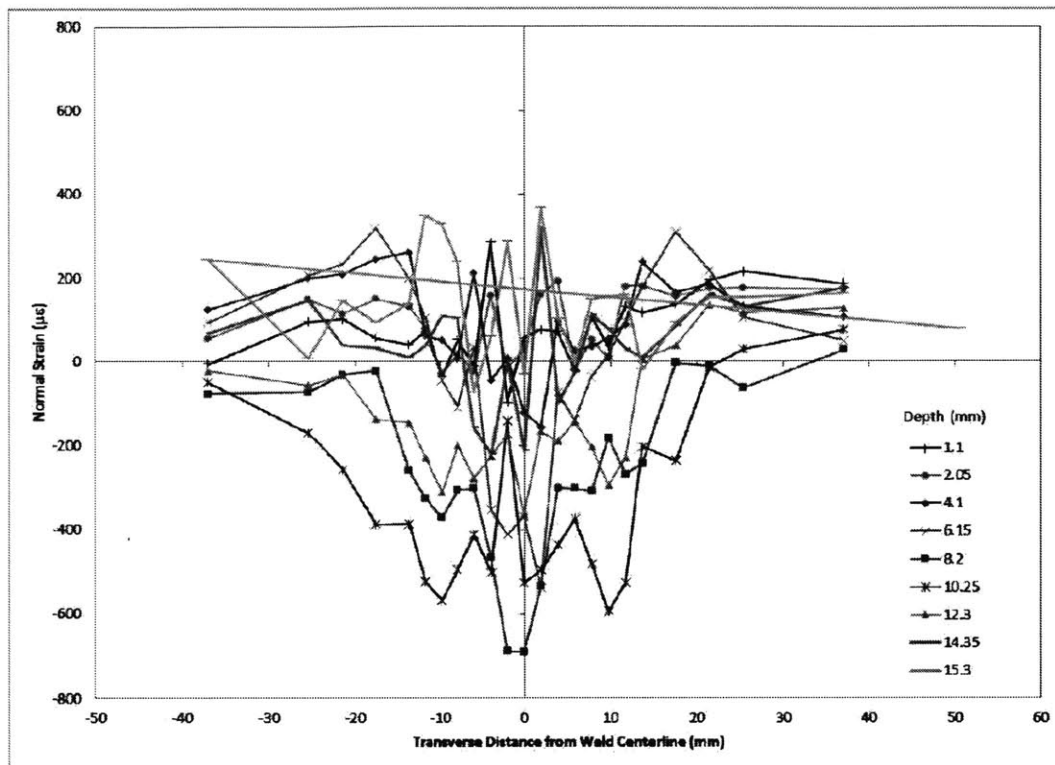
¹¹⁷Additional photographs of the measurement setup and the original proposal for beamtime are omitted in this version of the thesis, but can be made available for reference. Contact information: seferry@mit.edu.

sample plate (approximately 5 mm below the center of the sample).



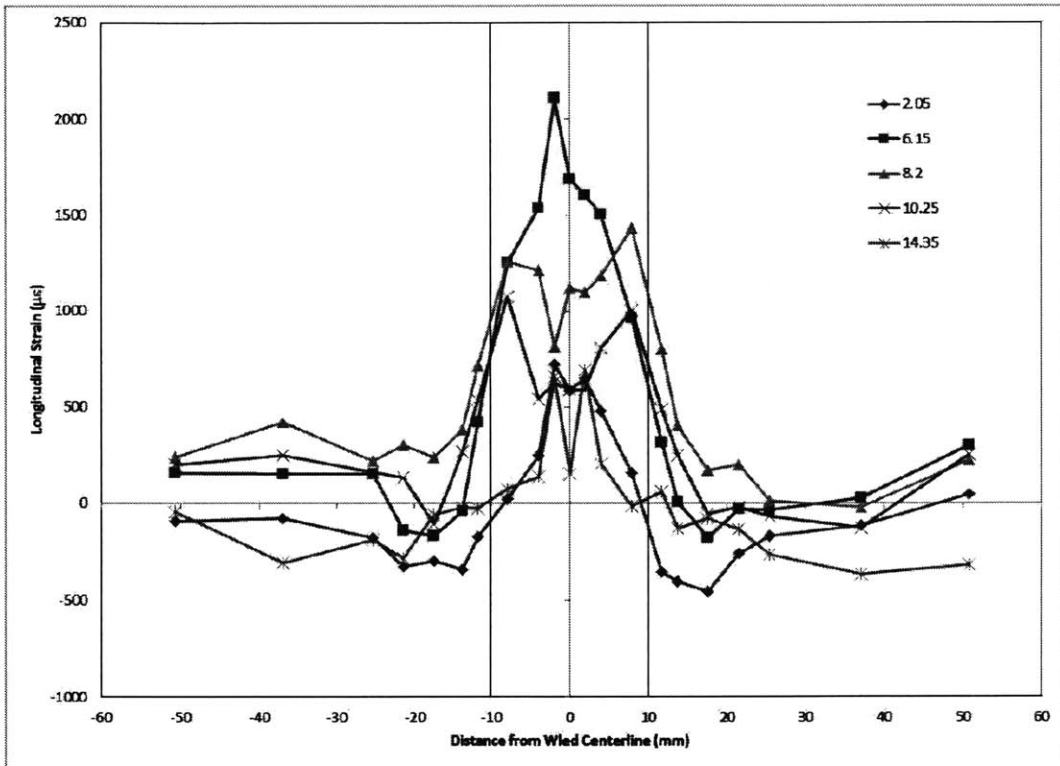
Transverse Strain Data, Analysis Plane #1

Figure 104: Preliminary results from [105].



Normal Strain Data, Analysis Plane #1

Figure 105: Preliminary results from [105].



Longitudinal Strain Data, Analysis Plane #1

Figure 106: Preliminary results from [105].

References

- [1] How many nuclear power plants are in the U.S. and where are they located? Online, 6 2014. <http://www.world-nuclear.org/info/Country-Profiles/Countries-T-Z/USA-Nuclear-Power/>.
- [2] Nuclear Power in the U.S.A. Online, 6 2014. <http://www.eia.gov/tools/faqs/faq.cfm?id=207t=3>.
- [3] Nuclear Regulatory Commission. Map of I.S.F.S.I.s in the United States. Online, 6 2014. <http://www.nrc.gov/waste/spent-fuel-storage/map-fuel-storage-facilities.pdf>.
- [4] Connecticut Yankee. "Fuel Storage". Online, 6 2014. http://www.connyankee.com/html/fuel_storage.html.
- [5] UxC Consulting. Dry cask storage in the U.S. by vendor. (164), 2012. <http://www.uxc.com/products/pdf/STF164.pdf>.
- [6] Denny A. Jones. *Principles and prevention of corrosion*. Macmillan, 1992.
- [7] N. Sato. A theory for breakdown of anodic oxide films on metals. *Electrochimica Acta*, 16(10):1683–1692, 1971.
- [8] L. F. Lin, C. Y. Chao, and D. D. Macdonald. A point defect model for anodic passive films, II: Chemical breakdown and pit initiation. *Journal of the Electrochemical Society*, 128(6):1194–1198, 1981.
- [9] Y. Chao, L. F. Lin, and D. D. Macdonald. A point defect model for anodic passive films, (I: Film growth kinetics). *Journal of the Electrochemical Society*, 128(6):1187–1194, 1981.

- [10] T. Okada. Halide nuclei theory of pit initiation in passive metals. *Journal of the Electrochemical Society*, 131(2):241–247, 1984.
- [11] T. Shibata and T. Takeyama. Pitting corrosion as a stochastic process. *Nature*, 260:315–316, 1976.
- [12] T. Shibata and T. Takeyama. Stochastic theory of pitting corrosion. *Corrosion*, 33(7):243–251, 1977.
- [13] H. W. Pickering and R. P. Frankenthal. On the mechanism of localized corrosion of iron and stainless steel I. Electrochemical studies. *Journal of the Electrochemical Society*, 119(10):1297–1304, 1972.
- [14] T. R. Beck and R. C. Alkire. Occurrence of salt films during initiation and growth of corrosion pits. *Journal of the Electrochemical Society*, 126(10):1662–1666, 1979.
- [15] E. E. Mola, B. Mellein, E. M. R. de Schiapparelli, J. L. Vicente, R. C. Salvarezza, and A. J. Arvia. Stochastic approach for pitting corrosion modeling, I: The case of quasi-hemispherical pits. *Journal of the Electrochemical Society*, 137(5):1384–1390, 1990.
- [16] G. A. Henshall. Stochastic modeling of the influence of environment on pitting corrosion damage of radioactive-waste containers. In *MRS Proceedings*, volume 353, page 679. Cambridge University Press, 1994.
- [17] G. A. Henshall. Modeling pitting degradation of corrosion resistant alloys. Technical report, Lawrence Livermore National Lab., CA (United States). Funding organization: USDOE Office of Civilian Radioactive Waste Management, Washington, D.C. (United States), 1996.

- [18] Y. Kondo. Prediction of fatigue crack initiation life based on pit growth. *Corrosion*, 45(1):7–11, 1989.
- [19] P. L. Andresen and F. P. Ford. Life prediction by mechanistic modeling and system monitoring of environmental cracking of iron and nickel alloys in aqueous systems. *Materials Science and Engineering: A*, 103(1):167–184, 1988.
- [20] T. Nakayama and M. Takano. Application of a slip dissolution-repassivation model for stress corrosion cracking of AISI 304 stainless steel in a boiling 42% MgCl₂ solution. *Corrosion*, 42(1):10–15, 1986.
- [21] T. Shoji, S. Suzuki, and R. G. Ballinger. Theoretical prediction of SCC growth behavior—threshold and plateau growth rate. In *Seventh International Symposium on Environmental Degradation of Materials in Nuclear Power Systems—Water Reactors: Proceedings and symposium discussions. Volume 2*, 1995.
- [22] M. M. Hall Jr. Critique of the Ford–Andresen film rupture model for aqueous stress corrosion cracking. *Corrosion Science*, 51(5):1103–1106, 2009.
- [23] D. D. MacDonald and M. Urquidi-MacDonald. A coupled environment model for stress corrosion cracking in sensitized Type 304 stainless steel in LWR environments. *Corrosion Science*, 32(1):51–81, 1991.
- [24] K. Saito and J. Kuniya. Mechanochemical model to predict stress corrosion crack growth of stainless steel in high temperature water. *Corrosion Science*, 43(9):1751–1766, 2001.
- [25] O. F. Aly, A. H. P. Andrade, M. Mattar Neto, M. Szajn bok, and H. J. Toth. Modelling of primary water stress corrosion cracking (PWSCC) at control rod drive mecha-

- nism (CRDM) nozzles of pressurized water reactors (PWR). In *Environment-Induced Cracking of Metals International Conference*, volume 2, 2004.
- [26] J. Hickling, A. McIlree, and R. Pathania. Materials reliability program (MRP): Crack growth rates for evaluating primary water stress corrosion cracking (PWSCC) of thick-wall Alloy 600 materials (MRP-55) Revision 1. *Rapport EPRI*, 1006695, 2002.
- [27] G. Wu. A probabilistic-mechanistic approach to modeling stress corrosion cracking propagation in Alloy 600 components with applications. Master's thesis, 2011.
- [28] R. Ihara, M. Mochizuki, and S. Fujimoto. Probabilistic study of SCC initiation stage based on statistical analysis in 316L austenitic stainless steel. In *ASME 2013 Pressure Vessels and Piping Conference*, pages V06AT06A024–V06AT06A024. American Society of Mechanical Engineers, 2013.
- [29] O. Buck and R. Ranjan. Evaluation of a crack-tip-opening displacement model under stress corrosion conditions. In R. H. Jones and W. W. Gerberich, editors, *Modeling Environmental Effects on Crack Growth Processes*, pages 209–223. 1986.
- [30] G. Engelhardt, D. D. Macdonald, Y. Zhang, and B. Dooley. Deterministic prediction of corrosion damage in low pressure steam turbines. *Centre for Electrochemical Science and Technology, The Pennsylvania State University, University Park, PA*, 2005.
- [31] A. Turnbull, L. N. McCartney, and S. Zhou. A model to predict the evolution of pitting corrosion and the pit-to-crack transition incorporating statistically distributed input parameters. *Corrosion Science*, 48(8):2084–2105, 2006.

- [32] B. P. Black. Effect of residual stress on the life prediction of dry storage canisters for used nuclear fuel. Master's thesis, Massachusetts Institute of Technology, Cambridge, MA, 5 2013.
- [33] T. Ahn, G. Oberson, and S. DePaula. Chloride-induced stress corrosion cracking of austenitic stainless steel used for dry storage of spent nuclear fuel. *ECS Transactions*, (50):211–226, 31 2013.
- [34] G. Engelhardt and D. D. Macdonald. Estimation of corrosion cavity growth rate for predicting system service life. *Corrosion Science*, 46(5):1159–1187, 2004.
- [35] G. A. Henshall. Modeling pitting corrosion damage of high-level radioactive-waste containers using a stochastic approach. *Journal of Nuclear Materials*, (195):109–125, 1992.
- [36] M. A. M Ibrahim, S. S. Abd El Rehim, and M. M. Hamza. Corrosion behavior of some austenitic stainless steels in chloride environments. *Materials Chemistry and Physics*, 115(1):80–85, 2009.
- [37] G. Lorang, M. D. C. Belo, A. M. P. Simoes, and M. G. S. Ferreira. Chemical composition of passive films on AISI 304 stainless steel. *Journal of the Electrochemical Society*, 141(12):3347–3356, 1994.
- [38] M. Schütze, D. R. Holmes, and R. B. Waterhouse. *Protective oxide scales and their breakdown*. Wiley Chichester, 1997.
- [39] Y. Kobayashi, S. Virtanen, and H. Böhni. Microelectrochemical studies on the influence of Cr and Mo on nucleation events of pitting corrosion. *Journal of the Electrochemical Society*, 147(1):155–159, 2000.

- [40] L. F. Lin, G. Cragnolino, Z. Szklarska-Smialowska, and D. D. Macdonald. Stress corrosion cracking of sensitized Type 304 stainless steel in high temperature chloride solutions. *Corrosion*, 37(11):616–627, 1981.
- [41] D. B. Rigby. Evaluation of the technical basis for extended dry storage and transportation of used nuclear fuel. Technical report, U. S. Nuclear Waste Technical Review Board, 2010.
- [42] S. Chu. Failure modes and effects analysis (FMEA) of welded stainless steel dry cask storage systems. Technical Report 3002000815, EPRI, 2013.
- [43] H. Ahluwalia. Stress corrosion cracking. Online, 4 2014. <http://csidesigns.com/flowgeeks/stress-corrosion-cracking/>.
- [44] R. B. Mears and U. R. Evans. The probability of corrosion. *Transactions of the Faraday Society*, 31:527–542, 1935.
- [45] J. C. Farmer and R. D. McCright. Crevice corrosion and pitting of high level waste containers: integration of deterministic and probabilistic models. *Corrosion 98*, 1998. Paper No. 160.
- [46] J. C. Farmer et al. Crevice corrosion and pitting of high-level waste containers: a first step towards the integration of deterministic and probabilistic models. Technical report, 1997.
- [47] J. C. Farmer, G. E. Gdowski, R. D. McCright, and H. S. Ahluwalia. Corrosion models for performance assessment of high-level radioactive-waste containers. *Nuclear Engineering and Design*, (129):57–88, 1991.

- [48] J. C. Farmer, G. E. Gdowski, R. D. McCright, and H. S. Ahluwalia. Corrosion models for performance assessment of high-level radioactive-waste containers. *Nuclear engineering and design*, 129(1):57–88, 1991.
- [49] R. W. Staehle. Combining design and corrosion for predicting life. In R. N. Parkins, editor, *Life Prediction of Corrodible Structures*, volume 1, pages 138–291. NACE International, Houston, 1994.
- [50] ASTM. *Standard guide for examination and evaluation of pitting corrosion*, G46-05 edition, 2013.
- [51] D. A. Horner, B. J. Connolly, S. Zhou, L. Crocker, and A. Turnbull. Novel images of the evolution of stress corrosion cracks from corrosion pits. *Corrosion Science*, 53(11):3466–3485, 2011.
- [52] C. Brown. Technical article: Metallurgical evaluation of corroded paper processing equipment. Online, 2007. Element Materials Technology Group, <http://www.element.com/nl/informatie/resources/publicaties/technical-article-metallurgical-evaluation-of-corroded-paper-processing-equipment>.
- [53] Metallurgical Technologies Inc. Analysis of chloride and mic pitted still condenser tubes. Online, 2014. <http://met-tech.com/chloride-and-mic-pitting-in-condensortube.html>.
- [54] Swagelok Inc. Selecting fluid system components for use in sour oil fields. Online, 2010. <http://www.processonline.com.au/articles/44377-Selecting-fluid-system-components-for-use-in-sour-oilfields>.
- [55] J. R. Galvele. Transport processes and the mechanism of pitting of metals. *Journal of the Electrochemical Society*, (119):1297–1304, 10 1972.

- [56] G. S. Chen, K. C. Wan, M. Gao, R. P. Wei, and T. H. Flournoy. Transition from pitting to fatigue crack growth: modeling of corrosion fatigue crack nucleation in a 2024-T3 aluminum alloy. *Materials Science and Engineering A*, (219):126–132, 1996.
- [57] T. Shibata. Stochastic studies of passivity breakdown. *Corrosion Science*, (31), 1990.
- [58] R. B. Mears and R. H. Brown. Corrosion probability. *Industrial and Engineering Chemical Research*, (29), 1937.
- [59] D. E. Williams, C. Westcott, and M. Fleischmann. Stochastic models of pitting corrosion of stainless steels II. Measurement and interpretation of data at constant potential. *Journal of the Electrochemical Society*, 132(8):1804–1811, 1985.
- [60] F. P. Ford. Current understanding of the mechanisms of stress corrosion and corrosion fatigue. *Environment-Sensitive Fracture: Evaluation and Comparison of Test Methods*, pages 32–51.
- [61] M. M. Hall Jr. Film rupture model for aqueous stress corrosion cracking under constant and variable stress intensity factor. *Corrosion Science*, 51(2):225–233, 2009.
- [62] Weibull distribution. Online, 2012. en.wikipedia.org/wiki/Weibull_distribution.
- [63] A. Turnbull, L. N. McCartney, and S. Zhou. Modelling of the evolution of stress corrosion cracks from corrosion pits. *Scripta Materialia*, 54(4):575–578, 2006.
- [64] A. Turnbull, D. A. Horner, and B. J. Connolly. Challenges in modelling the evolution of stress corrosion cracks from pits. *Engineering Fracture Mechanics*, 76(5):633–640, 2009.

- [65] O. F. Aly, M. M. Neto, and M. Schwartzman. Preliminary study for extension and improvement on modeling of primary water stress corrosion cracking at control rod drive mechanism nozzles of pressurized water reactors. In *2009 International Nuclear Atlantic Conference (INAC 2009)*, 2009.
- [66] Omar. F. Aly, M. M. Neto, and M. Schwartzman. A methodology for modeling stress corrosion cracking with an example. 2011.
- [67] D. B. Wells, J. Stewart, A. W. Herbert, P. M. Scott, and D. E. Williams. The use of percolation theory to predict the probability of failure of sensitized, austenitic stainless steels by intergranular stress corrosion cracking. *Corrosion*, 45(8):649–660, 1989.
- [68] H. Böhni and H. H. Uhlig. Environmental factors affecting the critical pitting potential of aluminum. *Journal of the Electrochemical Society*, 116(7):906–910, 1969.
- [69] M. Kamaya and T. Kitamura. A simulation on growth of multiple small cracks under stress corrosion. *International Journal of Fracture*, 130(4):787–801, 2004.
- [70] H. H. Strehblow. Nucleation and repassivation of corrosion pits for pitting on iron and nickel. *Materials and Corrosion*, 27(11):792–799, 1976. Also published in *Werkst. Korros.*
- [71] C. L. McBee and J. Kruger. Localized corrosion. *NACE, Houston*, page 252, 1974.
- [72] T. P. Hoar. The production and breakdown of the passivity of metals. *Corrosion Science*, 7(6):341–355, 1967.
- [73] T. P. Hoar and W. R. Jacob. Breakdown of passivity of stainless steel by halide ions. 1967.

- [74] J. M. Kolotyrkin. Effects of anions on the dissolution kinetics of metals. *Journal of the Electrochemical Society*, 108(3):209–216, 1961.
- [75] K. J. Vetter, H. H. Strehblow, R. W. Staehle, et al. Localized Corrosion. *NACE, Houston*, page 240, 1974.
- [76] B. W. Brisson, R. G. Ballinger, and A. R. McIlree. Intergranular stress corrosion cracking initiation and growth in mill-annealed Alloy 600 tubing in high-temperature caustic. *Corrosion*, 54(7):504–514, 1998.
- [77] M. R. Wenman, K. R. Trethewey, S. E. Jarman, and P. R. Chard-Tuckey. A finite-element computational model of chloride-induced transgranular stress-corrosion cracking of austenitic stainless steel. *Acta Materialia*, 56(16):4125–4136, 2008.
- [78] Y. Zhang, R. Zhang, E. Chu, S. Zhou, and J. Liu. Numerical simulation of the surface corrosion damage evolution. In *International Association of Computer Science and Information Technology - Spring Conference, 2009*, pages 167–170. IEEE, 2009.
- [79] D. G. Harlow and R. P. Wei. A probability model for the growth of corrosion pits in aluminum alloys induced by constituent particles. *Engineering fracture mechanics*, 59(3):305–325, 1998.
- [80] A. R. Hoch, A. Honda, F. M. Porter, S. M. Sharland, and N. Taniguchi. Development of mathematical models for long-term prediction of corrosion behaviour of carbon steel overpacks for radioactive waste disposal. In *MRS Proceedings*, volume 465, page 683. Cambridge University Press, 1996.
- [81] E. I. Cote, J. Ferguson, and N. Tehsin. Statistical predictive modelling: A methodology to prioritize site selection for near-neutral pH stress corrosion cracking. In *2010*

- 8th International Pipeline Conference*, pages 967–975. American Society of Mechanical Engineers, 2010.
- [82] S. Jain, J. A. Beavers, F. Ayello, N. Sridhar, et al. Probabilistic model for stress corrosion cracking of underground pipelines using Bayesian networks. *CORROSION 2013*, 2013.
- [83] K. G. Papakonstantinou and M. Shinozuka. Probabilistic model for steel corrosion in reinforced concrete structures of large dimensions considering crack effects. *Engineering Structures*, 57:306–326, 2013.
- [84] A. Kosaki. Evaluation method of corrosion lifetime of conventional stainless steel canister under oceanic air environment. *Nuclear Engineering and Design*, 238(5):1233–1240, 2008.
- [85] D. D. McCracken and W. S. Dorn. Numerical methods and FORTRAN programming with applications in engineering and science. *Numerical methods and FORTRAN programming with applications in engineering and science*, 1, 1965. New York, NY.
- [86] G. V. Jeffreys and V. G. Jenson. *Mathematical methods in chemical engineering*. Academic Press, 1963.
- [87] J. Crank and P. Nicolson. A practical method for numerical evaluation of solutions of partial differential equations of the heat-conduction type. In *Mathematical Proceedings of the Cambridge Philosophical Society*, volume 43, pages 50–67. Cambridge University Press, 1947.
- [88] E. A. Nystrom, J. B. Lee, A. A. Sagüés, and H.W. Pickering. An approach for estimating anodic current distributions in crevice corrosion from potential measurements. *Journal of the Electrochemical Society*, 141(2):358–361, 1994.

- [89] Y. Xu and H. W. Pickering. The initial potential and current distributions of the crevice corrosion process. *Journal of the Electrochemical Society*, 140(3):658–668, 1993.
- [90] P. O. Gartland. A simple model of crevice corrosion propagation for stainless steels in seawater. Technical report, NACE International, Houston, TX (United States), 1997. Corrosion 97, Paper 417.
- [91] T. Liu and R. W. Weyers. Modeling the dynamic corrosion process in chloride contaminated concrete structures. *Cement and Concrete Research*, 28(3):365–379, 1998.
- [92] J. E. Strutt, J. R. Nicholls, and B. Barbier. The prediction of corrosion by statistical analysis of corrosion profiles. *Corrosion Science*, 25(5):305–315, 1985.
- [93] W. E. King, A. Arsenlis, C. Tong, and W. L. Oberkampf. Uncertainties in predictions of material performance using experimental data that is only distantly related to the system of interest. In *Uncertainty Quantification in Scientific Computing*, pages 294–311. Springer, 2012.
- [94] G. P. Sabol and S. B. Dalgaard. The origin of the cubic rate law in zirconium alloy oxidation. *Journal of the Electrochemical Society*, 122(2):316–317, 1975.
- [95] A. S. Khanna. *Introduction to high temperature oxidation and corrosion*. ASM International, 2002.
- [96] G. E. Gdowski and D. B. Bullen. Survey of degradation modes of candidate materials for high-level radioactive-waste disposal containers, Vol. 2, Oxidation and corrosion. *Lawrence Livermore National Laboratory Report UCID-21362 Vol.*

- [97] A. Turnbull and J. G. N. Thomas. A model of crack electrochemistry for steels in the active state based on mass transport by diffusion and ion migration. *Journal of the Electrochemical Society*, 129(7):1412–1422, 1982.
- [98] K. Zhao. 22.71 lecture, 10 2012. MIT.
- [99] T. M. Ahn. An approach to model abstraction of stress corrosion cracking damage in management of spent nuclear fuel and high-level waste. In *ASME 2013 Pressure Vessels and Piping Conference*, pages V06AT06A083–V06AT06A083. American Society of Mechanical Engineers, 2013.
- [100] R. G. Ballinger. Neup final narrative, cfp 11-1775, 2011.
- [101] T. Prosek, A. Iversen, C. Taxén, and D. Thierry. Low-temperature stress corrosion cracking of stainless steels in the atmosphere in the presence of chloride deposits. *Corrosion*, 65(2):105–117, 2009.
- [102] M. Mayuzumi, J. Tani, and T. Arai. Chloride induced stress corrosion cracking of candidate canister materials for dry storage of spent fuel. *Nuclear Engineering and Design*, 238(5):1227–1232, 2008.
- [103] C. S. Tedmon, D. A. Vermilyea, and J. H. Rosolowski. Intergranular corrosion of austenitic stainless steel. *Journal of the Electrochemical Society*, 118(2):192–202, 1971.
- [104] A. Turnbull. Modelling of environment assisted cracking. *Corrosion Science*, 34(6):921–960, 1993.
- [105] R. G. Ballinger, D. Jonart, and R. Rogge. Preliminary report: strain plots of prototypical canister weld sample, measured by neutron diffraction. Technical report, MIT and Canadian Institute for Neutron Scattering, 2014. Available upon request.

- [106] G. S. Schajer. *Practical residual stress measurement methods*. John Wiley & Sons, 2013.
- [107] M. Mochizuki and T. Hayashi, M. and Hattori. Numerical analysis of welding residual stress and its verification using neutron diffraction measurement. *Journal of engineering materials and technology*, 122(1):98–103, 2000.
- [108] S. Pratihari, M. Turski, L. Edwards, and P. J. Bouchard. Neutron diffraction residual stress measurements in a 316L stainless steel bead-on-plate weld specimen. *International Journal of Pressure Vessels and Piping*, 86(1):13–19, 2009.
- [109] A. P. Reynolds, W. Tang, T. Gnaupel-Herold, and H. Prask. Structure, properties, and residual stress of 304L stainless steel friction stir welds. *Scripta Materialia*, 48(9):1289–1294, 2003.
- [110] H. J. Engell and N. D. Stolica. Untersuchungen über lochfraß an passiven elektroden aus unlegiertem stahl in chlorionenhaltiger schwefelsäure. *Archiv für das Eisenhüttenwesen*, 30:239–248, 1959.
- [111] M. Janik-Czachor. An assessment of the processes leading to pit nucleation on iron. *Journal of the electrochemical society*, 128(12):513C–519C, 1981.
- [112] G. R. Matamala. Correlation model of the AISI 316 stainless steel pitting potential with cellulose bleach process variables. *Corrosion*, 43(2):97–100, 1987.
- [113] P. Glansdorff and I. Prigogine. *Thermodynamic Theory of Structure, Stability, and Fluctuations*. Wiley-Interscience, 1974.
- [114] T. Okada. A theory of perturbation-initiated pitting. *Journal of the Electrochemical Society*, 132(3):537–544, 1985.

- [115] S. Tsujikawa, Z. Heng, and Y. Hisamatsu. Critical potentials for crevice corrosion of Type 444 steel in NaCl solutions at 80 deg C (retroactive coverage). *Boshoku Gijutsu(Corros. Eng.)*, 32(3):149–156, 1983.
- [116] G. Salvago, G. Fumagalli, A. Mollica, and G. Ventura. A statistical evaluation of AISI 316 stainless steel resistance to crevice corrosion in 3.5% NaCl solution and in natural sea water after pre-treatment in HNO₃. *Corrosion Science*, 27(9):927–936, 1987.
- [117] T. Shibata and T. Takamiya. Critical issues in reducing the corrosion of steels (H. Leidheiser, Jr. & S. Haruyama Eds.), 1985.
- [118] G. Herbsleb and H. J. Engell. Untersuchungen über die lochfraßkorrosion des passiven eisens in chlorionenhaltiger schwefelsäure. *Materials and Corrosion*, 17(5):365–376, 1966.
- [119] A. Broli, H. Holtan, and T. B. Andreassen. Kinetics for pitting corrosion of a 13 Cr steel in neutral chloride solutions. *Materials and Corrosion*, 27(7):497–504, 1976.
- [120] Z. Szklarska-Smialowska and M. Janik-Czachor. Electrochemical investigation of the nucleation and propagation of pits in iron-chromium alloys. *British Corrosion Journal*, 4(3):138–145, 1969.
- [121] J. R. Scully. Appendix D, elicitation interview summaries. *Waste Package Degradation Expert Elicitation Project Final Report*, K. J. Coppersmith, R. C. Perman, M. Pendleton, J. L. Younker, *Civilian Radioactive Waste Management System Management and Operating Contractor*, 1997. San Francisco, CA.

- [122] D. D. Macdonald. On the modeling of stress corrosion cracking in iron and nickel base alloys in high temperature aqueous environments. *Corrosion Science*, 38(6):1003–1010, 1996.
- [123] E. M. Gutman. An inconsistency in “film rupture model” of stress corrosion cracking. *Corrosion science*, 49(5):2289–2302, 2007.
- [124] T. Magnin, R. Chieragatti, and R. Oltra. Mechanism of brittle fracture in a ductile 316 alloy during stress corrosion. *Acta Metallurgica et Materialia*, 38(7):1313–1319, 1990.
- [125] T Magnin, A Chambreuil, and B Bayle. The corrosion-enhanced plasticity model for stress corrosion cracking in ductile fcc alloys. *Acta Materialia*, 44(4):1457–1470, 1996.
- [126] F. P. Ford, D. F. Taylor, P. L. Andresen, and R. G. Ballinger. Environmentally controlled cracking of stainless and low alloy steels in light water reactor environments. *EPRI Report*, 1987.
- [127] M. O. Speidel and R. Magdowski. Stress corrosion crack growth in Alloy 600 exposed to PWR and BWR environments. In *CORROSION National Association of Corrosion Engineers Annual Conference*. NACE, 2000.
- [128] H. Nishitani and Y. Murakami. Stress intensity factors for elliptical and semi-elliptical cracks. *Transactions of the Japan Society of Mechanical Engineers*, 40:31–40, 1974.
- [129] Peter M Scott. An analysis of primary water stress corrosion cracking in pwr steam generators. 1991.

- [130] R. B. Rebak, Z. Xia, and Z. Szklarska-Smialowska. Effect of temperature and cold work on the crack growth rate of Alloy 600 in primary water. *Corrosion*, 51(9):689–697, 1995.
- [131] L. G. Ljungberg, D. Cubicciotti, and M. Trolle. Effect of water impurities in BWR on environmental crack growth under realistic load conditions. In *Proceedings of the Fourth International Symposium on Environmental Degradation of Materials in Nuclear Power Systems-Water Reactors*, pages 4–59, 1989.
- [132] B. Alexandreanu, O. K. Chopra, and W. J. Shack. Crack growth rates and metallographic examinations of Alloy 600 and Alloy 82/182 from field components and laboratory materials tested in PWR environments. Technical report, Argonne National Laboratory (ANL), 2008.
- [133] Electric Power Research Institute. Effects of marine environments on stress corrosion cracking austenitic stainless steels. Technical report, Electric Power Research Institute, 2005. 1011820.
- [134] T. H. McCloskey, R. B. Dooley, and W. P. McNaughton. Turbine steam path damage: theory and practice. *Electric Power Research Institute*, 1999. Palo Alto, CA.
- [135] K. Shirai, J. Tani, T. Arai, M. Wataru, H. Takeda, and T. Saegusa. SCC evaluation of multi-purpose canister. In *Proceedings of 2011 International Radioactive Waste Management Conference (IHLRWMC)*, pages 10–14.
- [136] J. A. Gorman, K. D. Stavropoulos, W. S. Zemitis, and M. E. Dudley. Pwscc prediction guidelines. *EPRI Final Report TR-104030 Project*, pages 2812–15, 1994.
- [137] F. P. Ford, D. F. Taylor, P. L. Andresen, and R. G. Ballinger. Epri np-5064m, project 2006-6, final report. *Electric Power Research Institute*, 1987. Palo Alto, CA.

- [138] G. P. Marsh, K. J. Taylor, and Z. Sooi. The kinetics of pitting corrosion of carbon steel. In *SKB Technical Report 88-09*. Swedish Nuclear Fuel and Waste Management Company Box 5864, S-102 48, 1988. Stockholm, Sweden.